Université de Paris

Marie Skłodowska-Curie Actions

Ecole doctorale Chimie Physique et Chimie analytique ED388

Laboratoire ITODYS UMR-CNRS 7086

ELABORATION OF FUNCTIONAL MATERIALS TOWARDS WIRELESS PHOTOELECTROCHEMICAL MICROMOTORS

Par Eswaran Murugasen

Thèse de doctorat de Chimie/Chimie physique

Spécialité : Chimie Energie Nanosciences Surfaces

Dirigée par Hyacinthe Randriamahazaka

Présentée et soutenue publiquement le 10 Décembre 2019

Devant un jury composé de:

Prof. Samy REMITA	Conservatoire National des Arts et Metiers (CNAM) & Université Paris Sud	Rapporteur
Dr. Cédric PLESSE	Université de Cergy- Pontoise	Rapporteur
Prof. François MAUREL	Université de Paris	Examinateur
Prof. Pierre AUDEBERT	École normale supérieure Paris-Saclay	Examinateur
Dr. Jalal GHILANE	Université de Paris	Co-encadrant
Prof. Hyacinthe RANDRIAMAHAZAKA	Université de Paris	Directeur de thèse

Except where otherwise noted, this work is licensed under https://creativecommons.org/licenses/by-nd/3.0/fr/

Acknowledgements

Any accomplishment needs the effort of many people and this thesis is no different. Here I wish to express my gratitude to those who have contributed to this thesis.

Foremost, I am highly indebted to Prof. Hyacinthe RANDRIAMAHAZAKA for accepting me as a doctoral candidate in his group. His constant supervision and diligence enable me to obtain these results. Apart from multitasking, I have also learned from him how to systematically approach the research problems. Also thank Dr. Jalal GHILANE for his co-supervision and his timely help in solving some difficulties in experiments.

Thanks to the jury members: Prof. Samy REMITA, Dr. Cédric PLESSE, Prof. François MAUREL and Prof. Pierre AUDEBERT for their acceptance to ameliorate this thesis by their critical evaluation.

Special mention to EU-H2020-MSCA ITN MICACT network that provides financial support and lot of opportunities to learn new scientific and career oriented topics, to interact with people from diverse scientific backgrounds. I thank all the people - ESRs, supervisors, coordinators - involved in MICACT project.

Extend my gratitude to Prof. Edwin JAGER, Linköping University – Sweden for accepting me as a visiting researcher in his group and offered conducive friendly research environment, great support and guidance. I thank his group members specially Jose, Yong, Manav and my other friends in IFM department.

Extend my thanks to all the members of ITODYS for the pleasant working atmosphere, particularly to the director Prof. François MAUREL and co-director Prof. Jean Christophe LACROIX for constant support and advice. Also Pierre-François QUENIN for administrative stuffs and Aymeric NOËL for Computer and softwares. Many thanks to technicians for the sample characterization. Special thanks to my friends, colleagues and office mates especially Ai Yong, Thuan, Dihia, Quỳnh, Quyền and Andrés etc., I thank profoundly each and every one who directly and indirectly contributed to this thesis.

I would deeply appreciate my former supervisors and their teams: Prof.S.Yashonath and Prof. N.Munichandraiah from Indian Institute of Science – Bengaluru for providing me the opportunity to enter the research field and Prof. W.Jaegermann, TU Darmstadt, Germany for coming to Europe. I have learned many things from them to inculcate in my research path.

Finally, I thank all my family members particularly my parents, wife and daughter for their valuable support.

Appreciate all of you !!!

Titre : ELABORATION DE MATERIAUX FONCTIONNELS VERS DES MICROMOTAURS PHOTOELECTOCHIMIQUE

Résumé :

L'objectif principal de cette thèse est la fabrication et l'étude de dispositif pour le développement d'un micromoteur photoélectrochimique sans fil bioinspiré. Dans ce cadre, pour convertir l'énergie solaire en énergie chimique, en particulier en peroxyde d'hydrogène, des photoanodes à base d'hématite fonctionnalisées ont été réalisées. Des matériaux à base d'anthraquinone ont été utilisées et déposer sur la surface de l'électrode. Pour la conversion de l'énergie chimique en énergie mécanique, un micromoteur à l'oxyde de manganèse a été utilisé. La première partie de ce travail traite la fabrication du micromoteur moteur à base de MnO_2 en utilisant un procédé d'électrodéposition. Ce processus est assez simple, peu coûteux et efficace. Le micromoteur à base de MnO_2 ainsi préparé présentait une propulsion sans fil induite par la génération de H_2O_2. Diverses formes telles que des formes carrées, rectangulaires et circulaires de micromoteurs ont été préparées et étudier. Par la suite, nous avons développé des microvéhicules par procédé de microfabrication. Ces derniers fournissent ainsi une stimulation mécanique individuelle à différentes tensions. Enfin, nous avons étudié la fonctionnalisation des surfaces de photoanodes d'hématite avec des molécules redox déposées par électrogreffage et par des méthodes de polymérisation sur la surface SI-ATRP. L'étude des surfaces modifiées, par des techniques électrochimiques, montre que les performances photoélectrochimiques de l'hématite électrogreffée par la molécule redox sont inférieures à celles immobilisée via un procède de polymérisation.

Mots clefs : Electrochimie, électrodéposition,photo-électrochimie, micromoteurs, autopropulsion.

Title : Elaboration of Functional Materials towards wireless photoelectrochemical micromotors

Abstract :

The main objective of this thesis is the fabrication and device study for the development of a bioinspired wireless photoelectrochemical micromotor. In this context, to convert solar energy into chemical energy, in particular hydrogen peroxide, functionalized hematite-based photoanodes have been produced. Anthraquinone-based materials have been used and deposited on the surface of the electrode. For the conversion of chemical energy into mechanical energy, a micromotor with manganese oxide was used. The first part of this work deals with the manufacture of the MnO_2 micromotor using an electroplating process. This process is quite simple, inexpensive and effective. The MnO_2-based micromotor exhibited wireless propulsion induced by the generation of H_2O_2. Various shapes such as square, rectangular and circular forms of micromotors have been prepared and studied. Subsequently, we developed microcarriers by microfabrication process. The latter provide individual mechanical stimulation at different voltages. Finally, we studied the functionalization of hematite photoanode surfaces with redox molecules deposited by electrografting and by polymerization methods on the surface “SI-ATRP”. The study of the modified surfaces, by electrochemical techniques, shows that the photoelectrochemical performances of the hematite electrografted by the redox molecule are lower than those immobilized via a polymerization process.

Keywords : Electrochemistry, electrodeposition, photo-electrochemistry, micromotors, self-propulsion.

The results obtained in this thesis have been presented as oral and poster presentations in the following international scientific meetings / conferences:

Posters

- Fabrication of flexible nickel electrode for wireless self-propelling actuators, in Sixth international conference on Electromechanically Active Polymer (EAP) transducers & artificial muscles **(EuroEAP-2016) Helsingør (Copenhagen), Denmark**. 14-15 June 2016

- MnO_2 based micromotor : fabrication, characterization and potential application, in Seventh international conference on Electromechanically Active Polymer (EAP) transducers & artificial muscles **(EuroEAP-2017) Cartagena, Spain.** 6-7 June 2017

- Catalytic micromotor based on MnO_2: facile fabrication and toward chemotactic application, in Eighth international conference on Electromechanically Active Polymer (EAP) transducers & artificial muscles **(EuroEAP-2018) Lyon, France**. 5-6 June 2018

Oral Presentation

- Flash talks on 'Fabrication of flexible nickel electrode for wireless self-propelling actuators', in **EuroEAP-2016, Denmark**. 14-15 June 2016 and on 'MnO_2 based micromotor: fabrication, characterization and potential application' in **EuroEAP-2017, Spain**. 6-7 June 2017 and on 'Catalytic micromotor based on MnO_2: facile fabrication and toward chemotactic application' in **EuroEAP-2018, France**. 5-6 June 2018

- 'Towards photoelectrochemical actuator' in Congrès des doctorants, ITODYS, University Paris Diderot, France. 03-November-2016

- "Self-propelling wireless micromotor based on MnO_2 composite and H_2O_2 fuel" in 9th World Congress of Biomimetics, Artificial Muscles and Bio-Nano **(BAMN-2017), Wollongong, Australia**, 25-27 September-2017

- "Poly ionic liquid immobilized hematite for photoelectrochemical water splitting " in 3rd Journee de GDR Solar Fuels, **College de France – Paris, France**. 30th May & 1st June-2018.

- "Elaboration of multifunctional hybrid materials for photoelectrochemical micromotor" in 2018 MICACT Yearly Meeting Workshop in **Lyon, France**. 07th June-2018.

ABBREVIATIONS

ACN	Acetonitrile
AFM	Atomic force microscopy
AQ	anthraquinone
AQH_2	hydroanthraquinone
Bu_4NBF_4	Tetrabutylammomium tetrafluoroborate
CH_2Cl_2	Dichloromethane
CV	cyclic voltammogram
C_{bulk}	Direct charge transfer capacitance
C_{trap}	Chemical / Surface state / indirect charge transfer capacitance
DA	Dopamine
DMAB	DiMethyl Amino Borane
DMF	dimethylformamide
DMSO	Dimethyl sulfoxide
E^o	formal potential
E	potential
E_p	peak potential
ΔE	peak separation
[EMIM]	1,3-dimethylimidazolium
[EdMIm][TFSI]:	1-Ethyl-2,3-dimethylimidazolium bis(trifluoromethylsulfonyl)imide
equiv.	Equivanlent
F_{max}, ω_{max}	Maximum frequency
Fc	ferrocene
Fc^+:	Ferrocenium
Fc-MIM TFSI	1-ferrocenylmethyl-3-

	methylimidazolium bis(trifluoromethanesulfonyl)amide
GC	glassy carbon
HTFSI	trifluoromethanesulfonimide
hrs	hours
IL	ionic liquid
ITO	Indium tin oxide electrode
IMPS	Intensity Modulated Photocurrent Spectroscopy
IR (ATR)	Infrared (Attenuated Total Reflection)
K_{trans}	Charge Transfer rate constant
K_{rec}	Charge Recombination rate constant
k_{app}	apparent rate constants for electron transfer
LSV	Linear Sweep Voltammetry
[MAEImMFc][TFSI]	(2-methacryloyloxy ethyl)-1- (N-(ferrocenylmethyl) imidazolium bis(trifluoromethylsulfonyl)imide
mn	Minute
MNM	Micro-Nano-motor
NBD	4-nitrobenzenediazonium tetrafluoroborate
NMR	nuclear magnetic resonance
NBu_4Br	tetrabutylammonium bromide
NP	Nitrophenyl
η_{trans}	Charge transfer efficiency
PANI	Poly Aniline
PEIS	PhotoElectrochemical Impedance Spectroscopy

PMDETA	pentamethyl-diethylenetriamine
PIL, poly(IL)	poly(ionic liquid)
poly(FcIL)	poly(ionic liquid) containing ferrocene
PFcMA	Poly ferrocene methacrylate
R_s	Solution resistance
$R_{trapping}$	Recombination resistance
$R_{ct,trap}$	Indirect charge transfer resistance
$R_{ct,bulk}$	Direct charge transfer resistance
RT	room temperature
RTIL	Room Temperature Ionic Liquids
SCE	saturated calomel electrode
SDS	sodium dodecyl sulfate
SEEP	Surface Electro-initiated Emulsion Polymerization
SI-ATRP	Surface-initiated atom transfer radical polymerization
[TFSI]	bis(trifluoromethanesulfonyl)amide
THF	Tetrahydrofuran
T_m	melting temperature
TSILs	task-specific ionic liquids
UME	Ultramicroelectrode
UV-vis	ultraviolet-visible
[VAQIm][TFSI]:	N-ethyleneamidoanthraquinone-N-vinylimidazoliumbis (trifluoromethylsulfonyl)imide
XPS	X-ray photoelectron spectroscopy
Γ	surface concentration

CONTENTS

Acknowledgments

Summary

Sommaire

Contents

CHAPTER 1: Elaboration and Properties of Actuators and Micromotors

1. Artificial Muscles **1**

1.1. Actuators – General Introduction **1**

1.2. Electronic Artificial Muscles **2**

1.2.1. Dielectric elastomer actuators (DEAs) 2

1.2.2. Electrostrictive relaxor ferroelectric polymers 4

1.2.3. Electrostrictive graft elastomers 5

1.2.4. Liquid crystal elastomers 6

1.3. Ionic Artificial Muscles **6**

1.3.1. Conducting polymers 7

1.3.2. CNT actuators 8

1.3.3. Ionic polymer-metal composites (IPMCs) 9

2. Micromotor – General Introduction **11**

2.1. Propulsion Mechanism **14**

2.2. Micromotor Fabrication Methods **15**

2.2.1. Electroless and Electrochemical deposition methods 15

2.2.1.1. Membrane Template Assisted Electrodeposition Methods 15

2.2.1.2. Other Template Assisted Electrodeposition Methods 18

2.2.1.3. Bipolar Electrodepostion Method 19

2.2.2. Physical Vapour Deposition (PVD) methods 20

2.2.3. Original materials 23

2.3. Motion manipulation of Micro/Nanomotors 24

2.3.1. Light control 25

2.3.2. Magnetic control 26

2.3.3. Acoustic control 27

2.3.4. Electric field control 27

2.3.5. Thermal control 28

2.3.6 Chemotaxis 28

2.4. Applications of Micro/Nanomotors 28

2.4.1. For cargo transport 28

2.4.2. For biomedical applications 29

2.4.3. For environmental applications 30

References 31

Chapter – 2 Fabrication and Characterization of Manganese Oxide Based Micromotor

2. Manganese oxide micromotors 39

2.1. Introduction 39

2.2. Surface-Grafted Polymer Assisted Metal Deposition (PAMD) 41

2.2.1. Cationic polymers as anchoring layer 42

2.2.2. Anionic polymers as anchoring layer 44

2.2.3. Non-ionic polymers as anchoring layer 46

2.2.4. Downsides of PAMD 47

2.3. Preparation of flexible nickel substrate 47

2.3.1. Flexible Nickel substrate as an electrode 48

2.3.2. Electrodeposition of PANI 49

2.3.3. Electrodeposition of MnO_2 51

2.3.4. Surface characterization 52

2.4. Self-propulsion mechanism 53

2.4.1. Influence of shape, fuel concentration and pH 55

2.5. Controlled movement of micromotors – An overview 57

2.5.1. Aim of this part 58

2.6. Control of movement by chemotaxis 58

2.6.1. Chemotaxis – A bio-inspired approach 59

2.7. Control of micromotor movement by tuning the porosity of PPy 65

2.7. 1. MnO_2 electrodeposition 65

2.7.2. Electrodeposition of PPy(DBS) 66

2.7.3. Porosity tuning of PPy(DBS) 67

2.7.4. Photolithography – A brief overview 69

2.7.4.1. Wafer and Wafer Cleaning 70

2.7.4.2. Barrier Layer Formation 71

2.7.4.3. Photoresist Application 71

2.7.4.4. Soft Baking or Prebaking 71

2.7.4.5. Mask Alignment 71

2.7.4.6. Photoresist Development and Exposure 72

2.7.4.7. Hard Baking 72

2.7.4.8. Etching 72

2.7.4.9. Photoresist Removal 74

2.7.5. Microfabrication 74

2.8. Conclusion 77

References 78

Chapter – 3 : Preparation, Surface Functionalization and Characterization of Hematite photoanode

3.1. Introduction to solar to chemical energy conversion 87

3.1.1. Energy crisis 87

3.1.2. Hydrogen as an Energy source 88

3.1.3. Possibility & Comparison of Hydrogen Production routes 89

3.2. Photoelectrochemical(PEC) water Splitting 91

3.2.1. PEC water splitting reaction – Brief Overview 91

3.2.2. Semiconductor – Electrolyte Interface (SEI) 92

3.2.3. Criteria for Semiconductor electrode materials 98

3.3. State of the art photoanodes 100

3.4. Hematite photoanode 101

3.5. Surface Modification of Photoelectrodes 102

3.5.1. Stabilization of photoelectrode surfaces by semiconductor coating 103

3.5.2. Surface states passivation 104

3.5.3. Improving kinetics by catalyst layer 104

3.6. Hydrogen peroxide production – Current status 106

3.7. Aim of this chapter 110

3.8. Synthesis of Iron Oxide (Fe_2O_3) Photoelectrodes 110

3.8.1. Preparation of Hematite Photoanodes By Anodic Electrodeposition Process **111**

3.8.2. Anthraquinone Modified Hematite By Reductive Electrografting Process 114

3.8.3. Hematite Surface Modified with poly-vinyl Anthraquinone Ionic Liquid 120

3.8.3.1. Synthesis of Monomer N-ethyleneamidoanthraquinone -N-vinylimidazolium bis(trifluoromethylsulfonyl)imide: 120

3.8.3.2. Surface Initiated Atom Transfer Radical Polymerization (SI-ATRP) : A brief note: 121

3.8.4. Surface Modification of glassy carbon electrode (GCE) by SI-ATRP 124

3.8.4.1. Initiation and polymerization: 124

3.8.4.2. Characterization of immobilized AQ moieties 126

3.8.5. Surface Modification of Hematite by SI-ATRP 127

3.8.5.1. Initiation process on hematite 127

3.8.5.2. Bromine termination by exploiting the surface hydroxyl groups 128

3.8.5.3. SI-ATRP of AQ & characterization 129

3.8.6. Surface Modification of Hematite by SI-ATRP with aryl bromide initiator 132

3.8.6.1. Initiation on hematite 132

3.8.6.2. SI-ATRP of AQ & characterization 133

3.8.7. Surface Modification of Hematite by SI-ATRP with N-methyl-N`-vinylimidazolium bis(trifluoromethylsulfonyl)imide 134

3.8.7.1. Synthesis of N-methyl-N`-vinylimidazolium bis(trifluoromethylsulfonyl)imide 134

3.8.7.2. Immobilization of N-methyl-N`-vinylimidazolium bis(trifluoromethylsulfonyl)imide on hematite 135

3.9. Photoelectrochemical Investigation 138

3.9.1. Introduction 138

3.9.1.1. Aim of this part 139

3.10. IMPS & IS theory and our methodology 139

3.11. Photoelectrochemical characterization details 144

3.11.1. Photoelectrochemical (PEC) characterization setup 144

3.11.2. Linear sweep (LSV) and Chopped light voltammetry 144

3.11.3. IMPS measurements 144

3.11.4. Impedance measurements 144

3.12. Influence of Diazonium AQ on hematite photoelectrochemistry 145

3.12.1. In non-aqueous medium 145

3.12.2. In aqueous medium 148

3.13. Diazonium AQ vs ATRP AQ – A comparision 150

3.14. Linear Sweep Voltammograms (LSV) 152

3.15. IMPS analysis 155

3.16. PEIS analysis 157

3.17. Mott – Schottky analysis 160

3.18. Conclusion 162

References 164

Chapter – 4 General Conclusion & Perspective 177

4.1. Conclusion 178

4.2. Challenges & Perspective 182

(i) pH of the solution 182

(ii) Integration 182

4.3. Résumé 185

CHAPTER 1

Elaboration and Properties of Actuators and Micromotors

1. Artificial Muscles:

1.1. Actuators – General Introduction :

Actuators are nothing but materials or composites that are highly deformable which can be activated by external stimuli such as voltage, current, pressure, temperature and light etc., to produce desired movements, torques and forces. A class of materials and devices that show deformation because of external stimulus generally coined as artificial muscles. The topic of artificial muscle is highly interdisciplinary which intersects with different fields like material science, chemical engineering, mechanical engineering, electrical engineering, and chemistry.

To evaluate the performance of artificial muscles, some metrics are commonly used and their definitions are given below[1]:

Output strain ($\mathcal{E}$): Compared to the initial length, upon excitation the change in length is coined as output strain.

Output stress (σ) : Compared to the initial cross-sectional area of the actuator at rest or at the excited state, during excitation the generated force is given as output stress.

Energy (Work) density (W) : Compared to the mass or volume of the muscle, upon excitation the generated output work by the muscle is defined as energy density or work density. The volumetric energy density is generally calculated as $W = \mathcal{E} \times \sigma$.

Power density (P) : The energy/work density normalized to the actuation period is referred as power density.

Catch state (Lock-up state) : While without consuming any energy, when the actuator holds its actuated state is generally reported as lock-up state.

Actuation directionality : Some actuators have the potential either to contract or expand and they are called as unidirectional, whereas the actuators that can expand as well as contract are known as bidirectional.

Cycle life : Before death or failure, how many number of cycles an actuator can survive is given as cycle life.

Efficiency: The ratio of output work compared to the input energy gives the efficiency of an actuator.

Bandwidth : The range of frequencies can be used to excite an actuator continuously is referred as bandwidth of the actuator.

To provide easy deformation, mostly actuators are designed from low elastic modulus materials or those which incorporate fluids. To convert electrical energy to mechanical energy, there are plenty of soft, flexible materials available such as polymers, paper, textiles, gels, fluids and stand-alone carbon nanotubes. Electrically responsive soft actuators are generally driven by electric fields, E (V),(electroactive or electromechanical) that allow the easy modulation of phase, frequency and magnitude[2]. Polymeric artificial muscles are commonly categorized into two major groups: first one is actuation (dimensional change) in response to an electric field and the other one is showing actuation because of the presence and movement of ions. The first group is known as electric or electronic electroactive polymers (EAPs) whereas the second group is referred as ionic EAPs or wet EAPs because it generally requires electrolyte phase for the efficient movement of ions. Dielectric elastomer actuators (DEAs), ferroelectric polymers and liquid crystal elastomers fall under the category of electronic EAPs whereas gel actuators, conducting polymer actuators, ionic polymer metal composites (IPMC) and carbon nanotubes (CNTs) actuators fit into the category of ionic EAPs.

1.2. Electronic Artificial Muscles :

As a result of electrostatic interactions between electrodes, there will be field driven actuation mechanism that usually prevails in low modulus materials like dielectric elastomers which provides huge strains (>40%). Electrostrictive polymers exhibit another kind of mechanism in which the applied field push or pull the electric dipoles within the polymer that leads to displacement. In the case of ferroelectric polymers, to interrupt long range order, imperfections are introduced to cause conformation changes in the backbone that resulting in polarization and large strain. Albeit these materials have better electromagnetic coupling coefficients and high work densities, to say hundred times more than that of natural muscles, the main drawback of the electronic artificial muscles is that they need very high voltage, typically >1 kV, however this problem is commonly addressed by minimizing the film dimension and enhancing the dielectric constant[3].

1.2.1. Dielectric elastomer actuators (DEAs):

DEAs are one of the extensively investigated polymer actuators because of its capability of generating huge strains and strain rates and as a result, various applications have been developed such as conformal skins for Braille screens, electroactive fluid pumps, insect-like robots etc[4]., These actuators are nothing but capacitors with dielectrics and electrodes and at once the voltage is applied across these actuators, the electrostatic repulsion of like charges and the attraction of opposite charges creates stress that elongates and compresses in the dielectric and this stress is directly proportional to the square of applied field and to the dielectric constant[5]. At high applied fields, because of low modulus (~1 MPa) and high dielectric strength (>100 MV/m), huge strain upto 380% can be obtained.

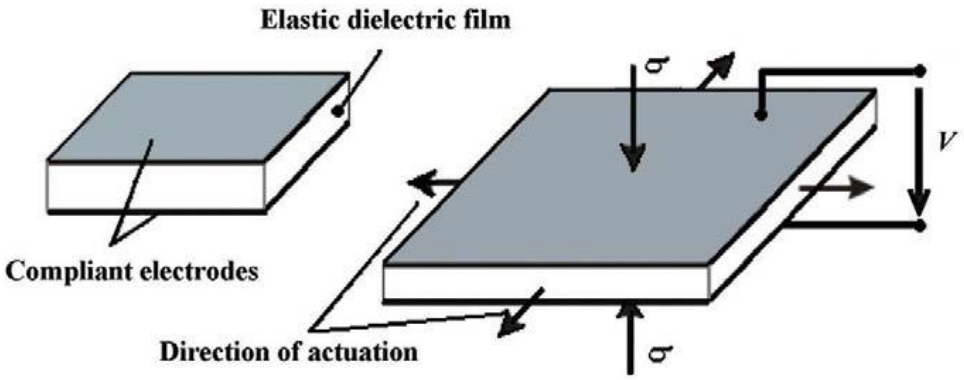


Figure 1. Common actuation mechanism in DEAs. The applied voltage, V, between the two electrodes generate the stress σ, causing the dielectric compression and leading to lateral expansion.

Usually, silicone or acrylic elastomer is used as elastomer; in certain cases, to enhance the dielectric constant, elastomers are loaded with heavy particles like TiO_2 [6]. Conductive carbon or silver pastes, sprayed graphite particles and spin-coated conductive rubbers are commonly employed to make compliant electrodes. The two parameters dielectric strength and conductivity govern the main role in preparing compliant electrodes with huge strain. The electromechanical coupling for silicone elastomers is 90% whereas that of for acrylic elastomers is around 60-80% [4, 5b]. The electrostatic energy stored within a dielectric elastomer increases in proportion to the square of the applied field, while the mechanical energy density is roughly proportional to the fourth power of field[3]. Hence by working near to breakdown and employing materials with maximum dielectric strength, electromechanical coupling and mechanical energy density can be enhanced. Mostly, the elastomers are prestrained to increase the dielectric strength that helps to enhance strain[7].

To drive DEAs, generally high voltage (>1 kV) is used. Since dielectric field is driving the actuation, not the voltage, by employing thinner elastomer sheets[8] or by enhancing dielectric constant[6], there is a possibility to keep the same field while cutting down the required voltage. To produce larger forces, multiple thin layers of DEAs are made into stalking in layers[8] or rolling into tubes so that their actuation forces are in parallel. These actuators are commonly used in devices like robotic insects[3].

1.2.2. Electrostrictive relaxor ferroelectric polymers:

Ferroelectric materials are like ferromagnets, that have dipoles and over the Curie point they throw away their permanent polarization. Ferroelectric polymer actuators exhibit faster actuation and higher work density (1 MJ/m^3), similar to inorganic piezo- and ferroelectrics[9]. Among various ferroelectric polymer actuators, the P(VDF-TrFE), i.e., poly(vinylidene fluoride)-based (PVDF) polymers copolymerized with trifluoroethylene showing the best performance because of the high electronegativity of fluorine that makes the backbones of the polymer more polar. While applying the field there will be alignment of polar groups that leads to reversible conformational changes which cause actuation as shown in the Fig.2 [9].

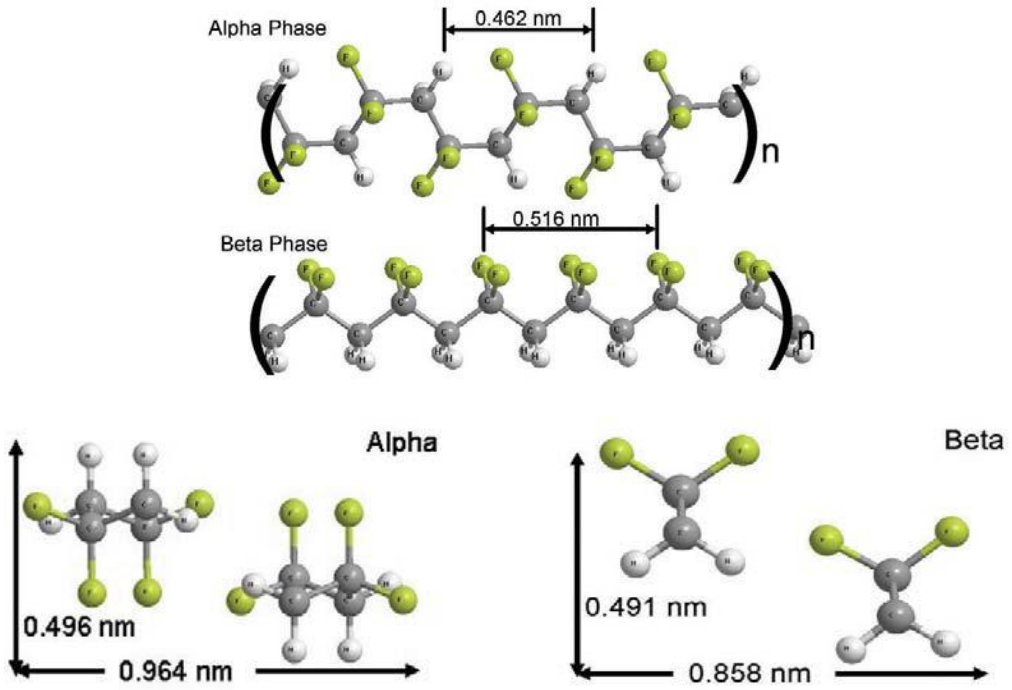


Figure 2. Alpha and beta phases in PVDF, looking along the chains (top) and perpendicular to the chains (bottom). A similar alpha-to-beta phase change is induced in P(VDF-TrFE) relaxor ferroelectrics that begin in the nonpolar alphaphase and switch to the polar beta phase upon the application of an electric field. This results in dimensional changes (expansion along the chain length and contraction perpendicular to the chain direction). Taken from Ref.[3]

The perpendicular field-driven alignment causes a transition between the non polar (alpha phase) and polar phases (ferroelectric beta phase) and as a result, there will be contraction in the polarization direction and an expansion along the perpendicular direction. To realize this transition, the long range order must be interrupted, to do so, P(VDF-TrFE) is illuminated or a small amount of a monomer such as chlorofluoroethylene (<10%) is mixed. Because of this interruption, the domain formation and the hysteretic characteristic behaviour of ferroelectrics are removed and the resulting material is called as a relaxor ferroelectric.

Compared to DEAs, the ferroelectric relaxors is having 1000 times higher the elastic modulus (0.3-1.2 GPa), ~20 times higher the dielectric constant, and the similar dielectric strength. In total, this ferroelectric relaxors have smaller strains but similar energy densities (~ 1 MJ/m^3) and coupling[3].

1.2.3. Electrostrictive graft elastomers:

In this case, the polar groups are aggregated to form a polar crystalline regions which attached as side chains to a flexible backbone of a polymer and these polar crystalline regions undergo field-driven alignment resulting out dimensional changes within the polymer as shown in Fig.3. Usually to trigger strain[9], in the case of using a chlorotrifluoroethylene and trifluoroethylene backbone with P(VDF-TrFE) polar sidechains, applied fields are required in the order of 10MV/m to achieve the strains of 2.5% and give an elastic energy density of ~0.5 MJ/m^3.

In general, the applied fields and the actuator strains are lower compared to relaxor ferroelectrics because of the size of the polar aggregates.

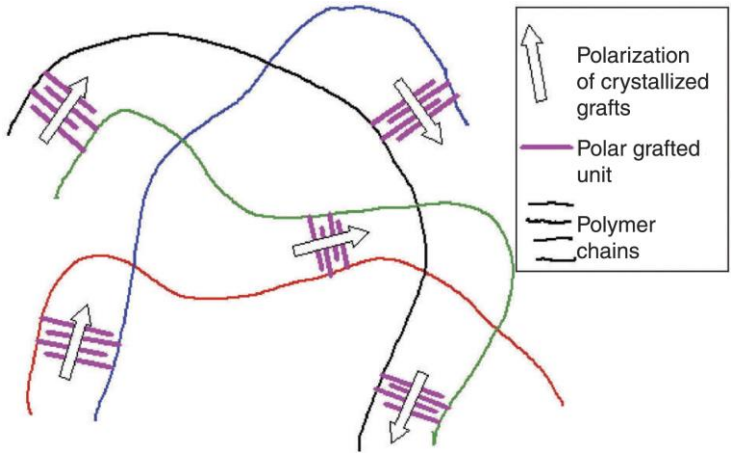


Figure 3. Schematic of graft elastomer without any applied field.

1.2.4. Liquid crystal elastomers:

It is well known that liquid crystals are under applied field capable of changing their phase and orientation and hence by integrating those liquid crystals into a polymer backbone or as a side chain, actuation can be observed by inducing the field driven phase change[10] as depicted in Fig.4. This field is still in early stage of investigation and their performance is lower compared to relaxor ferroelectrics.

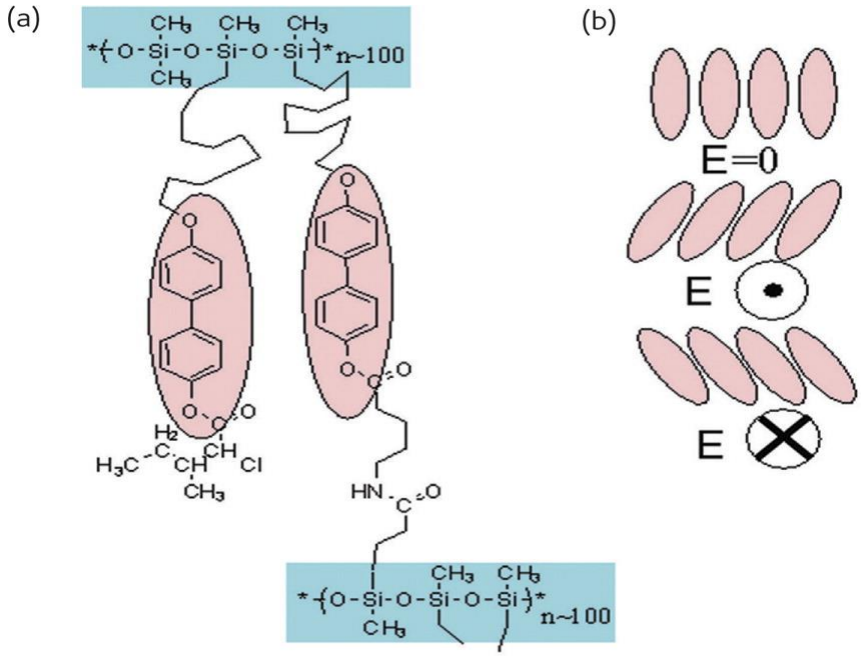


Figure 4. Ferroelectric liquid crystal elastomer. (a) Over siloxane polymer backbone, liquid crystals are integrated, (b) Field driven reversible rotation produces dimensional changes. From Ref.[11]

Likewise in other field driven actuators, reducing dielectric loss is vital; because high loss minimizes the efficiency and causes failure and heating.

1.3. Ionic Artificial Muscles :

Another type of actuation is realized in the case of EAPs by using mobile ions which move along with solvent under applied electric field resulting out swelling or contraction while the ions enter or leave the polymeric region. When the potential is changed, the ions are balancing the generated charge on the electronically conducting polymer and thus generating a very strong local field with overall low voltage. Although the low voltages (1-7 V) are used for these materials, the energies are high due to close spacing between ions and electronic charges and the huge amount of charge that can be transferred[3].

1.3.1. Conducting polymers:

Depending upon the doping and undoping with donor or acceptor ions, the conducting polymers behave typically as conductor and semiconductor respectively[12]. Doping is commonly achieved by chemical or electrochemical means. Commonly used two conducting polymers, namely polypyrrole and poly aniline, are given in Fig.5.

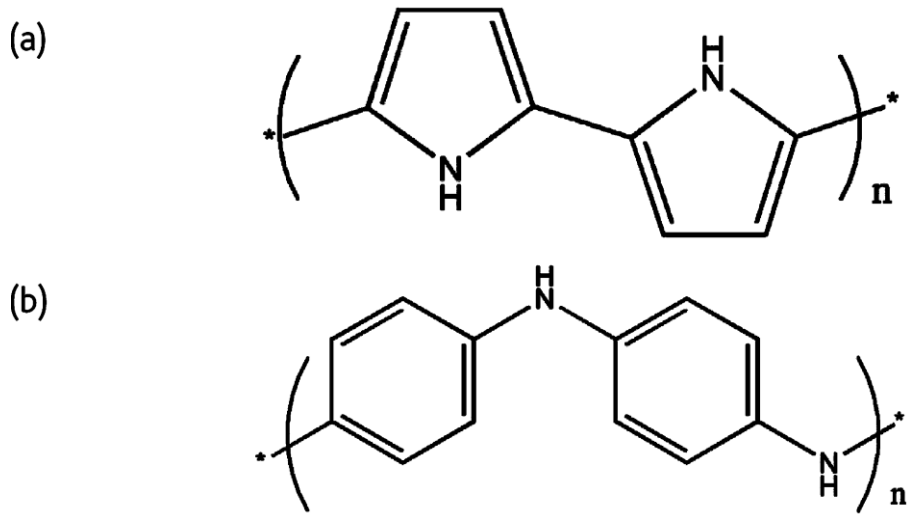


Figure 5. Commonly used two conducting polymers; (a) Polypyrrole and (b) Poly aniline

In 1990, Baughman et al., demonstrated the first conducting polymer artificial muscle[13]. Since then huge improvements have been made. As a result of electrochemical ion insertion and deinsertion along with solvating speicies, these conducting polymers artificial muscles undergo dimensional changes. Both the electrodes can be made up of conducting polymers. Based on the conducting polymer/electrolyte combination, the initial state and the actuation potential, volume increase or volume decrease at one electrode can occur during cation insertion and removal of anion respectively. Counter electrode also can exhibit the similar process. Apart from this property, time-dependent changes of the inserted/deinserted species, can perplex the control of actuation[14].

Usually the conducting polymers exhibit the strain in the range of 2-10%, however Hara et al., showed that the strain can reach upto 40%[15]. Also they show slow rate of actuation (<<1%/s) owing to relatively sluggish transport of ions within the polymer and the greater extent of doping[16]. However by employing metal contacts, porous polymers, fast charging or thin films and fibers, the actuation rate can be exceeded to 10%/s [17]. High quality films are obtained by electrochemically grown or solution-spun fibers and they have high

tensile strength in the order of 100 MPa which can be further enhanced by mixing with carbon nanotube[18]. Work densities upto 100 MJ/m^3 have been obtained[19].

The main advantage of conducting polymer artificial muscle over the electronic EAPs is their low operating voltage. They are cheap, possess low electromechanical coupling and have higher strain. Various applications have been developed like catheters, Braille displays and valves[20].

1.3.2. CNT actuators:

Single layer of graphite rolled into a cylinder shape is known as Single-walled CNTs (SWNTs) whereas the nested SWNTs make Multiwalled CNTs (MWNTs). They have excellent mechanical properties. For example, the tensile modulus of SWNTs is almost equivalent to that of diamond (640 GPa) and their tensile strength is around 20–40 GPa [21].

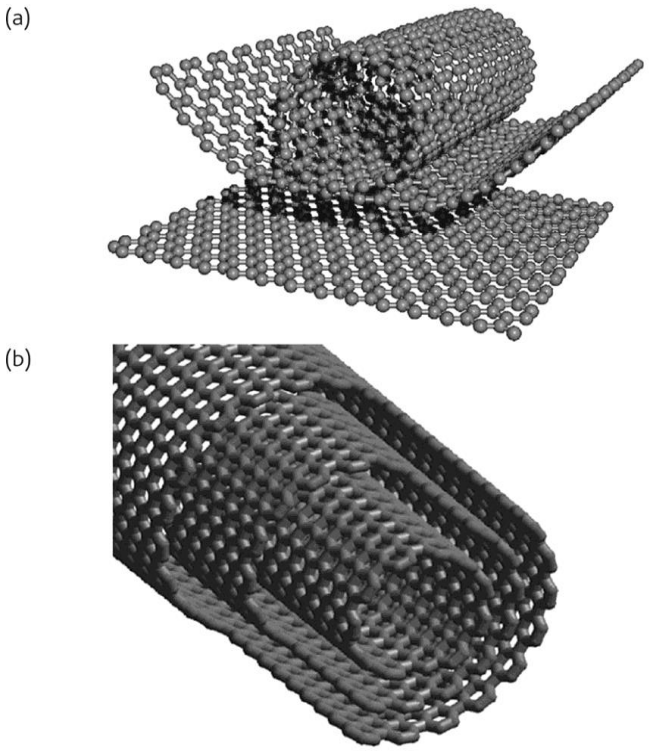


Figure 6. (a) SWNT; (b) MWNT

Like DEAs, the major cause of actuation in CNTs is electrostatic. Consider the working and counter electrodes made up of CNTs placed in ion containing solution and the voltage is applied between them as given in Fig.7. causing charging. As a result of the electrostatic repulsive forces between the like charges on the CNTs function against the strong

carbon-carbon bonds in the nanotubes leading to the elongation and expansion of the nanotubes[22]. Because of its extreme stiffness, the CNTs show low strain compared to dielectric elastomers[23].

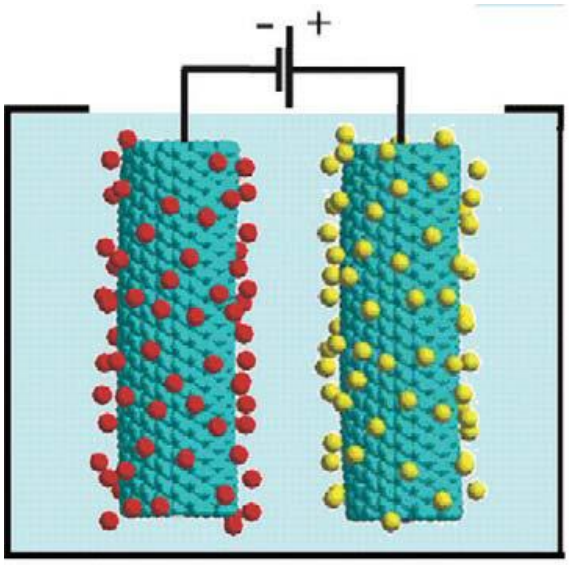


Figure 7. Charge injection in a CNT-based electromechanical actuator. An applied potential injects charges in the two nanotube electrodes in solution (red: positive ions, yellow: negative ions)[3].

MWNTs films or yarns are generally used to achieve actuation owing to its porous nature thus enables faster ion transport with response time of <10 ms [24]. The thickness, the interelectrode separation and the ionic conductivity of electrolyte govern the response rate. Compared to DEAs and ferroelectric polymers, the calculated work densities in CNT fibres and yarns are the same (~1 MJ/m^3). It has the potential to reach the energy density of 10^8 J/m^3. Because of its high work density and along with good temperature stability (>450°C in air, >1000°C in an inert environment) provide CNTs as a potential candidate for aerospace applications[3]. Strains are comparatively lower, however it can be increased by using ionic liquids which enable to achieve large potential range sans reacting electrochemically. CNT actuators can be employed as electrodes in a fuel cell which has higher energy density than that of batteries offer promising future applications[25].

1.3.2. Ionic polymer-metal composites (IPMCs):

In this case, poly electrolyte is used as an ionic conducting layer, where the polymer chains give one type of ions and the mobile solvated ions provide the other and opposite type. This polyelectrolyte is placed in between the two high surface area flexible metal electrodes in such a way that those metal electrodes interpenetrate with the polyelectrolyte. Generally,

the metal electrodes are made up of percolated Pt nanoparticles or Au [26]. As shown in Fig.8, while applying voltage, solvated mobile cations migrate toward the negatively charged electrode, leads to swelling near this negative electrode, shrinkage at the positive electrode, and bending of the actuator trilayer [3, 27].

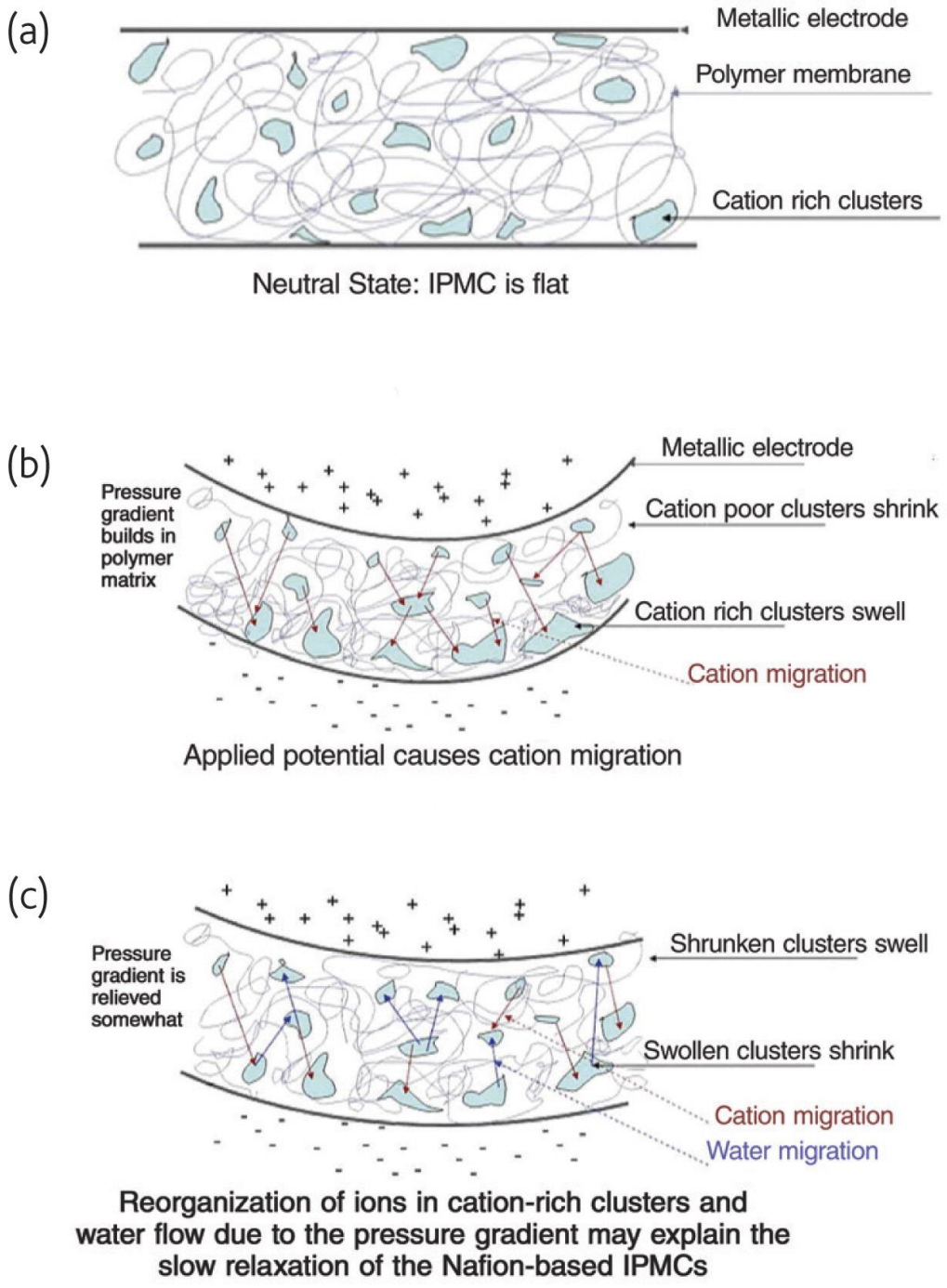


Figure 8. Actuation model for IPMC type actuator. (a) Prior to the applied voltage; (b) after the applied voltage.

Commonly used polyelectrolytes are Nafion (SO_3^-), Flemion (COO^-) and styrene/divinyl benzene based polymers. The ionic groups on the polyelectrolyte develop hydrophilic clusters where the polar solvent and the mobile ions accumulate. These clusters are encircled by hydrophobic regions made up of the nonpolar parts of the polymer. Channels through these hydrophobic regions facilitate ion and solvent transport needed for actuation[28]

For Nafion-based IPMCs, while applying a step voltage, there will be initial fast actuation and then followed by a slow relaxation in the opposite direction to the initial actuation whereas in Flemion-based IPMCs for the similar conditions, the initial fast actuation is then followed by a slow actuation in the same direction as the initial actuation. It is mainly due to the interaction between the cations and the strongly-polar sulfonate groups in Nafion; at the beginning, the cations show repulsion against the electric dipoles associated with these sulfonate groups, causing a fast and large actuation. Eventually, the cations are rearranged, the dipoles reorient themselves and the IPMC relaxes. But in the case of Flemion the weakly-polar carboxylate groups do not strongly interact with the cations so it does not exhibit the relaxation in the opposite direction[3, 28].

Due to the slow leakage of water, the IPMCs generally moving the position from their initial displacement and hence some steady current is needed to retain the position. This property decreases efficiency and degrading the performance, to overcome this, inert non volatile ionic liquid electrolytes must be used[29]. There are various applications for IPMC actuators like mechanical grippers, metering valves and an IPMC-operated artificial eye developed by Eamex[3, 26b, 30]

2. Micromotor – General Introduction :

Movement is an important part of life in any living beings. For such movement, nature has provided many biomotors that show remarkable motion capabilities with controlled directional movement and speed. Inspired from those biomotors, researchers have attempted to design artificial motors in nano and micro scale with improved capabilities and functionalities. One of the most interesting topics of nanotechnology is the development of artificial motors that can convert energy into motion and force. Since micro/nanomotors (MNM) have great promising applications in various fields like nanosurgery, transporting therapeutic cargo and cleaning hazardous chemicals etc., scientists and engineers around the world are actively pursuing the design of MNMs with functionalities comparable to the biological motors. In 2016, Jean-Pierre Sauvage, Fraser Stoddart and Bernard Feringa have

got the Nobel prize in chemistry for the design and synthesis of molecular machines. To date, there are two kinds of MNMs : one is externally powered motors that requires actuation by external fields such as magnetic[31], electric[32] or an acoustic field[33] and the other one is chemically powered propellers which is completely autonomous getting powered by catalytic decomposition of fuel molecules in solution and hence it is also known as chemically self-powered MNMs.

However, it is not an easy task to design self propelling MNMs owing to many constraints such as Brownian collisions, viscous drag and other surface related phenomena. Since the absence of inertial forces, it is highly challenging to get the propulsion for MNMs in liquid. The ratio of the inertial forces to viscous forces is given by a dimensionless quantity called *Reynolds number (Re)* and is defined as follows:

$$\text{Re} = \text{Inertial forces} / \text{Viscous forces} = \rho V l / \mu \qquad (15)$$

Where, ρ is the fluid density; V is the particle velocity: l is the length of the object and μ is the viscosity of the medium[34]. The higher Re number means that the inertial forces control over the viscous forces and this is the case for the macroscopic world. But for the smaller length scales such as MNMs and microorganisms like bacteria, the viscous forces dominate over the inertial forces and exhibit the smaller Re number. For instance, the Re number for a person swimming in water is 10^4 whereas that of a swimming bacterium is 10^{-4}. According to Purcell's "Scallop theorem" , reciprocal motion cannot yield net displacement and thus cannot be employed for small scale swimmers with low Re numbers[34] . Hence, for small scale swimmers, non-reciprocal motion by deforming their shape is mandatory to get net displacement[35]. The requirement of shape deformation adds additional burden to the design of MNMs.

Another main constraint is Brownian motion which is responsible for irregular random movement of small size particles in fluid that is caused by thermal induced collision. According to Stokes – Einstein relationship,

$$D = k_B T / 6\pi\eta r \qquad (16)$$

Where k_B is Boltzmann constant; T is abolute temperature; η is the viscosity and r is radius of the particle. As indicated, the temperature of the system and the size of the particle define the diffusion coefficient and hence for the smaller size particles, the Brownian motion interferes remarkably on the movement and directionality.

Keeping these constraints in mind, developing the MNMs as similar to biological motors is a big challenge. The biological motors, also known as workhorses of cells, are the best examples given by nature and these highly efficient motors carry out complex tasks like protein synthesis, cell migration, cell division and DNA transcription etc., autonomously[36]. Biomotors are divided into two groups namely linear and rotary motors. Kinesins, dyneins and myosins are the examples for linear motors. Kinesins is responsible for the cargo transportation of vesicles and molecules along microtubules for intracellular transport and myosins move along the actin filaments and cause muscle contraction. To convert chemical energy to mechanical energy, biomotors use the hydrolysis of adenosine triphosphate (ATP) as a catalyst. Membrane protein ATP synthase is a perfect example for rotary motor that synthesizes ATP from adenosine diphosphate and inorganic phosphate by utilizing the electroosmotic energy derived from a sodium or proton gradient and eventually converts chemical energy into electrochemical energy for the rotation of flagella in bacteria.

Researchers have tried to enhance the performance by modifying the biomotors with synthetic components. Nanopatterned devices were made up by integrating motor proteins in vitro to transport inorganic and biological cargo and nanofluidics, and they also employed as nano-biosensors as well as nanoscale probes for scrutinizing the surfaces[37,38,39,40,41]. Single enzymes can also be used for self propulsion, for instance, urease and catalase exhibit higher diffusivity toward the higher concentration of H_2O_2 that acts as a substrate for the enzymes[41]. Attempts were made to incorporate synthetic components to enzymes for the performance enhancement. Glucose oxidase (GOx) and bilirubin oxidase coupled with carbon fiber showed bioelectrochemical propulsion in presence of glucose in the solution[42], similarly GOx and catalase were covalently coupled to carbon nanotube exhibited bubble propulsion when glucose and oxygen present in the solution and induce the autonomous migration of nanotube[43]. As shown in Fig 9., by exploiting self assembled monolayer(SAM) approach, catalase enzyme was immobilized onto microtubular structure and observed oxygen bubble propelled microjets by catalytically decomposing H_2O_2 in a more efficient manner than Pt based microjets[44]. Also hybrid bio-micromotors were developed by integrating synthetic components with motile cells, for example bacteria driven microswimmers that can be used for biomedical application such as targetted drug delivery[45]. The main advantage of bio-hybrid motor is its biocompatibility and hence plethora of applications can be envisaged particularly in biomedical applications.

The MNMs are generally classified into molecular artificial motors and catalytic artificial motors. One can have a look at the latest review by Ben Feringa and David Leigh groups to know the progress in the field of molecular motors[46]. In the coming part, the fabrication and motion control of catalytic motors will only be discussed.

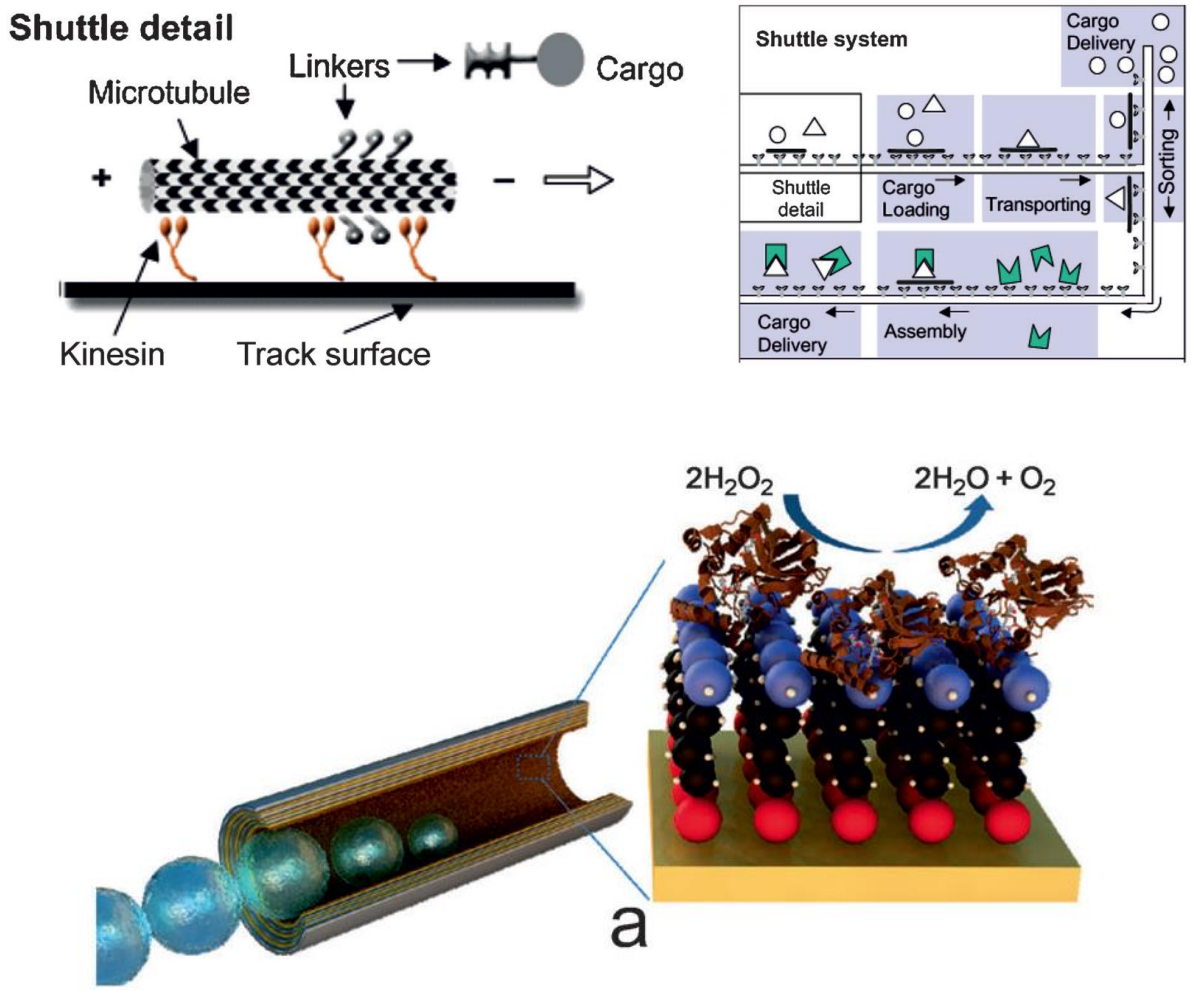


Figure 9. (Top) Hybrid microtor, by coupling biomotor with synthetic components to load, transport and deliver the cargo. **(Bottom)** Catalase immobilized microjets for decomposing H_2O_2 to O_2 bubbles. (Adapted from Ref.[47])

2.1. Propulsion Mechanism :

Mainly the MNMs are classified into self propelling and externally controlled based on their cause of movement. There are several propulsion mechanisms behind the self-movement of MNMs. The Marangoni effect which causes an imbalance of forces because of surface tension gradients along the interface can create the motion on the macroscale motors[48,49]. By creating local field gradient or concentration gradient, an object can move itself is known as self-phoresis. If the movement is due to field gradient, then its called as self-electrophoresis and for concentration gradient is known as self-diffusiophoresis. Usually,

bimetallic catalytic Janus particles and nanowires show self-electrophoresis because of the two different and opposite electrochemical half reactions occuring at the two terminals of the Janus particle. For instance, in the case of Pt/Au particle the H_2O_2 oxidation and reduction happening at the two ends create electron flow inside the particle and proton flow outside the particle leading to the movement of particle in the opposite direction. In the case of self-diffusiophoresis, concentration gradient of solute across the particle interface induce water to flow from low to high solute concentration regime and hence the particle will move according to the fluid flow. Another mechanism is propulsion by gas bubbles that are formed by the catalytic or non catalytic decomposition reactions of fuel. H_2O_2, bromide or iodide solutions[50], acidic and alkaline solutions[51,52] and hydrazine[53] etc., can be used as a fuel. Interestingly, Joseph Wang group has showed that even water can be employed as a fuel, but the poor lifetime of these motors hinders the further development[54,55].

However self-propulsion seems interesting, the usage of chemical fuels that are not biocompatible impedes its *in vivo* biomedical applications. Hence the externally controlled micromotors gaining advantage. For example, magnetic field controlled MNMs can be exploited for biomedical applications since low intensity magnetic fields are harmless to human beings. Sitti et al., used magnetically controlled microswimmer to destroy kidney stones non-invasively[56]. Sukho Park and his colleagues developed a microrobot with an electromagnetic actuation system for intravascular therapy[57]. Externally powered micromotors can also be used for ocular drug delivery[58]. But the decrease of magnetic field strength with distance causes a big challenge for magnetic control, to overcome that helical structured micromotor were proposed by Bradley Nelson and his group[59]. Similarly ultrasound assisted MNMs were developed and demonstrated its propulsion in living cells[33, 60]. Also electric field and light can be used as the source of propulsion for micromotors[32]

2.2. Micromotor Fabrication Methods :

2.2.1. Electroless and Electrochemical deposition methods:

Electrodeposition needs external electrical current for the deposition of materials whereas electroless deposition exploits chemical redox reactions. The advantages of these methods are they do not require very expensive instruments and extremely harsh conditions and also can be used to deposit variety of materials ranging from metals to conducting polymers.

2.2.1.1. Membrane Template Assisted Electrodeposition Methods :

This method uses a nanoporous membrane such as porous alumina membrane or etched polycarbonate membrane that contains cylindrical pores of uniform diameter and each pore acts as a reactor for the synthesis of different materials with wire and tube morphology [61, 62]. The length of the nanostructure is defined by charge whereas the diameter is controlled by the pore diameter. Chemistry of the pore wall and the properties of the material determine whether the nanostructure be a nanotube or a nanowire.

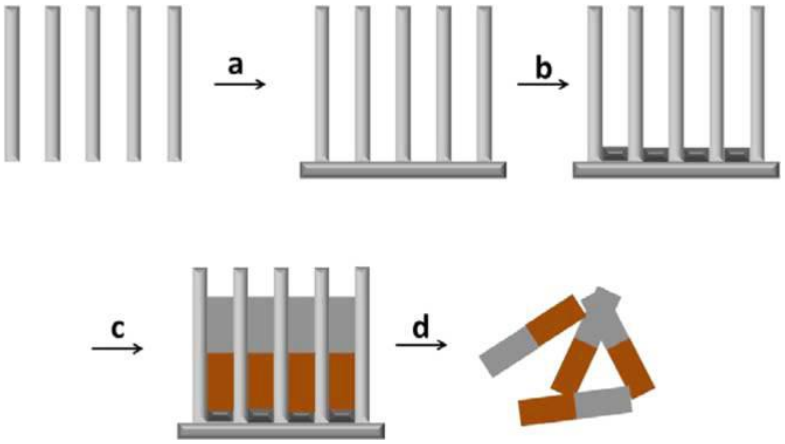


Figure 10. Membrane template assisted deposition of nanowires: **a)** PVD of backing layer, **b)** electrodeposition of sacrificial layer, **c)** electrodeposition of desired material and **d)** release of nanowires by removing the backing and sacrificial layer as well as by dissolving the membrane template.

The bimetallic Au-Pt[63] and Au-Ni[64] nanowire motors were made by membrane template assisted electrodepsotion process as shown in Fig 10., By using physical vapour deposition (PVD) method, a thin layer of gold or silver is deposited on the bottom of the membrane that play the role as a backing layer as well as a working electrode, over which a sacrificial layer usually made up of copper or silver is then deposited followed by the deposition of desired materials. With the help of chemical etching or mechanical polishing, the backing and sacrificial layers are removed that followed by the dissolution of alumina membrane releases the bimetallic nanowire motors that can be gathered after rinsing and centrifugation.

Gao et al., fabricated the micromotors with tube morphology by employing a similar electrochemical setup but with a cyclopore polycarbonate membrane that consists of double-cone pore structure as shown in Fig 11.,. At first, poly aniline (PANI) was electroplated followed by the electrodeposition of Pt yields bilayer conical PANI/Pt microtube engines. The length of the microtube is in the micrometer range and the diameter depends upon the pore

size of the membrane. Even at low fuel concentration of around 0.2%, this microtube show ultrafast speed of over 350 body lengths per second[65].

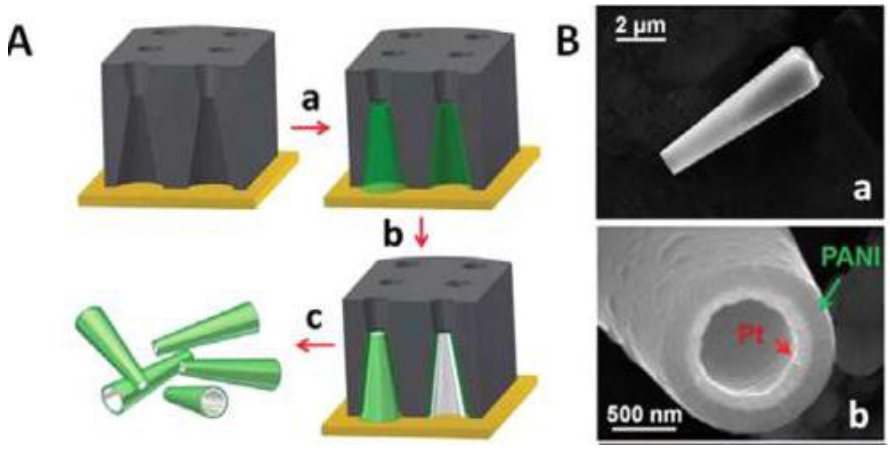


Figure 11. A) Membrane template assisted electrodeposition of microtubes; **A) a)** Electropolymerization of aniline, **b)** electrodeposition of platinum and c) release of microtubes by removing the remaining stuffs. **B)** SEM images of a microtube **B) a)** longitudinal view of a microtube, **b)** cross sectional view of a microtube

With the help of anodic aluminium oxide (AAO) nanoporous membrane, Lichun Liu *et al.*, synthesized palladium nanosprings by template assisted electrodeposition method[66]. At acidic conditions with certain pH, the hydroxyl terminated alumina nanopore surface selectively adsorb H^+ ions from the solution to form a compact layer based on Guoy-Chapman-Stern model as displayed in Fig 12., and this hydrogen atoms reduce $PdCl_4^{2-}$ to Pd nanotubes, the influence from the interfacial double layer, then localized hydrogen evolution and the screw dislocation during crystal growth due to the internal stress and strain was proposed to be the reason behind the growth of Pd nanosprings at the periphery of the pores. If the $CuCl_2$ is used along with $PdCl_4^{2-}$ in the electroplating solution, then the coelectrodeposition of Pd/Cu nanorods will be formed, then the selective etching of copper by using 30%(volume ratio) nitric acid resulting out Pd nanosprings.

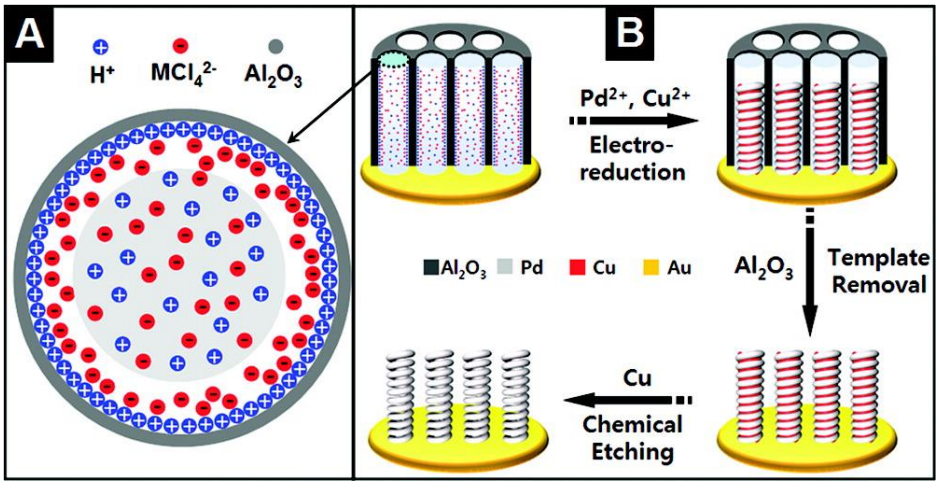


Figure 12. (A) Scheme shows the cross sectional distribution of ions in AAO nanopore and M stands for Pd or Cu **(B)** various steps involved in the fabrication of helical micromotor

Helical micromotors are highly preferred in biomedical applications particularly when the micromotor is propelled by magnetic field. The geometry of the nanosprings can be tailored in such a way that the diameter of the spring will be adjusted by tuning the pore diameter, and the length of the helices can be controlled by the charge density.

2.2.1.2. Other Template Assisted Electrodeposition Methods :

Apart from porous membranes, other templates can also be used to electrodeposit to obtain different shapes and structures. Manesh *et al.,* developed an approach to electrodeposit microtubes by using an etched silver wire as an template[67] and they obtained conical catalytic microtube based on sequential electrodeposition of platinum and gold on the template followed by dicing and removal of the template as depicted in Fig 13.,

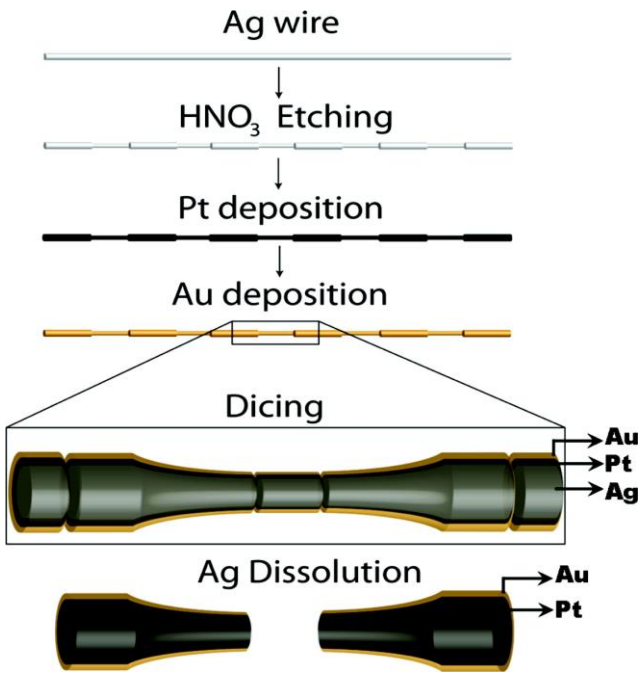


Figure 13. Schematic illustratration of steps involved in the silver wire template assisted electrodeposition of microtube engine

After the sequential of electrodeposition of Pt and Au layer, template silver wire is subjected to dicing to get the microcones of certain length, then the silver wire is etched away by using nitric acid resulting out conical microtubes of Pt/Au bilayer with the diameter of the larger opening is 50 μm that is the diameter of the template silver wire and thus the diameter of the template decides the diameter of the larger opening of the microcone.

Shuerle and his colleagues employed lipid as a template to fabricate helical and tubular magnetic structures as given in Fig 14.,. Firstly, the lipid molecule is converted to tubular and helical forms, after that Pd metal clusters are electrolessly deposited followed by the electroless deposition of magnetic multialloy CoNiReP on microtubules and microhelices[68]

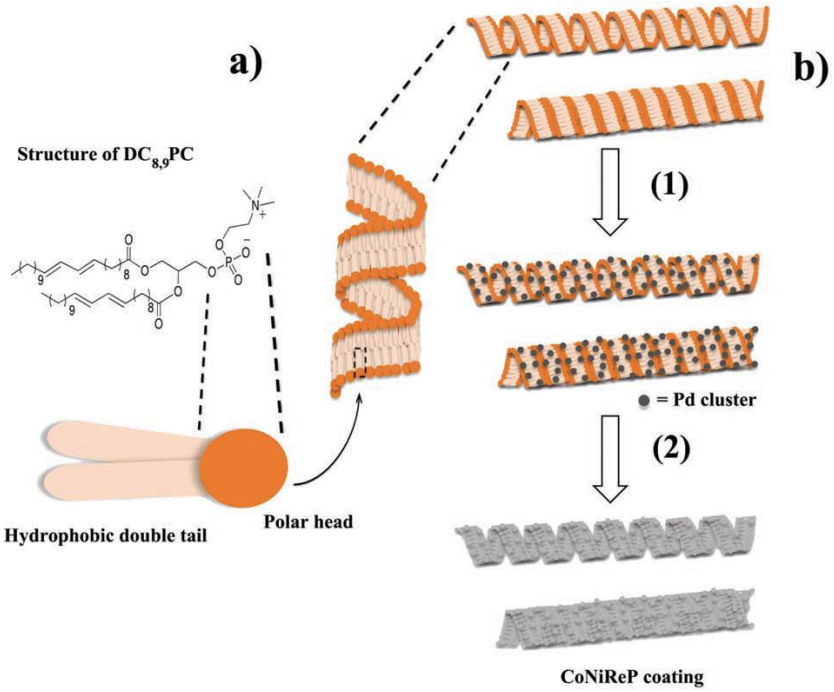


Figure 14. a) structure of the liposome molecule, **b) 1)** electroless deposition of Pd clusters on the lipid surface **2)** electroless deposition of magnetic multialloy CoNiReP

2.2.1.3. Bipolar Electrodepostion Method :

In bipolar electrochemistry, a conductive object is placed in between the two electrodes and apply the strong electric field that creates the potential difference between the two terminals of the conductor, the strength of polarization depends on the applied electric field strength and thus develops an asymmetric reactivity on the surface of the conducting material without any wires. If the polarization is stronger, the electrochemical reactions taking place at the opposite poles break the symmetry of the object to create Janus characteristics. By tuning the orientation and amplitude of the electric field and the medium's viscosity, the morphology of the deposit can be modified. This method enables to synthesize Janus motors with various materials, shapes and sizes in a large scale[69,70,71]

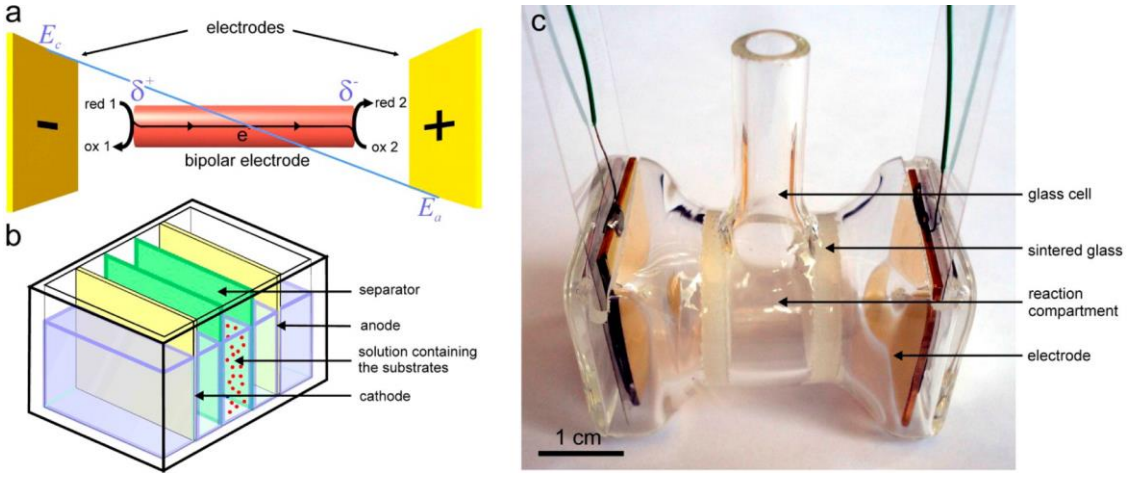


Figure 15. a) Schematic of the behaviour of a conducting object in a strong electric field dipped in electroactive species containing solution, **b)** design of a electrodeposition cell, **c)** Glass cell using for producing Janus motors by bipolar electrodeposition

Fattah et al., prepared dissymmetric carbon microtube (CMT) with Pt cluster at one end by bipolar electrochemistry and the Pt catalyst decomposes H_2O_2 to O_2 bubbles that trigger the propulsion of the CNT[72] and similarly the same research group reported dissymmetric carbon tubes with nickel deposit at one end that was magnetically manipulated[73]

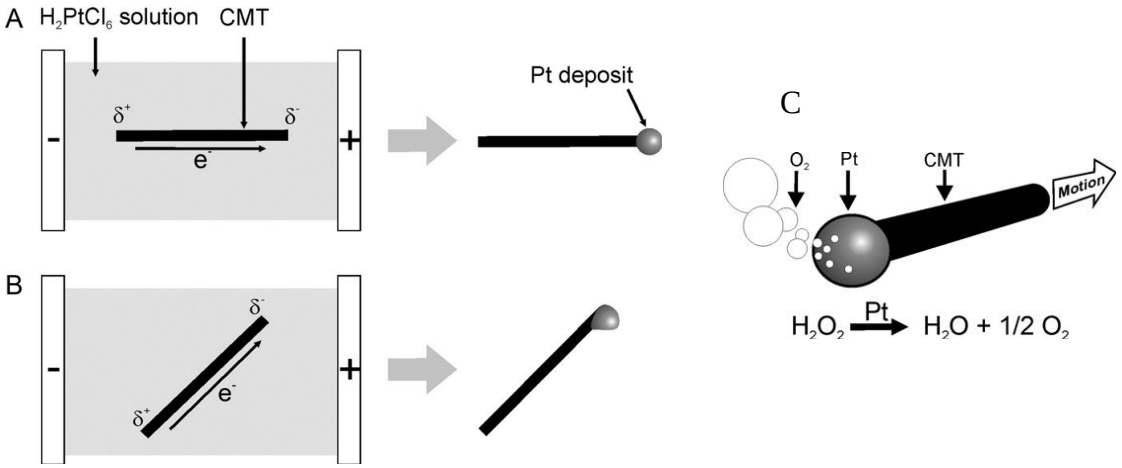


Figure 16. Schematic explanation of the influence of alignment of the conducting object with respect to the orientation of the electric field on the metal deposit formation **A)** aligned with electric field, **B)** non-aligned with electric field, **C)** catalytic decomposition of H_2O_2 by Pt.

2.2.2. Physical Vapour Deposition (PVD) methods

PVD is generally used to prepare thin layers of materials by vapourizing a solid target to a substrate surface at high temperature vacuum or plasma. PVD is generally classified into sputtering and electron beam evaporation. In sputtering, ionized argon gas bombards with the

target and creates vapour that deposits on the substrate whereas in the case of electron beam evaporation, an electron beam is used to atomize the target into the gaseous phase which is eventually deposited onto the substrate surface.

In PVD, the evaporated gas will stick only on one side of the substrate and if the substrate orientation is not reversed, it will create asymmetry. For instance, Qin et al deposited Au-Cr bilayer by thermal evaporation method on Au-Pt-Au nanowires to break the symmetry and observed rotation instead of linear movement in H_2O_2 solution[74] as explained in the Fig 17.,

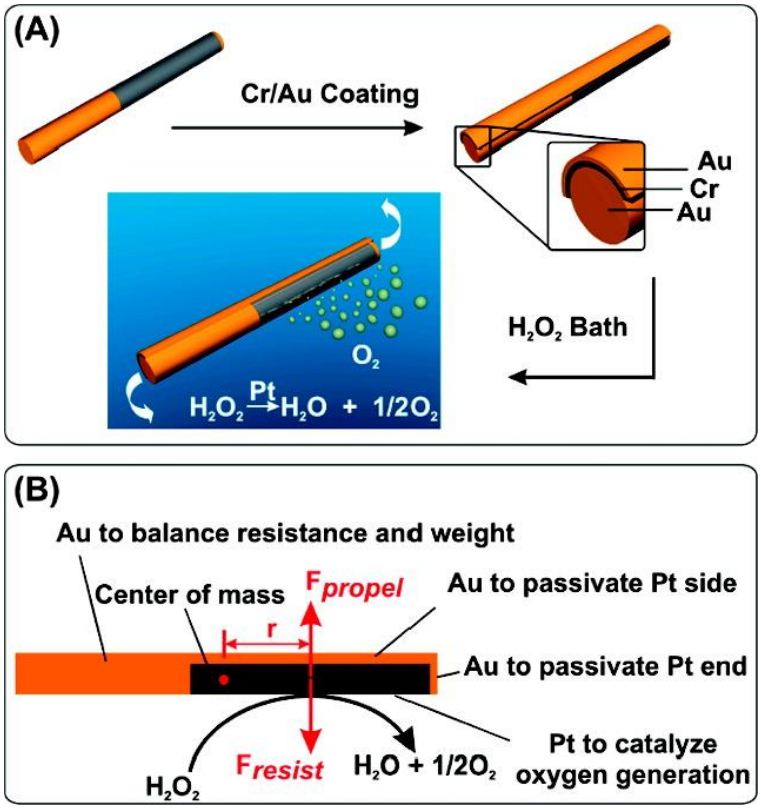


Figure 17. A) Schematic explaining the fabrication of Au-Pt nanorod and its propulsion in H_2O_2 containing bath **B)** Structure and force analysis of the nanorod to understand the reason behind rotational movement

Joseph Wang group developed iridium based catalytic Janus micromotor by evaporating iridium metal over one side of the hemisphere of the silica particles and the iridium acts as a catalyst to decompose hydrazine to hydrogen, nitrogen and ammonium resulting out movement due to diffusiophoresis even with minimum amount, 0.0000001%, of hydrazine[53]

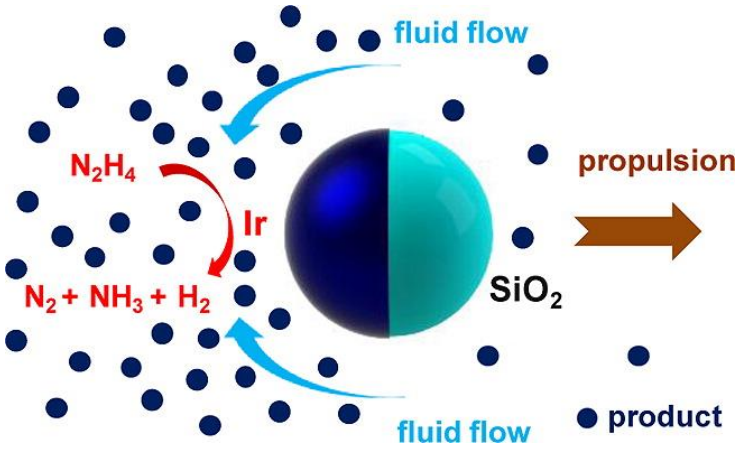


Figure 18. Schematic of the hydrazine powered Ir/SiO_2 catalytic Janus micromotor.

Alternative to conventional PVD methods where the substrate is fixed parallel to the target and the vapour is vertically deposited onto the substrate, there is a glancing angle deposition (GLAD) method in which at grazing incidence the vapour is deposited onto the substrate and thus it enables to rotate and tilt the substrate with vapour phase accordingly and hence this method allows to produce complex three dimensional structures like helical and Janus type structures[75]. To obtain a homogeneous helical structures, the substrate must be functionalized with seeds prior to further deposition and the shape, size and homogeneity of the seeds determine the resulting helical structures. Ghosh developed a helical chiral colloidal propellers by GLAD method. The rotating substrate stage was packed with silica beads and kept at an oblique angle then evaporated the SiO_2 vapour flux for the fabrication of silica helical structure at first. To obtain the magnetic controlled micromotor, cobalt was thermally then evaporated on the helical structure

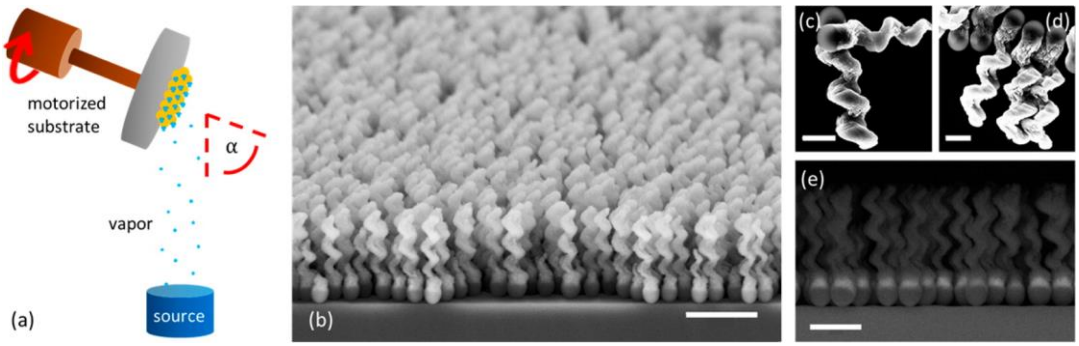


Figure 19. (a) Schematic of the GLAD process **(b)** SEM image of helical structures prepared by GLAD technique.[76]

2.2.3. Original materials:

Directly, some materials with unique features such as catalytic or photoresponsive can be used as MNMs without any modification. Catalytic materials like Ag and MnO_2 can split H_2O_2 into O_2 bubbles and show wireless autonomous propulsion. Due to the geometrical asymmetry of the particle, the bubbles generation occur in an asymmetric manner resulting out the movement[77]. The Pt-free low cost micromotor exhibit a greater speed at 0.1% H_2O_2. Another kind of materials is photocatalytic materials that can create concentration gradient in the vicinity by light induced reactions and exhibiting the movement due to photoinduced self-diffusiophoretic mechanism. Ayunsman Sen and his group developed TiO_2 based micromotor/micropump[78] and showed the schooling effect of AgCl nanoparticles in water under UV light[79].

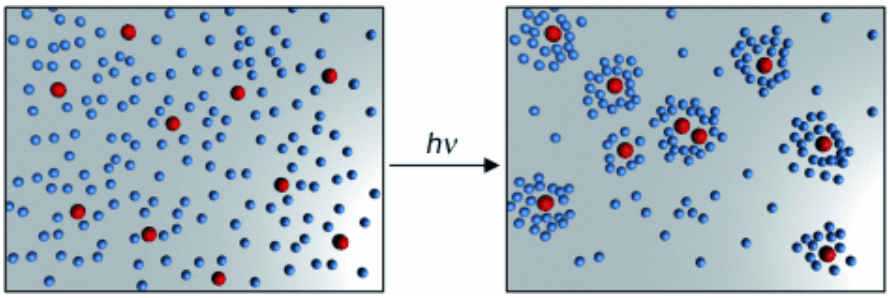


Figure 20. Photoinduced self diffusiophoresis movement of AgCl particles (red colour) and show schooling effect by chemical secretion. Photoinactive silica (blue) particles respond to the chemical secretion then move and surround the AgCl particles.

Assymmetry developing by bipolar electrochemistry can also be used as a tool to move objects under electric field. Alexander Kuhn developed a dynamic bipolar self-regeneration mechanism for the propulsion of conductive microobjects. Based on the different redox reactions occuring at the two terminals of a conductive metal, simultaneous dissolution and deposition of metal take place and the microswimmer will get the directed movement towards the metal deposition side. Zinc based micro- and macroswimmers were developed based on this approach and demonstrated the speed of 80 μm s^{-1} [80]. Similarly, asymmetric bubble generation have also been employed to generate the propulsion. Glassy carbon beads are used as bipolar electrodes and exhibited oxidation of hydroquinone at one side and proton reduction at the other end and thus create asymmetric bubbles production at the surface which propel the beads in opposite direction to the bubble production[81]

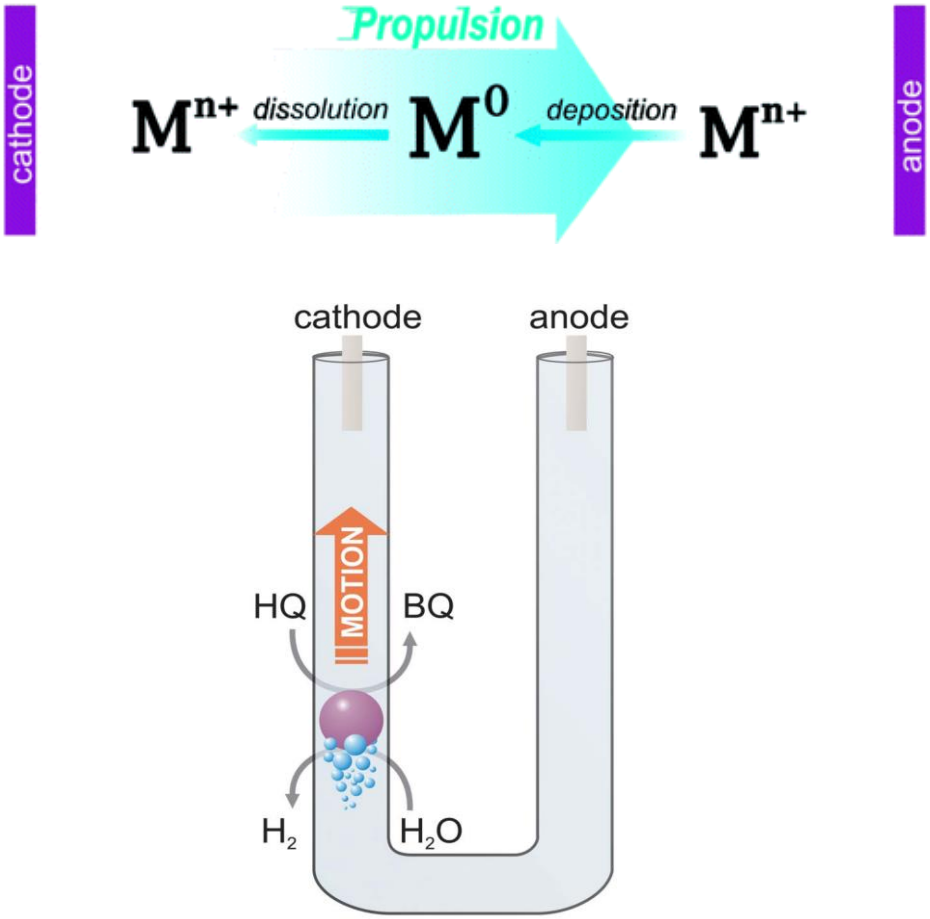


Figure 21. Schematic illustration of : **(Top)** dynamic bipolar self- regeneration mechanism for the propulsion of conductive microobjects, **(bottom)** levitation mechanism for a glassy carbon bead under applied electric field.

Apart from the above described methods, plethora of other fabrication methods available for the preparation of MNMs. For example, by layer-by-layer (LbL) deposition method[82], by direct laser cutting[83], by rolled up nanotechnology[84] to name the few. For further details, one can refer these[85,86,87] latest review articles.

2.3. Motion manipulation of Micro/Nanomotors :

Since the first report from the Whitesides group on centimeter scale motor[88], there is a huge development in the field of artificial MNMs and various applications of MNMs ranging from environmental remediation[89,90,91], cargo and drug delivery[92,93], and biomedical applications[94] are explored. To achieve and improve these potential applications, controlled movement of MNMs is very crucial but it is always sensitive to Brownian motion and low Reynolds number. However scientists have developed several strategies to manipulate the motion control of MNMs and that will be discussed in the following section.

2.3.1. Light control:

Light controlled MNMs receive particular attention because of the easiness, safety and spatial control of the light source. Three main approaches are genereally employed to realize light regulated MNMs. At first, controlling motion based on photocatalytic fuel decomposition or photoinduced degradation reactions. As for example, usage of TiO_2 semiconductor that can decopose H_2O_2 photocatalytically and showed the propulsion in presence of UV light by self-diffusiophoretic mechanism was demonstrated by Sen's group in 2010[78]. Apart from self-diffusiophoresis, other mechanisms like bubble propulsion[95, 96] and self-electrophoresis[97,98,99] were also proposed for light induced movement. In self-diffusiophoresis mechanism, the light induced asymmetric chemical reactions that occur on the surface of MNMs develop a net chemical gradient that induces osmotic flow and set up a temporary electric field which results in motion whereas in the case of self-electrophoresis, asymmetric photoactive reactions on the MNMs create a net electric gradient resulting in autonomous movement of MNMs. By switching on/off the light source or by manipulating the intensity of the light, the speed of the MNMs based on photocatalytic fuel decomposition or degradation can be controlled. As shown by Chen et al.,[98] under 1W/cm^2 UV illumination the TiO_2 microtubes exhibit a maximum speed of 325 μm s^{-1} which was stopped immediately once the light source is switched off because there is no more oxygen bubbles, the movement is recovered within 0.2 seconds once the light is switched on again. The photocatalytic efficiency of TiO_2 was adjusted by modulating the intensity of the applied UV light which inturn affects the concentration of oxygen bubbles and when the intensity of the UV light varied from 0.2 to 1W/cm^2, the speed of the TiO_2 micromotor increased from 62 to 264 μm s^{-1}. Not only a single micromotor, but microarrays of TiO_2 have been controlled in the similar approach and good cargo loading and transportation in fluids also demonstrated[100].

Secondly, the nanoparticles are immobilized of light responsive materials such as azobenzene and spiropyran that undergo light induced trans – cis isomerization at a wavelength of 300-380 nm and exhibit cis – trans isomerization under visible light. As a result of this conformational transformation in a non-polar solvent, the solvation layer of azobenzene immobilized nanoparticles will disappear and dipole-dipole interaction will be created between the polar cis-azobenzene molecules in the non-polar medium resulting in the self assembly of nanoparticles in the UV light which will disassemble under visible light illumination. This light induced self assembly and disassembly in UV and visible light leading to schooling and dispersing behaviour of these immobilized nanoparticles[101, 102]

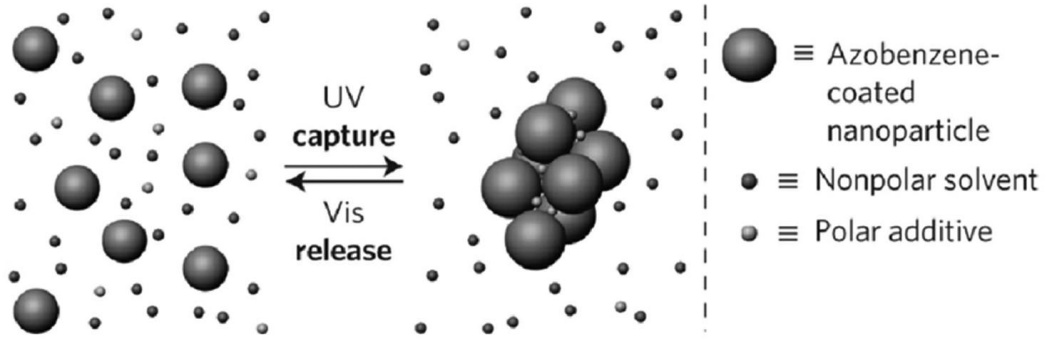


Figure 22. Schematic illustration showing the light induced self assembly and disassembly of photoactive molecule immobilized nanoparticles

Thirdly, inducing the movement control by using photothermal effect. As we know that, based on the size and shape, gold absorb light from visible to near infrared (NIR) regime owing to surface plasmon resonance (SPR) oscillations and thus gold nanorods and nanoshells generate local hyperthermia while exposing to NIR light. In a microtube, platinum catalytic nanoparticles were deposited on the inner surface and the outer surface was covered with gold nanoshells. When the H_2O_2 fuel concentration was 0.1%, there is no propulsion of the microtube but under NIR irradiation, the kinetics of the Pt catalyst nanoparticles was triggered due to the increase of temperature by photothermal effect and hence the tubular motor speed increased accordingly. By turning on/off the NIR light, the controlled motion of tubular micromotor was achieved[103].

2.3.2. Magnetic control:

Because of the non-invasiveness, good controllability and penetration, magnetic fields are generally used to generate propulsion for MNMs that consist of ferromagnetic components[104, 105]. Magnetic field powered surface walkers, flexible and helical swimmers were demonstrated[106, 107]. For the movement of flexible swimmers, the deformation of flexible elements in a asymmetric manner is required[104, 108] whereas for the helical swimmers the rotation of the structure under magnetic field will triggert he movement. By turning on and off the magnetic field, the movement of these MNMs can be controlled and also the magnetic field is used for direction control of the motion of MNMs[109, 110, 111]. Highly active dual mode nanoreactors were made by using Pt and Ni nanostructures, Pt acts as a catalyst to decompose the fuel whereas Ni helps to achieve magnetic control and thus precise control over movement was achieved under homoeneous magnetic field in presence of H_2O_2 fuel and irregular movement was seen in the absence of magnetic field[112]. Similarly tubular

micromotors were developed by using graphene oxide nanosheets, Pt and Ni layer; the Pt as a catalyst, the Ni layer for magnetic control and the the oxygen moieties available in the graphene oxide used for heavy metal like lead (Pb) adsorbtion and used for environmetal remediation[113, 90]

2.3.3. Acoustic control:

Ultrasound is having frequency above the normal human hearing level and owing to its high penetration strength and insensitivity to the surrounding environment, it is widely used for bio-related applications. By modulating the direction or frequency of the ultrasound or turning on/off of the source, the movement of MNMs can be controlled. First acoustic controlled MNM was reported by Mallouk group in 2012[114]. In this work, asymmetric nanorods with concave Au to concentrate the applied acoustic energy and convex Ru to dissipate the energy were prepared by template assisted electrodeposition method and thus creates unequal distribution of ultrasonic pressure which triggers the Ru end to move forward. It also exhibited movement towards Au end in the presence of H_2O_2[115].

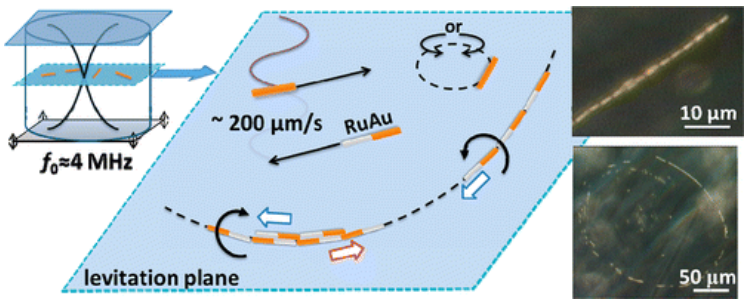


Figure 23. Ultrasound controlled Au-Ru bimetallic nanorod

2.3.4. Electric field control:

Since MNMs are made up of conducting materials, they are easily affected by electric field and thus by modulating the surface charge or tuning the electrochemical reactions at the interface of the MNMs, their motion can be controlled. Because of the polarization induced by electric field, water splitting occurs at the interface and produces localized electric current that triggers the directional movement in a controlled manner[116, 32, 117]. Joseph Wang group developed electrochemically controlled movement of catalytic micromotors made up of Au-Pt nanowire that shows movement in H_2O_2 and also controlled by applied electric field[118], while changing the electric field from +1.0 V to -0.4 V, the nanowire motor in 5% H_2O_2 solution showed an increment of speed from 4 to 22 µm s^{-1}, but if there is no electric field the motor showed only a speed of 9 µm s^{-1}.

2.3.5. Thermal control:

The main mechanism of catalytic MNMs is the catalytic decomposition of H_2O_2 to water and oxygen bubbles. The increase in temperature not only enhance the kinetics of this catalytic reaction but also decreasing the viscosity of the medium[119]. Balasubramanian *et al.*, fabricated Pt/Au bisegment nanowires and by applying short heat pulses demonstrated the reversible acceleration or slowed down of the motion. The accelerated movement is mainly attributed to the thermal activation of the redox reaction of H_2O_2 at Pt and Au metals and also to lowering of the viscosity of the medium at higher temperature. The speed of the bimetallic nanowire increased from 14 to 45 μm s^{-1} while changing the temperature from 25°C to 65°C and thus by adjusting the temperature the speed varied accordingly[120]

2.3.6 Chemotaxis:

Chemotaxis is an important behaviour in small microorganisms that helps especially to find food or to escape away from toxins. These organisms can sense chemical environment and move toward or away from a particular chemical that termed as positive or negative chemotaxis. Sperm cells move towards egg cells is a perfect example of chemotaxis. Although this chemotactic behaviour is commonly existing in biology, the first non biological example was demonstrated by Sen and Velegol's group in 2007[121] by using bimetallic Pt-Au colloidal nanorods that showed directed movement towards higher gradient of H_2O_2 fuel concentration due to active diffusion.

2.4. Applications of Micro/Nanomotors :

2.4.1. For cargo transport:

Similar to biomotors that carry out intracellular transport of vesicles, catalytic MNMs also have the potential to load, transport and unload the cargoes precisely at desired position. Firstly Sen group demonstrated an approach to load a cargo by exploiting the electrostatic interaction between cargo and nanomotor. In this work, they transport polystyrene (PS) microspheres on the Pt-Au nanomotor, they electropolymerized pyrrole at one end of the rod which helps to attach positively charged PS-amidine cargo by electrostatic interaction and by using biotin-streptavidin interaction, PS-streptavidin microspheres were immobilized on Au which is at the other end of the rod as shown in Fig 24.,

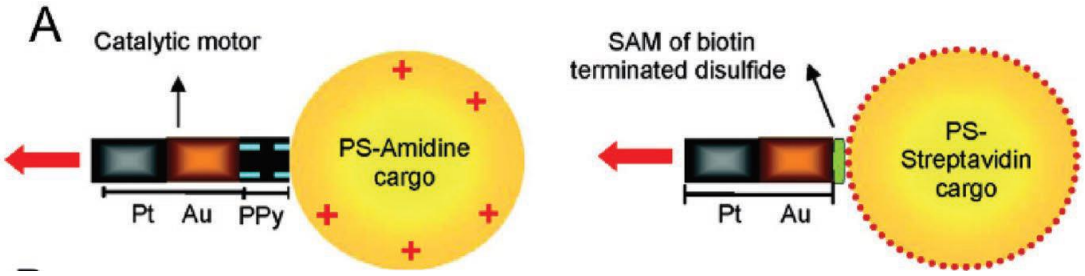


Figure 24. Fabrication and cargo transport of polystyrene microspheres on Pt-Au micromotor.

The nanomotor transfer the cargo particles based on self-electrophoresis mechanism. If the weight of the cargo increases, the speed of the motor decreases due to higher viscous drag. Motors with nickel segment showed unidirectional motion under external magnetic field and by quickly reversing the motor direction by external magnet, the drag force on the particle dominates the magnetic attraction between the particle and nickel and hence the cargo particle is released[122]. Alternatively, Ag segment can be incorporated in between Pt and Au part and subsequently Ag will be dissolved in presence of H_2O_2, chloride ions and exposure to UV light for 10-20 seconds to drop-off the cargo, and also photocleavable linker can be used but it takes a little time (60 – 100 seconds) to release the cargo[123]

2.4.2. For biomedical applications:

In traditional drug delivery systems, the drug molecules carried by blood reaching the unhealthy as well as healthy organs and hence the directed drug delivery particularly to the unhealthy parts is crucial[124]. The MNMs are the potential candidates for targetted drug delivery because of their controlled directional motion and tissue penetration capability[125, 126]. Sen group recently demonstrated that micromotors can be used in vitro to identify and repair the bone crack based on diffusiophoretic mechanism[127]. Generally, H_2O_2 powered motors are not suitable for biomedical applications because of the toxicity of H_2O_2 that causes apoptosis and hence motors powered by other sources are used for biomedical applications. The first *in vivo* demonstration using artificial micromotor was shown by Joseph Wang group in a mouse model. They used zinc based micromotor that triggered by acid-driven propulsion in the stomach. These motors slowly dissolved by gastric acid and releasing the cargo without any toxins[128]. Kagan *et al* developed tubular microbullet that was triggered by ultrasound and used for penetration and deformation of tissues[129]. Magnetic intraocular microdevices were proposed by Nelson group in 2012 and they showed targeted retinal drug delivery and oxygen sensing with the magnetic stimuli[130]. Recently Pal et al has shown that in the living cells how

the magnetically powered motors can be used for cellular internalization and intracellular manipulation[131].

2.4.3. For environmental applications:

The low cost and energy efficient technologies are required to eradicate chemical and biological pollutants from water reservoirs. Because of their good catalytic properties and self propulsion, MNMs are believed to be potential candidates for environmental remediation processes. The first example of using micromotor for environmental cleaning was reported by Guix and co-workers in 2012[132]. They used alkanethiols functionalized Pt based microtube (Au/Ni/PEDOT/Pt) for loading and transporting small oil droplets and showed as a model system for cleaning oil spillage. By tuning the surface hydrophobicity, the amount of interaction can be modified. The same group developed Janus micromotor made up of magnesium microparticles and nickel-gold bilayer surface modifed with SAMs of long chain thiols and used in sea water by utilizing the processes of microgalvanic and chloride pitting corrosion and thus no additional fuels. Thanks to the presence of nickel, this micromotor had been controlled by external magnetic field[54]. However, the poor binding of thiols to the Pt led to the deactivation of the catalyst and the efficiency of the micromotor severely lost. To overcome this, Do Minh *et al* used MnO_2 to protect Pt based micromotor before thiol functionalization[133] and they showed that MnO_2 protected micromotor retained superior performance even after alkanethiol treatment and used for capture and removal of oil droplets. Mou *et al* used magnetically controllable $MnFe_2O_4$ micromotors without any surface modification for oil removal[134].

Based on the response (either enhancing or deactivating/poisoning) in catalytic activity of MNMs, they can be used for environmental sensing. For instance, nanomotor made up of bimetallic Pt and Au exhibited enhanced speed in presence of silver ions, because these silver ions reduced to metallic silver on Pt surface by H_2O_2 fuel and hence the electrocatalytic property of nanomotor increased that resulting in enhanced movement[135]. Since the rate of enhancement depend upon the silver ions concentration, this can be exploited to get quantitative information on silver ion toxicity in the nanomolar range. Singh et al showed that enzyme powered nanomotors can sense the nerve agents and be used for chemical vapour detection[136]. This catalase powered nanomotors be active when there is no chemical vapour in the environment, but becomes inactive if there is chemical vapour because the vapour inhibits the catalase activity. Wani et al showed that MnO_2 micromotors can be used for catalytic

degradation of rhodamine 6G and methylene blue dyes, they showed 90% decoloration in just 1 hour[137].

References

1. Mirvakili, S. M.; Hunter, I. W., Artificial Muscles: Mechanisms, Applications, and Challenges. *Advanced Materials* **2018,** *30* (6), 1704407.
2. Hines, L.; Petersen, K.; Lum, G. Z.; Sitti, M., Soft Actuators for Small-Scale Robotics. *Advanced Materials* **2017,** *29* (13), 1603483.
3. Mirfakhrai, T.; Madden, J. D. W.; Baughman, R. H., Polymer artificial muscles. *Materials Today* **2007,** *10* (4), 30-38.
4. Pelrine, R.; Sommer-Larsen, P.; Kornbluh, R. D.; Heydt, R.; Kofod, G.; Pei, Q.; Gravesen, P., *Applications of dielectric elastomer actuators*. SPIE: 2001; Vol. 4329.
5. (a) Kornbluh, R., EAP actuators, devices and mechanisms Application of dielectric elastomers. *Electroactive Polymer (EAP) Actuators as Artificial Muscles Reality, Potential and Challenges* **2004**; (b) Pelrine, R.; Kornbluh, R. D.; Pei, Q.; Stanford, S.; Oh, S.; Eckerle, J.; Full, R. J.; Rosenthal, M. A.; Meijer, K., *Dielectric elastomer artificial muscle actuators: toward biomimetic motion*. SPIE: 2002; Vol. 4695.
6. Carpi, F.; Rossi, D. D., Improvement of electromechanical actuating performances of a silicone dielectric elastomer by dispersion of titanium dioxide powder. *IEEE Transactions on Dielectrics and Electrical Insulation* **2005,** *12* (4), 835-843.
7. Kofod, G., *Dielectric Elastomer Actuators: Ph. D. Thesis*. Risø National Laboratory: 2001.
8. Schlaak, H. F.; Jungmann, M.; Matysek, M.; Lotz, P., *Novel multilayer electrostatic solid state actuators with elastic dielectric*. SPIE: 2005; Vol. 5759.
9. Zhang, Q.; Huang, C.; Xia, F.; Su, J., Electric EAP. *Electroactive Polymer (EAP) Actuators as Artificial Muscles: Reality, Potential, and Challenges* **2001,** *2*.
10. Lehmann, W.; Skupin, H.; Tolksdorf, C.; Gebhard, E.; Zentel, R.; Krüger, P.; Lösche, M.; Kremer, F., Giant lateral electrostriction in ferroelectric liquid-crystalline elastomers. *Nature* **2001,** *410*, 447.
11. Madden, J. D. W.; Vandesteeg, N. A.; Anquetil, P. A.; Madden, P. G. A.; Takshi, A.; Pytel, R. Z.; Lafontaine, S. R.; Wieringa, P. A.; Hunter, I. W., Artificial muscle technology: physical principles and naval prospects. *IEEE Journal of Oceanic Engineering* **2004,** *29* (3), 706-728.
12. Skotheim, T. A.; Reynolds, J., *Handbook of Conducting Polymers, 2 Volume Set*. CRC press: 2007.
13. Baughman, R. H., Conducting polymer artificial muscles. *Synthetic Metals* **1996,** *78* (3), 339-353.
14. Pei, Q.; Inganäs, O., Electrochemical applications of the bending beam method; a novel way to study ion transport in electroactive polymers. *Solid State Ionics* **1993,** *60* (1), 161-166.
15. Hara, S.; Zama, T.; Takashima, W.; Kaneto, K., Gel-like Polypyrrole Based Artificial Muscles with Extremely Large Strain. *Polymer Journal* **2004,** *36*, 933.
16. (a) Madden, J. D.; Madden, P. G.; Hunter, I. W., *Conducting polymer actuators as engineering materials*. SPIE: 2002; Vol. 4695; (b) Warren, M. R.; Madden, J. D., Electrochemical switching of conducting polymers: A variable resistance transmission line model. *Journal of Electroanalytical Chemistry* **2006,** *590* (1), 76-81.
17. (a) Madden, J. D.; Cush, R. A.; Kanigan, T. S.; Hunter, I. W., Fast contracting polypyrrole actuators. *Synthetic Metals* **2000,** *113* (1), 185-192; (b) Hara, S.; Zama, T.; Takashima, W.; Kaneto, K., Free-standing polypyrrole actuators with response rate of

10.8%s−1. *Synthetic Metals* **2005,** *149* (2), 199-201; (c) Ding, J.; Liu, L.; Spinks, G. M.; Zhou, D.; Wallace, G. G.; Gillespie, J., High performance conducting polymer actuators utilising a tubular geometry and helical wire interconnects. *Synthetic Metals* **2003,** *138* (3), 391-398; (d) Smela, E.; Inganäs, O.; Lundström, I., Controlled Folding of Micrometer-Size Structures. *Science* **1995,** *268* (5218), 1735-1738.

18. Spinks, G. M.; Mottaghitalab, V.; Bahrami-Samani, M.; Whitten, P. G.; Wallace, G. G., Carbon-Nanotube-Reinforced Polyaniline Fibers for High-Strength Artificial Muscles. *Advanced Materials* **2006,** *18* (5), 637-640.
19. Spinks, G. M.; Truong, V.-T., Work-per-cycle analysis for electromechanical actuators. *Sensors and Actuators A: Physical* **2005,** *119* (2), 455-461.
20. (a) Spinks, G. M.; Wallace, G. G.; Ding, J.; Zhou, D.; Xi, B.; Gillespie, J., *Ionic liquids and polypyrrole helix tubes: bringing the electronic Braille screen closer to reality*. SPIE: 2003; Vol. 5051; (b) Pettersson, P. F.; Jager, E. W.; Inganas, O. In *Surface micromachined polymer actuators as valves in PDMS microfluidic system*, 1st Annual International IEEE-EMBS Special Topic Conference on Microtechnologies in Medicine and Biology. Proceedings (Cat. No. 00EX451), IEEE: 2000; pp 334-335.
21. Baughman, R. H.; Zakhidov, A. A.; de Heer, W. A., Carbon Nanotubes--the Route Toward Applications. *Science* **2002,** *297* (5582), 787-792.
22. Baughman, R. H.; Cui, C.; Zakhidov, A. A.; Iqbal, Z.; Barisci, J. N.; Spinks, G. M.; Wallace, G. G.; Mazzoldi, A.; De Rossi, D.; Rinzler, A. G.; Jaschinski, O.; Roth, S.; Kertesz, M., Carbon Nanotube Actuators. *Science* **1999,** *284* (5418), 1340-1344.
23. Terrones, M.; Terrones, H.; Endo, M.; Hayashi, T.; Kim, Y. A.; Terrones, M.; Dresselhaus, M. S., Applications of carbon nanotubes in the twenty–first century. *Philosophical Transactions of the Royal Society of London. Series A: Mathematical, Physical and Engineering Sciences* **2004,** *362* (1823), 2223-2238.
24. Madden, J. D. W.; Barisci, J. N.; Anquetil, P. A.; Spinks, G. M.; Wallace, G. G.; Baughman, R. H.; Hunter, I. W., Fast Carbon Nanotube Charging and Actuation. *Advanced Materials* **2006,** *18* (7), 870-873.
25. Ebron, V. H.; Yang, Z.; Seyer, D. J.; Kozlov, M. E.; Oh, J.; Xie, H.; Razal, J.; Hall, L. J.; Ferraris, J. P.; MacDiarmid, A. G.; Baughman, R. H., Fuel-Powered Artificial Muscles. *Science* **2006,** *311* (5767), 1580-1583.
26. (a) Shahinpoor, M.; Kim, K. J., Ionic polymer-metal composites: I. Fundamentals. *Smart Materials and Structures* **2001,** *10* (4), 819-833; (b) Kim, K. J.; Shahinpoor, M., A novel method of manufacturing three-dimensional ionic polymer–metal composites (IPMCs) biomimetic sensors, actuators and artificial muscles. *Polymer* **2002,** *43* (3), 797-802; (c) Nemat-Nasser, S.; Thomas, C. W., Ionomeric polymer–metal composites. *Electroactive Polymer (EAP) Actuators as Artifical Muscles. Reality, Potential, and Challenges, SPIE Press, Washington* **2001**.
27. Shahinpoor, M., Mechanoelectrical Phenomena In Ionic Polymers. *Mathematics and Mechanics of Solids* **2003,** *8* (3), 281-288.
28. Nemat-Nasser, S., Micromechanics of actuation of ionic polymer-metal composites. *Journal of Applied Physics* **2002,** *92* (5), 2899-2915.
29. Bennett, M. D.; Leo, D. J., *Ionic liquids as novel solvents for ionic polymer transducers*. SPIE: 2004; Vol. 5385.
30. (a) Bar-Cohen, Y.; Bar-Cohen, Y., *Electroactive polymer (EAP) actuators as artificial muscles: reality, potential, and challenges*. SPIE press Bellingham, WA: 2004; Vol. 136; (b) Kim, K. J.; Shahinpoor, M., Ionic polymer metal composites: II. Manufacturing techniques. *Smart Materials and Structures* **2003,** *12* (1), 65-79.
31. Wei, G.; Daniel, K.; Shun, P. O.; Corbin, C.; Susana, C.; Erdembileg, C. E.; Erik, S.; E., F. E.; Liangfang, Z.; Eric, L.; Joseph, W., Cargo-Towing Fuel-Free Magnetic Nanoswimmers for Targeted Drug Delivery. *Small* **2012,** *8* (3), 460-467.

32. Loget, G.; Kuhn, A., Electric field-induced chemical locomotion of conducting objects. *Nature Communications* **2011,** *2*, 535.
33. Wei, W.; Sixing, L.; Lamar, M.; Suzanne, A.; Jun, H. T.; E., M. T., Acoustic Propulsion of Nanorod Motors Inside Living Cells. *Angewandte Chemie* **2014,** *126* (12), 3265-3268.
34. Purcell, E. M., Life at low Reynolds number. *American Journal of Physics* **1977,** *45* (1), 3-11.
35. Lauga, E., Life around the scallop theorem. *Soft Matter* **2011,** *7* (7), 3060-3065.
36. Agarwal, A.; Hess, H., Biomolecular motors at the intersection of nanotechnology and polymer science. *Progress in Polymer Science* **2010,** *35* (1), 252-277.
37. Sujatha, R.; Karl-Heinz, E.; D., B. G.; Viola, V.; Henry, H., Selective Loading of Kinesin-Powered Molecular Shuttles with Protein Cargo and its Application to Biosensing. *Small* **2006,** *2* (3), 330-334.
38. Hess, H.; Clemmens, J.; Qin, D.; Howard, J.; Vogel, V., Light-Controlled Molecular Shuttles Made from Motor Proteins Carrying Cargo on Engineered Surfaces. *Nano Letters* **2001,** *1* (5), 235-239.
39. Hess, H.; Matzke, C. M.; Doot, R. K.; Clemmens, J.; Bachand, G. D.; Bunker, B. C.; Vogel, V., Molecular Shuttles Operating Undercover: A New Photolithographic Approach for the Fabrication of Structured Surfaces Supporting Directed Motility. *Nano Letters* **2003,** *3* (12), 1651-1655.
40. Goel, A.; Vogel, V., Harnessing biological motors to engineer systems for nanoscale transport and assembly. *Nature Nanotechnology* **2008,** *3*, 465.
41. Fischer, T.; Agarwal, A.; Hess, H., A smart dust biosensor powered by kinesin motors. *Nature Nanotechnology* **2009,** *4*, 162.
42. Mano, N.; Heller, A., Bioelectrochemical Propulsion. *Journal of the American Chemical Society* **2005,** *127* (33), 11574-11575.
43. Pantarotto, D.; Browne, W. R.; Feringa, B. L., Autonomous propulsion of carbon nanotubes powered by a multienzyme ensemble. *Chemical Communications* **2008,** (13), 1533-1535.
44. Sanchez, S.; Solovev, A. A.; Mei, Y.; Schmidt, O. G., Dynamics of Biocatalytic Microengines Mediated by Variable Friction Control. *Journal of the American Chemical Society* **2010,** *132* (38), 13144-13145.
45. Wright, C. R.; Metin, S., Bio-Hybrid Cell-Based Actuators for Microsystems. *Small* **2014,** *10* (19), 3831-3851.
46. Kassem, S.; van Leeuwen, T.; Lubbe, A. S.; Wilson, M. R.; Feringa, B. L.; Leigh, D. A., Artificial molecular motors. *Chemical Society Reviews* **2017,** *46* (9), 2592-2621.
47. Samuel, S.; Lluís, S.; Jaideep, K., Chemically Powered Micro- and Nanomotors. *Angewandte Chemie International Edition* **2015,** *54* (5), 1414-1444.
48. Nakata, S.; Doi, Y.; Kitahata, H., Synchronized motion of a mobile boundary driven by a camphor fragment. *Journal of Colloid and Interface Science* **2004,** *279* (2), 503-508.
49. Guanjia, Z.; Hui, S. T.; Martin, P., External-Energy-Independent Polymer Capsule Motors and Their Cooperative Behaviors. *Chemistry – A European Journal* **2011,** *17* (43), 12020-12026.
50. Liu, R.; Sen, A., Autonomous Nanomotor Based on Copper–Platinum Segmented Nanobattery. *Journal of the American Chemical Society* **2011,** *133* (50), 20064-20067.
51. Gao, W.; Uygun, A.; Wang, J., Hydrogen-Bubble-Propelled Zinc-Based Microrockets in Strongly Acidic Media. *Journal of the American Chemical Society* **2012,** *134* (2), 897-900.
52. Wei, G.; Mattia, D. A.; Victor, G. G.; Jahir, O.; Joseph, W., Multi-Fuel Driven Janus Micromotors. *Small* **2013,** *9* (3), 467-471.

53. Gao, W.; Pei, A.; Dong, R.; Wang, J., Catalytic Iridium-Based Janus Micromotors Powered by Ultralow Levels of Chemical Fuels. *Journal of the American Chemical Society* **2014,** *136* (6), 2276-2279.
54. Gao, W.; Feng, X.; Pei, A.; Gu, Y.; Li, J.; Wang, J., Seawater-driven magnesium based Janus micromotors for environmental remediation. *Nanoscale* **2013,** *5* (11), 4696-4700.
55. Gao, W.; Pei, A.; Wang, J., Water-Driven Micromotors. *ACS Nano* **2012,** *6* (9), 8432-8438.
56. Edd, J.; Payen, S.; Rubinsky, B.; Stoller, M. L.; Sitti, M. In *Biomimetic propulsion for a swimming surgical micro-robot*, Proceedings 2003 IEEE/RSJ International Conference on Intelligent Robots and Systems (IROS 2003) (Cat. No.03CH37453), 27-31 Oct. 2003; 2003; pp 2583-2588 vol.3.
57. Hyunchul, C.; Jongho, C.; Semi, J.; Chungsun, Y.; Jong-oh, P.; Sukho, P., Two-dimensional locomotion of a microrobot with a novel stationary electromagnetic actuation system. *Smart Materials and Structures* **2009,** *18* (11), 115017.
58. Fusco, S.; Ullrich, F.; Pokki, J.; Chatzipirpiridis, G.; Özkale, B.; Sivaraman, K. M.; Ergeneman, O.; Pané, S.; Nelson, B. J., Microrobots: a new era in ocular drug delivery. *Expert Opinion on Drug Delivery* **2014,** *11* (11), 1815-1826.
59. Abbott, J. J. P., K. E.; Dong, L.; Nelson, B. J, How Should Microrobots Swim? *13th International Symposium of Robotics Research* **2007**, 1−11.
60. Jagajjanani, R. K.; Fei, L.; Long, M.; Hairong, Z.; Feiyan, C.; Wei, W., A Force to Be Reckoned With: A Review of Synthetic Microswimmers Powered by Ultrasound. *Small* **2015,** *11* (24), 2836-2846.
61. Martin, C. R., Membrane-Based Synthesis of Nanomaterials. *Chemistry of Materials* **1996,** *8* (8), 1739-1746.
62. Wang, J., Template electrodeposition of catalytic nanomotors. *Faraday Discussions* **2013,** *164* (0), 9-18.
63. Paxton, W. F.; Kistler, K. C.; Olmeda, C. C.; Sen, A.; St. Angelo, S. K.; Cao, Y.; Mallouk, T. E.; Lammert, P. E.; Crespi, V. H., Catalytic Nanomotors: Autonomous Movement of Striped Nanorods. *Journal of the American Chemical Society* **2004,** *126* (41), 13424-13431.
64. Fournier-Bidoz, S.; Arsenault, A. C.; Manners, I.; Ozin, G. A., Synthetic self-propelled nanorotors. *Chemical Communications* **2005,** (4), 441-443.
65. Gao, W.; Sattayasamitsathit, S.; Orozco, J.; Wang, J., Highly Efficient Catalytic Microengines: Template Electrosynthesis of Polyaniline/Platinum Microtubes. *Journal of the American Chemical Society* **2011,** *133* (31), 11862-11864.
66. Liu, L.; Yoo, S.-H.; Lee, S. A.; Park, S., Wet-Chemical Synthesis of Palladium Nanosprings. *Nano Letters* **2011,** *11* (9), 3979-3982.
67. Manesh, K. M.; Cardona, M.; Yuan, R.; Clark, M.; Kagan, D.; Balasubramanian, S.; Wang, J., Template-Assisted Fabrication of Salt-Independent Catalytic Tubular Microengines. *ACS Nano* **2010,** *4* (4), 1799-1804.
68. Simone, S.; Salvador, P.; Eva, P.; Jordi, S.; D., B. M.; J., N. B., Helical and Tubular Lipid Microstructures that are Electroless-Coated with CoNiReP for Wireless Magnetic Manipulation. *Small* **2012,** *8* (10), 1498-1502.
69. Gabriel, L.; Jérome, R.; Alexander, K., True Bulk Synthesis of Janus Objects by Bipolar Electrochemistry. *Advanced Materials* **2012,** *24* (37), 5111-5116.
70. Loget, G.; Zigah, D.; Bouffier, L.; Sojic, N.; Kuhn, A., Bipolar Electrochemistry: From Materials Science to Motion and Beyond. *Accounts of Chemical Research* **2013,** *46* (11), 2513-2523.
71. Walther, A.; Müller, A. H. E., Janus Particles: Synthesis, Self-Assembly, Physical Properties, and Applications. *Chemical Reviews* **2013,** *113* (7), 5194-5261.

72. Fattah, Z.; Loget, G.; Lapeyre, V.; Garrigue, P.; Warakulwit, C.; Limtrakul, J.; Bouffier, L.; Kuhn, A., Straightforward single-step generation of microswimmers by bipolar electrochemistry. *Electrochimica Acta* **2011,** *56* (28), 10562-10566.
73. Loget, G.; Larcade, G.; Lapeyre, V.; Garrigue, P.; Warakulwit, C.; Limtrakul, J.; Delville, M. H.; Ravaine, V.; Kuhn, A., Single point electrodeposition of nickel for the dissymmetric decoration of carbon tubes. *Electrochimica Acta* **2010,** *55* (27), 8116-8120.
74. Qin, L.; Banholzer, M. J.; Xu, X.; Huang, L.; Mirkin, C. A., Rational Design and Synthesis of Catalytically Driven Nanorotors. *Journal of the American Chemical Society* **2007,** *129* (48), 14870-14871.
75. Zhao, Y.; Ye, D.; Wang, G.-C.; Lu, T.-M. In *Designing nanostructures by glancing angle deposition*, Optical Science and Technology, SPIE's 48th Annual Meeting, SPIE: 2003; p 15.
76. Schamel, D.; Pfeifer, M.; Gibbs, J. G.; Miksch, B.; Mark, A. G.; Fischer, P., Chiral Colloidal Molecules And Observation of The Propeller Effect. *Journal of the American Chemical Society* **2013,** *135* (33), 12353-12359.
77. Wang, H.; Zhao, G.; Pumera, M., Beyond Platinum: Bubble-Propelled Micromotors Based on Ag and MnO2 Catalysts. *Journal of the American Chemical Society* **2014,** *136* (7), 2719-2722.
78. Yiying, H.; Misael, D.; M., C. F. U.; Ayusman, S., Light-Driven Titanium-Dioxide-Based Reversible Microfireworks and Micromotor/Micropump Systems. *Advanced Functional Materials* **2010,** *20* (10), 1568-1576.
79. Michael, I.; E., M. T.; Ayusman, S., Schooling Behavior of Light-Powered Autonomous Micromotors in Water. *Angewandte Chemie International Edition* **2009,** *48* (18), 3308-3312.
80. Loget, G.; Kuhn, A., Propulsion of Microobjects by Dynamic Bipolar Self-Regeneration. *Journal of the American Chemical Society* **2010,** *132* (45), 15918-15919.
81. Loget, G.; Kuhn, A., Bipolar electrochemistry for cargo-lifting in fluid channels. *Lab on a Chip* **2012,** *12* (11), 1967-1971.
82. Zhiguang, W.; Yingjie, W.; Wenping, H.; Xiankun, L.; Jianmin, S.; Qiang, H., Self-Propelled Polymer-Based Multilayer Nanorockets for Transportation and Drug Release. *Angewandte Chemie International Edition* **2013,** *52* (27), 7000-7003.
83. Sangwon, K.; Famin, Q.; Samhwan, K.; Ali, G.; Cheil, M.; Li, Z.; J., N. B.; Hongsoo, C., Fabrication and Characterization of Magnetic Microrobots for Three-Dimensional Cell Culture and Targeted Transportation. *Advanced Materials* **2013,** *25* (41), 5863-5868.
84. A., S. A.; Yongfeng, M.; Esteban, B. U.; Gaoshan, H.; G., S. O., Catalytic Microtubular Jet Engines Self-Propelled by Accumulated Gas Bubbles. *Small* **2009,** *5* (14), 1688-1692.
85. Jemish, P.; Xing, M.; Jaideep, K.; Juliane, S.; Morgan, M. S.; Carolina, T.-P.; Lluís, S.; Samuel, S., Nano and micro architectures for self-propelled motors. *Science and Technology of Advanced Materials* **2015,** *16* (1), 014802.
86. Wang, H.; Pumera, M., Fabrication of Micro/Nanoscale Motors. *Chemical Reviews* **2015,** *115* (16), 8704-8735.
87. Wang, H.; Pumera, M., Emerging materials for the fabrication of micro/nanomotors. *Nanoscale* **2017,** *9* (6), 2109-2116.
88. F., I. R.; Alexander, S.; Ned, B.; M., W. G., Autonomous Movement and Self-Assembly. *Angewandte Chemie International Edition* **2002,** *41* (4), 652-654.
89. Gao, W.; Wang, J., The Environmental Impact of Micro/Nanomachines: A Review. *ACS Nano* **2014,** *8* (4), 3170-3180.

90. Vilela, D.; Parmar, J.; Zeng, Y.; Zhao, Y.; Sánchez, S., Graphene-Based Microbots for Toxic Heavy Metal Removal and Recovery from Water. *Nano Letters* **2016,** *16* (4), 2860-2866.
91. Wang, H.; Khezri, B.; Pumera, M., Catalytic DNA-Functionalized Self-Propelled Micromachines for Environmental Remediation. *Chem* **2016,** *1* (3), 473-481.
92. Baraban, L.; Makarov, D.; Streubel, R.; Mönch, I.; Grimm, D.; Sanchez, S.; Schmidt, O. G., Catalytic Janus Motors on Microfluidic Chip: Deterministic Motion for Targeted Cargo Delivery. *ACS Nano* **2012,** *6* (4), 3383-3389.
93. Patra, D.; Sengupta, S.; Duan, W.; Zhang, H.; Pavlick, R.; Sen, A., Intelligent, self-powered, drug delivery systems. *Nanoscale* **2013,** *5* (4), 1273-1283.
94. Kumar, S. S.; Mariana, M. S.; Britta, K.; G., S. O., Medibots: Dual-Action Biogenic Microdaggers for Single-Cell Surgery and Drug Release. *Advanced Materials* **2016,** *28* (5), 832-837.
95. Li, Y.; Mou, F.; Chen, C.; You, M.; Yin, Y.; Xu, L.; Guan, J., Light-controlled bubble propulsion of amorphous TiO2/Au Janus micromotors. *RSC Advances* **2016,** *6* (13), 10697-10703.
96. Fangzhi, M.; Yan, L.; Chuanrui, C.; Wei, L.; Yixia, Y.; Huiru, M.; Jianguo, G., Single-Component TiO2 Tubular Microengines with Motion Controlled by Light-Induced Bubbles. *Small* **2015,** *11* (21), 2564-2570.
97. Dai, B.; Wang, J.; Xiong, Z.; Zhan, X.; Dai, W.; Li, C.-C.; Feng, S.-P.; Tang, J., Programmable artificial phototactic microswimmer. *Nature Nanotechnology* **2016,** *11*, 1087.
98. Chuanrui, C.; Fangzhi, M.; Leilei, X.; Shaofei, W.; Jianguo, G.; Zunpeng, F.; Quanwei, W.; Lei, K.; Wei, L.; Joseph, W.; Qingjie, Z., Light-Steered Isotropic Semiconductor Micromotors. *Advanced Materials* **2017,** *29* (3), 1603374.
99. Zhou, D.; Li, Y. C.; Xu, P.; McCool, N. S.; Li, L.; Wang, W.; Mallouk, T. E., Visible-light controlled catalytic Cu2O-Au micromotors. *Nanoscale* **2017,** *9* (1), 75-78.
100. Mihail, E.; Maria, G.; Vitalie, P.; Vladimir, C.; M., F. V.; G., S. O.; Ion, T., Light-Induced Motion of Microengines Based on Microarrays of TiO2 Nanotubes. *Small* **2016,** *12* (39), 5497-5505.
101. Klajn, R.; Bishop, K. J. M.; Grzybowski, B. A., Light-controlled self-assembly of reversible and irreversible nanoparticle suprastructures. *Proceedings of the National Academy of Sciences* **2007,** *104* (25), 10305-10309.
102. Zhao, H.; Sen, S.; Udayabhaskararao, T.; Sawczyk, M.; Kučanda, K.; Manna, D.; Kundu, P. K.; Lee, J.-W.; Král, P.; Klajn, R., Reversible trapping and reaction acceleration within dynamically self-assembling nanoflasks. *Nature Nanotechnology* **2015,** *11*, 82.
103. Wu, Z.; Lin, X.; Wu, Y.; Si, T.; Sun, J.; He, Q., Near-Infrared Light-Triggered "On/Off" Motion of Polymer Multilayer Rockets. *ACS Nano* **2014,** *8* (6), 6097-6105.
104. Gao, W.; Sattayasamitsathit, S.; Manesh, K. M.; Weihs, D.; Wang, J., Magnetically Powered Flexible Metal Nanowire Motors. *Journal of the American Chemical Society* **2010,** *132* (41), 14403-14405.
105. Rikken, R. S. M.; Nolte, R. J. M.; Maan, J. C.; van Hest, J. C. M.; Wilson, D. A.; Christianen, P. C. M., Manipulation of micro- and nanostructure motion with magnetic fields. *Soft Matter* **2014,** *10* (9), 1295-1308.
106. Tailin, X.; Wei, G.; Li-Ping, X.; Xueji, Z.; Shutao, W., Fuel-Free Synthetic Micro-/Nanomachines. *Advanced Materials* **2017,** *29* (9), 1603250.
107. Tianlong, L.; Jinxing, L.; Hongtao, Z.; Xiaocong, C.; Wenping, S.; Yanan, H.; Guangbin, S.; Elodie, S.; Guangyu, Z.; Longqiu, L.; Joseph, W., Magnetically Propelled Fish-Like Nanoswimmers. *Small* **2016,** *12* (44), 6098-6105.

108. Dreyfus, R.; Baudry, J.; Roper, M. L.; Fermigier, M.; Stone, H. A.; Bibette, J., Microscopic artificial swimmers. *Nature* **2005,** *437*, 862.
109. Wei, Z.; Jinxing, L.; J., L. Y.; Isaac, R.; Xin, Q.; Renfeng, D.; Zhiguang, W.; Wei, G.; H., C. P.; Joseph, W.; Shaochen, C., 3D-Printed Artificial Microfish. *Advanced Materials* **2015,** *27* (30), 4411-4417.
110. R., K. T.; F., P. W.; E., M. T.; Ayusman, S., Catalytic Nanomotors: Remote-Controlled Autonomous Movement of Striped Metallic Nanorods. *Angewandte Chemie International Edition* **2005,** *44* (5), 744-746.
111. Veronika, M.; Maria, G.; Franziska, H.; G., S. O., Dynamic Polymeric Microtubes for the Remote-Controlled Capture, Guidance, and Release of Sperm Cells. *Advanced Materials* **2016,** *28* (21), 4084-4089.
112. Marcos, S. S.; Moisés, P. L.; Benito, R. G.; Verónica, S.; A., C. D. M., Highly Active Nanoreactors: Nanomaterial Encapsulation Based on Confined Catalysis. *Angewandte Chemie International Edition* **2012,** *51* (16), 3877-3882.
113. Zhao, G.; Li, J.; Ren, X.; Chen, C.; Wang, X., Few-Layered Graphene Oxide Nanosheets As Superior Sorbents for Heavy Metal Ion Pollution Management. *Environmental Science & Technology* **2011,** *45* (24), 10454-10462.
114. Wang, W.; Castro, L. A.; Hoyos, M.; Mallouk, T. E., Autonomous Motion of Metallic Microrods Propelled by Ultrasound. *ACS Nano* **2012,** *6* (7), 6122-6132.
115. Wang, W.; Duan, W.; Zhang, Z.; Sun, M.; Sen, A.; Mallouk, T. E., A tale of two forces: simultaneous chemical and acoustic propulsion of bimetallic micromotors. *Chemical Communications* **2015,** *51* (6), 1020-1023.
116. Velev, O. D.; Gangwal, S.; Petsev, D. N., Particle-localized AC and DC manipulation and electrokinetics. *Annual Reports Section "C" (Physical Chemistry)* **2009,** *105* (0), 213-246.
117. Roche, J.; Carrara, S.; Sanchez, J.; Lannelongue, J.; Loget, G.; Bouffier, L.; Fischer, P.; Kuhn, A., Wireless powering of e -swimmers. *Scientific Reports* **2014,** *4*, 6705.
118. Calvo-Marzal, P.; Manesh, K. M.; Kagan, D.; Balasubramanian, S.; Cardona, M.; Flechsig, G.-U.; Posner, J.; Wang, J., Electrochemically-triggered motion of catalytic nanomotors. *Chemical Communications* **2009,** (30), 4509-4511.
119. Rumble, J. R.; Rumble, J., *CRC Handbook of Chemistry and Physics, 98th Edition*. CRC Press LLC: 2017.
120. Shankar, B.; Daniel, K.; Manian, M. K.; Percy, C. M.; Gerd-Uwe, F.; Joseph, W., Thermal Modulation of Nanomotor Movement. *Small* **2009,** *5* (13), 1569-1574.
121. Hong, Y.; Blackman, N. M. K.; Kopp, N. D.; Sen, A.; Velegol, D., Chemotaxis of Nonbiological Colloidal Rods. *Physical Review Letters* **2007,** *99* (17), 178103.
122. Sundararajan, S.; Lammert, P. E.; Zudans, A. W.; Crespi, V. H.; Sen, A., Catalytic Motors for Transport of Colloidal Cargo. *Nano Letters* **2008,** *8* (5), 1271-1276.
123. Shakuntala, S.; Samudra, S.; E., I. M.; Ayusman, S., Drop-Off of Colloidal Cargo Transported by Catalytic Pt–Au Nanomotors via Photochemical Stimuli. *Small* **2010,** *6* (14), 1479-1482.
124. Li, J.; Esteban-Fernández de Ávila, B.; Gao, W.; Zhang, L.; Wang, J., Micro/nanorobots for biomedicine: Delivery, surgery, sensing, and detoxification. *Science Robotics* **2017,** *2* (4).
125. Abdelmohsen, L. K. E. A.; Peng, F.; Tu, Y.; Wilson, D. A., Micro- and nano-motors for biomedical applications. *Journal of Materials Chemistry B* **2014,** *2* (17), 2395-2408.
126. Gao, W.; Wang, J., Synthetic micro/nanomotors in drug delivery. *Nanoscale* **2014,** *6* (18), 10486-10494.

127. Vinita, Y.; D., F. J.; Mark, G.; Ayusman, S., Bone-Crack Detection, Targeting, and Repair Using Ion Gradients. *Angewandte Chemie International Edition* **2013,** *52* (42), 10997-11001.
128. Gao, W.; Dong, R.; Thamphiwatana, S.; Li, J.; Gao, W.; Zhang, L.; Wang, J., Artificial Micromotors in the Mouse's Stomach: A Step toward in Vivo Use of Synthetic Motors. *ACS Nano* **2015,** *9* (1), 117-123.
129. Kagan, D.; Campuzano, S.; Balasubramanian, S.; Kuralay, F.; Flechsig, G.-U.; Wang, J., Functionalized Micromachines for Selective and Rapid Isolation of Nucleic Acid Targets from Complex Samples. *Nano Letters* **2011,** *11* (5), 2083-2087.
130. Bergeles, C.; Kratochvil, B. E.; Nelson, B. J., Visually Servoing Magnetic Intraocular Microdevices. *IEEE Transactions on Robotics* **2012,** *28* (4), 798-809.
131. Malay, P.; Neha, S.; Anumeha, S.; Ramray, B.; M., E. S.; K., S. D.; Ambarish, G., Maneuverability of Magnetic Nanomotors Inside Living Cells. *Advanced Materials* **2018,** *30* (22), 1800429.
132. Guix, M.; Orozco, J.; García, M.; Gao, W.; Sattayasamitsathit, S.; Merkoçi, A.; Escarpa, A.; Wang, J., Superhydrophobic Alkanethiol-Coated Microsubmarines for Effective Removal of Oil. *ACS Nano* **2012,** *6* (5), 4445-4451.
133. Do, M. T.; Muhammad, S.; Janne, J., Protection of Platinum-Based Micromotors from Thiol Toxicity by Using Manganese Oxide. *Chemistry – A European Journal* **2017,** *23* (34), 8134-8136.
134. Fangzhi, M.; Deng, P.; Chuanrui, C.; Yirong, G.; Leilei, X.; Jianguo, G., Magnetically Modulated Pot-Like MnFe2O4 Micromotors: Nanoparticle Assembly Fabrication and their Capability for Direct Oil Removal. *Advanced Functional Materials* **2015,** *25* (39), 6173-6181.
135. Kagan, D.; Calvo-Marzal, P.; Balasubramanian, S.; Sattayasamitsathit, S.; Manesh, K. M.; Flechsig, G.-U.; Wang, J., Chemical Sensing Based on Catalytic Nanomotors: Motion-Based Detection of Trace Silver. *Journal of the American Chemical Society* **2009,** *131* (34), 12082-12083.
136. Singh, V. V.; Kaufmann, K.; Esteban-Fernandez de Avila, B.; Uygun, M.; Wang, J., Nanomotors responsive to nerve-agent vapor plumes. *Chemical Communications* **2016,** *52* (16), 3360-3363.
137. M., W. O.; Muhammad, S.; Niko, K.; Janne, J., Dual Effect of Manganese Oxide Micromotors: Catalytic Degradation and Adsorptive Bubble Separation of Organic Pollutants. *Chemistry – A European Journal* **2016,** *22* (4), 1244-1247.

Chapter – 2

Fabrication and Characterization of Manganese Oxide Based Micromotor

2. Manganese oxide micromotors:

2.1. Introduction:

Driven by inspiration from the biological nanomotors[1], Ozin and Mallouk group pioneered the development of artificial catalytic micro-/nanoscale motors that can convert chemical energy into autonomous motion. Locomotion induced by the electrocatalytic decomposition of hydrogen peroxide fuel received much attention[2] and its capabilities and potential applications are reviewed recently[3]. The chemically powered, autonomous and self-propelling micro- and nano-motors are vital components in wireless miniature functional devices. The self-propulsion is mainly attributed to the conversion of chemical energy of fuel into mechanical force in the form of motion and this mechanical motion is due to either chemical gradient or bubble formation at the solid-liquid interface. However, the main obstacle for the propulsion of micro objects in liquid is the domination of viscous forces and Brownian motion, so the careful fabrication and propulsion methods are crucial. The micromotors are fabricated by numerous methods such as electrochemical deposition, physical vapour deposition, strain engineering and three dimensional direct laser writing to name the few and was excellently reviewed by Pumera's group[4]. Platinum(Pt) and Silver(Ag) are widely used for the fabrication of micromotors because of their better catalytic properties but the cost of Pt and the toxicity of Ag to the aquatic life are impeding their further developments. Enzymes are also used for the fabrication of micromotors but they are hindered by poor lifetime and cost related issues.

Manganese oxide receives much attention in recent days for micromotor fabrication because of its interesting features such as low cost, earth abundant, high catalytic and non-toxic behavior and also it can be synthesized easily in a cost effective manner. Based on the oxidation state of manganese, manganese oxide available in several forms such as MnO, MnO_2, MnO_3, Mn_2O_3, Mn_2O_7 and Mn_3O_4. Because of its biocompatibility, it is not hazardous to environment. Owing to these attributes, manganese oxide is highly preferred over Pt and Ag for the fabrication of MNMs. By using commercial manganese dioxide (MnO_2) particles, Wang et al., fabricated the Ag-MnO_2 based micromotors, superior than Pt, that can decompose the hydrogen peroxide(H_2O_2) fuel and produce oxygen gas bubbles that propel the system. However, the commercial MnO_2 showed only 50 μm s^{-1} in 12% H_2O_2 because of the poor catalytic behaviour of this type of MnO_2[5]. Self propelling micromotor consists of MnO_2-graphene crumples composites prepared by ultrasonic spray pyrolysis method could push 3D

printed boat-like structure has also been reported. In this motor, gas produced by catalytic decomposition at first accumulated in a confined space and then released and thereby developed a thrust to push enough a boat like structure[6]. Yan group developed MnO_2 nanosheets immobilized graphene layers by hydrothermal method and fabricated the micromotor that exhibited powerful propulsion with the requirement of minimum fuel. It showed 16 μm s^{-1} at 0.15% H_2O_2 fuel and also showed a speed of 111 μm s^{-1} in 2.5% of H_2O_2. But due to the dissolution and degradation, this micromotor showed a poor life time of around 2 minutes[7]. Singh et al., developed paper microjet by coating MnO_2 nanoparticles on printed waste paper and the printed ink consists of ferromagnetic material, hence this microjet can be controlled by external magnetic field and showed propulsion by catalytic decomposition of fuel by MnO_2 but the speed and lifetime of the micromotor is poor, it showed a movement of 2 body lengths per second in 16% of fuel with a life time of 6 min[8]. Safdar *et al.,* systematically investigated the influence of shapes like tubular, rod-shaped and spherical *etc.,* and polymorphism of MnO_2 on the motion behavior[9,10]. Manganese oxide is available with different crystalline forms and its catalytic activity based on crystal structure, for instance, MnO_2 exists in four crystalline forms namely α-MnO_2, β-MnO_2, γ-MnO_2, and ε-MnO_2. Template assisted electrodeposition method were used to produce tubular and rod-like structures, but they were in amorphous in nature and showed poor catalytic activity and hence low speed. Spherical particles consists of Mn_2O_3 and birnessite-type MnO_2 exhibited greater velocities. Synthesized as well as commercially available ε-MnO_2 showed the best performance and enhanced lifetime of around 40 minutes. Wang et al., prepared a bilayer tubular micromotor in which the outer layer was made up of PEDOT and the inner layer had high surface area MnO_2 with alveolate structure that showed higher speed of 318.80 μm s^{-1} at 10% fuel solution and even moved in 0.4% H_2O_2 fuel. But all these MnO_2 based motors need some additional material to form a composite for the better movement and involve complicated fabrication procedures.

Electrochemistry and micro-/nanomotors have strong relationship and it has recently been adumbrated by Pumera's group[11]. Generally, electrochemical micromotor fabrication methods classified into template based and template-less. Also the catalytic motors are usually rigid in structure and tubular in shape[12]. Thus in literature, the reported micromotors are fabricated in a complex way and they need high amount of H_2O_2 fuel and also the surfactants to create the bubbles efficiently on the micromotor surface.

Aim of this chapter:

- To fabricate the micromotor by simple approach using electroless and electrochemical deposition methods and show the propulsion with less fuel consumption and without any surfactant.
- To characterize the micromotors with different shapes, different concentration of fuel and at various pH of the solution.

2.2. Surface-Grafted Polymer Assisted Metal Deposition (PAMD) :

In general, any material in its ultrathin form exhibit flexibility to some extent, because bending strain linearly decreases with the thickness. For example, a well-known brittle & rigid single crystalline silicon at its ultrathin forms such as nanowires, nano ribbons and nano membranes are flexible. Albeit materials are flexible in ultra thin forms, not stretchable. However stretchability can be realized by either employing the distinct configurations such as wavy structures, percolating networks, 2D serpentine interconnects, 3D coiled structures and nano meshes or by using novel nano materials such as carbon nano tubes, graphene and their composites and various nano forms. These novel nano materials show excellent mechanical characteristics such as yield strength and elastic modulus while compared to metal thin films. Because of small size, the nano materials can be easily & evenly dispersed and dissolved in normal solvents and hence it can be easily fabricated via cost effective solution processes such as electrospinning, nanocrystal inks and polymer assisted metal deposition (PAMD) etc., So it does not need high temperature, high vacuum and corrosive chemical etching. Also this solution process is compatible with printing and roll-to-roll coating techniques for cheaper and scalable manufacturing.

Metal is although rigid in bulk, can be made flexible and stretchable at sufficiently thin state and at proper shapes as mentioned earlier. Usually, conventional microfabrication process is employed to deposit metal on different substrates. But it is not suitable in the case of elastomeric substrate owing to its dimensionless instability under harsh environments such as vacuum, heat and solvents. Conversely, printing inks of metal nano particles or precursors onto soft substrates has some drawbacks. The post thermal annealing and the lower conductivity of the fabricated metal interconnects impede the extensive usage of this method. More information regarding the fabrication and importance of flexible and stretchable materials can be found in these references[13].

As alternatively, a new strategy - the surface grafted polymer assisted electroless deposition of metals (PAMD) for flexible and stretchable electronics has been explored[14]. In this, the substrate surface is modified with the polymer upon which the catalyst particles are deposited or patterned. These catalyst particles help to deposit metals by electroless deposition (ELD).

ELD is an auto catalytic redox reaction and it is suitable for plastic substrates because of no high temperature treatment, also it does not require any expensive equipment and conducting substrates. In ELD process, metal ions are first reduced into nano particles in situ with the help of reducing agents such as formaldehyde, sodium borohydride and dimethylamine borane and the as-resultant nano particles act as seeds to catalyze the formation of metal coating.

PAMD usually has three steps:

1. Substrate's surface initiation and grafting the anchoring (polymer) layer
2. Immobilization of the catalyst on the anchoring layer by chemi/physi-sorption
3. Subsequent in-situ growth of metal particles in ELD bath.

Role of anchoring layer:

1. Improve the uptake efficiency of the catalyst
2. Selectivity of the catalyst
3. Act as an adhesive layer between the metal thin films and substrate

Compared to self assembled monolayer, polymers provide large number of binding sites along the chain for attracting catalysts. Polymers can also form an interpenetrating network with deposited catalyst, so the adhesive and mechanical stability is improved while stretching / bending. Based on the types of polymers used, the PAMD can be classified into following three types:

2.2.1. Cationic polymers as anchoring layer:

In this, positively charged poly electrolytes in aqueous solution is used as the anchoring layer. The typical example is that PMETAC – poly [2-(methacryloyloxy) ethyltrimethyl ammonium chloride]. Then the metal anion is used as the catalyst ex.,$[PdCl_4]^{2-}$

, which is immobilized on quarternary ammonium group of PMETAC by ion exchange. Then the copper metal is deposited by ELD.

Hulk et al., prepared poly electrolyte brushes with copper by ELD [15]. Microcontact printing method was adopted to produce initiators on the surface of the substrates. ω-sulfanylundecylbromobutyrate was used as a thiol initiator, 2-bromo-2-methyl propionic acid 3-trichlorosilanyl propylester was used as a silane initiator for growing the polyelectrolyte brushes from Au and Si/SiO_2 substrate respectively. Surface initiated atom transfer radical polymerization (SI-ATRP) has been applied to grow thin films of polymer brushes on different substrates.

The polymerization solution is prepared as follows: 75 wt%, 46.3 g of METAC was dissolved in 46 cm^3 MeOH at 20°C and the solution is continuously stirred for 20 min, then degassing with the passage of nitrogen. To this, a solution made up of 2.411g of 2,2'-dipyridyl, 0.611 g of Cu(I)Cl and 0.083 g of Cu(II)Cl_2. Again the solution is stirred and then degassed with N_2 for 15 minutes. Then the substrates with the surface initiators were dipped in polymerization solution in Schlenk line for 2-3 hours. After polymerization, the sample was washed with methanol and water, then dried under nitrogen stream. This polymerization process produced well defined patterned brushes with 16-20 nm thick.

The METAC modified samples were then immersed for 20 minutes in 1mM $PdCl_4^{2-}$ solution (pH~1). During this step, the Cl^- ions present in the PMETAC brushes will be replaced by $PdCl_4^{2-}$ species. After immobilizing this catalyst, immersed the substrate in copper electroless plating bath for 30 to 60 seconds which was prepared by the following procedure: Two freshly prepared solutions namely A & B were taken in the ratio 1:1. Solution A contained 12 g/L NaOH + 13 g/L $CuSO_4.5H_2O$ + 29 g/L $KNaC_4H_4O_6.4H_2O$ (potassium sodium tartarate) and solution B was 9.5 mL/L HCHO. The whole procedure is schematically shown in figure 1. Similar procedure can be applied to cotton as the substrate[16]

Drawbacks:

- This method involves SI-ATRP process which needs surface initiation
- Rate of polymerization of SI-ATRP is very low
- SI-ATRP process needs N_2 or Ar atmosphere
- PMETAC brushes always need noble metal catalyst

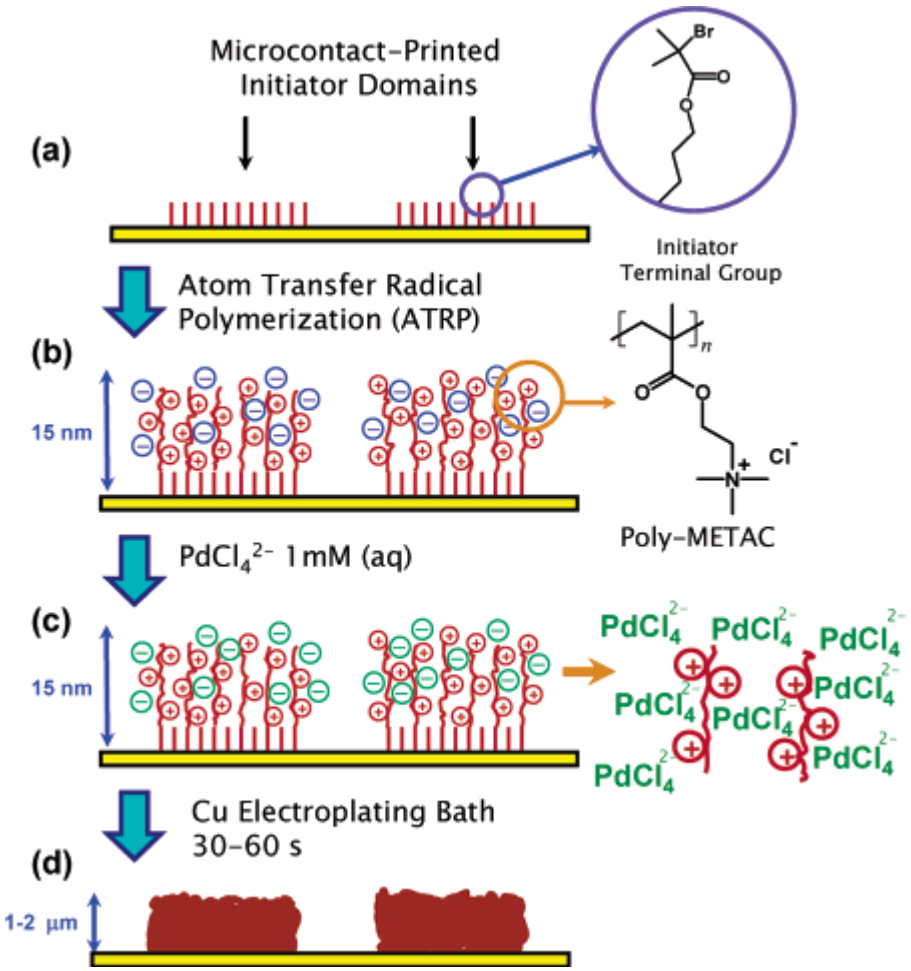


Figure 1. (a) initiator molecules are micro contact printed on the substrate, (b) SI-ATRP of the PMETAC layer, (c) immobilization of catalyst by ion exchange, (d) ELD of copper

2.2.2. Anionic polymers as anchoring layer:

Poly electrolytes with negative charges in aqueous solution are used in this method to capture positively charged catalyst for the efficient fabrication of ELD metal coating. Typical example for these anionic polymers are poly(methacryloyl ethyl phosphate) – PMEP and poly(acrylicacid) – PAA. Bimetallic patterns can be created by using cationic as well as anionic polymers on the same substrate[17]. The anionic polymer - PMEP has phosphate groups which shows higher affinity for $Pd(NH_3)_4^{2+}$ species and as seen previously the PMETAC with quarternary ammonium group has strong affinity towards $PdCl_4^{2-}$ species.

As in the previous case, initiator molecules are micro contact printed on the substrate. Then the polymerization was carried out as given below: MEP – Na 9 g was dissolved in 27 ml of water with continuous stirring and degassing with dry nitrogen for 15 minutes. 0.62 mg of bipyridyl and 0.288 g of CuBr were added to this solution. Again stirred and degassed the

solution for 15 minutes and by raising the temperature to 60°C. Initiator patterned gold substrates were sealed and degassed in Schlenck tubes, and the polymerization solution was injected to that tube to proceed the polymerization reaction for 1 hour. Later, for the cationic polymer growth, polymerization solution consists of 20 ml of 3 mol/L METAC solution (60 mmol monomer), 0.144g, 1 mmol of CuBr and 0.33g, 2 mmol of bipyridine was injected and allowed the polymerization process for 5h at room temperature.

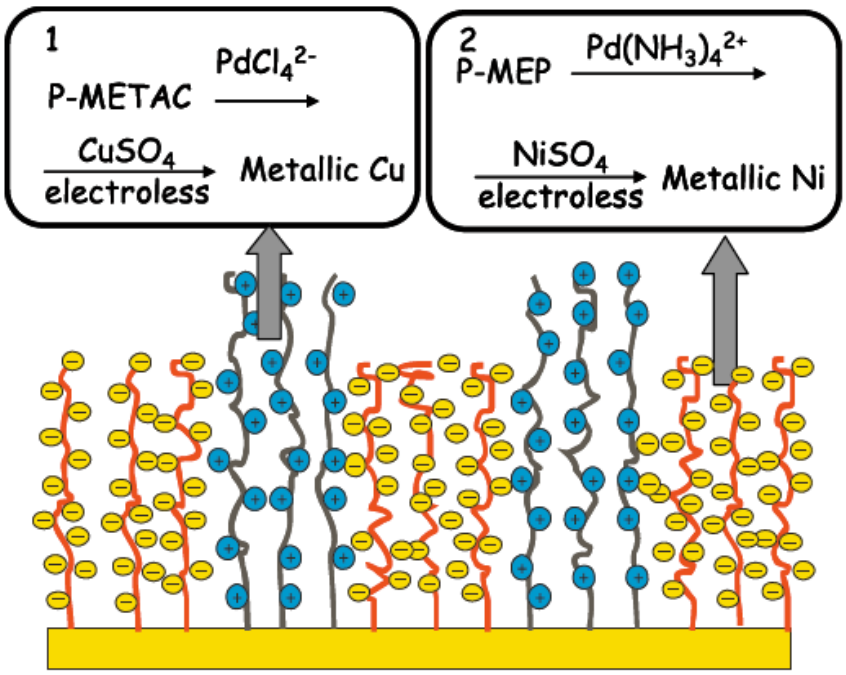


Figure 2. Schematic of anchored cationic and anionic polymer brushes for the selective pattering of Cu and Ni.

Then the copper electroplating was done with the electrolytic bath containing 1:1 mixture of freshly prepared solutions of A and B. Solution A is made up of 12 g/L NaOH, 13 g/L $CuSO_4.5H_2O$ and 29 g/L potassium sodium tartrate ($KNaC_4H_4O_6.4H_2O$). Solution B is 9.5 mL/L HCHO in water. For Ni electroless plating, 4(nickel solution):1(reductant) ratio of 40 g/L nickel sulfate hexahydrate, 20 g/L sodium citrate, 10 g/L lactic acid, and 1 g/L dimethylamine borane (DMAB) in water was used. All the ELD was carried out in room temperature. The whole process is schematically depicted in figure 2.

The SI-ATRP process has several downsides such as the requirement of surface initiation, nitrogen protection and the slow rate of polymerization. To circumvent these, Palacin and Berthelot et al., developed Ligand Induced Electroless Plating (LIEP) process[18], in this – Graftfast method[19] was adopted to graft PAA covalently onto the polymeric substrate. In Graftfast method, aryl diazonium salts are reduced to produce surface active aryl

radicals in the presence of iron powder. These radicals act as initiator for the radical polymerization of the vinylic monomer in the monomer solution. After PAA was surface grafted, it was immersed in alkaline solution containing ammonia and Cu^{2+} ions. These Cu^{2+} ions react with the carboxylate groups of the PAA and inturn anchored on the surface of the PAA, which were reduced to Cu^0 by $NaBH_4$ in-situ. The as-formed Cu^0 species act like seeds for the electroless deposition of copper. The significance of this method is that it doesn't require expensive palladium catalyst, nitrogen atmosphere and it can be applied to most of the polymeric substrates.

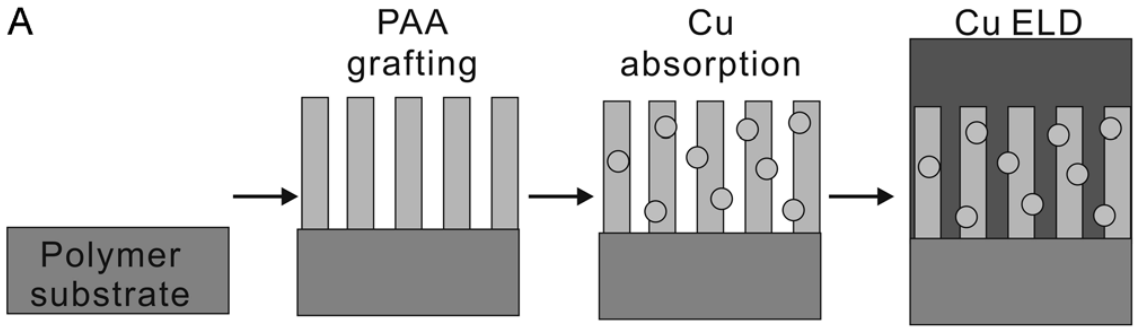


Figure 3. Schematic illustration of LIEP process, PAA was anchored on the substrate by Graftfast method

2.2.3. Non-ionic polymers as anchoring layer:

Besides ionic polymers, non-ionic polymers such as PAN-poly(acrylonitrile) & P4VP – poly(4-vinylpyridine) can also be used as anchoring layers for the metallization process. Here the catalysts are attached through the coordination interaction of lone pair of nitrogen and hence the strength and efficiency of the binding is higher. Also these type of polymers can be grafted onto most of the polymeric substrates. The procedure and principle are similar to the ionic polymers[20] and the process is schematically illustrated in figure 4.

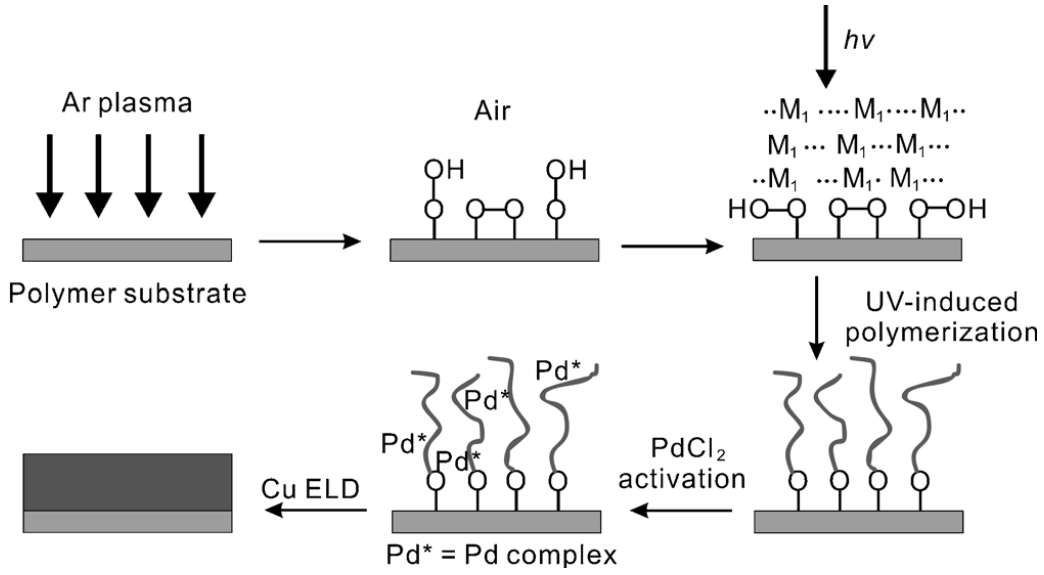


Figure 4. Use of non-ionic polymer for the metallization process involves Ar-plasma treatment, UV induced copolymerization, $PdCl_2$ activation followed by ELD deposition of copper

2.2.4. Downsides of PAMD:

1. This process is limited to certain polymers

2. It depends upon the ELD deposition which has some limitations too, especially aluminium can not be deposited by ELD and as a result by PAMD too.

3. This process involves lot of immersion steps and hence moisture-sensitive materials cannot be handled by this technique.

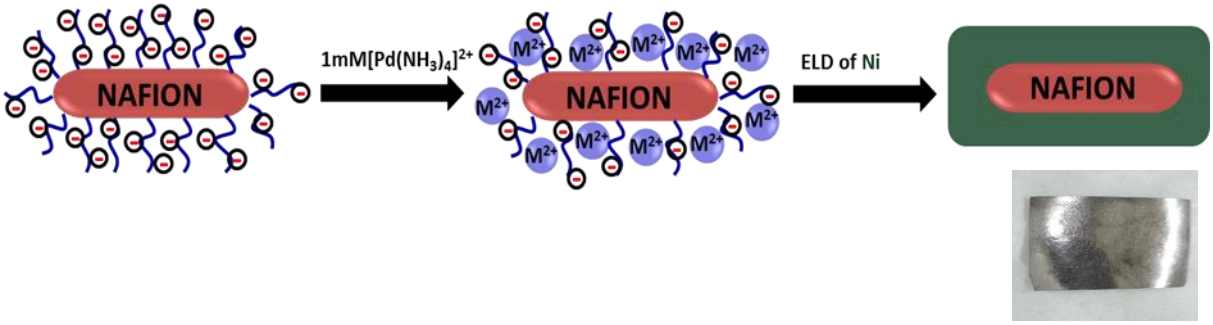
2.3. Preparation of flexible nickel substrate:

Conductive flexible nickel substrate is fabricated by employing polymer assisted electroless metal deposition(PAMD) process[21]. As mentioned above, this method has received particular attention in recent days because of its versatility, cost-effectiveness and it does not require high temperature treatment and conducting substrates. The detailed procedure of this method and its applications are outlined elsewhere[21]. In brief, at first the polymers are grown over a substrate – the charge on the polymeric architecture determines the selectivity of the catalyst and enhancing the adhesion of metal layer, then immobilize the catalyst, usually metal ions or colloidal particles, over the polymeric architecture either by physisorption or chemisorption followed by the in-situ growth of metal layer in electroless deposition bath where the autocatalytic redox reaction of metal ions takes place in which metal ions in solution are reduced to form a metal layer on the substrate. In our case, Nafion has been chosen as flexible substrate since it is an anionic polymer by nature. The Nafion substrate was immersed for an hour in 1mM $Pd(NH_3)_4^{2+}$ solution . During this step, the H^+ ions present in the Nafion will be replaced by $Pd(NH_3)_4^{2+}$ species. Since Nafion is an anionic polymer, it has a strong tendency towards the cation $Pd(NH_3)_4^{2+}$ as shown in the Scheme 1 where M^{2+} represents $Pd(NH_3)_4^{2+}$.

Electroless or autocatalytic Ni plating was invented by Brenner and Riddell in 1946[22]. Generally, in electroless deposition, there will be no electrodes but the charge transfer will occur, the bath usually contains a chemical reductant to reduce metallic ions to metal, the metal salt acts as an anode provides the metal to be deposited, the substrate acts as a cathode and the reducing agent provides electrons and the deposition happens only on the catalytic surface[23]. For Ni electroless plating, solution made up of 4(nickel solution):1(reductant) that

contains 30.4mM of nickel sulfate hexahydrate, 13.6mM of sodium citrate, 22.2mM of lactic acid, and 3.39mM of dimethylamine borane (DMAB) in water adjusted to a pH of 6.8 by ammonium hydroxide was used and metallic nickel layer was formed as per the following equation[24]:

$$3Ni^{2+} + 3\ R_2NHBH_3 + 6\ H_2O \rightarrow 3\ Ni^0 + B + 3\ R_2NH_2^+ + 2\ B(OH)_3 + 9/2\ H_2 + 3H^+ \quad (1)$$



Scheme 1. Illustration of ductile nickel electrode preparation upon anionic Nafion membrane by polymer assisted electroless metal deposition process.

2.3.1. Flexible Nickel substrate as an electrode:

The conductivity and the electrochemical quality of the electroless deposited nickel over Nafion substrate was assessed by recording cyclic voltammogram using a small strip of flexible nickel substrate as an electrode in 1M KOH aqueous solution and the resulting voltammogram is shown in figure 5. The oxidation peak at 0.35V vs SCE can be assigned to the oxidation of nickel to nickel oxide and nickel hydroxide as proposed in the equations (2-4) and it was also proved by XRD & XPS in the literature that nickel forms a layer structure during oxidation in which nickel oxide in the inner layer and nickel hydroxide or nickel oxyhydroxide in the outer layer[25].

$$2\ Ni + 2OH^- \rightleftharpoons NiO + H_2O + 2\ e^- \quad (2)$$

$$Ni + 2OH^- \rightleftharpoons Ni(OH)_2 + 2\ e^- \quad (3)$$

$$Ni(OH)_2 + OH^- \rightleftharpoons NiOOH + H_2O + e^- \quad (4)$$

The NiOOH is well known as oxygen evolution catalyst[26] at pH > 11 and it is mainly responsible for the steep increase of current after 0.55V vs SCE due to the evolution of oxygen. Lyons et al carried out series of experiments and proposed the following mechanism(equations 5-8) corresponding to the oxygen evolution of NiOOH[27] in alkaline solution.

$$[Ni(III)O_m(OH)_n]^{p-} + OH^- \rightarrow [Ni(III)O_m(OH)_{n+1}]^{p-} + e^- \quad (5)$$

$$[Ni(III)O_m(OH)_{n+1}]^{p-} \rightarrow [Ni(III)O_m(OH)_{n-1}]^{(p-1)-} - H_2O_2 + e^- \quad (6)$$

$$[Ni(III)O_m(OH)_{n-1}]^{(p-1)-} - H_2O_2 + 2\ OH^- \rightarrow [Ni(III)O_m(OH)_n]^{p-} - HO_2 + H_2O + e^- \quad (7)$$

$$[Ni(III)O_m(OH)_n]^{p-} - HO_2 + OH^- \rightarrow [Ni(III)O_m(OH)_n]^{p-} + O_2(g) + H_2O + e^- \quad (8)$$

The reduction peak at 0.3V vs SCE is due to the reduction of nickel oxide and nickel hydroxide to nickel as given in equations 2-4.

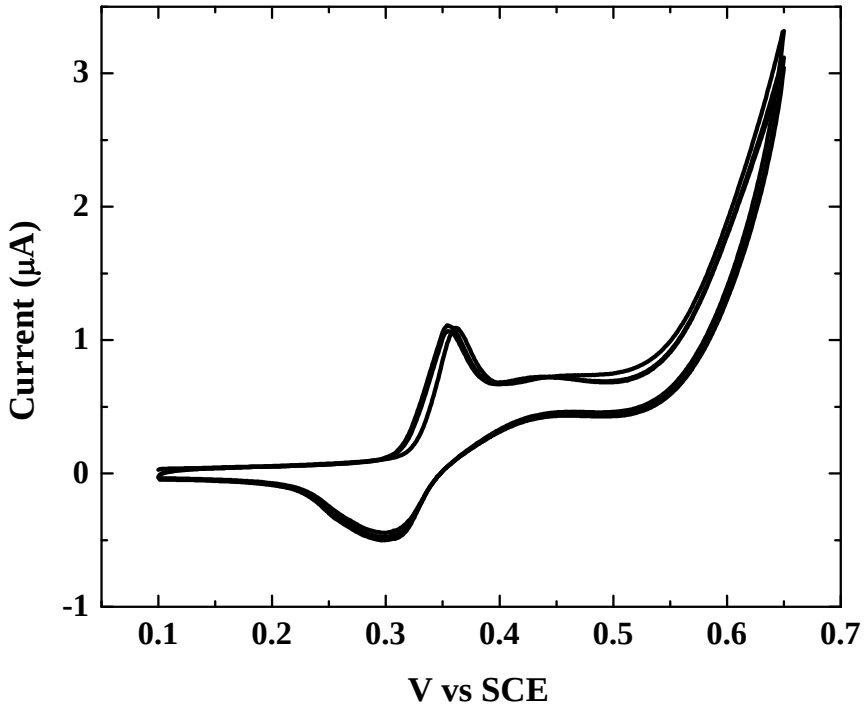


Figure 5. CV of nickel plated Nafion in 1M KOH at a scan rate of 50 mV/sec. the oxidation peak corresponds to nickel oxide and hydroxide formation and the reduction peak is due to the reduction of nickel oxide and hydroxide to nickel. The steep increase of current after 0.5V is mainly due to the oxygen evolution reaction.

2.3.2. Electrodeposition of PANI:

Poly aniline (PANI) is well known for its protection against corrosion[28]. Inorder to enhance the stability as well as to act as matrix to hold manganese dioxide (MnO_2), PANI was electrodeposited over flexible nickel substrate by cyclic voltammetry in aqueous solution containing 0.5M aniline in 0.5M H_2SO_4 at the scan rate of 0.1V/sec. Eventhough many electrochemical methods are used to polymerize aniline on inert electrodes, cyclic voltammetry with high scan rate yields homogeneous and compact PANI layers[29]. The first cycle of polymerization was performed from -0.2V to +0.85V vs SCE inorder to initiate the

polymerization by oxidizing the monomer, and the electrochemical oxidation of aniline monomer involves a two electron transfer process as given in equation (9) while the remaining 19 cycles were done at the potential range of -0.2V to +0.75V vs SCE.

$$xC_6H_5 - NH_2 \rightarrow (C_6H_4 - NH)_x + 2xH^+ + 2xe^- \quad (9)$$

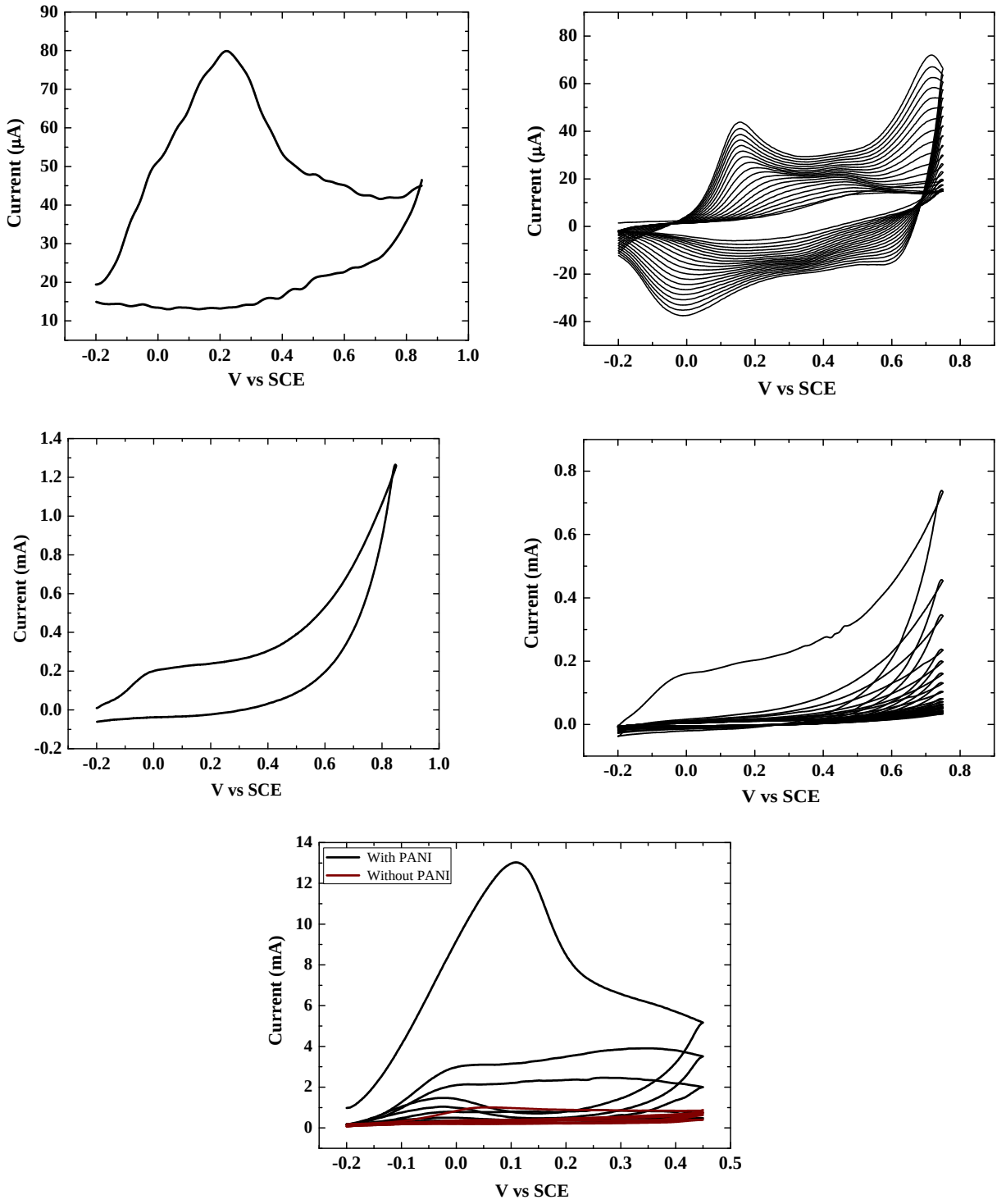


Figure 6. Electrochemical polymerization of aniline on nickel electrode (Top), on flexible nickel electrode (Middle) and Stabilization/characterization of PANI coated flexible nickel electrode in 0.5M H_2SO_4 aqueous solution (Bottom).

For the comparison purpose, the electrochemical polymerization of PANI was done on nickel electrode (looking similar to glassy carbon electrode) and on flexible nickel electrode. During the first potential cycling on nickel electrode, there is an anodic peak at 0.15V because of the oxidation of nickel surface, the similar peak is reported in the literature[30] the monomer oxidation took place at 0.8V vs SCE yielding in nucleation of PANI and because of the catalytic effect of PANI, the subsequent cycles took place at lower potentials resulting in polymer growth[31]. The anodic peak at 0.2V is ascribed to the conversion of PANI from the reduced leucoemaraldine (LE) to the partly oxidized emaraldine (EM) state and the anodic peak at 0.7V is attributable to the conversion of PANI from LE to pernigraniline (PE) state[29-30]. The increase of voltammogram peak current with increase of cycle number clearly indicates the polymer growth. Whereas, in the case of flexible nickel electrode, there is no characteristic feature on the voltammogram, however, after polymerization the greenish colour observed in both the electrodes. Then the coating of PANI was stabilized and confirmed by doing cycling voltammetry in 0.5M H_2SO_4 in the range of -0.2V to +0.45V.

2.3.3. Electrodeposition of MnO_2 :

MnO_2 was electrodeposited upon PANI coated flexible nickel electrode by employing cyclic voltammetry in 0.3M aqueous solution of $MnSO_4$ solution with pH adjusted to 1.8 by H_2SO_4 and the cyclic voltammogram is given in Fig.7.,

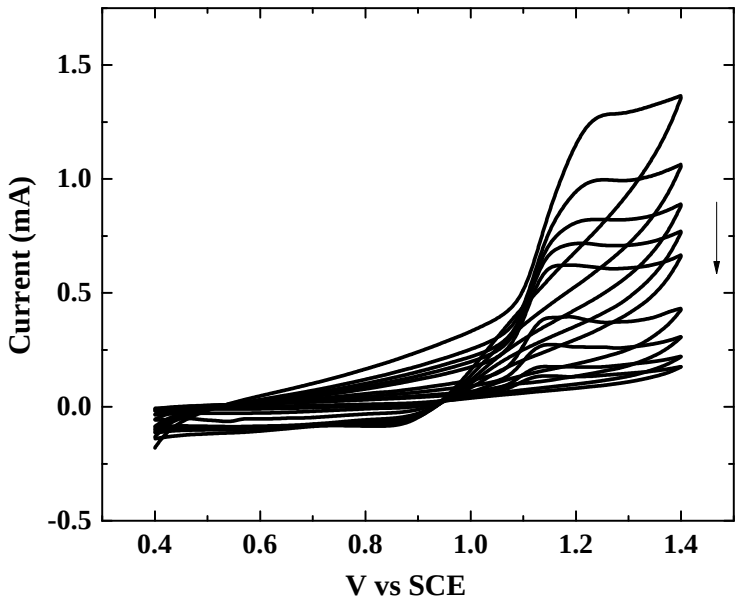


Figure 7. Cyclic voltammogram of PANI coated nickel flexible electrode in 0.3M $MnSO_4$ solution at pH-1.8. The conductivity of the electrode is decreasing with increase of cycle numbers due to the electrodeposition of poorly conductive MnO_2.

As observed in the first anodic potential sweep in CV, there is an anodic oxidation peak at 1.2V vs SCE with a steep increase and the global reaction of this oxidation reaction can be written as follows:

$$Mn^{2+} + 2H_2O \rightleftharpoons MnO_2 + 4H^+ + 2e^- \quad (10)$$

But this reaction takes place in three steps with ECE mechanism[32,33]. During this process, first Mn^{2+} is oxidized to Mn^{3+} that forms MnOOH which is unstable at pH=1.8 and thus disproportionates into MnO_2, the whole ECE reaction mechanism is given below[34]:

$$Mn^{2+} \rightleftharpoons Mn^{3+} + e^- \quad (11)$$

$$Mn^{3+} + 2H_2O \rightleftharpoons MnOOH + 3H^+ \quad (12)$$

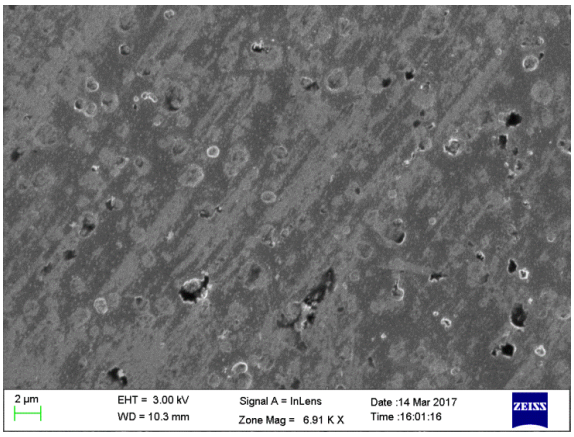
$$MnOOH \rightleftharpoons MnO_2 + H^+ + e^- \quad (13)$$

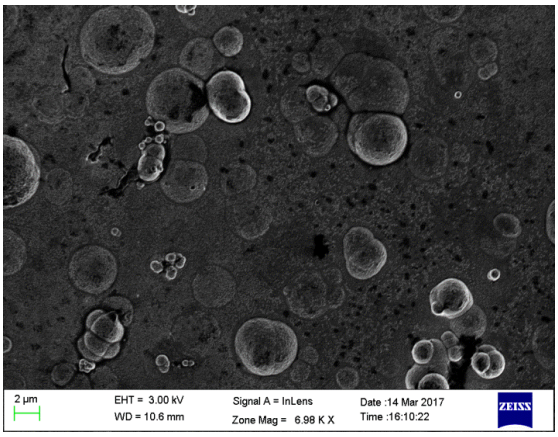
Upon cycling the current decreases with increase of cycle numbers which confirms the successful electrodeposition of MnO_2 because MnO_2 is poorly conductive and hence the electrode is becoming less and less conductive with increase of the amount of MnO_2 on the flexible electrode.

2.3.4. Surface characterization:

The surface of the MnO_2 deposited and bare flexible nickel substrate were characterized by using scanning electron microscopy (SEM) and contact angle measurements. The bare nickel flexible substrate had rather rough morphology whereas MnO_2 microparticles were deposited over the smooth PANI layer with round shape but various sizes. From the contact angle measurement it is evident that MnO_2 micromotor shows low wettability with a contact angle of 108.42° .Wetting is less addressed parameter that influence the motion behavior of micromotors. As reported by Safdar et al., the speed of the micromotor made up of MnO_2@$MnCO_3$ increases gradually and they ascribed this behavior to the slow wetting of the MnO_2 surface[9]. In our case, the flexible nickel electrode shows a contact angle of 71.98° and that of PANI/MnO_2 electrodeposited micromotor is 108.42°. The micromotor is less hydrophilic than the bare flexible nickel electrode.

Figure 8. (Top Left) SEM image of bare flexible nickel electrode and (Top Right) SEM image of MnO_2 micromotor. Contact angle of bare flexible nickel electrode is 71.98° (Bottom Left) and that of MnO_2 micromotor is 108.42° (Bottom Right)





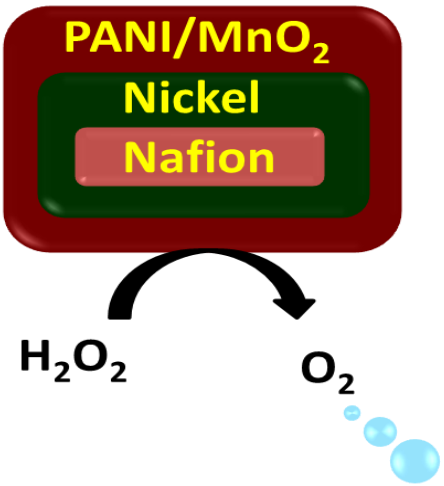




2.4. Self-propulsion mechanism:

The MnO_2 covered nickel flexible electrode decomposes H_2O_2 solution in pH-5.5 citrate buffer solution into oxygen that evolves as bubbles on the surface of the electrode and act as propellant to induce movement of the micromotor. The driving force behind the movement is the gradient of pressure that forms during the reaction between MnO_2 and H_2O_2. Bubble propulsion usually takes place in three steps: firstly nucleation of the bubbles, then growth of the bubbles followed by the detachment from the catalytic surface and enhancing the interfacial pressure[35]. This gradient of pressure induces the convection which is mainly responsible for the self-propulsion.

The reaction between MnO_2 and H_2O_2 can be explained through two mechanisms as given in equations 12 and 13. This reaction is very fast and spontaneous, during this reaction, H_2O_2 was first adsorbed on the active sites of the MnO_2 surface, then the MnO_2 is reduced by H_2O_2 to Mn_2O_3 and then $Mn(OH)_2$ with the evolution of oxygen bubbles as mentioned below.





Scheme 2. Schematic & image of bubble propelled PANI & MnO_2 coated nickel flexible electrode in H_2O_2 containing pH-5.5 citrate buffer solution.

Because of the evolution of oxygen bubbles, there is a huge increase of local pressure at the interface that develops the pressure gradient which results in convection induced movement. Through this reaction, the energy stored in chemical bonds is converted into mechanical energy. It showed a movement of about 1 cm/min.

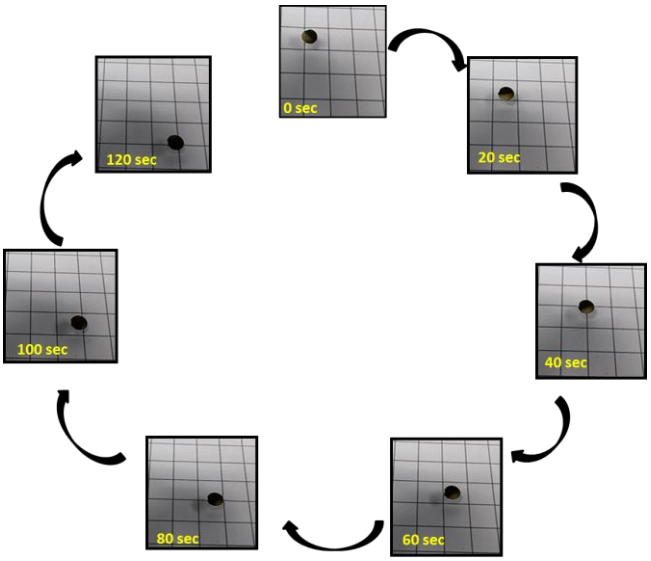
$$2MnO_2 + H_2O_2 \rightarrow Mn_2O_3 + O_2 \uparrow + H_2O \quad (12)$$

$$MnO_2 + H_2O_2 \rightarrow Mn(OH)_2 + O_2 \uparrow \quad (13)$$

Then Mn_2O_3 and $Mn(OH)_2$ will be oxidized back to regenerate MnO_2 by H_2O_2 as per the following equations[36]:

$$Mn_2O_3 + H_2O_2 \rightarrow 2MnO_2 + H_2O \quad (14)$$

$$Mn(OH)_2 + H_2O_2 \rightarrow MnO_2 + 2H_2O \quad (15)$$



Scheme 3. Images at different time frames showing the displacement of micromotor in pH-5.5 citrate buffer containing 10 mM H_2O_2 solution

2.4.1. Influence of shape, fuel concentration and pH:

The amount of deposited MnO_2 and also the amount of H_2O_2 fuel determines the lifetime of the micromotor. The speed of the micromotor depends upon many parameters namely amount of MnO_2 and fuel, temperature, pH, crystallographic phases, size and shape of the particles and surface morphology to name a few[9]. By modulating the environmental condition such as temperature, the speed of the micromotor can be adjusted as reported by Balasubramanian and co-workers[37], because the kinetics of the catalytic decomposition of fuel will be enhanced with increase of temperature. Also the viscosity of the medium decreases with increase of temperature, this is another factor that impact the movement of microsized motors[38,39]. Janis group investigated different shapes of MnO_2 micromotors like microtubes, microrods and spherical and found out that spherical $MnO_2@MnCO_3$ showed greater speed and they proposed that electrochemically prepared microtubes and rods having different phases of MnO_2 like MnO, MnO_2, Mn_3O_4 whereas spherical $MnO_2@MnCO_3$ synthesized by oxidation of $MnCO_3$ has a pure nanostructured ε-MnO_2 phase and hence showing higher speed[9]. Although they investigated micromotors with different shapes, they used different fabrication methods and have different phases of catalytic MnO_2 which makes this comparision meaningless. In our work, we prepared the micromotors by the same fabrication method and then cut into a desired shape to make comparision easier. Then different shapes such as circle, square and rectangular of MnO_2 micromotors were investigated and the circular shape performed well and exhibited the higher speed than the other two shapes. The higher speed exhibiting by circular form compared to square and rectangular may be ascribed to the curvature of the circular shape that helps to get higher speed. At low fuel concentration of 5 and 10% H_2O_2, the rectangular and square shapes showed similar speed and at 20% fuel concentration, the square shape showed higher performance than the rectangular. But in all the concentration range, the circular shape outperformed other shapes and the exact reason for its superior performance is not known. Also the speed of the circular micromotor can be tuned with the concentration of H_2O_2 fuel. The speed of the micromotor increases with increase of concentration of fuel as shown in figure 9. It is shown by Wei Gao *et al.*, that the increase of fuel concentration increases the speed of the micromotor[40], but the amount of fuel should be limited, if it exceeds certain limit that will lead to self-destruction of micromotors[9].

The influence of pH on the micromotor movement was also investigated in phosphate buffer solution at different pHs ranging from pH-5.5 to 13 with a fuel concentration of 10 and 100%. The micromotor exhibited a greater speed in pH-5.5 solution with a value of 0.7

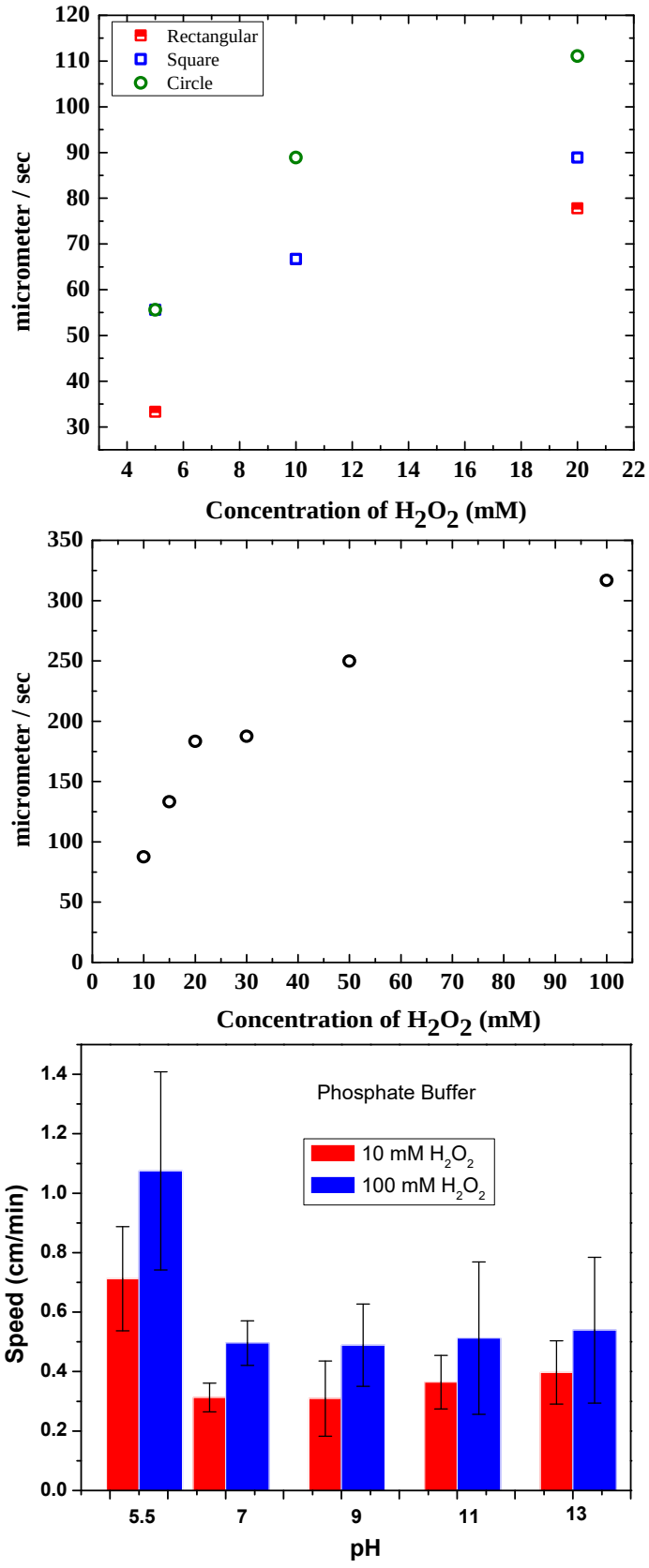


Figure 9. (Top) The speed of different shapes of micromotor, the circular shape outperforms the other shapes. **(Middle)** Enhancement of speed of circular micromotor with the concentration of H_2O_2 fuel. **(Bottom)** The circular micromotor works in a wider pH range.

cm/min in 10% fuel solution and nearly 1.1 cm/min in 100% fuel solution. Subsequently, the speed decreases with increase of pH until pH-9 and then the speed increases gradually with the further increment of pH. At pH-13, the micromotor showed a speed of 0.4 and 0.5 cm/min in 10 and 100% H_2O_2 respectively. It is worth metioning that the micromotor can work in alkaline pH because this pH range is used to produce H_2O_2 by AQ immobilized hematite photoanode and thus make it possible to integrate hematite photoanode with MnO_2 micromotor to develop photoelectrochemical micromotor. Interestingly, it is known that the rate of decomposition of hydrogen peroxide is higher in alkaline medium[41,42,43,44,45]. However, Joseph Wang group reported the first example of self propelling micromotor in alkaline (pH > 11) environment[46] followed by the report of Dey *et al*.,[47] showed the movement of polymer microsphere with catalytic palladium nanoparticles towards pH gradient. Then Pumera and coworkers systematically investigated the influence of pH on the micromotor movement and found out that the velocity of the Cu/Pt micromotor increases with increase of pH. Since the micromotor is working in a wider pH range, it is particularly beneficial to develop and design photoelectrochemical part with higher efficiency.

2.5. Controlled movement of micromotors – An overview:

Movement is an essential part of life in all the living beings but it is of no use unless otherwise directed in appropriate directions. In the case of MNMs, they have to overcome the Brownian motion during the conversion of chemical energy into controlled directional motion. To meet the demands of future applications of miniature devices, for instance delivering a drug to a particular location, it is of vital to control the speed and trajectories of catalytic motors. Hence it is required to develop a control system that would regulate the speed and movement of MNMs over specified locations and times along defined trajectories. But the biggest challenge in developing a control system is that it has to operate against the force exerted by motors. So far various external stimuli such as light, potential, ultrasound or temperature have been used for active steering and on/off switching[48] For instance, Kagan et al developed a tubular microbullet that was triggered by ultrasound and used for penetration and deformation of tissues[49]. External magnetic steering was shown for targeted retinal drug delivery and oxygen sensing[50]. Recently Pal et al has shown how the magnetically powered motors can be used for cellular internalization and intracellular manipulation in living cells[51]. Thermal modulation of the speed was also demonstrated, but this required altering the ambient temperature[52]. Besides thermal and magnetic control, other means to drive microvehicles have been developed such as light[53], acoustic[54], or chemical gradients,[55] but

they all rely again on external means. The detailed discussion about motion control is given in Section 2.3. in the bibliography chapter.

For the future applications of MNMs, it is highly desired to guide them without the use of external means. For that, there is an attractive method called chemotaxis in which the movement is a result of chemical gradient in the surrounding medium and this is a well known phenomenon in biological systems. Based on the direction of the movement, i.e., towards or against the chemical concentration gradient, chemotaxis can be divided into positive or negative respectively. For example, in the case of *Escherichia coli* bacteria, chemotaxis is main reason for its response toward food and against toxin[56]. The movement of sperms towards egg is an another well known example for chemotaxis. Although this chemotactic behaviour is commonly existing in biological organisms, the first non biological example was demoed by Sen and Velegol's group in 2007[57] by using bimetallic Pt-Au colloidal nanorods that exhibited directed movement towards higher gradient of H_2O_2 fuel concentration due to active diffusion. The controlled movement of micromotors is of particular interest in developing future miniature devices such as biomedical applications.

2.5.1. Aim of this part :

- To achieve directionality based on the chemical gradient (chemotaxis)
- To examine a new approach to control the steering and directionality of MNMs based on the porosity of polypyrrole. (microfabrication)

2.6. Control of movement by chemotaxis :

Chemotaxis is observed in some cases called chemotactic swimmers that is working based on stochastic, random walk process (reorientation and running) in which the directionality of the microrocket is not only influenced by active or propulsive part of the micromotor but also by the external stimulus (fuel) of the environment. If the fuel concentration is smaller, the motor movement is dominated by the Brownian motion and at the higher fuel concentration, the motor will move in the opposite direction to the bubble generation and this process is generally called as advanced chemokinesis or macroscopic chemotaxis.[57-58]

In another sort of chemotactic machines, chemotaxis is achieved by combining biological part with artificial motors and these biohybrid micromotors use the intrinsic chemotactic property of biological moiety. The cargo is directly attached either to the biological part or to the artificial motor part. Because of some restrictions of biological part, the application of this hybrid motors is predestined. The epitome for this kind of biohybrid motors is fabricated by

utilizing the affinity of neutrophils towards E.coli for targeted delivery of doxorubicin. The neutrophil cells are integrated with bacteria membranes coated mesoporous silica nanoparticles.[59]

Instead of chemical reaction, some motors show chemotactic behaviour because of physical process known as Marangoni effect, in which surface tension gradient of a liquid induces the mass transfer. Usually, the motors show Marangoni effect are in macro size scale (millimeter size) and they work without any external sources like magnetic or acoustic and without any external fuels such as hydrogen peroxide or glucose, they work only because of the surface tension difference in the surrounding medium. They move from lower surface tension to higher surface tension to achieve the lowest free energy state. Hence this property is highly desirable in cleansing oil pollution[60].

2.6.1. Chemotaxis – A bio-inspired approach:

In nature, to detect and respond to the surrounding chemicals, organisms generally depend upon a phenomenon called chemotaxis which commonly exists in biological systems. Chemotaxis is nothing but migration of organisms along with concentration gradient toward or away from a particular chemical which is taking place by a biased random walk process as proved in Bacteria [61]. Thus based on the direction of the movement, whether the movement is toward or away from the chemical the chemotaxis called as positive or negative chemotaxis respectively. In biological world, one can witness plenty of examples of organisms that use chemotaxis to communicate and achieve collective tasks. For example, in the case of *Escherichia coli*, chemotaxis is mainly used to identify food and escape from toxins[61a, 62]. By employing spatial and temporal sensing, bacterial respond to external stimulus. Thus bacteria can feel the concentration gradient of attractant (move toward) and toxin (move away)[61c]. It is achieved by controlling the rotation of flagellar direction, from counter clockwise to clockwise, with the help of chemotaxis protein called CheY, which governs the swimming of the bacteria either towards the attractant or away from the toxin[63].

During fertilization, the movement of sperm towards eggs is an another perfect example for chemotaxis which involves the movement of flagellar *spermatozoa* toward the attractant. Apart from chemical gradient, there will be other factors like temperature, light or magnetic field can also cause tactic behavior and those are known as thermotaxis, phototaxis or magnetotaxis respectively. Thermotaxis is mainly responsible for the movement of *spermatozoa* from a cooler place to the warmer female's oviduct[64]. Thus the term 'taxis'

means that feeling and responding to various gradients in the surroundings and then controlled movement by the gradient.

Certain non biological systems are also showing the chemotaxis behaviour[65]. Instead of applying external fields, if the micromotors move based on chemotactic behavior, then it can open up new avenues in *in-vivo* biomedical applications to accomplish directional spatial control. First non biological chemotactic system was designed by Sen *et al.*, to show that how a device can follow a concentration gradient of the fuel by using Pt-Au nanowire motors that showed slow accumulation in high fuel concentration region while kept in H_2O_2 gradient[65a]. pH taxis is also reported in which the micromotor move towards the higher pH region[66]. Magnetotactic behavior is also observed in the case of Ni containing microjets which shows alignment based on the external magnetic field, moving toward or away from the magnetic source[67].

In this thesis, we adopted a new approach for the controlled movement of motors by electrochemically reduce oxygen to generate hydrogen peroxide and the motors will sense and move towards the source of H_2O_2 generation.

Prior to the discussion, brief overview of electrochemical production of H_2O_2 by means of oxygen reduction reaction(ORR) will be described below:

It is well known that ORR is a multi-electron transfer process in which O_2 is reduced either to H_2O_2 by two electron pathway or to H_2O by four electron pathway as given in the following equations:

The four electron pathway:

In alkaline medium: $O_2 + 2H_2O + 4e^- \rightarrow 4OH^-$ $E° = 0.40$ V (16)

In acidic medium : $O_2 + 4H^+ + 4e^- \rightarrow 2H_2O$ $E° = 1.23$ V (17)

The two electron pathway:

In alkaline medium: $O_2 + H_2O + 2e^- \rightarrow HO_2^- + OH^-$ $E° = 0.06$ V (18)

This process is followed by two processes; either another two electron reduction process(4) or chemical decomposition process(5).

$HO_2^- + H_2O + 2e^- \rightarrow 3OH^-$ $E° = 0.86$ V (19)

$$2HO_2^- \rightarrow 2OH^- + O_2 \quad (20)$$

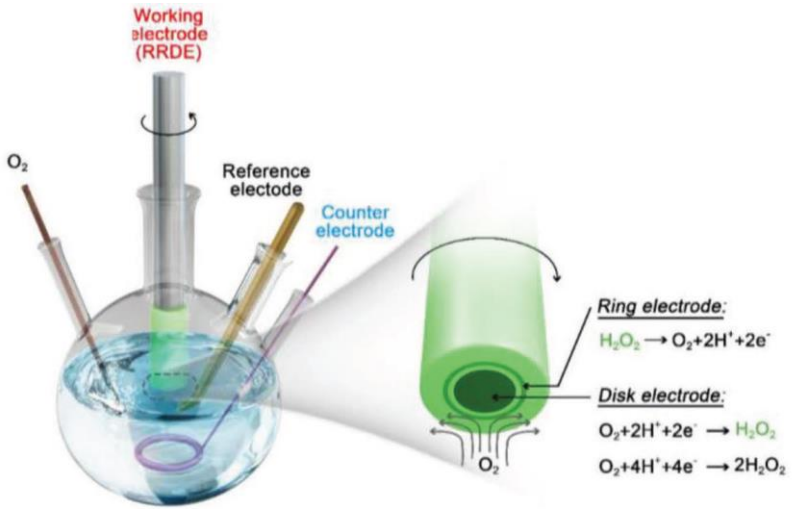
In acidic medium : $O_2 + 2H^+ + 2e^- \rightarrow H_2O_2$ $E° = 0.70$ V (21)

This reaction is also followed by two processes; either further two electron reduction reaction or chemical disproportionation as given in equations (7) and (8) respectively.

$$H_2O_2 + 2H^+ + 2e^- \rightarrow 2H_2O \quad E° = 1.76 \text{ V} \quad (22)$$

$$2H_2O_2 \rightarrow 2H_2O + O_2 \quad (23)$$

Typical three electrode cell setup with rotating ring disc electrode(RRDE) as shown in fig.10. was used to obtain H_2O_2 by electrochemical ORR in oxygen purged pH-13 phosphate buffer solution. Graphite rod and calomel electrode were used as a counter electrode and reference electrode respectively. The measured potentials are corrected with respect to reversible hydrogen electrode(RHE). Linear sweep voltammograms were obtained with various electrode rotation speeds(rpm – rotation per minute) and the voltammograms are given in fig.10.



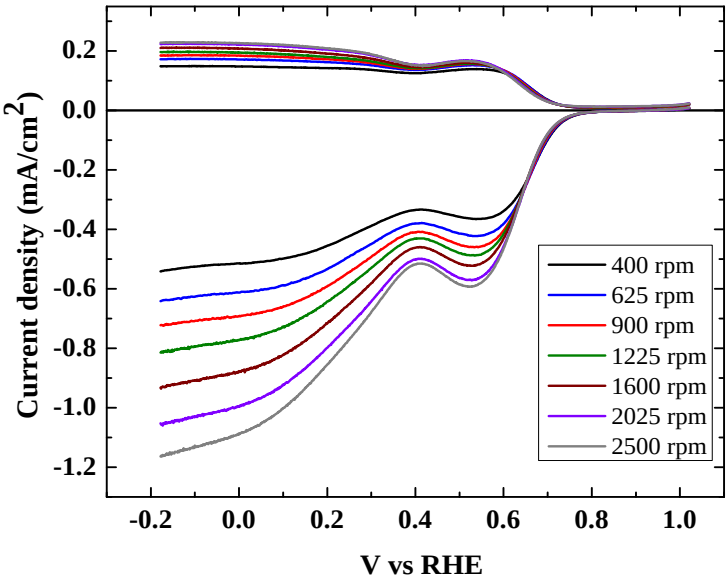


Figure 10. (top) Schematic of an electrochemical cell setup with RRDE used for obtaining H_2O_2 by means of ORR based on Ref.[68] (bottom) Linear sweep voltammograms corresponding to ORR recorded with various rotation speeds of the working electrode in O_2 purged pH-13 phosphate buffer solution.

In ORR, the number of electron transferred (n) can be calculated from the following equation:

$$N = n = 4 \times \frac{I_D}{I_D + I_R/N} \quad (24)$$

Where, I_D is the disc current; I_R is the ring current and N is the collection efficiency (N = 0.37 in our case).

Thus, based on the above equation, the calculated number of electrons are plotted against the potential inorder to obtain the corresponding potential for two electron reduction, because this is the potential corresponding to H_2O_2 production by the electrochemical oxygen reduction with the two electron pathway.

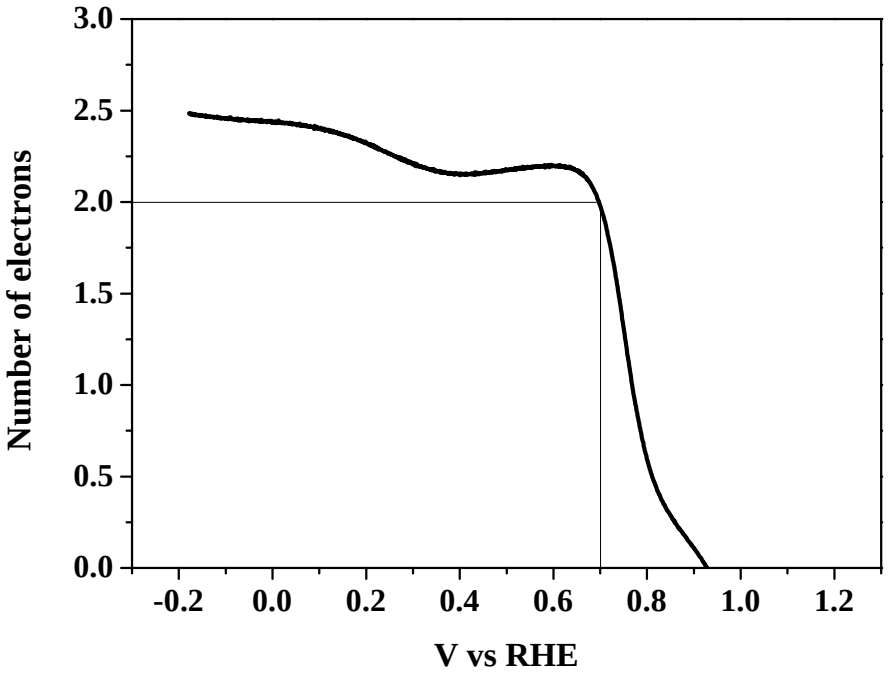


Figure 11. Plot of number of electrons with respect to the applied potential to get the information about the potential required to obtain two electron reduction process for the generation of H_2O_2.

From this fig.11. it is identified that 0.7V vs RHE is needed to proceed ORR with two electron pathway to generate H_2O_2. The H_2O_2 production efficiency at various potentials can be calculated from the following equation:

$$H_2O_2\% = 200 \text{ X } \frac{I_{R/N}}{I_D + I_{R/N}} \quad (25)$$

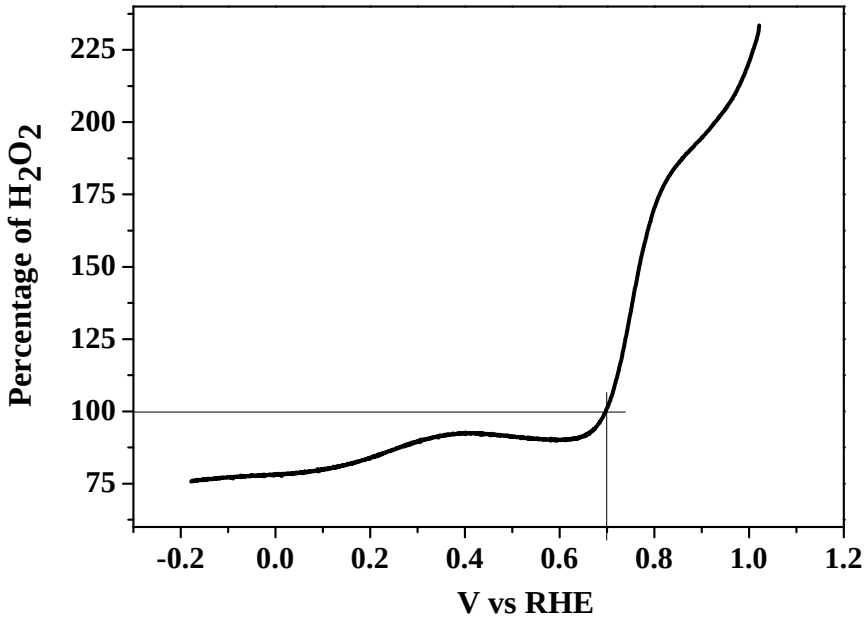


Figure 12. Production of H_2O_2 percentage with respect to the applied potentials.

The main idea here is that in a typical electrochemical cell generate H_2O_2 electrochemically in the working electrode and place the micromotor at a certain distance away from the working electrode. The micromotor gradually sense the concentration of H_2O_2 and migrate towards the working electrode surface which is similar to positive chemotaxis. After identified the required potential to generate H_2O_2 electrochemically as 0.7V vs RHE, five different potentials have been chosen in such a way that two potentials higher than 0.7V (i.e., 0.8V and 0.9V vs RHE) and two potentials lower than the 0.7V (i.e., 0.5V and 0.6V).

While applying 0.7V in oxygen purged pH-13 buffer solution, the working electrode generates H_2O_2 by following two electron ORR pathway. The micromotor gradually sense the H_2O_2 and at the beginning moves slowly towards it and eventually as the concentration gradient increases the micromotor moves very fast towards the working electrode and reaches the surface. The similar observation holds true for the case of lower potentials of 0.5V and 0.6V whereas for the higher potentials of 0.8V and 0.9V, no movement of micromotor can be seen even holding at these potentials for longer time (30 minutes). This may be due to the fact that at these potentials the corresponding number of electrons are less than two as shown in **Fig.12.** and hence these potentials are not capable of electrochemically generating H_2O_2.

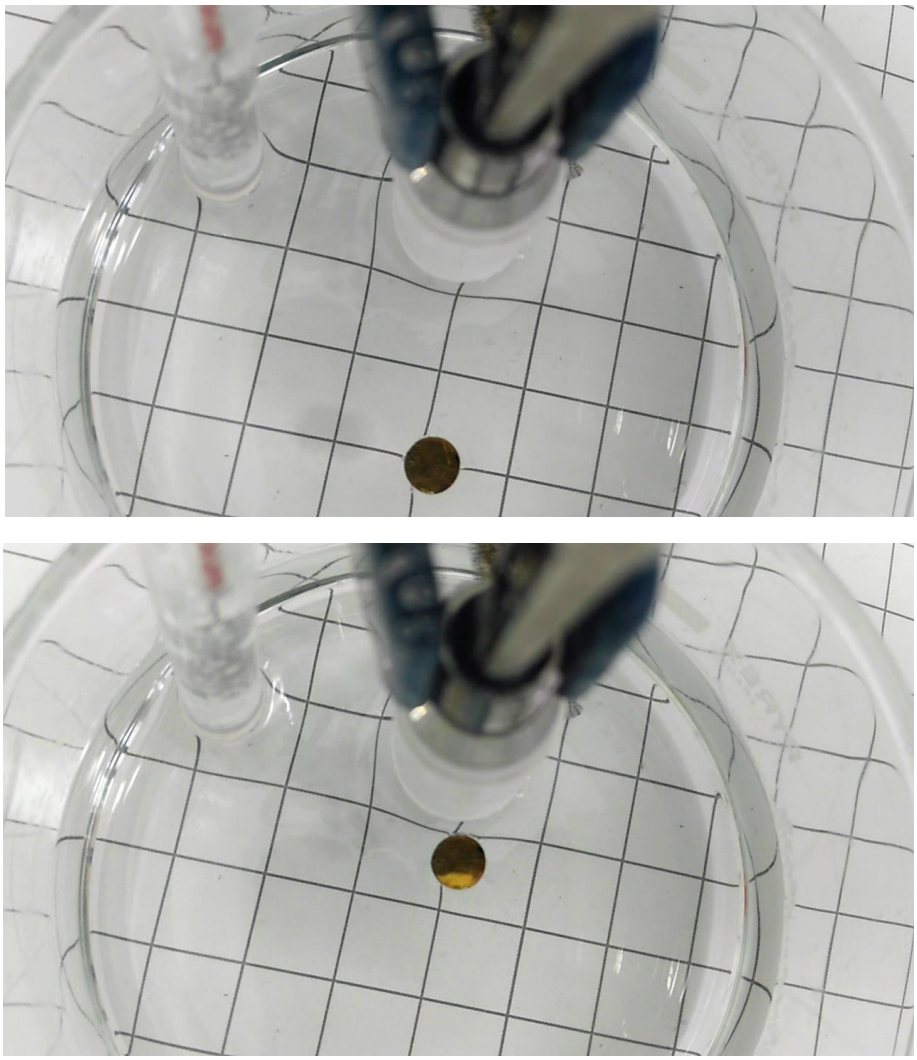


Figure 13. Electrochemically reduce O_2 to H_2O_2 in the RRDE by applying 0.7V vs RHE which is identified as the corresponding potential for two electron ORR pathway. (Top) At the beginning of the experiment, the micromotor is placed around 2 cm far away from the RRDE, (Bottom) After few minutes, the micromotor sense the concentration gradient of H_2O_2 and migrate towards the working electrode surface.

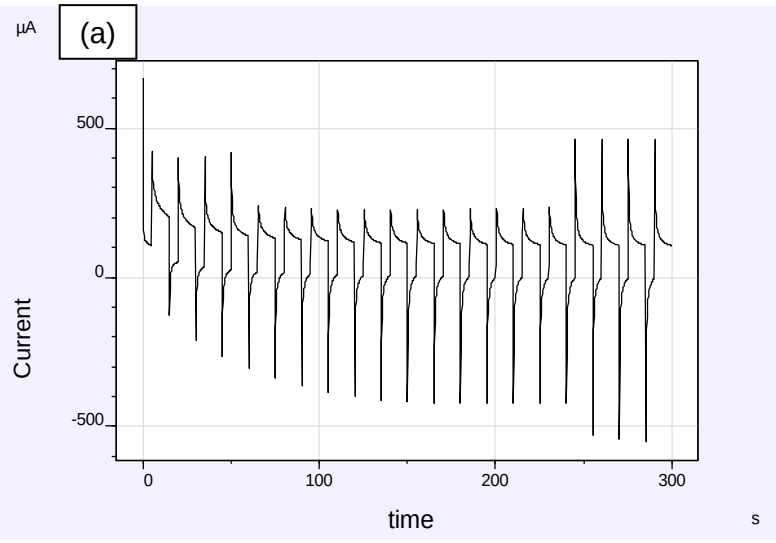
In this part, we have developed a new and simple electrochemical approach and shown the proof-of-concept for controlling the micromotor movement by exploiting the positive chemotaxis property. However, still further work is required to understand the exact mechanism behind it and also it is important to know that upto how much distance the micromotor can sense the fuel concentration gradient, in our electrochemical cell setup we have placed the micromotor between 2 and 2.5 cm far away from the working electrode and it works well in this range, but further distance range has to be investigated.

2.7. Control of micromotor movement by tuning the porosity of PPy :

As mentioned earlier, the control over steering and on/off switching are important requirements for bubble propelled micromotors. In this part, attempt has been made to achieve this control over the bubble generation by covering the catalytic MnO_2 layer with a thin layer of the conducting polymer polypyrrole (PPy). PPy is a so-called smart material that changes its material properties (e.g. conductivity, surface energy, and porosity) in response to electrical stimulation[69]. So, the electrically controlled porosity of PPy can be used to enable and stop diffusion of H_2O_2 to MnO_2 surface, thus turning on or turning off the bubble generation.

2.7. 1. MnO_2 electrodeposition:

The electrodeposition of MnO_2 was performed based on the report by Kang et al[70]. In short, the lithographed PET sheet with certain defined open areas for MnO_2 electrodeposition and the remaining area is covered by photoresist is dipped into an aqueous solution consists of 0.2M manganese acetate ($Mn(CH_3COO)_2$) and 0.2M sodium sulphate (Na_2SO_4). Three electrode setup was used for the electrodeposition of MnO_2 with a Ag/AgCl reference electrode and a stainless steel mesh as a counter electrode in Iviumstat electrochemical analyzer. Two step pulse electrodepostion method was used for the deposition by applying 0.4V for 10 seconds and 0.45V for 20 seconds and the total electrodepostion time was 5 minutes and the estimated thickness of MnO_2 film was about 700 nm determined using a Dektak profilometer.



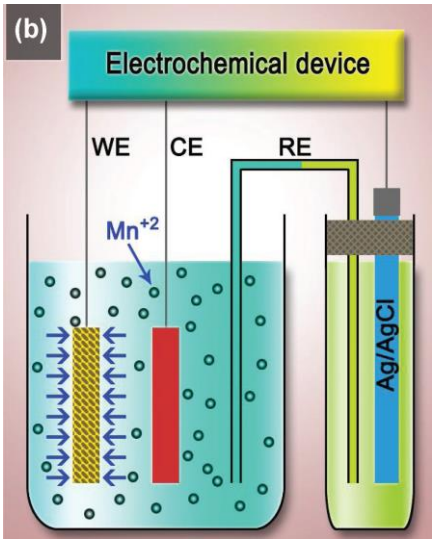


Figure 14. (a) Pulse electrodeposition of MnO_2 from aq solution of 0.2M Manganese acetate & 0.2M Sodium sulphate by applying 0.4V for 10 sec and 0.45V for 20 seconds (b) Electrochemical setup used for depositon.

2.7.2. Electrodeposition of PPy(DBS):

The PPy layer was electrodeposited over MnO_2 by chronoamperometry method as shown in **Figure 15**. The electrodeposition bath contains 0.1M pyrrole monomer in 0.1M sodium dodecylbenzenesulfonate (NaDBS) aqueous solution. The potential was held at 0.7V vs Ag/AgCl for 10 to 20 minutes for the underlayer to achieve a desired thickness and for 1 or 2 minutes for the top layer until the MnO_2 layer is completely covered and did not show any bubbles while keep it in H_2O_2 solution. In chronoamperometry, at once the potential is applied, there is a steep increase of current because of double layer capacitive charging. After that the current gradually increases that is associated with nucleation and growth. During electrodeposition, the bath is not stirred since it hinders the polymerization**.

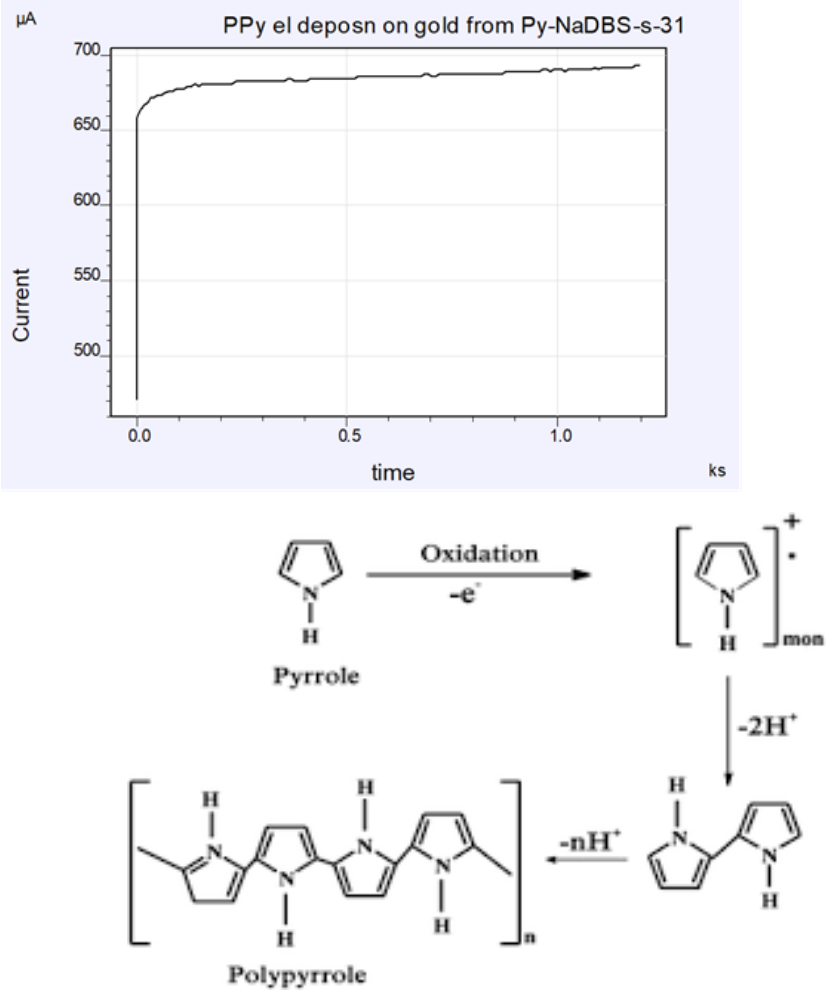


Figure 15. Chronoamperometric electrodeposition of polypyrrole upon MnO_2 from 0.1M pyrrole monomer in 0.1M NaDBS aqueous solution by holding the potential at 0.7V vs Ag/AgCl and insert shows the mechanism behind the polymer growth.

During polymerization, an electron from the pyrrole will be removed and thus creates a reactive radical cation which reacts with another radical to form a dimer and grows further like this. Since protons are generated during this polymerization process, the pH adjacent to the working electrode decreases over the time. Because of the lower oxidation potential of dimer, trimer and oligomer compared to that of monomer, the polymer chain is growing easily with the addition of units. After reaching a particular chain length, it is no more soluble and begins to precipitate on the working electrode. Once the oligomers covered the working electrode, growth on the surface is increased and also the current increases because at this stage, there are more oligomers which have lower oxidation potential than monomer.

2.7.3. Porosity tuning of PPy(DBS):

Conjugated polymers also known as conducting polymers because they conduct electricity in its doped state but unlike in semiconductors, the doping level in conducting polymers is much higher, reversible and can be controlled[71]. By changing the doping level in conducting polymers, several of its properties such as volume, colour(electrochromism) can be changed. For instance, the volume change associated with doping change used to make actuators[72]. The electrochemical doping and undoping process can be given as follows:

$$P^{+}(A^{-}) + C^{+} + e^{-} \leftrightarrow P^{0}(AC) \quad (26)$$

$$P^{+}(A^{-}) + C^{+} + e^{-} \leftrightarrow P^{0} + A^{-} + C^{+} \quad (27)$$

Where, P^{+} and P^{0} represent doped(oxidized) state and undoped(reduced, neutral) state of the polymer respectively. A^{-} and C^{+} represent the anion and cation respectively. $P^{+}(A^{-})$ means that the polymer is doped with anion A^{-}.

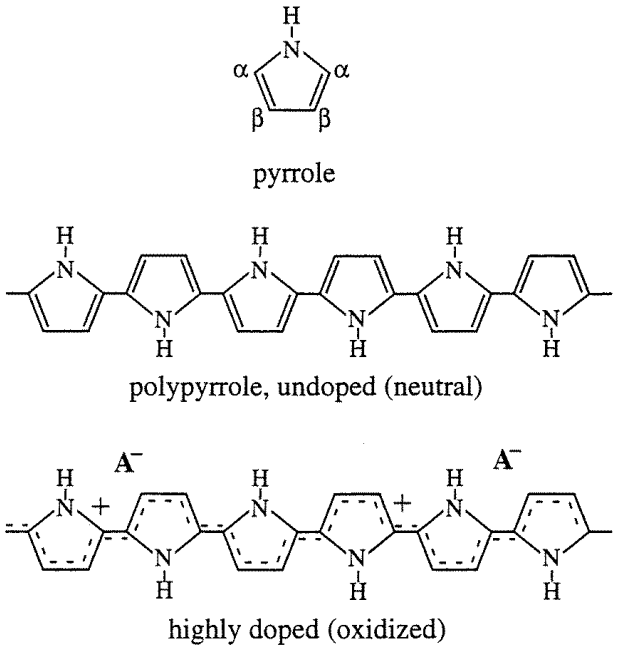


Figure 16. Chemical structures showing the pyrrole monomer and polypyrrole in undoped (neutral) and doped (oxidized) forms

Electrochemistry behind the volume change can be discussed as follows[73]: According to the equation (26), if the anion A^- is immobile, to maintain the charge neutrality the cation C^+ enters the film during undoping (reduction) leading to the volume expansion. As shown in equation (27), if the anion A^- is mobile, then it will be expelled resulting in volume contraction while reduction.

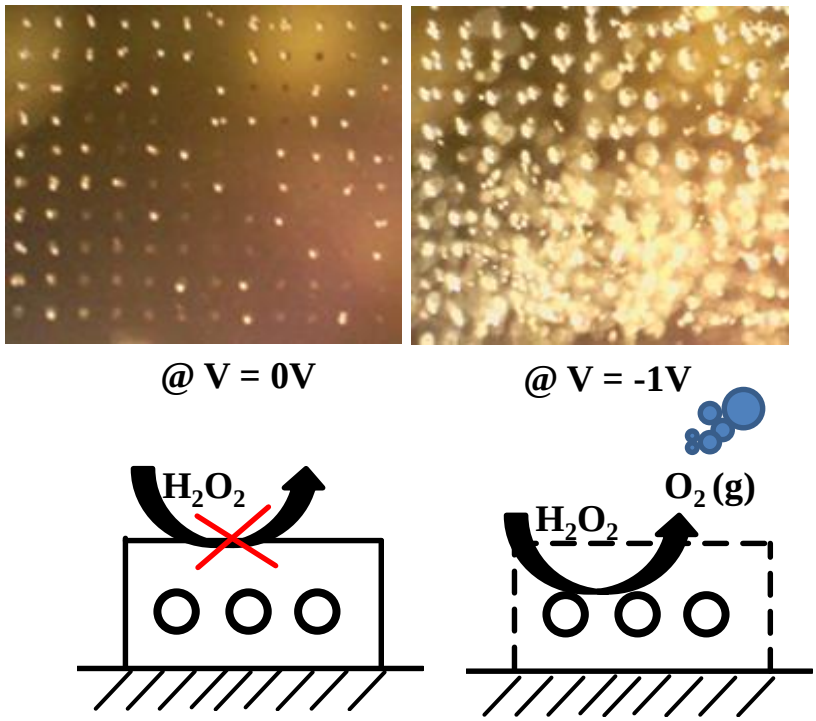


Figure 17 (Left). Schematic description showing the off/on switching of the micromotors. (Middle). Array of micropatterned MnO_2 squares (100x100 μm^2) coated with PPy in the off state. (Right) A negative potential is applied, switching the porosity of PPy and O_2 bubbles are generated due to the catalytic conversion at the underlaying MnO_2.

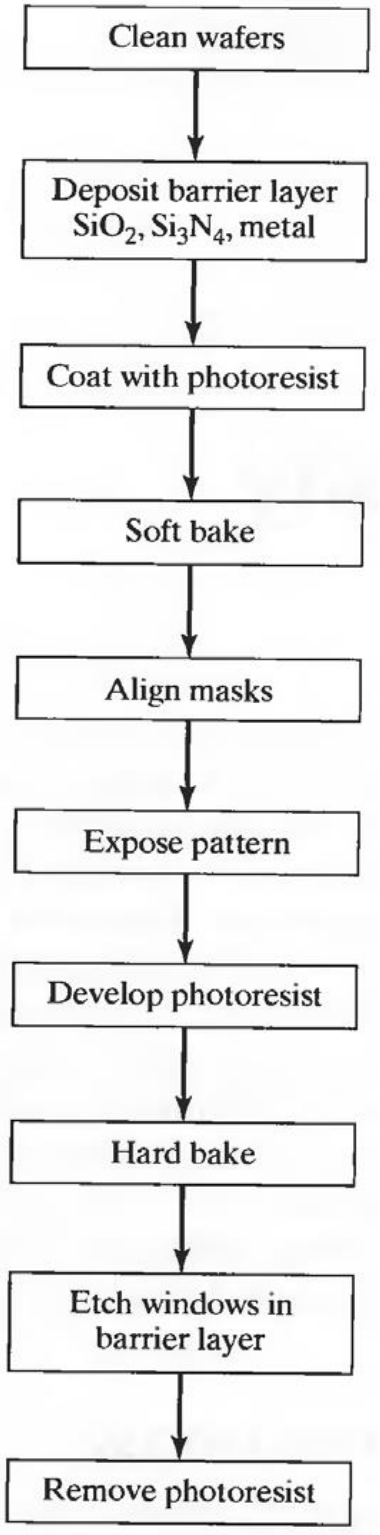
By exploiting this property of PPy, electrically tune the PPy porosity to enable and stop the diffusion of H_2O_2 on MnO_2 surface and thereby turn on or off the bubble generation. To show the proof of concept, array of micropatterned MnO_2 squares (100x100 μm^2) with the depth of 1.5 μm is prepared and then filled the squares with around 0.2 μm thickness of MnO_2 as estimated with Dektak profilometer, then the surface of MnO_2 is coated with thin layer of PPy. While doing redox cycling in 10 mM H_2O_2 in 0.1M NaDBS solution, at oxidation by applying the voltage of V = 0V vs Ag/AgCl the PPy is oxidized to PPy^+, the cations are repelled out from the polymer film and hence the volume shrinks and the film becomes compact, hence the H_2O_2 can not penetrate to the MnO_2 surface as shown in the left side of the figure 17. But at reduction by applying V = −1V vs Ag/AgCl, the PPy is reduced to its

neutral state PPy^0 and hence to counter balance the negative charge of the immobile DBS anions, Na^+ cations from the electrolyte migrate into the film and so the volume increases. During the volume expansion of the polymer film, there will be openings for H_2O_2 to access MnO_2 surface resulting out the bubble generation as depicted in the right side of the figure 8. The whole redox process can be summarized as the following reation:

$$PPy^+(DBS^-) + e^- + Na^+(aq) \leftrightarrow PPy^0(DBS^-Na^+) \quad (28)$$

2.7.4. Photolithography – A brief overview:

As the name suggests, photo-litho-graphy means photo is light; litho means stone and graphy means writing. It roughly means that writing on the stone or hard materials with the help of light. Thus photolithography consists of various steps to trasfer a pattern from a mask to the silicon wafer surface and those steps are depicted in Scheme 4 [74]. This lithography process requires ultraclean environment for fabricating the final device, because the dust particles on the substrate create defects in the final device which result in failure of the device. Thus in clean rooms vertical laminar – flow hoods are used to filtrate the dust particles from air and eradicate particulate contamination during the fabrication process. Based on the presence of maximum number of particles per cubic foot or cubic meter of air, clean rooms are classified into various types, like class 100 or class 1 etc.,



Scheme 4. Various steps involved in photolithographic process in fabricating a device[74].

2.7.4.1. Wafer and Wafer Cleaning:

n- or *p*-type silicon wafers are commonly used with thickness varying from 250 to 500 μm. Before using, wafers are cleaned by using chemical to eradicate particulate dust

and other impurities on the surface. To remove solvent and residual organic and ionic contamination, firstly wash it with acetone and ethanol then immerse the wafer in 5:1:1 solution of H_2O-NH_4OH-H_2O_2 and then heat the solution to 75-80°C for 10 minutes followed by rinsing in deionized (DI) water for 5 minutes. Then to remove surface hydrous oxide, immerse in 1:50 solution of HF-H_2O for 15 seconds followed by washing with DI water.

2.7.4.2. Barrier Layer Formation:

Next to the wafer cleaning, the materials such as SiO_2, Si_3N_4, photoresist and metal that act as a barrier layer is coated over the silicon wafer. SiO_2 is commonly used as barrier layer which is coated over the wafer by thermal oxidation, sputtering, chemical vapor deposition and vacuum evaporation process.

2.7.4.3. Photoresist Application:

After the barrier layer coating, the surface of the wafer is covered with a light sensitive material known as photoresist. To ensure a good adhesion of photoresist, the wafer surface must be dry and clean. To enhance adhesion, sometimes the wafer surface is pretreated with hexamethyldisilazane (HMDS) which acts as adhesion promoter. Mostly the photoresist is in liquid state which is poured over the wafer that is placed on a vacuum chuck and then spun at high speed for 60 to 90 seconds to get a thin photoresist layer. Viscosity of the resist and the spinning speed govern the thickness of the resist layer.

2.7.4.4. Soft Baking or Prebaking:

After covering with photoresist, the wafer is heated for few minutes at 60 to 100°C in air or nitrogen atmosphere for the purpose of enhancing adhesion and removing solvent from the photoresist and this process is called soft baking or prebaking. The soft baking treatment varies from photoresist to photoresist and that procedure must be carefully followed.

2.7.4.5. Mask Alignment:

To transfer the complex pattern from a mask to the wafer surface, mask must be cautiously aligned to the previous pattern on the wafer surface. In the alignment equipment, the wafer is placed over a vacuum chuck and then moved below the mask with the help of adjustable x-y stage and during alignment the mask is spaced 25 to 125 μm above the wafer surface. In the case of contact printing, the mask is put into contact with the wafer after

alignment. Each mask has alignment marks that are transferred to the wafer surface and these marks are useful in aligning every mask level to its previous levels

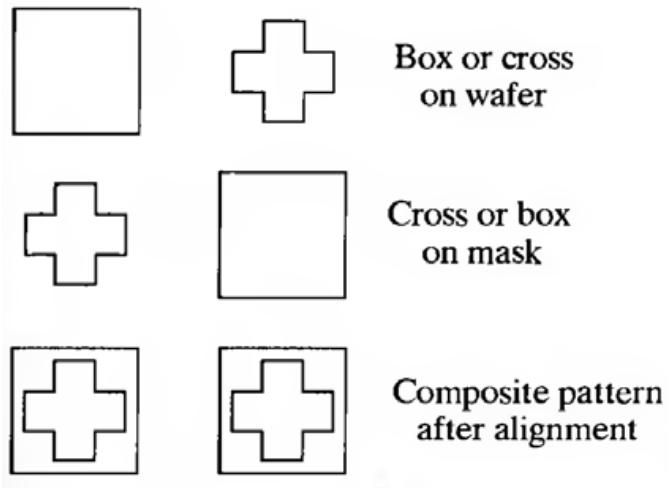


Figure 18. An example showing the alignment marks

2.7.4.6. Photoresist Development and Exposure:

After alignment, by using high intensity UV light, the photoresist is exposed through the mask. Wherever the barrier layer has to be removed, the resist is exposed. There are two kinds of photoresists; namely positive and negative photoresists. In the case of positive photoresist, the UV light exposed resist is washed away and leaving behind the barrier layers and the exact pattern of the mask will remain on the wafer surface whereas in negative photoresist, the resist remains on the surface wherever it is exposed with UV light and hence the opposite pattern of the mask will remain on the wafer surface as shown in the following figure.19.

2.7.4.7. Hard Baking:

Then to improve the adhesion of the photoresist and also to harden it, baking must be done at 120 to 180°C for 20 to 30 minutes based on the photoresist used.

2.7.4.8. Etching:

To remove barrier material which are not protected by photoresist, wet chemical or dry etching process is used. Based on the materials to be etched, the etchants are chosen. Care must be given in choosing the proper etchant that can etch away only the unprotected barrier layer quickly without destroying the photoresist layer. A buffered oxide

etch (BOE) which is made up of hydrofluoric acid is mostly used to etch windows in silicon dioxide layers.

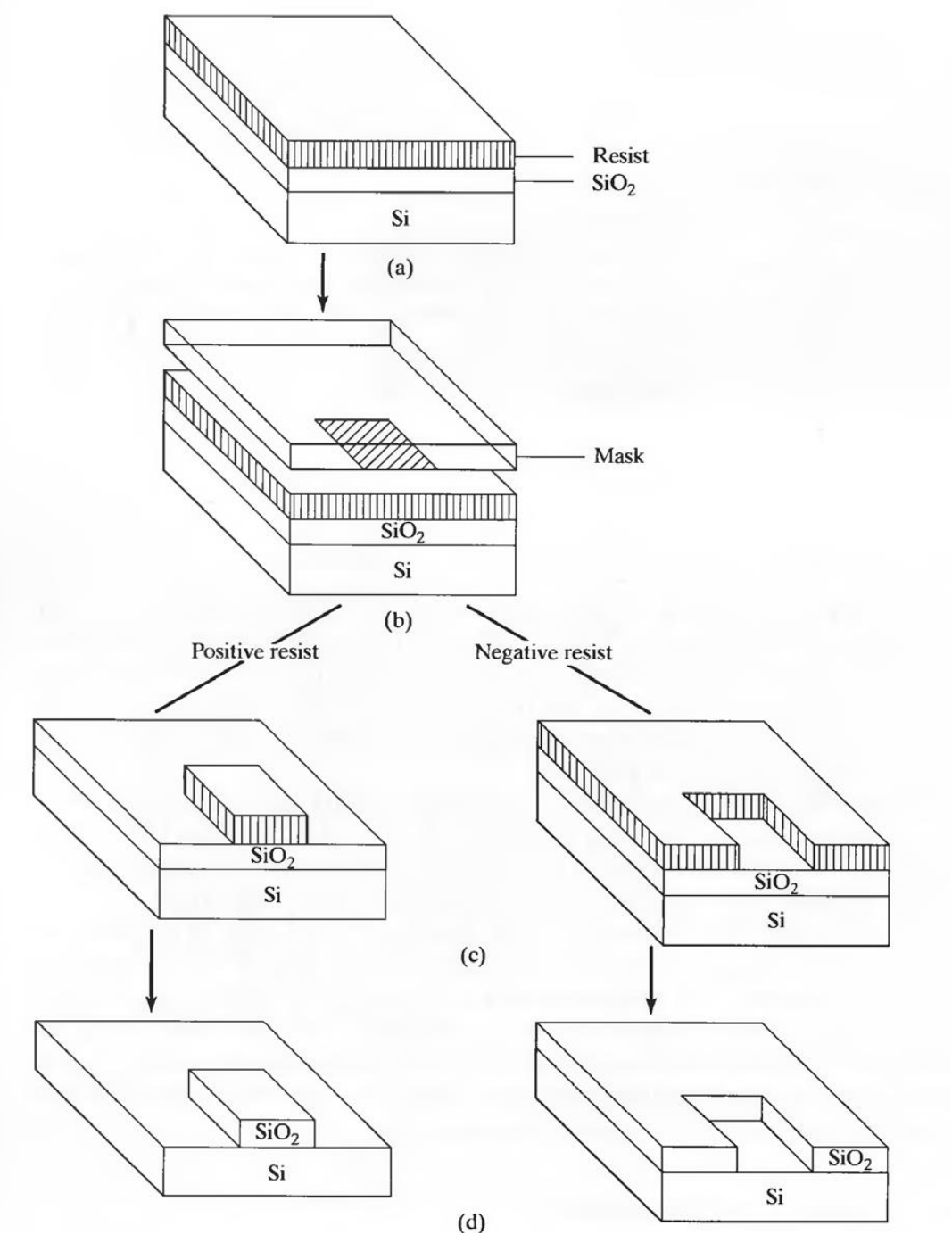


Figure 19. Schematic showing the impact of positive and negative photoresists

For instance, if the barrier layer is SiO_2, then

$$SiO_2 + 6\ HF \rightarrow H_2SiF_6 + 2\ H_2O \qquad (29)$$

H_2SiF_6 is a gaseous product that can dissolve in water and as the etching progresses, the SiO_2 is completely removed. NH_4F is commonly used as buffer, because during the course of etching, to avoid the depletion of fluorine ions and thus maintain the potency of the BOE. The etching rate depends on the thickness of the oxide film. This etching process is isotropic that means the etching is same in all the directions, but some etchants are anisotropic which means that etching is faster in one direction than others. For example, etching silicon by using a solution KOH in water results in anisotropic etching. The main drawback with isotropic etching is undercutting. The isotropic etching not only etching downwards but also on the sideways which causes undesirable effects.To avoid undercutting, dry etching is preferred in which small amount of gases ionized to get free radicals that react at the wafer surface. Mostly the dry etching is anisotropic process.

2.7.4.9. Photoresist Removal:

Finally, the photoresist is removed by using strippers which makes the resist to swell at first and then lose adhesion from the substrate.

2.7.5. Microfabrication:

Using microfabrication, we down scaled this to micrometre-sized motors on a delivery vehicle. In short, our aim of this part is as follows: Two of such micropatterned micromotors will be positioned at the rear of the microvehicle. By applying a potential to both PPy covered micromotors, both motors will be turned on or off, resulting in a movement or stopping of the vehicle. Likewise, by applying a potential to either one of the micromotors, we can control the direction of the movement (turn left or right). By adding multiple micromotors (3 or more) we could even control the speed, by turning on more motors. This should result in full control of the bubble propulsion that has not been achieved today

The microvehicles are fabricated using photolithography and microfabrication. **Figure 20** shows the process flow to fabricate the microvehicle. First the substrate, an oxidized silicon wafer or PET sheet, will be cleaned and thereafter a thin layer of chromium is thermally evaporated around a thickness of 30Å and then thin gold layer is deposited onto the surface typically to a thickness of 200 – 300Å using sputtering. Then using a spin coater, positive photoresist is homogeneously deposited, exposed using the designated photomask and developed to obtain a patterned surface. In the patterned openings, the MnO_2 and PPy are electrodeposited exactly without any overgrowth. The thickness of the resist layer governs the thickness of PPy and MnO_2, above that they will overgrow laterally. First, the lithographically

patterned substrate is submerged into an aqueous solution consisting 0.1M pyrrole monomers and 0.1M NaDBS (Na-dodecyl benzenesulfonate). A constant potential of 0.7V vs Ag/AgCl is applied for 10-20 minutes for the bottom PPy layer to achieve the desired thickness. Next, MnO_2 is deposited in an aqueous solution of 0.2M manganese acetate ($Mn(CH_3COO)_2$) and 0.2M sodium sulphate (Na_2SO_4) by a two-step pulse electrodepostion method, resulting in MnO_2 film with a thickness of about 700 nm. In the patterned surface, the electrodeposition growth rate is faster compared to the macrosize electrodes because of the higher availability of reactants and lower diffusion of oligomers away from the surface[71]. Finally, the sample is rinsed and again submerged in the aqueous pyrrole-NaDBS solution and the PPy synthesis is repeated for 1-2 minutes to cover MnO_2 layer completely with PPy. After that, the photoresist that covered the remaining areas will be removed by rinsing with acetone to develop patterned micromotors on the surface. Thereafter a new photoresist layer is deposited, patterned, and the Au layer is wet chemically etched to form the electrical connections and contact pads needed to individually control the micromotors. Care must be taken to ensure that all the resist has been removed over the PPy surface, however it is not so easy to see a thin layer of resist, otherwise ion transport in and out of PPy is not possible. Finally, the wafer or PET sheet is cut into individual vehicles and electrical wires to apply the switching potentials to the individual motors are bonded. The microvehicles are put into a 10 mM H_2O_2 in 0.1M NaDBS solution in which H_20_2 act as the fuel. The individual micromotors are controlled using an external power supply and the movement is recorded using a digital video camera.

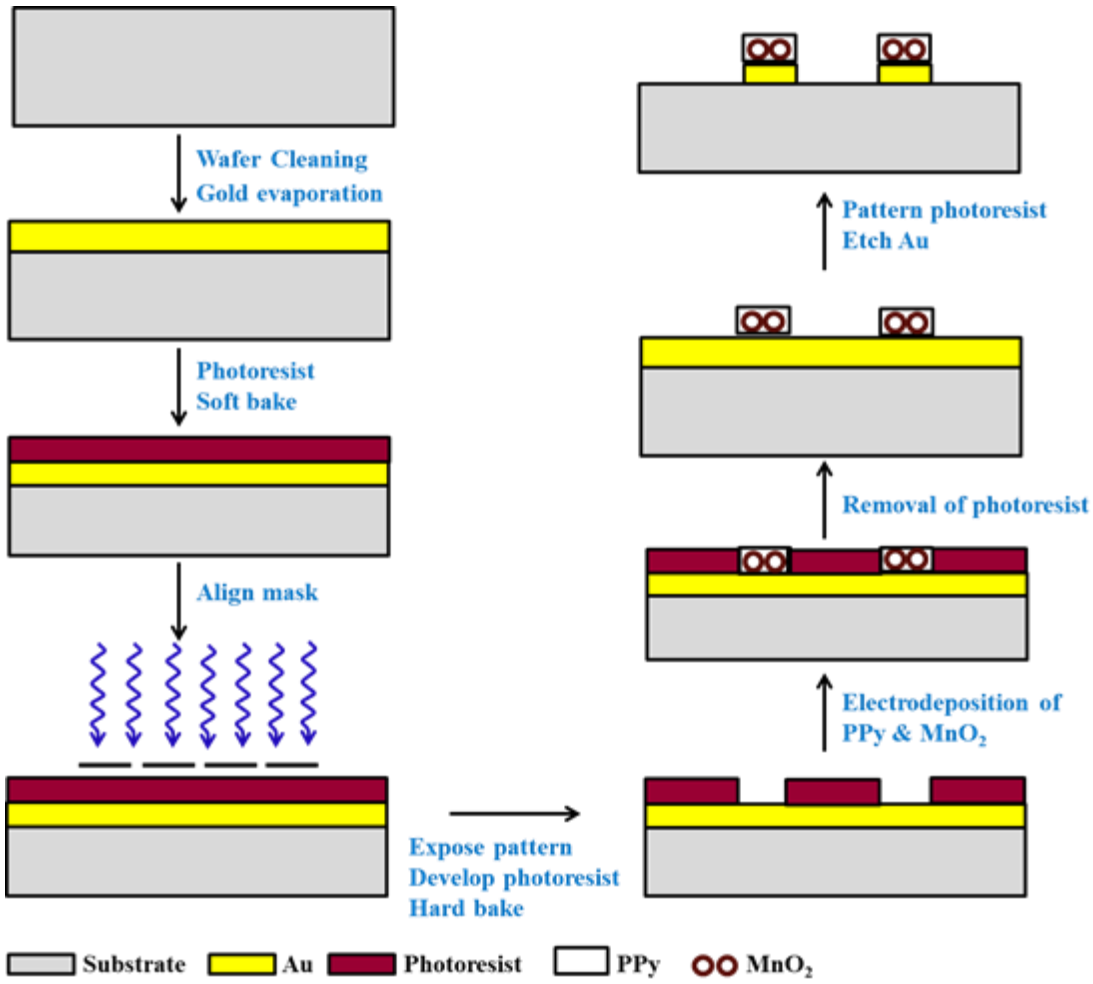


Figure 20. The process scheme of the microfabrication of the micromotors

As microfabricated microvehicles are shown in Fig.10. This shows the microvehicle consists of PPy covered MnO_2 with different sizes and numbers connected with gold contact pad and also rectangular gold counter electrode. The area of the PPy covered MnO_2 is varied from 50 x 50 μm^2, 100 x 100 μm^2, 200 x 200 μm^2 and 500 x 500 μm^2. Apart from microvehicles, micropianos are also fabricated with varying sizes of micromotors. To check the performance, the individual microvehicle is put into a 10 mM H_2O_2 in 0.1M NaDBS solution to see the turn on/off the bubble generation. The bubbles are generating in on/off manner depending upon the applied potential in not only the PPy covered MnO_2 region but also from the electrical contacts.

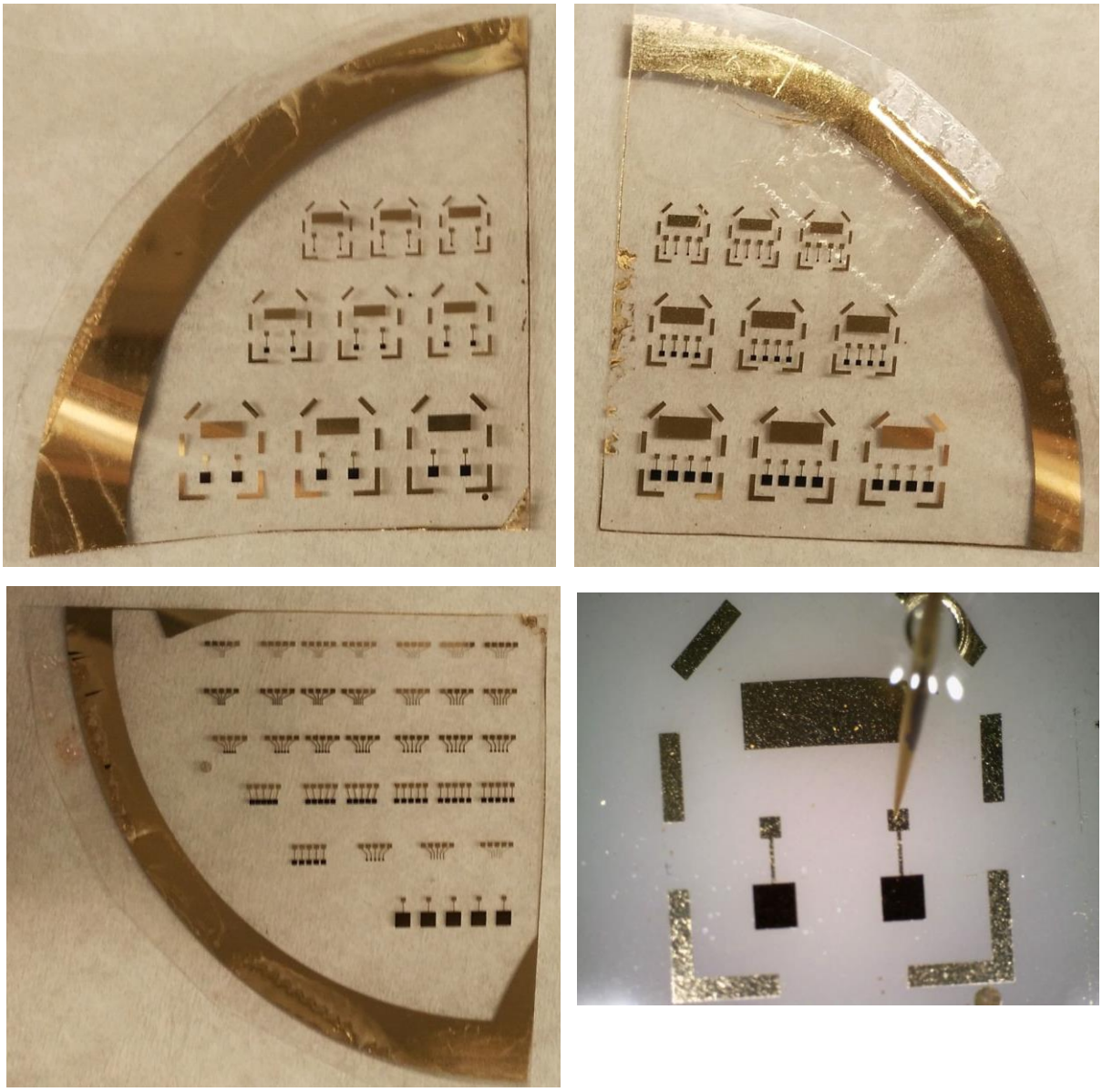


Figure 21. Microfabricated micromotors on the PET sheet with different sizes and numbers of PPy covered MnO_2 region.

2.8. Conclusion:

The facile and rapid fabrication of Micromotor based on MnO_2 have been shown. PAMD and ELD methods have been employed to prepare flexible nickel electrode followed by the electrodeposition of PANI and MnO_2. The micromotor showed bubble propelled movement in a surfactant free buffer solution. Impact of different shapes and various fuel concentration and pH range have been examined and the circular form outperformed the square and rectangular forms, speed enhances with increase of fuel concentration and the

movement in wider pH range shows the potentiality of the micromotor. The mechanism behind the oxygen bubbles formation was given.

To realize the potential applications from bubble propelled micromotors, it is vital to control its speed and direction. One very interesting application that can use the catalytic conversion of the surrounding solution into bubbles for propulsion is self-propelled drug delivery vehicles. However, this technology has two major issues which restricted its use in vivo: The "fuels" commonly used were typically not biologically relevant such as H_2O_2 and the propulsion could not be controlled, neither on/off switching nor steering. The former has recently been solved as it has been demonstrated that glucose could be used as a biologically relevant fuel for bubble-propulsion[75].

Potential use of micromotor as a carrier for drug delivery:

Because of novel properties like very fast drug transport as well as the potentiality of high tissue penetration and controlled motion, micro- and nano- motors are receiving a huge attention to be used as efficient drug delivery platforms. Generally, these motors are guided and/or propelled by exogenous or endogenous stimuli. Chemotaxis is an example for endogenous stimulus and light, magnetic field and ultrasound are the perfect examples for exogenous stimulus. To improve the drug targeting, these stimuli are used to trigger the release of a therapeutic payload once the motor arrives at a particular location.

References :

1. (a) Stocker, R.; Seymour, J. R.; Samadani, A.; Hunt, D. E.; Polz, M. F., Rapid chemotactic response enables marine bacteria to exploit ephemeral microscale nutrient patches. *Proceedings of the National Academy of Sciences* **2008,** *105* (11), 4209-4214; (b) Barbara, G. M.; Mitchell, J. G., Bacterial tracking of motile algae. *FEMS Microbiology Ecology* **2003,** *44* (1), 79-87; (c) Mitchell, J. G.; Pearson, L.; Bonazinga, A.; Dillon, S.; Khouri, H.; Paxinos, R., Long lag times and high velocities in the motility of natural assemblages of marine bacteria. *Applied and Environmental Microbiology* **1995,** *61* (3), 877-82.
2. (a) Paxton, W. F.; Kistler, K. C.; Olmeda, C. C.; Sen, A.; St. Angelo, S. K.; Cao, Y.; Mallouk, T. E.; Lammert, P. E.; Crespi, V. H., Catalytic Nanomotors: Autonomous Movement of Striped Nanorods. *Journal of the American Chemical Society* **2004,** *126* (41), 13424-13431; (b) Fournier-Bidoz, S.; Arsenault, A. C.; Manners, I.; Ozin, G. A., Synthetic self-propelled nanorotors. *Chemical Communications* **2005,** (4), 441-443; (c) Ozin, G. A.; Manners, I.; Fournier-Bidoz, S.; Arsenault, A., Dream Nanomachines. *Advanced Materials* **2005,** *17* (24), 3011-3018.

3. (a) Samuel, S.; Martin, P., Nanorobots: The Ultimate Wireless Self-Propelled Sensing and Actuating Devices. *Chemistry – An Asian Journal* **2009,** *4* (9), 1402-1410; (b) Mirkovic, T.; Zacharia, N. S.; Scholes, G. D.; Ozin, G. A., Fuel for Thought: Chemically Powered Nanomotors Out-Swim Nature's Flagellated Bacteria. *ACS Nano* **2010,** *4* (4), 1782-1789; (c) Wang, J., Can Man-Made Nanomachines Compete with Nature Biomotors? *ACS Nano* **2009,** *3* (1), 4-9; (d) Sen, T. E. M. A., Powering Nanorobots. *Scientific American* **2009,** *300*, 72 - 77.
4. Wang, H.; Pumera, M., Fabrication of Micro/Nanoscale Motors. *Chemical Reviews* **2015,** *115* (16), 8704-8735.
5. Wang, H.; Zhao, G.; Pumera, M., Beyond Platinum: Bubble-Propelled Micromotors Based on Ag and MnO2 Catalysts. *Journal of the American Chemical Society* **2014,** *136* (7), 2719-2722.
6. Chen, X.; Wu, G.; Lan, T.; Chen, W., Autonomous micromotor based on catalytically pneumatic behavior of balloon-like MnOx-graphene crumples. *Chemical Communications* **2014,** *50* (54), 7157-7159.
7. Feng, X.; Zhang, Y.; Li, Y.; Huang, Z.; Chen, S.; Ma, Y.; Zhang, L.; Wang, L.; Yan, X., Graphene-based Highly Efficient Micromotors. *Chemistry Letters* **2015,** *44* (3), 399-401.
8. Singh, A. K.; Mandal, T. K.; Bandyopadhyay, D., Magnetically guided chemical locomotion of self-propelling paperbots. *RSC Advances* **2015,** *5* (79), 64444-64449.
9. Safdar, M.; Wani, O. M.; Jänis, J., Manganese Oxide-Based Chemically Powered Micromotors. *ACS Applied Materials & Interfaces* **2015,** *7* (46), 25580-25585.
10. Safdar, M.; Minh, T. D.; Kinnunen, N.; Jänis, J., Manganese Oxide Based Catalytic Micromotors: Effect of Polymorphism on Motion. *ACS Applied Materials & Interfaces* **2016,** *8* (47), 32624-32629.
11. Sheng, M. J. G.; C., M. M. C.; Hong, W.; Bahareh, K.; Zhe, T. W.; Martin, P., Nano/Microrobots Meet Electrochemistry. *Advanced Functional Materials* **2017,** *27* (12), 1604759.
12. Veronika, M.; Georgi, S.; Leonid, I.; Samuel, S.; G., S. O., Stimuli-Responsive Microjets with Reconfigurable Shape. *Angewandte Chemie International Edition* **2014,** *53* (10), 2673-2677.
13. (a) Wagner, S.; Bauer, S., Materials for stretchable electronics. *MRS Bulletin* **2012,** *37* (3), 207-213; (b) Dae-Hyeong, K.; A., R. J., Stretchable Electronics: Materials Strategies and Devices. *Advanced Materials* **2008,** *20* (24), 4887-4892; (c) Benight, S. J.; Wang, C.; Tok, J. B. H.; Bao, Z., Stretchable and self-healing polymers and devices for electronic skin. *Progress in Polymer Science* **2013,** *38* (12), 1961-1977; (d) Perelaer, J.; Smith, P. J.; Mager, D.; Soltman, D.; Volkman, S. K.; Subramanian, V.; Korvink, J. G.; Schubert, U. S., Printed electronics: the challenges involved in printing devices, interconnects, and contacts based on inorganic materials. *Journal of Materials Chemistry* **2010,** *20* (39), 8446-8453; (e) Liu, Z.; Xu, J.; Chen, D.; Shen, G., Flexible electronics based on inorganic nanowires. *Chemical Society*

Reviews **2015,** *44* (1), 161-192; (f) Rogers, J. A.; Someya, T.; Huang, Y., Materials and Mechanics for Stretchable Electronics. *Science* **2010,** *327* (5973), 1603-1607.

14. Xuqing, L.; Xuechang, Z.; Yi, L.; Zijian, Z., Surface-Grafted Polymer-Assisted Electroless Deposition of Metals for Flexible and Stretchable Electronics. *Chemistry – An Asian Journal* **2012,** *7* (5), 862-870.
15. Azzaroni, O.; Zheng, Z.; Yang, Z.; Huck, W. T. S., Polyelectrolyte Brushes as Efficient Ultrathin Platforms for Site-Selective Copper Electroless Deposition. *Langmuir* **2006,** *22* (16), 6730-6733.
16. Liu, X.; Chang, H.; Li, Y.; Huck, W. T. S.; Zheng, Z., Polyelectrolyte-Bridged Metal/Cotton Hierarchical Structures for Highly Durable Conductive Yarns. *ACS Applied Materials & Interfaces* **2010,** *2* (2), 529-535.
17. Liu, Z.; Hu, H.; Yu, B.; Chen, M.; Zheng, Z.; Zhou, F., Binary oppositely charged polyelectrolyte brushes for highly selective electroless deposition of bimetallic patterns. *Electrochemistry Communications* **2009,** *11* (2), 492-495.
18. Garcia, A.; Polesel-Maris, J.; Viel, P.; Palacin, S.; Berthelot, T., Localized Ligand Induced Electroless Plating (LIEP) Process for the Fabrication of Copper Patterns Onto Flexible Polymer Substrates. *Advanced Functional Materials* **2011,** *21* (11), 2096-2102.
19. Mévellec, V.; Roussel, S.; Tessier, L.; Chancolon, J.; Mayne-L'Hermite, M.; Deniau, G.; Viel, P.; Palacin, S., Grafting Polymers on Surfaces: A New Powerful and Versatile Diazonium Salt-Based One-Step Process in Aqueous Media. *Chemistry of Materials* **2007,** *19* (25), 6323-6330.
20. Yang, G. H.; Kang, E. T.; Neoh, K. G., Electroless deposition of copper and nickel on poly(tetrafluoroethylene) films modified by single and double surface graft copolymerization. *Applied Surface Science* **2001,** *178* (1–4), 165-177.
21. (a) Liu, X.; Zhou, X.; Li, Y.; Zheng, Z., Surface-Grafted Polymer-Assisted Electroless Deposition of Metals for Flexible and Stretchable Electronics. *Chemistry – An Asian Journal* **2012,** *7* (5), 862-870; (b) Yu, Y.; Yan, C.; Zheng, Z., Polymer-Assisted Metal Deposition (PAMD): A Full-Solution Strategy for Flexible, Stretchable, Compressible, and Wearable Metal Conductors. *Advanced Materials* **2014,** *26* (31), 5508-5516.
22. Riddell, A. B. a. G., Nickel Plating on Steel by Chemical Reduction. *J. Res. Nat. Bur. Std.*, **1946,** *37*, 31.
23. SCHLESINGER, M., *ELECTROLESS DEPOSITION OF NICKEL* John Wiley & Sons, Inc.: 2010.
24. Lancaster, J. R.; Jehani, J.; Carroll, G. T.; Chen, Y.; Turro, N. J.; Koberstein, J. T., Toward a Universal Method To Pattern Metals on a Polymer. *Chemistry of Materials* **2008,** *20* (21), 6583-6585.

25. (a) El-Nagar, G. A.; Mohammad, A. M.; El-Deab, M. S.; El-Anadouli, B. E., Electrocatalysis by design: Enhanced electrooxidation of formic acid at platinum nanoparticles–nickel oxide nanoparticles binary catalysts. *Electrochimica Acta* **2013,** *94*, 62-71; (b) Hoppe, H.-W.; Strehblow, H.-H., XPS and UPS examinations of passive layers on Ni and FE53Ni alloys. *Corrosion Science* **1990,** *31*, 167-177.
26. Diaz-Morales, O.; Ferrus-Suspedra, D.; Koper, M. T. M., The importance of nickel oxyhydroxide deprotonation on its activity towards electrochemical water oxidation. *Chemical Science* **2016,** *7* (4), 2639-2645.
27. Lyons, M. E.; Brandon, M. P., The oxygen evolution reaction on passive oxide covered transition metal electrodes in aqueous alkaline solution. Part 1-Nickel. *Int. J. Electrochem. Sci* **2008,** *3* (12), 1386-1424.
28. Özyılmaz, A. T.; Erbil, M.; Yazıcı, B., The influence of polyaniline (PANI) top coat on corrosion behaviour of nickel plated copper. *Applied Surface Science* **2005,** *252* (5), 2092-2100.
29. Nalwa, H. S., *Handbook of Organic Conductive Molecules and Polymers: Conductive polymers : synthesis and electrical properties*. Wiley: 1997.
30. Rajendra Prasad, K.; Munichandraiah, N., Potentiodynamic deposition of polyaniline on non-platinum metals and characterization. *Synthetic Metals* **2001,** *123* (3), 459-468.
31. Stilwell, D. E.; Park, S. M., Electrochemistry of Conductive Polymers: III . Some Physical and Electrochemical Properties Observed from Electrochemically Grown Polyaniline. *Journal of The Electrochemical Society* **1988,** *135* (10), 2491-2496.
32. Paul, R. L.; Cartwright, A., The mechanism of the deposition of manganese dioxide: Part III. Rotating ring-disc studies. *Journal of Electroanalytical Chemistry and Interfacial Electrochemistry* **1986,** *201* (1), 123-131.
33. Petitpierre, J. P.; Comninellis, C.; Plattner, E., Oxydation Du MnSO4 en dioxyde de manganese dans H2SO4 30%. *Electrochimica Acta* **1990,** *35* (1), 281-287.
34. Cherchour, N.; Deslouis, C.; Messaoudi, B.; Pailleret, A., pH sensing in aqueous solutions using a MnO2 thin film electrodeposited on a glassy carbon electrode. *Electrochimica Acta* **2011,** *56* (27), 9746-9755.
35. Yingfeng, T.; Fei, P.; A., W. D., Motion Manipulation of Micro- and Nanomotors. *Advanced Materials* **2017,** *29* (39), 1701970.
36. (a) Do, S.-H.; Batchelor, B.; Lee, H.-K.; Kong, S.-H., Hydrogen peroxide decomposition on manganese oxide (pyrolusite): Kinetics, intermediates, and mechanism. *Chemosphere* **2009,** *75* (1), 8-12; (b) Xu, B.; Ye, M.-L.; Yu, Y.-X.; Zhang, W.-D., A highly sensitive hydrogen peroxide amperometric sensor based on MnO2-modified vertically aligned multiwalled carbon nanotubes. *Analytica Chimica Acta* **2010,** *674* (1), 20-26.

37. Shankar, B.; Daniel, K.; Manian, M. K.; Percy, C. M.; Gerd-Uwe, F.; Joseph, W., Thermal Modulation of Nanomotor Movement. *Small* **2009,** *5* (13), 1569-1574.
38. Soler, L.; Martinez-Cisneros, C.; Swiersy, A.; Sanchez, S.; Schmidt, O. G., Thermal activation of catalytic microjets in blood samples using microfluidic chips. *Lab on a Chip* **2013,** *13* (22), 4299-4303.
39. Sanchez, S.; Ananth, A. N.; Fomin, V. M.; Viehrig, M.; Schmidt, O. G., Superfast Motion of Catalytic Microjet Engines at Physiological Temperature. *Journal of the American Chemical Society* **2011,** *133* (38), 14860-14863.
40. Gao, W.; Sattayasamitsathit, S.; Orozco, J.; Wang, J., Highly Efficient Catalytic Microengines: Template Electrosynthesis of Polyaniline/Platinum Microtubes. *Journal of the American Chemical Society* **2011,** *133* (31), 11862-11864.
41. Staehelin, J.; Hoigne, J., Decomposition of ozone in water: rate of initiation by hydroxide ions and hydrogen peroxide. *Environmental Science & Technology* **1982,** *16* (10), 676-681.
42. Chen, J.-H.; Xu, J.-W.; Shing, C.-X., Decomposition rate of hydrogen peroxide bleaching agents under various chemical and physical conditions. *The Journal of Prosthetic Dentistry* **1993,** *69* (1), 46-48.
43. Nicoll, W. D.; Smith, A. F., Stability of Dilute Alkaline Solutions of Hydrogen Peroxide. *Industrial & Engineering Chemistry* **1955,** *47* (12), 2548-2554.
44. Meng, X.; Xianpeng, G.; Mengjiao, C.; Guannan, J.; Yajun, Z.; Feng, S., pH-Responsive On-Off Motion of a Superhydrophobic Boat: Towards the Design of a Minirobot. *Small* **2014,** *10* (5), 859-865.
45. Lingling, Y.; Mengjiao, C.; Mengmeng, S.; Dequn, Z.; Meng, X.; Feng, S., pH-Responsive Round-Way Motions of a Smart Device through Integrating Two Types of Chemical Actuators in One Smart System. *Advanced Functional Materials* **2015,** *25* (36), 5786-5793.
46. Wei, G.; Mattia, D. A.; Victor, G. G.; Jahir, O.; Joseph, W., Multi-Fuel Driven Janus Micromotors. *Small* **2013,** *9* (3), 467-471.
47. Kanti, D. K.; Satyapriya, B.; Dipankar, B.; Saurabh, B.; Arun, C., The pH Taxis of an Intelligent Catalytic Microbot. *Small* **2013,** *9* (11), 1916-1920.
48. Wang, J.; Manesh, K. M., Motion control at the nanoscale. *Small* **2010,** *6* (3), 338-45.
49. Kagan, D.; Campuzano, S.; Balasubramanian, S.; Kuralay, F.; Flechsig, G.-U.; Wang, J., Functionalized Micromachines for Selective and Rapid Isolation of Nucleic Acid Targets from Complex Samples. *Nano Letters* **2011,** *11* (5), 2083-2087.
50. Bergeles, C.; Kratochvil, B. E.; Nelson, B. J., Visually Servoing Magnetic Intraocular Microdevices. *IEEE Transactions on Robotics* **2012,** *28* (4), 798-809.
51. Pal, M.; Somalwar, N.; Singh, A.; Bhat, R.; Eswarappa, S. M.; Saini, D. K.; Ghosh, A., Maneuverability of Magnetic Nanomotors Inside Living Cells. *Advanced Materials* **2018,** *30* (22), 1800429.

52. Balasubramanian, S.; Kagan, D.; Manesh, K. M.; Calvo-Marzal, P.; Flechsig, G. U.; Wang, J., Thermal modulation of nanomotor movement. *Small* **2009,** *5* (13), 1569-74.

53. Chen, C.; Mou, F.; Xu, L.; Wang, S.; Guan, J.; Feng, Z.; Wang, Q.; Kong, L.; Li, W.; Wang, J.; Zhang, Q., Light-Steered Isotropic Semiconductor Micromotors. *Advanced Materials* **2017,** *29* (3), 1603374.

54. Wang, W.; Castro, L. A.; Hoyos, M.; Mallouk, T. E., Autonomous Motion of Metallic Microrods Propelled by Ultrasound. *ACS Nano* **2012,** *6* (7), 6122-6132.

55. Dey, K. K.; Bhandari, S.; Bandyopadhyay, D.; Basu, S.; Chattopadhyay, A., The pH taxis of an intelligent catalytic microbot. *Small* **2013,** *9* (11), 1916-20.

56. Berg, H. C., Chemotaxis in bacteria. *Annual review of biophysics and bioengineering* **1975,** *4* (00), 119-36.

57. Hong, Y.; Blackman, N. M.; Kopp, N. D.; Sen, A.; Velegol, D., Chemotaxis of nonbiological colloidal rods. *Phys Rev Lett* **2007,** *99* (17), 178103.

58. (a) Baraban, L.; Harazim, S. M.; Sanchez, S.; Schmidt, O. G., Chemotactic Behavior of Catalytic Motors in Microfluidic Channels. *Angewandte Chemie International Edition* **2013,** *52* (21), 5552-5556; (b) Pavlick, R. A.; Sengupta, S.; McFadden, T.; Zhang, H.; Sen, A., A Polymerization-Powered Motor. *Angewandte Chemie International Edition* **2011,** *50* (40), 9374-9377.

59. Shao, J.; Xuan, M.; Zhang, H.; Lin, X.; Wu, Z.; He, Q., Chemotaxis-Guided Hybrid Neutrophil Micromotors for Targeted Drug Transport. *Angewandte Chemie (International ed. in English)* **2017,** *56* (42), 12935-12939.

60. (a) Jin, C.; Krüger, C.; Maass, C. C., Chemotaxis and autochemotaxis of self-propelling droplet swimmers. *Proceedings of the National Academy of Sciences* **2017,** *114* (20), 5089-5094; (b) Zhao, G.; Pumera, M., Liquid–Liquid Interface Motion of a Capsule Motor Powered by the Interlayer Marangoni Effect. *The Journal of Physical Chemistry B* **2012,** *116* (35), 10960-10963; (c) Zhao, G.; Pumera, M., Marangoni self-propelled capsules in a maze: pollutants 'sense and act' in complex channel environments. *Lab on a Chip* **2014,** *14* (15), 2818-2823; (d) Zhao, G.; Seah, T. H.; Pumera, M., External-Energy-Independent Polymer Capsule Motors and Their Cooperative Behaviors. *Chemistry – A European Journal* **2011,** *17* (43), 12020-12026.

61. (a) Berg, H. C., Chemotaxis in Bacteria. *Annual Review of Biophysics and Bioengineering* **1975,** *4* (1), 119-136; (b) Macnab, R. M.; Koshland, D. E., Jr., The gradient-sensing mechanism in bacterial chemotaxis. *Proceedings of the National Academy of Sciences of the United States of America* **1972,** *69* (9), 2509-2512; (c) Scharf, B. E.; Fahrner, K. A.; Turner, L.; Berg, H. C., Control of direction of flagellar rotation in bacterial chemotaxis. *Proceedings of the National Academy of Sciences* **1998,** *95* (1), 201-206.

62. Berg, H. C., *Random walks in biology*. Princeton University Press: 1993.

63. Eisenbach, M., Control of bacterial chemotaxis. *Molecular Microbiology* **1996,** *20* (5), 903-910.

64. Bahat, A.; Eisenbach, M., Sperm thermotaxis. *Mol Cell Endocrinol* **2006,** *252* (1-2), 115-119.

65. (a) Hong, Y.; Blackman, N. M. K.; Kopp, N. D.; Sen, A.; Velegol, D., Chemotaxis of Nonbiological Colloidal Rods. *Physical Review Letters* **2007,** *99* (17), 178103; (b) Sen, A.; Ibele, M.; Hong, Y.; Velegol, D., Chemo and phototactic nano/microbots. *Faraday Discussions* **2009,** *143* (0), 15-27.

66. Dey, K. K.; Bhandari, S.; Bandyopadhyay, D.; Basu, S.; Chattopadhyay, A., The pH Taxis of an Intelligent Catalytic Microbot. *Small* **2013,** *9* (11), 1916-1920.

67. Zhao, G.; Pumera, M., Magnetotactic Artificial Self-Propelled Nanojets. *Langmuir* **2013,** *29* (24), 7411-7415.

68. Yang, S.; Verdaguer-Casadevall, A.; Arnarson, L.; Silvioli, L.; Čolić, V.; Frydendal, R.; Rossmeisl, J.; Chorkendorff, I.; Stephens, I. E. L., Toward the Decentralized Electrochemical Production of H2O2: A Focus on the Catalysis. *ACS Catalysis* **2018,** *8* (5), 4064-4081.

69. (a) Pei, Q.; Inganläs, O., Conjugated polymers and the bending cantilever method: Electrical muscles and smart devices. *Advanced Materials* **1992,** *4* (4), 277-278; (b) Pei, Q.; Inganaes, O., Electrochemical applications of the bending beam method. 2. Electroshrinking and slow relaxation in polypyrrole. *The Journal of Physical Chemistry* **1993,** *97* (22), 6034-6041; (c) Smela, E.; Inganäs, O.; Pei, Q.; Lundström, I., Electrochemical muscles: Micromachining fingers and corkscrews. *Advanced Materials* **1993,** *5* (9), 630-632.

70. Kang, J.; Chen, L.; Hou, Y.; Li, C.; Fujita, T.; Lang, X.; Hirata, A.; Chen, M., Electroplated Thick Manganese Oxide Films with Ultrahigh Capacitance. *Advanced Energy Materials* **2013,** *3* (7), 857-863.

71. Smela, E., Microfabrication of PPy microactuators and other conjugated polymer devices. *Journal of Micromechanics and Microengineering* **1999,** *9* (1), 1-18.

72. Baughman, R. H., Conducting polymer artificial muscles. *Synthetic Metals* **1996,** *78* (3), 339-353.

73. (a) Scrosati, B., Electrochemical properties of conducting polymers. *Progress in Solid State Chemistry* **1988,** *18* (1), 1-77; (b) Otero, T. F.; Sansiñena, J. M., Artificial muscles based on conducting polymers. *Bioelectrochemistry and Bioenergetics* **1995,** *38* (2), 411-414; (c) Bilger, R.; Heinze, J., Application of electrochemical quartz microbalance to determine the stoichiometry of ion movement during doping - undoping processes in polypyrrole. *Synthetic Metals* **1991,** *43* (1), 2893-2896.

74. Jaeger, R. C., *Introduction to Microelectronic Fabrication*. Prentice Hall: 2002.

75. (a) Ma, X.; Jannasch, A.; Albrecht, U.-R.; Hahn, K.; Miguel-López, A.; Schäffer, E.; Sánchez, S., Enzyme-Powered Hollow Mesoporous Janus Nanomotors. *Nano Letters* **2015,** *15* (10), 7043-7050; (b) Dey, K. K.; Zhao, X.; Tansi, B. M.; Méndez-Ortiz, W. J.; Córdova-Figueroa,

U. M.; Golestanian, R.; Sen, A., Micromotors Powered by Enzyme Catalysis. *Nano Letters* **2015,** *15* (12), 8311-8315.

Chapter – 3

Preparation, Surface Functionalization and Characterization of Hematite photoanode

3.1. Introduction to solar to chemical energy conversion:

3.1.1. Energy crisis:

Energy demand increases with increase of human population and development whereas the carbon based energy resources are getting depleted. The main problem to the mankind is the unequal distribution and availability of energy resources. This energy crisis not only makes an impact on economy and environment but also to geopolitical issues and international conflicts. The political unrest in Arabian countries make oil prices more volatile and energy markets highly unstable. Further, the Fukushima incident forced energy policy makers to reconsider the nuclear energy agenda. Hence many countries, especially the developing countries, started to invest more money in renewable energy as given by the latest report[1] and as shown in the Fig., 1, the difference in amount between the developing and developed countries is minimal and also there is a tremendous growth in investment in renewable energy by the developing countries, particularly four fold enhancement in investment in 2016 compared to 2006.

German Advisory Council on Global Change(WBGU) in 2003 provided the outline for the transformation of global energy system[2]. According to that report, this transformation can be made possible by following three steps such as reducing fossil fuels, increasing the usage of renewables and enhancing the energy productivity but due to the lack of sufficient infrastructures and proven technologies, fossil fuels will prevail for next few decades for the energy production. In the mean time, ample technologies have to be developed to converse energy from renewables, so they do expect to achieve 50% of energy from renewables in 2050 and 90% in 2100 as shown in Fig., 2. Also the latest United Nations Climate Change Conferences held in Paris (COP-21), Marrakech (COP-22) and in Bonn (COP-23) have made an agreement that the world should shift its energy reliance from fossil fuels to renewable based resources, particularly minimizing the green house gas emission.

Among the several renewable energy options, solar energy has the capability of fulfilling our complete energy demands. For example, solar radiation provides 174000 TW to the planet, our energy demand is just 15 TW per year. So the efficient harnessing of solar energy for an hour, would satisfy the energy demand of a year for the whole world[1]. Since solar radiation is intermittent, it is necessary to store it in the form of either energy or fuels. Albeit, the photovoltaic and solar absorbers can convert solar energy into electrical energy

and heat energy respectively, storage of those energies is not an easy task. Converting solar energy into storable fuels such as hydrogen or hydrogen peroxide is an alternative solution. For that, photoelectrochemical(PEC) water splitting plays a pivotal role.

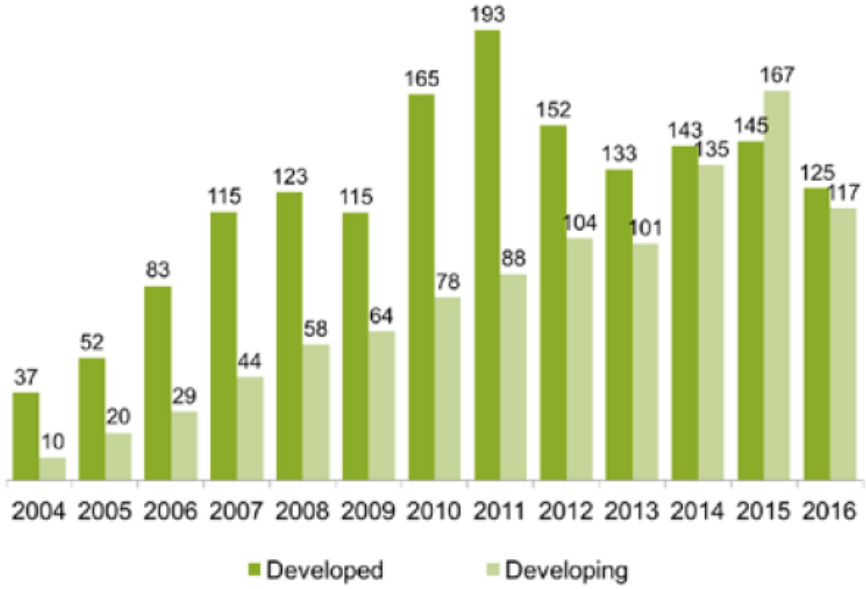


Figure 1. Global investment in renewable energy of developed vs developing countries from 2004 to 2016 (Money in billion dollars). Source: Global trends in renewable energy investment 2017.

3.1.2. Hydrogen as an Energy source:

Hydrogen is colorless, odorless and non-toxic. Although it is lightest, hydrogen has the most energy density. One pound of hydrogen has the energy of 55 MJ which is 3 times higher than that of gasoline[4]. While combustion, hydrogen yields out only water as the product, whereas the fossil fuels emit the green house gases. Moreover, hydrogen can be produced from many resources which are widely distributed among the world, anyone can utilize it. Owing to these advantageous attributes, hydrogen is believed to be the better substitute for fossil fuels.

In 1970, at General Motor(GM) Technical center, John Bockris first coined the term 'Hydrogen Economy'[4].This hydrogen economy mainly based on the following four pillars: production, transport, storage and usage. Hydrogen can be transported through the existing natural gas infrastructures however the main bottleneck to the hydrogen economy is the storage. Eventhough hydrogen has the higher energy density based on its weight because of its low molecular weight, based on volume it possesses very low energy density due to its low density of 0.09g/litre. Physical storage, chemical storage and molecular adsorption are the three main technologies available for storage. Physical storage mainly deals with compression

and liquefaction. This technique is mostly exploited by industries. The chemical storage method is storing hydogen as the chemical hydrides, while decomposing these materials yield back hydrogen. This method suffers from the requirement of high pressure and temperature to form hydrides and to release hydrogen. Another approach is to adsorb the hydrogen on the certain framework molecules such as metal-organic frameworks(MOFs). A detailed study regarding hydrogen storage by Züttel *et al.*, can be found here[5]. Hydrogen can be used as a fuel in fuel cells to produce the required energy. It leads to achieve zero emission and approximately two times higher efficient (on a fuel-to-wheel basis) than internal combustion engines (ICE). Since battery technology cannot meet the volume, weight and range required for todays automobile, hydrogen powered fuel cells would be the best option.

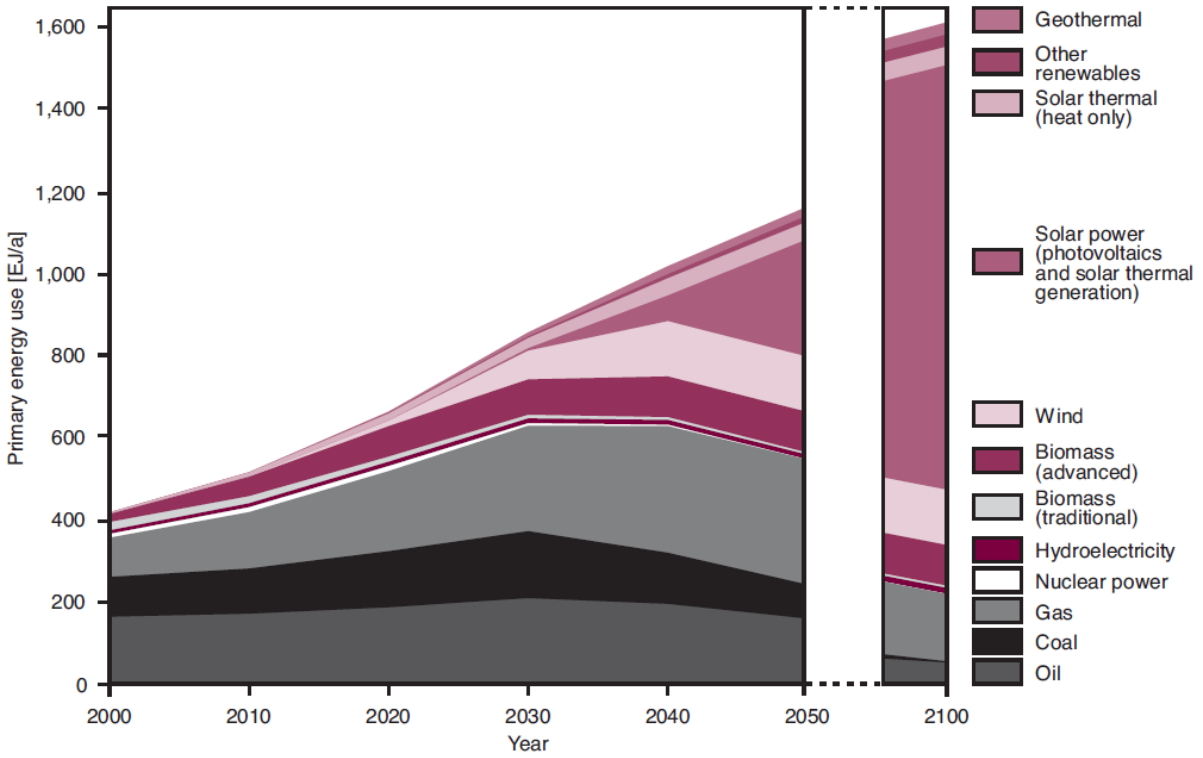


Figure 2. Projected global energy path in 2100 as suggested by WGBU

3.1.3. Possibility & Comparison of Hydrogen Production routes:

There are plenty of methods available to produce hydrogen. According to world energy resources[6], currently 96% of hydrogen is produced from fossil fuels, 48% from natural gas, 30% from liquid hydrocarbons and about 18% from coal. Now a days, the hydrogen is mainly used in fertilizer, chemical and petroleum industries and this hydrogen is mostly obtained from steam reforming of natural gas. In steam reforming, steam is allowed to react

with natural gas in presence of nickel catalyst at around 750 - 800°C to form hydrogen and carbon oxides as shown below:

$$C_xH_y + H_2O \rightarrow xCO + (x + 0.5y)\, H_2 \quad (1)$$

$$CO + H_2O \rightarrow CO_2 + H_2 \quad (2)$$

Since steam reforming uses non-renewable natural gas and producing lot of carbon dioxide, it is not a suitable process to produce hydrogen for the long term. To produce hydrogen in the long run, using renewable sources would be the best choice. Photovoltaic cell or wind mills coupled with electrolyzers could be the best way to produce hydrogen in the future[2]. With the help of european project ECTOS, Iceland exploited this approach to run hydrogen powered buses[8]. The low efficiencies of photovoltaics and electrolyzers as well as the energy loss (of about 75%) accompanied with "electricity – hydrogen – electricity" conversion[3] are the main hindrance to this approach. But the photoelectrochemical (PEC) water splitting is just a combination of electricity generation and electrolysis in a single unit. Since it involves the direct conversion of solar energy into hydrogen in a single system, the energy and efficiency losses involved at various steps could be avoided. This thesis addresses the direct transformation of solar energy into chemical energy through photoelectrochemical water splitting by using semiconductors. So the following part will discuss the basics of semiconductor photoelectrochemistry and the basic prinicples behind the PEC devices.

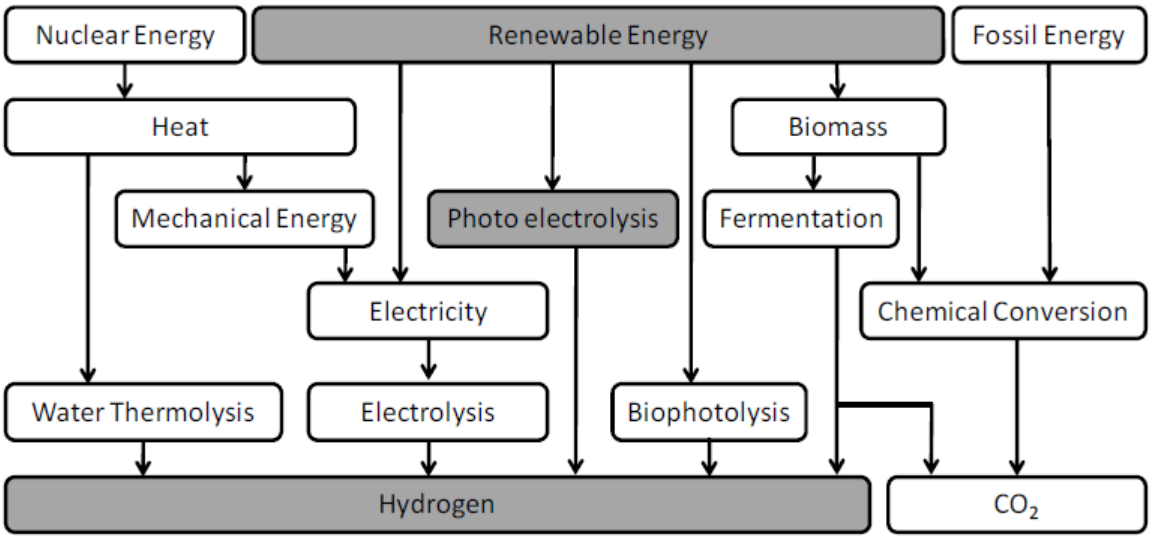


Figure 3. Various potential pathways to produce hydrogen, based on Ref [6].

3.2. Photoelectrochemical(PEC) water Splitting:

3.2.1. PEC water splitting reaction – Brief Overview:

Since water is abundant, PEC water splitting is believed to be the promising method to produce hydrogen renewably. The net reaction of the water splitting is given below:

	Acidic	Basic
Semiconductor	$4h\nu \rightarrow 4e^- + 4h^+$	
Anode	$2H_2O + 4h^+ \rightarrow O_2 + 4H^+$	$4h^+ + 4OH^- \rightarrow O_2 + 2H_2O$
Cathode	$4e^- + 4H^+ \rightarrow 2H_2$	$4H_2O + 4e^- \rightarrow 4OH^- + 2H_2$
Overall	$4h\nu + 2H_2O \rightarrow 2H_2 + O_2$	

The Gibb's free energy change $\Delta G°$ of the net water splitting reaction is 237 kJ/mol and its corresponding electromotive force $\Delta E°$ is -1.23 V. Since water splitting is an energetic uphill reaction, a working photoelectrode has to supply minimum 1.23 V in order to drive bias-free water splitting. Practically, a much higher potential of at least 1.6 to 2.0 V is required to split water due to cathodic and anodic overpotentials and other losses[4]. This required potential region almost corresponds to the wavelength of the visible region of the solar spectrum which means that the visible light has sufficient energy to split water into hydrogen and oxygen. Since water is transparent, it cannot absorb the visible light. So one has to use photoabsorber material which can produce energy by absorbing the light and tranform it to water to split it. In our case, semiconductors are doing the photoabsorber role. They produce electron in the conduction band (CB) and leaving behind the hole in the valence band (VB) while absorbing photon with energy equal to or higher than its bandgap energy. Electrons reduce the water at the semiconductor – electrolyte interface(SEI) to hydrogen whereas the holes move through the external circuit to the counter electrode to oxidize hydroxyl ions and evolve oxygen (in p-type semiconductor). The different steps involved in photolysis of water with n–type semiconductor are shown schematically in the Fig.,4. The step (1) involves the absorption of photon with energy equal to or greater than its band gap energy and producing an electron – hole pair in the semiconductor. In steps (2) & (3), the holes are moving towards SEI where the oxidation of water takes place. Step (4) corresponds to the movement of electrons through the external circuit to the metal counter electrode. The water reduction at the metal surface is step (5). All these steps(steps 1 to 5) are involved in governing efficiency of water photolysis. Except the kinetic steps (3 & 5) which can be

altered by a proper catalyst, the remaining steps can be attributed to the intrinsic properties of the semiconducing material.

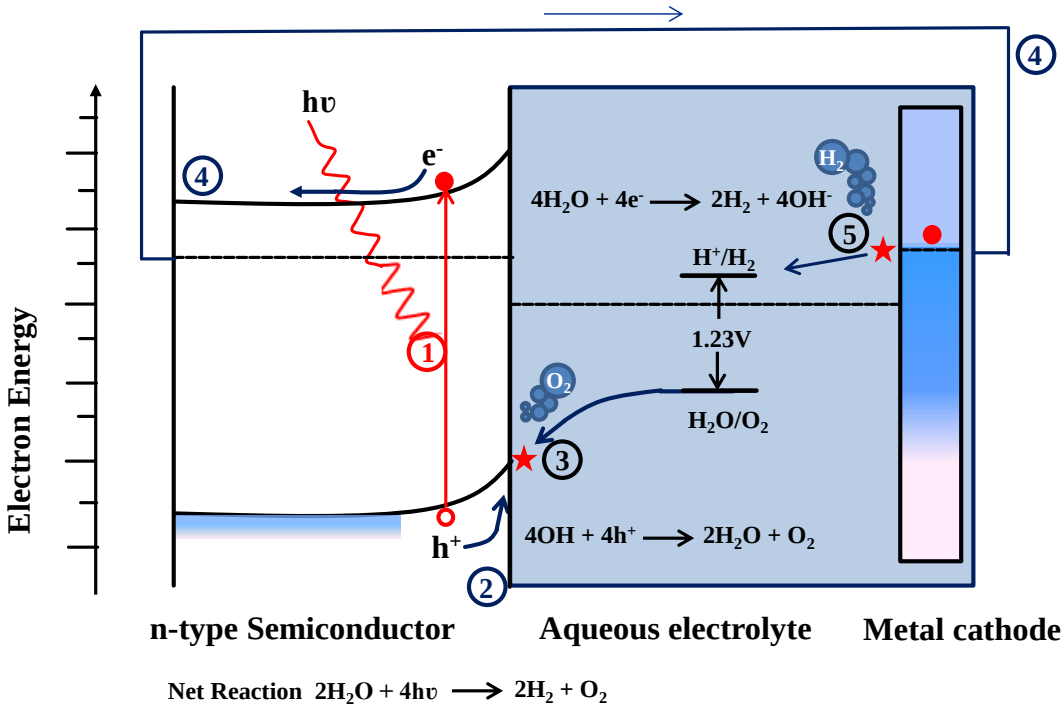


Figure 4. Schematic illustration of various steps involved in photoelectrochemical water oxidation.

3.2.2. Semiconductor – Electrolyte Interface (SEI):

Semiconductors are characterized by the valence band(E_{VB}) which is filled with electrons and the conduction band(E_{CB}) which is empty at absolute zero. The forbidden energy gap between these two bands is known as band gap (E_g) which determines the optical absorbtion property of the semiconductors. In general, the semiconductor absorbs the photon with energy equal to or higher than its band gap energy. The electrochemical potential of the solid is known as Fermi level (E_F). The position of Fermi level decides the transfer of charges from semiconductor to other phases. According to statistical mechanics, the Fermi level is defined as the energy level where the probability of finding an electron is one – half. For the intrinsic semiconductor, the Fermi level is situated at the middle of the band gap, whereas for the doped semiconductors, depending upon the doping process the Fermi level move either closer (n-type) or farther (p-type) to the vacuum level.

Consider the n–type semiconductor in contact with the solution having the redox pair A/A^- and the electrochemical potential of the semiconductor is more negative than that of the solution phase, $E_F < E(A/A^-)$. Thus, after contact, charge must flow between them inorder to

reach the equilibrium. Since semiconductor phase has the more negative initial electrochemical potential, charge will leave from the semiconductor to the solution phase which has the more positive electrochemical potential(Figure 5.A). This interfacial charge transfer leads to an excess of positive charges in the semiconductor and more negative charges in the solution (Figure 5.B). The charge transfer continues until the difference in electrochemical potentials is neutralized. At equilibrium, there will be electric field and electric gradients in both phases since no phase is electrically neutral. As solution is having huge number of available states per unit energy compared to semiconductor which has no states in the band gap region, the electrochemical potential of the solution is fixed without any further movement, whereas the n-type semiconductor becomes more positive till attain the value of the electrochemical potential of the solution. The number of charges to be transferred is greater than the number of dopant atoms present in one atomic layer of the semiconductor. Hence as shown in Figure 5.B, to obtain the enough number of ionizable charges, it reaches further into the bulk of the semiconductor(Figure 5.B). This width of the depth over which dopants are completely ionized is called *depletion width* (W), and the corresponding charged region is known as *depletion region*.

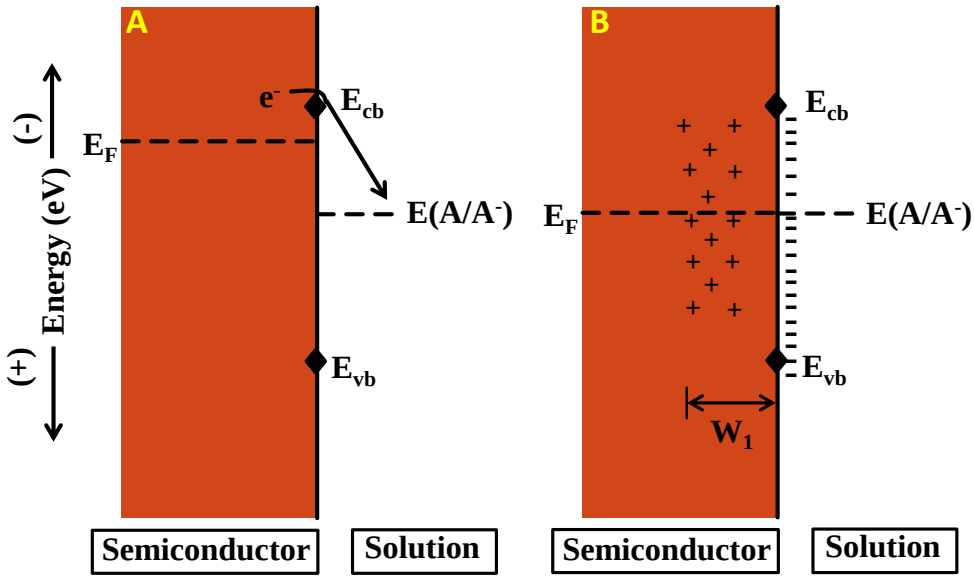


Figure 5. (A) Semiconductor – electrolyte interface before equilibration showing difference in electrochemical potential **(B)** after interfacial charge transfer, the equilibration of electrochemical potential is attained. W_1 represents the depletion width of the layer.

As mentioned above, there will be electric field and electric gradients in both the semiconductor and liquid phases after charge transfer equilibration. The Fig.,6 is known as band-bending diagram which is nothing but potential energy versus distance diagram. As shown in the Fig.,6, the absolute value of the potential difference between the interface and the semiconductor bulk is known as *built-in voltage* (V_{bi}). This value constitutes the potential drop across the semiconductor phase while charge transfer equilibration takes place. The built-in voltage (V_{bi}) can be related to the *depletion with* (W) as follows:

$$V_{bi} = \left(\frac{qN_d}{2\epsilon_s}\right) W^2 \tag{3}$$

$$W = \sqrt{\frac{2\epsilon_s V_{bi}}{qN_d}} \tag{4}$$

Where, V_{bi} is built-in voltage, W is depletion width, N_d is the dopant density, $\mathcal{E}_s$ is dielectric constant and q is the charge.

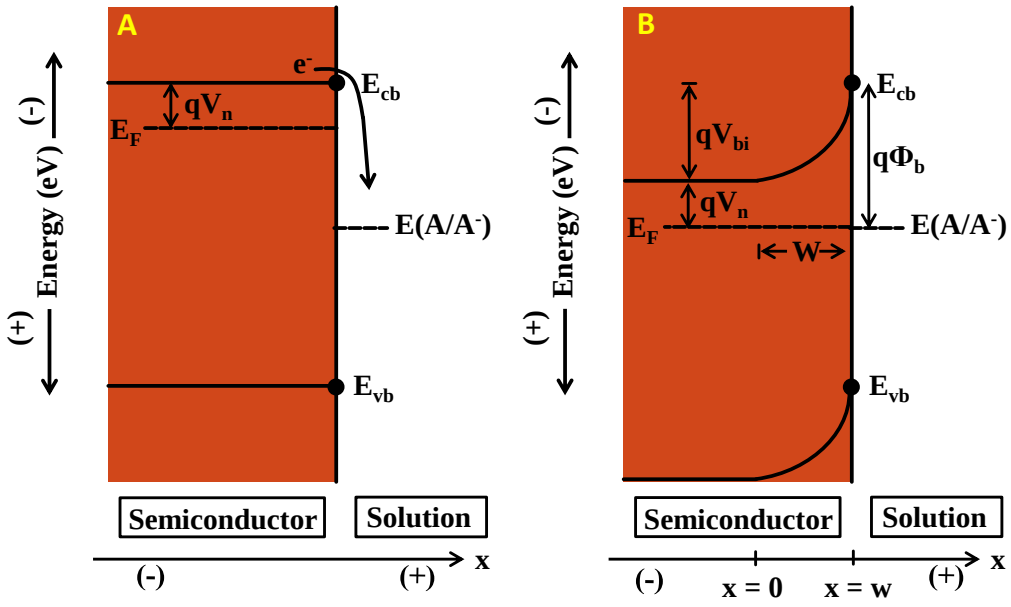


Figure 6. Energy diagram corresponding to an n-type semiconductor – electrolyte interface **(A)** before charge equilibration and **(B)** after charge equilibration

The difference between the energy of the CB at the interface and the equilibrium Fermi level is called as barrier height energy ($q\phi_b$) of the junction at the surface.

$$\phi_b = [E(A/A^-) - E_{CB}] / q \quad (5)$$

The difference between the energy of the CB in the bulk and the equilibrium Fermi level is denoted as V_n.

$$V_n = (E_F - E_{CB}) / q \quad (6)$$

Thus, $$\phi_b = V_n + V_{bi} \quad (7)$$

The electrochemical potential can be related to the vacuum scale as follows[5].

$$0 \text{ V vs NHE} = 4.43 \text{ eV} \quad (8)$$

So as per the above discussion, variation in redox potential of the solution should lead to alter the value of barrier height and built-in voltage. However, in some cases the change in redox potential does not yield any variation in semiconductor – electrolyte interface[6]. There must be interfacial charge transfer between these two phases to reach the equilibrium. But it is experimentally shown that there are some sources or sinks for keeping the charge. These sources and sinks are known as *surface states* which protect the semiconductor from the variation in redox potential of the solution and this effect is known as *Fermi level pinning*. The surface states usually located in the band gap region. 10^{13} states / cm^2 of surface state density is sufficient to engender Fermi level pinning[6a]

The current – voltage relationship for the semiconductor-liquid interface is generally given by

$$I = - I_o[\exp(-qV/kT) - 1] \quad (9)$$

Where, I is interfacial electron transfer current, Io is exchange current, q is charge, V corresponds to applied voltage, k is Boltzmann constant and T is absolute temperature

While the applied voltage is greater than zero ($V > 0$, i.e., *reverse bias*), since the concentration of surface electrons will be low, so electrons will be injected into the semiconductor from the solution. During *forward bias* wherein $V < 0$, the surface concentration of electrons will exponentially increase and hence the electrons will be transferred from semiconductor to solution.

From the equation(9), it is evident that the current can flow either in one direction depending upon the applied voltage and this phenomenon is known as *rectification* and the respective equation (9) is called as *diode equation*. This diode behavior cant be seen in the case of metal electrodes where the surface electron concentration is independent of applied voltage[13].

During illumination, the semiconductor produces majority and minority carriers. As the concentration of majority carriers remain almost unchanged[7], they do exhibit diode I – V characterestics. But the minority carrier photocurrent is dependent on the absorbed light intensity and given as: $I = I_{ph} - I_o [\exp(-qV/kT) - 1]$ (10)

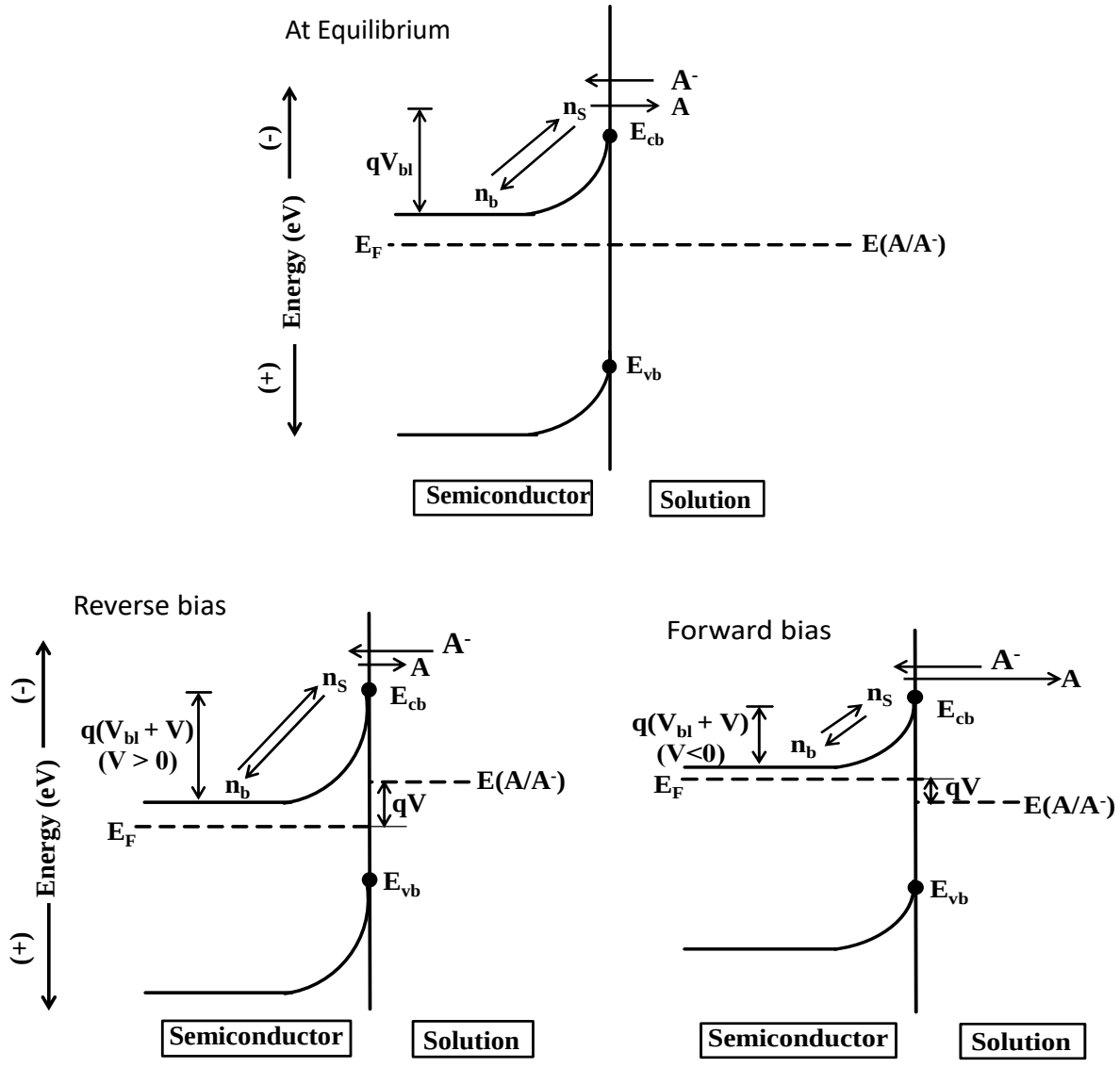


Figure 7. Energy diagram of an n-type semiconductor – electrolyte interface at different phases **(A)** at equilibrium stage **(B)** at reverse bias, **(C)** at forward bias condition. Based on the bias condition, the surface concentration of electrons changes and resulting a perturbation in equilibrium condition leading to net current flow across the semiconductor – electrolyte interface.

The maximum free energy that could be extracted from the illuminated SEI is given by the *open circuit voltage* (V_{oc}). At the open circuit condition, the net current in zero.

$$V_{oc} = kT/q \ln(I_{ph}/I_o) \quad (11)$$

The amount of collection efficiency of photogenerated carriers in the photoelectrochemical(PEC) cell is given by the *short-circuit current* (J_{sc}). At short circuit condition, the voltage is zero. The efficiency of the photocurrent collection is mainly assessed by two quantities such as *internal quantum yield*(IQY) and *external quantum yield*(EQY).

The internal quantum yield is just a measure of the number of collected charges based on the number of absorbed photons. Its value usually approaches unity because the recombination losses are not considered. The IQY is based on the intrinsic properties of semiconductor - liquid junction (SLJ). Whereas the EQY is defined as the number of collected charges based on the incident photon flux on the photoelectrochemical cell. Reflective and optical transmission losses are included in the measurement of EQY. So the semiconductor can absorb a fraction of the incident light, as a result, EQY is always lower than the IQY.

In the I – V curve (Fig.,8), a point at which the product of photocurrent and voltage is maximum is known as *maximum power point* of the PEC cell. Then the maximum energy conversion efficiency is given as

$$\text{Efficiency} = (P_{max} / P_{in}) \times 100 \qquad (12)$$

P_{max} is the maximum power point and P_{in} is the power of incident radiation

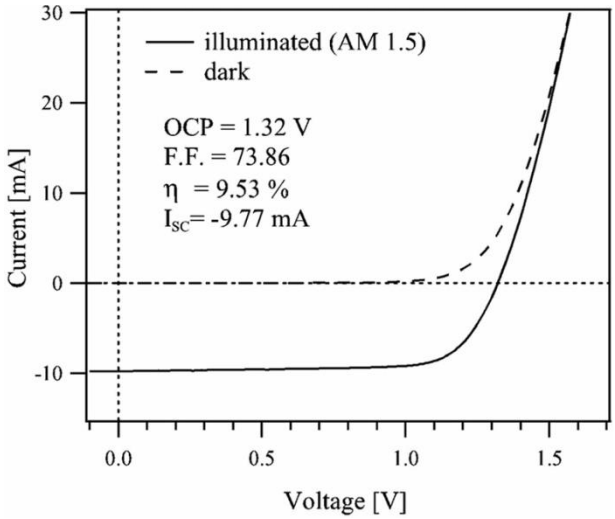


Figure 8. I-V curve of a silicon based tandem photovoltaic cell[8].

The ratio of the maximum power point divided by the open circuit voltage(V_{OC}) and short circuit current(J_{SC}) is called as fill factor (F.F).

$$F.F = V_{max} .J_{max} / V_{oc}.J_{sc} \qquad (13)$$

So the equation (12) can also be rewritten as

$$\text{Efficiency} = (V_{oc} \times J_{sc} \times F.F) \ / \ (P_{in} \times 100) \qquad (14)$$

It is clear from the above equation that the energy conversion efficiency of semiconductor – liquid junction (SLJ) is mainly based on three parameters namely V_{oc}, J_{sc} and F.F. A detailed information about SLJ can be found elsewhere[9]

3.2.3. Criteria for Semiconductor electrode materials :

Inorder to be efficient to split water, photoelectrodes have to meet several requirements such as cost, stability, good light absorption, proper position of band edges and fast charge transfer.

a. Bandgap:

The energy difference between the redox potential of water is 1.23 eV. Since oxygen evolution is involved with four electrons, it is required some overpotential, hence the semiconductors with the bandgap of ~ 1.9 eV are desired to split water[4a,10]. Also the band gap should be optimum enough to absorb reasonable part of the solar spectrum.

b. Band edge positions:

For hydrogen evolution, the CB (the quasi Fermi level of electrons) must be situated energetically above the hydrogen evolution potential whereas for oxygen evolution the VB (the quasi Fermi level of holes) must be located below the oxygen evolution potential[11].

c. Interfacial kinetics & Charge separation:

After absorbing the photon with energy greater than its bandgap, electrons will be excited into the CB by leaving behind the holes in the VB of the semiconductor. The holes and electrons should not recombine. To achieve this, the semiconductor with minimal bandgap states would be preferred. These bandgap states are produced because of contaminants, irregular crystal structure, grain boundaries and undesirable interactions with other materials. For efficient photoelectrolysis, the interfacial charge transfer kinetics should be fast enough. The charge transfer kinetics could be improved by the use of proper catalysts.

d. Stability:

As a rule of thumb, the stability decreases with decrease of semiconductor band gap energy. Most of the semiconductor materials used in solar cell industries are vulnerable to the aqueous electrolytes. Apart from electrolytes, holes produced during illumination can oxidize the semiconductor itself.

e. Cost:

Cost is a crucial issue. It generally depends upon the availability of raw material resources and the cost for manufacturing. Thus the material availability on the earth crust and the efficient thin film technology could reduce the cost of the material.

f. Eco-friendly:

Finally, the material should be environmental friendly and possess no harmfulness to anyone is very essential.

After the seminal work of Fujishima and Honda[12] several photoelectrodes have been explored for water splitting, but none of them satisfy the above mentioned criteria simultaneously and always show the trade-off between them. The following figure shows some of the semiconducting materials used for water splitting along with their band edge positions[13].

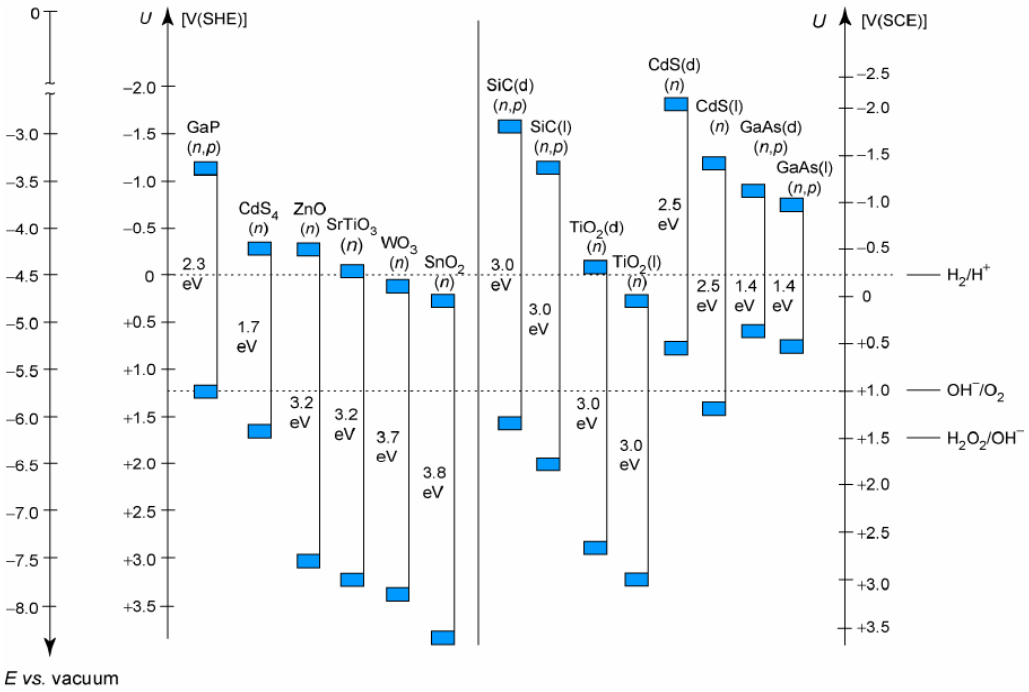


Figure 9. Various photoelectrode materials with their band edges corresponding to water splitting potentials.

3.3. State of the art photoanodes :

Mostly metal oxides are preferred as photoanodes owing to its stability in highly oxidizing conditions. The general electronic structure of these oxides possesses O 2p orbitals in the valence band and the valence d orbital of the metal atoms constitute the conduction band. Although the TiO_2 (E_g = 3.0 – 3.2 eV) and WO_3 (E_g = 2.7 eV) are quite stable and extensively investigated, their band gaps are too large to access the visible region of the solar spectrum and resulting out poor efficiency. As an example, TiO_2 can only absorb approximately 4% of the incident solar radiation, but because of its higher stability, thin layers of TiO_2 are deposited on the unstable semiconductor to bury the junction and enhance the protection[14], Since Fujishima's seminal report[12], many attempts have been made to improve the photoelectrochemical performance of TiO_2, but no success so far; however some recent efforts renewing its interest, particularly Samuel Mao et al., reduced the band gap by creating the midgap electronic states by tuning the lattice disorders of hydrogenated anatase[15]. In another report, the photocatalytic property of TiO_2 was 64 times enhanced by using plasmonic effect of gold nanoparticles[16]. WO_3 can absorb around 6% of the incident light. Similar to TiO_2, plasmonic effect of Ag nanoparticles on WO_3 was shown[17] and different types of doping was attempted[18].

Because of its optimal bandgap(~2.1 eV), wider availability and greater stability, hematite (α-Fe_2O_3) received spectacular interest since 1976[19]. Although several caveats at the earlier days, careful nanostructuring and with a proper OER catalyst – 3 mA/cm^2 at 1.23V vs RHE was achieved[20] and recently Jae Sung Lee group showed the record breaking 4.32 mA/cm^2 at 1.23V vs RHE[21]. For the practical application, the required photoelectrode efficiency is 10%, but in this remarkable work around 5% efficiency has been shown.

Although almost all the possible binary metal oxides compositions have been investigated, a suitable photoanode is still remaining elusive. Due to the limitations of binary oxides, recently ternary oxides are gaining particular interest and $BiVO_4$ (E_g = 2.4 eV) is one among them. Kudo et al., demonstrated the first photocatalytic activity of $BiVO_4$[22] and after 8 years the appreciable amount of photoeffect was reported[30]. Then to alleviate the poor electron transport of $BiVO_4$, dopants such as Mo^{6+} and and W^{6+} were introduced at the V^{5+} sites to enhance the electronic conductivity and carrier collection efficiency[23]. Y Pihosh et al

recently demonstrated that by fabricating $WO_3/BiVO_4$ nanorod to achieve the record value of 6.72 mA/cm^2 at 1.23V vs RHE[24].

Apart from $BiVO_4$, copper atom incorporated oxide such as $CuWO_4$ (E_g = 2.3 eV)[25] is particular to mention. Despite it is possible to achieve theoretically 9 mA/cm^2 with $CuWO_4$, only 0.3 mA/cm^2 was achieved so far[26] because of its poor charge separation and hole collection efficiency[27,28,29]. Doping and nanostructuring[30,31] have been tried to solve this problem, but still not possible to achieve 1 mA/cm^2 vs 1.23V vs RHE. The latest account from Bartlett group nicely summarizes the efforts carried out on $CuWO_4$[32].

Despite some investigations on complex or multinary metal oxides, from a materials perspective, these multinary oxides have huge combinations ranging from 8000 to 700 000[33,34]. Osterloh reviewed 134 catalysts for water splitting[35]. It is daunting task to choose a suitable photoelectrode among the vast possibilities, hence Parkinson developed a kit based on combinatorial method called SHArK (Solar Hydrogen Activity Research Kit) (http://www.uwyo.edu/parkinson/shark_project.html). This approach shows promising way to find out a better photoanode. For the recent developments in metal oxide photoanodes, one can refer the latest review by Abdi and Berglund[36].

3.4. Hematite photoanode :

The excellent features of hematite such as it is capable of absorbing 40% of solar radiation[37], possessing good photoelectrochemical stability in a wider pH range from 3 to 14 , and its earth abundance make it a strong candidate for photoanode. Also theoretically, based on its band gap of 2.1 eV, 12.5 mA/cm^2 photocurrent can be obtained under AM 1.5 solar illumination which corresponds to 15.4% solar to hydrogen (STH) conversion efficiency. The electrical and optical properties of hematite can be found in recent reviews[38,39,40] and it is clear that based on the preparation methods the band gap energy is varying from 1.9 (650 nm) to 2.2 eV (560 nm). Hematite has the indirect band gap and hence the absorption length ($1/\alpha$) is relatively longer[41]. For instance, at 550 nm it has the light penetration depth of 118 nm, but due to short lifetime and low charge carrier mobility the hole diffusion length is usually between 2 and 5 nm[42,43].

Oxygen evolution reaction (OER) is a slow process on hematite since it takes few seconds to take place[44] and the OER mechanism is still under investigation. Several pathways are suggested based on spectroelectrochemical studies such as electrochemical impedance spectroscopy (EIS)[45,46] intensity modulated photocurrent spectroscopy (IMPS)[45,47], Infrared

(IR) spectroscopy[48,49], and Transient absorption spectroscopy (TAS)[44,50] and the main conclusion from those studies are that some iron based intermediates are involved which are formed by trapping of holes and these intermediates are subsequently transferring the holes to the electrolyte. These intermediates are called as surface states that are initially regarded only as the recombination centers but with the help of sophisticated technics it is proved that these states are involved in charge transfer processes.

For any photoelectrode, three parameters are very essential, namely charge carrier generation, charge carrier transport and transfer of charge carrier to the electrolyte. As pointed out earlier, the diffusion length of holes for hematite is shorter and thus achieving efficient charge carrier generation and separation becomes difficult particularly for the flat geometry electrodes because of the accumulation of charge carriers. Although doping can enhance the electron conductivity, it decreases the depletion layer width. To alleviate this problem, nanostructured electrodes with different morphologies, heterojunctions, catalyst and surface modification have been explored[51].

3.5. Surface Modification of Photoelectrodes :

Semiconductor – Electrolyte interface (SEI) plays an important role in solar energy conversion. However, most of the semiconductors strongly interact with electrolytes and either forming new surface phases or undergoing chemical corrosion because of the unwanted chemical reaction with the electrolytes. Hence it is necessary to protect the semiconductor surface with buffer layers but without loosing photopotential and photocurrent. Most of the semiconductors are not good catalysts for hydrogen and oxygen evolution reactions and thus to overcome the kinetic overpotentials and to increase the formation of desired products , it is of utmost importance to deposit the appropriate cocatalysts (electrocatalysts) either on the semiconductor surface or on the buffer layer based on the chemical and electronic properties of the semiconductor surface. Compared to more covalent or less ionic semiconductors, the band edges of the oxide semiconducting surface exhibit a shift of 59 mV/pH because of the adsorption of H^+ or OH^- changes the surface charge of oxides. Also it is shown that the trapping of charge carriers under illumination shifting the band edges[52,53,54], rather than with the redox couple of the solution, the bulk semiconductor usually equilibrates with the surface states that influence the energetics of the semiconductors and thus lowering the band bending[55,56,57]. Similarly the orientaion of molecular dipoles on the semiconductor surface can affect its band edge positions[56,58,59], if the dipoles are oriented inwards increases the band energy and the outward orientation lowers the energy of the bands. As shown above, the

semiconductor surface governs the photoelectrochemical energy conversion process and careful surface engineering is required to enhance the stability, efficiency and to decrease the detrimental effects such as corrosion and surface trapping.

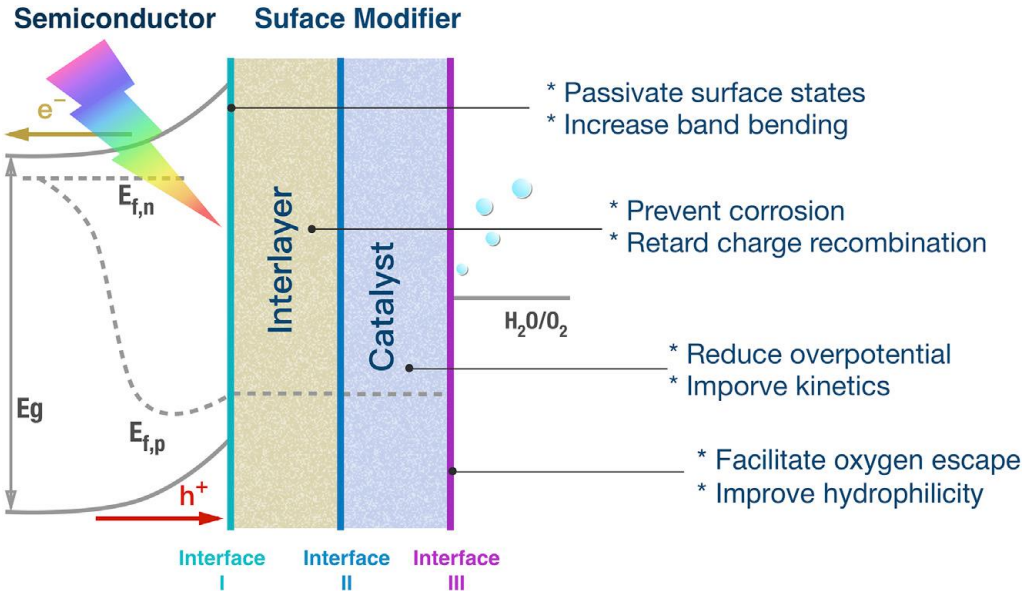


Figure 10 . The semiconductor surface modifications and their implications. Adapted from[60] Kuang et al.

3.5.1. Stabilization of photoelectrode surfaces by semiconductor coating :

As pointed out earlier, the semiconductor surface, for instance ZnO, Cu_2O, InP, Si, GaAs and GaP, interacts with electrolytes and undergoes photocorrosion that impacts the stability. To protect the photoactive material from photocorrosion, some stable material has to be overcoated on the surface of the semiconductor and this overcoating materials have to fulfil certain requirements such as (i) it should be stable enough in the electrolyte medium, (ii) it should be transparent and does not absorb solar spectrum in the visible range (iii) to avoid the formation of defects – it should have minimal lattice mismatch with the photoactive underlying semiconductor, otherwise defects will act as trapping and recombination centers. (iv) it should selectively allow either holes or electrons to the electrolyte from the semiconductor. Oxides, chalcogenides and organic polymers are usually employed as top layers. (v) it should be thick enough to protect the underlying semiconductor from the electrolyte, but at the same time it should facilitate the interfacial charge transfer. Particularly, TiO_2 is commonly used as a passivation layer owing to its stability and wide band gap. Recently Nathan Lewis *et al.*, demonstrated that 4 to 143 nm thick amorphous TiO_2

layer stabilize the photoanodic performance of Si, GaAs and GaP, in particular the Si coated with TiO_2 showed more than 100 hours PEC water oxidation[61]. The same group also employed TiO_2 overlayer to improve the stability of n-CdTe[62]. Cu_2O is unstable under reductive potential because of its reduction to metallic Cu and also known to suffer severe photocorrosion in aqueous electrolytes that hinders its usage as a photocathode in PEC water splitting. However, Gratzel *et al* showed that with the help of Al:ZnO (20 nm) and TiO_2(10 nm) overlayers Cu_2O exhibits enhanced stability with a higher photocurrent of 7.6 mA/cm^2 at 0V vs RHE[63,64]. In the case of hematite – which is stable in nature, this kind of overlayers not only improving the durability but also enhances the onset potential by reducing the density of surface states as showed by Gratzel and co-workers. They used group-13 oxides namely Al_2O_3, Ga_2O_3 and In_2O_3 and observed the 200 mV cathodic shift of onset potential and sustained the photocurrent for 24 hours[65,43].

3.5.2. Surface states passivation:

The presence of surface states deteriorate the performance of photoelectrodes by acting as recombination as well as trapping centers and charging of those centers resulting out Fermi level pinning. In the case of hematite, Bisquert's group demonstrated that how the density of surface traps varied with potential and how these surface states trap holes before they oxidize water[66], similarly $BiVO_4$ suffers from photocorrosion and poor photovoltage due to the surface recombination at surface defect states[67,68] and hence researchers have employed several materials as trap state passivation layers[65,43]. However, Co-Pi is a well known OER catalyst, TAS and IMPS studies confirmed that its photoelectrochemical performance enhancement on Fe_2O_3 and $BiVO_4$ mainly arises by suppression of charge carriers recombination and not by catalytic activity[69,70,71,72]. Similarly Dunwei Wang and co-workers have shown that water oxidation catalyst $NiFeO_x$ on hematite also not acting as a catalyst but as passivation layer to reduce the recombination[73,74]. whereas MnO_x enhances the charge transfer process but shifting the onset potential toward anodic side and decreasing the photoanodic performance of hematite due to the higher density of surface states and Fermi level pinning[75] although MnOx shows better OER behaviour compared to bare hematite in dark .

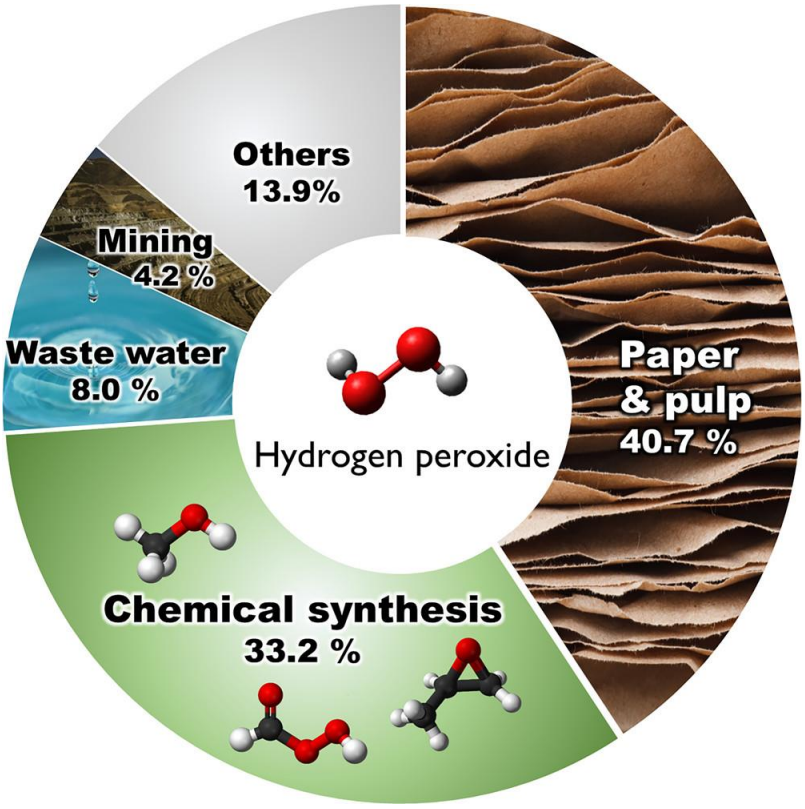
3.5.3. Improving kinetics by catalyst layer :

The usage of overlayers such as TiO_2, Al_2O_3 and Ga_2O_3 etc., may enhance the photoelectrode stability, but do not give a catalytic surface for water reduction or oxidation, thus additionally cocatalyst is required to reduce the overpotential and to improve the kinetics of water splitting reactions. This catalyst overlayer can be either as a continuous film or nanosized metal clusters, however nanosized metal clusters, if the size of the metal cluster is small compared to the depletion width of the semiconductor, provide better catalytic performance in terms of photovoltage than that of continuous layer as demonstrated by Tsubomura et al.,[76,77]. The amount of precious metals used as catalysts is minimal in the case of nanosized metal clusters, while illumination – the minority carriers are transferred to the metal clusters and then the Fermi level of the metal cluster is adjusted according to the redox potential of the electrolyte, eventually the charge transfer occurs to the electrolyte.

Gratzel and co-workers showed the cathodic shift of 200 mV onset potential and improved photocurrent with approximately 2 nm diameter IrO_2 nanoparticles modified nanostructured hematite photoanode[20] and Bisquert et al., achieved 300 mV cathodic shift of onset potential with electrodeposited IrOx nanoparticles on hematite[78]. Photoelectrodeposited Co-Pi yields 120 mV cathodic shift of onset potential[79]. Oxyhydroxides and layered double hydroxides (LDH) are also employed as cocatalysts on hematite[80,81]. Hamann deposited $Ni(OH)_2$ by photoelectrochemical conditioning of ALD deposited NiO on hematite and obtained a cathodic shift of 300 mV in onset potential and two fold enhancement of photocurrent[82].

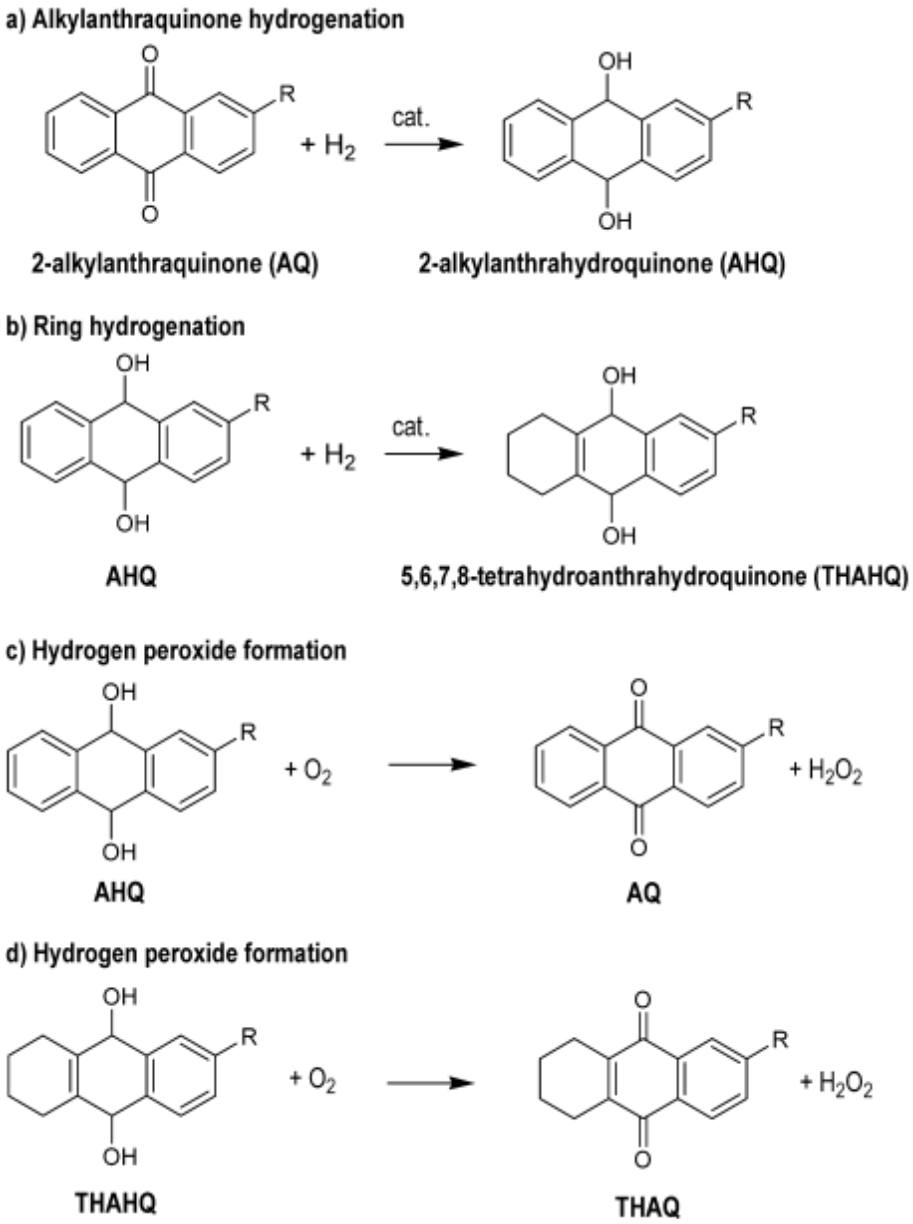
3.6. Hydrogen peroxide production – Current status:

Hydrogen peroxide (H_2O_2) is an environmentally benign chemical involving in variety of applications including disinfection kit, for bleaching pulp and textiles[83], wastewater remediation[84] and chemical synthesis[85]. Thus the utilization of H_2O_2 increased from 0.5 million tonnes per year in 30 years before to 4.5 million tonnes in 2014 and the requirement is still increasing[86] and in USA about 40% of H_2O_2 is used for pulp and paper bleaching and around 33% in chemical synthesis particularly in detergent applications as shown in the **scheme 1**.



Scheme 1. Distribution of H_2O_2 consumption in USA in 2015[87]

Currently, H_2O_2 is predominantly, around 95% [88], prepared by well established anthraquinone autooxidation (AO) process that was first introduced in the 1939 by IG Farbenindustrie AG by Riedl and Pfleiderer in Germany for the production of 1 metric ton H_2O_2/day[89]. The various steps involved in AO process is given in the following **scheme 2**.

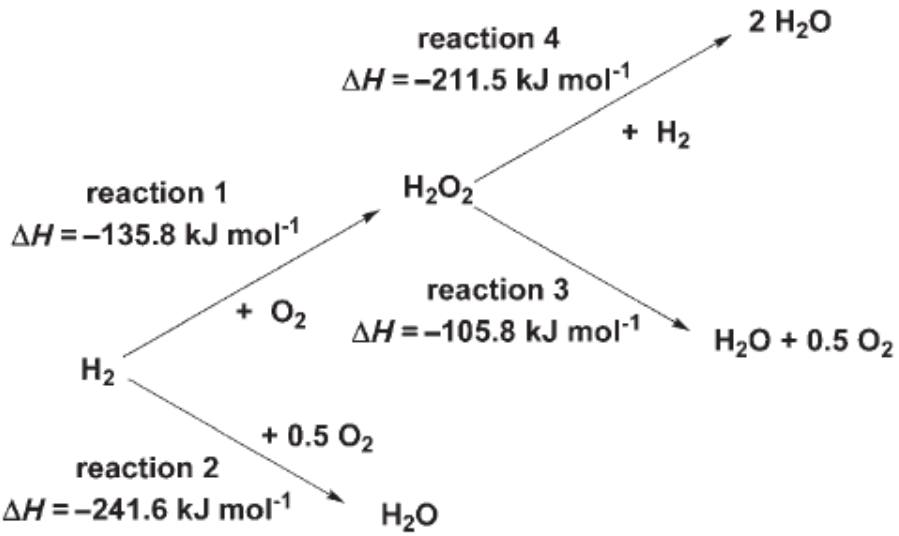


Scheme 2. Various steps involved in anthraquinone autooxidation process for H_2O_2 generation in industrial scale from Ref.[90]

As shown in scheme 2 (a), first step is hydrogenation of 2-alkylanthraquinone to anthraquinol or anthrahydroquinone and the second step is the side reaction of the unsubstituted aromatic ring to obtain 5,6,7,8-tetrahydroanthraquinone. Then the hydrogenation catalyst (usually Ni or Pd) is removed from the solution followed by the oxidation to get back the initial anthraquinone and parallelly yield H_2O_2 in equimolar amount. At this stage, some amount of H_2O_2 is taken out to produce 30% H_2O_2 and further distillation leads to get 70% H_2O_2. The final anthraquinone molecules will be regenerated and resused for the next cycle. Despite the yield of H_2O_2 is higher in this method, it has some disadvantages. For example, the catalyst

and the solution must be regenerated, the hydrogenation and oxidation steps are mass transport limited and the purification of H_2O_2 from organic contaminants by liquid-liquid separation causes more investment in purification equipments[90] and the addition of stabilizers to the concentrated H_2O_2 to prevent from decomposition.

These downsides of the AO process pushing industry and academia to find out new alternative methods for H_2O_2 production and in this regard direct and electrochemical synthesis of H_2O_2 gain particular attention. Direct synthesis of H_2O_2 is a straightforward one-pot process where the hydrogen and oxygen gases are allowed to react directly in presence of a catalyst to form H_2O_2 based on a reaction of $H_2 + O_2 \rightarrow H_2O_2$. The mechanism of the reaction is proposed as follows: at first on the catalytic surface, the hydrogen molecule dissociates into atoms followed by the adsorption of oxygen molecules on the catalyst to react with hydrogen atom and forms *OOH intermediate that generates H_2O_2 by reacting with another hydrogen atom and finally the H_2O_2 desorps from the catalyst surface[91]. There are some drawbacks in direct synthesis of H_2O_2, particularly this method needs hydrogen-oxygen mixtures in different concentrations that are susceptible to explosion, hence it needs addition of diluents in larger quantity such as carbon dioxide, nitrogen or argon to avoid explosion that decreases the productivity. Another issue is selectivity of a catalyst to form H_2O_2 rather than H_2O, moreover the catalysts enhance the combustion of reactant gas mixtures and also decompose H_2O_2[90].



Scheme 3. Schematic illustration of various steps involved in direct synthesis of H_2O_2 from ref[90]

Another approach is electrochemical synthesis of H_2O_2 in which dilute alkaline solution (NaOH) is electrolysed in an electrochemical cell that yields the efficiency of 90% and this process is also known as Dow process. The electrochemical reactions occur in this process are given below:

At Anode : $2\ OH^- \rightarrow H_2O + \frac{1}{2}\ O_2 + 2\ e^-$ (15)

At Cathode : $H_2O + O_2 + 2\ e^- \rightarrow HO_2^- + OH^-$ (16)

And Overall reaction : $NaOH + \frac{1}{2}\ O_2 \rightarrow HO_2Na$ (17)

Albeit the efficiency is comparable to AO process, there are some downsides in this process also. Particularly, the stability of H_2O_2 is poor in alkaline condition, hence H_2O_2 should be separated from the alkaline solution. The alkaline environment causes corrosion.

These kind of problems can be overcome by photoelectrochemical method that in a single step can produce H_2O_2 in a clean way by using H_2O as a resource under solar illumination. In this method, H_2O_2 can be obtained by two processes namely: (i) oxidative H_2O_2 generation from water, (ii) reductive H_2O_2 generation from oxygen[92]. Based on the redox potential, oxygen generation from water is $E(O_2/H_2O)$ = +1.23V vs RHE and the degradation of H_2O_2 to O_2 is $E(O_2/H_2O_2)$ = +0.68V vs RHE whereas that of H_2O_2 production from H_2O is $E(H_2O_2/H_2O)$ = +1.77V vs RHE. Hence the formation of H_2O_2 by the reduction of H_2O as described in the following equation is very difficult to take place.

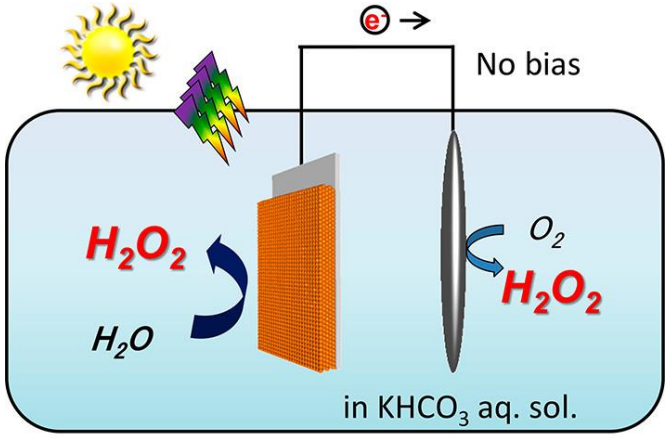
$2\ H_2O \rightarrow H_2O_2 + 2\ H^+ + 2\ e^-$; $E(H_2O_2/H_2O)$ = +1.77V vs RHE (18)

However Shiragami and coworkers obtained H_2O_2 by the reduction of H_2O by using TiO_2 photoanode sensitized with Ge-di(hydroxo)porphyrin dye in visible light[93] with a faradaic efficiency of around 92%. Sayama group published series of papers based on bicarbonate anion (HCO_3^-) effect on composite photoanodes made up of $BiVO_4/WO_3$ for oxidative generation of H_2O_2 [94,95,96]

Reductive H_2O_2 production from oxygen is based on the following equation

$O_2 + 2\ H^+ + 2\ e^- \rightarrow H_2O_2$; $E(O_2/H_2O_2)$ = +0.68V vs RHE (19)

Fuku *et al.,* combined reactions described in equations (18) & (19) in a single photoelectrochemical cell by employing oxidative H_2O_2 from water at $WO_3/BiVO_4$ photoanode and reductive H_2O_2 production from oxygen at the gold cathode and obtained anodic and cathodic faradaic efficiencies of H_2O_2 production of 50% and 90% respectively without any external bias in aqueous bicarbonate solution



$$2H_2O + O_2 \xrightarrow{2h\nu} 2H_2O_2$$

Figure 11. Generation of H_2O_2 by two electron – two proton process on both the electrodes without any external bias and ion exchange membrane with an overall efficiency of 140%, from ref[95]

From the discussion, it is clear that photoelectrochemical approach holds greater potential to generate H_2O_2 with greater efficiency in clean manner with abundant resources like solar irradiation and water without any membrane. Based on that, we planned to produce H_2O_2 by photoelectrochemical method.

3.7. Aim of this chapter:

- Prepare the hematite photoanode
- Functionalize the hematite photoanode with anthraquinone by diazonium electrografting process
- Immobilize anthraquinone poly ionic liquids on hematite by Surface Initiated Atom Transfer Radical Polymerization (SI-ATRP)
- Characterization of bare and surface modified hematite photoanodes.

3.8. Synthesis of Iron Oxide (Fe_2O_3) Photoelectrodes:

3.8.1. Preparation of Hematite Photoanodes By Anodic Electrodeposition Process:

Iron oxide photoanodes were prepared by anodic electrodeposition process by following the procedure developed by Spray and Choi[97]. First the substrate FTOs ($F:SnO_2$) are cleaned with soap solution, then in acetone, followed by ethanol and in distilled water for 20 min in each of the solvents by ultrasonication process. In a typical three electrode cell setup as shown in **Figure 12**, anodic electrodeposition was carried out at 75°C by applying positive potential of 1.2V vs SCE in an electrodeposition bath containing aqueous solution of 20mM $FeCl_2.5H_2O$ and the bath solution pH was maintained at 4.1 by the addition of NaOH solution. The potentiostatic electrodeposition curve is given in **Figure 13.** During this anodic process, at first, Fe^{2+} ions were oxidized to Fe^{3+} ions, then due to the poor solubility of Fe^{3+} at pH 4.1, it precipitated as γ─FeOOH on the working electrode (FTO)[98].

$$Fe^{2+} \rightarrow Fe^{3+} + e^- \quad (20)$$

$$Fe^{3+} + 2H_2O \rightarrow FeOOH + 3H^+ \quad (21)$$

The net reaction is: $Fe^{2+} + 2H_2O \rightarrow FeOOH + 3H+ e^-$ (22)

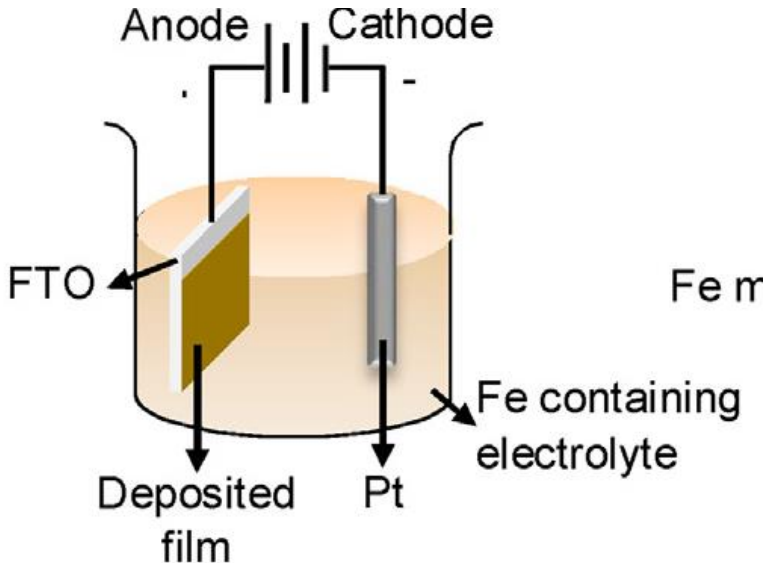


Figure 12. Schematic illustration of anodic electrodeposition method and setup employed for hematite photoanode preparation.

Then crystalline α-Fe_2O_3 films were obtained by annealing the FeOOH films at 520°C for 30 minutes at a ramping temperature of 2°C/min.

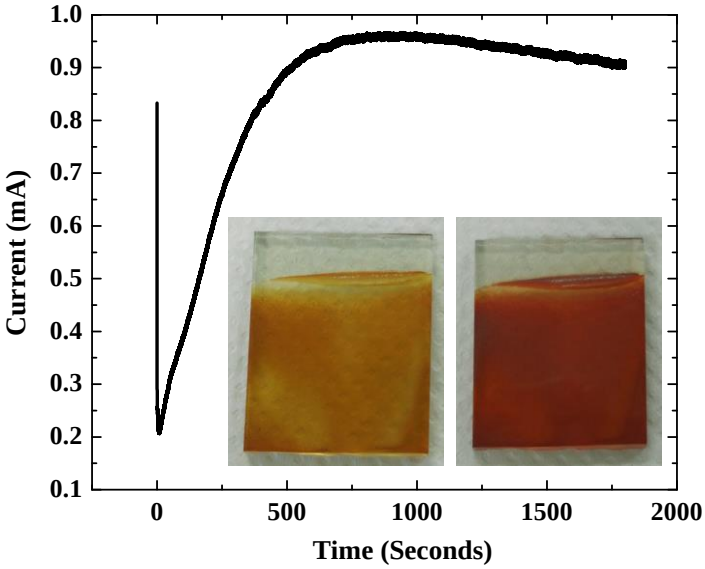
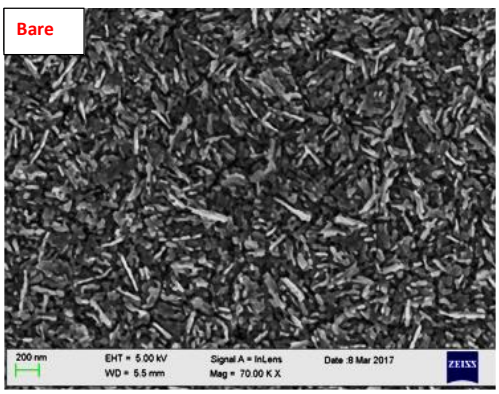
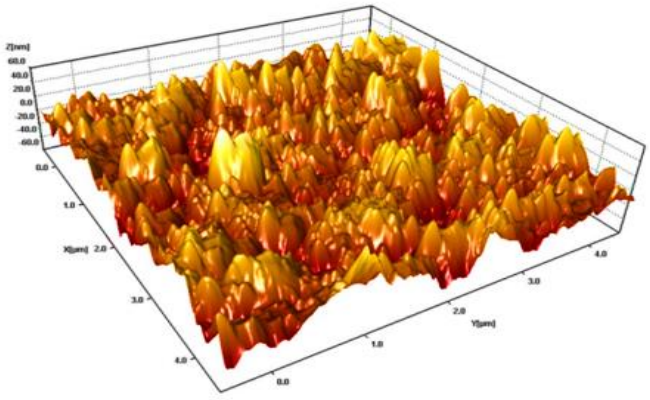


Figure 13. Anodic electrodeposition curve corresponding to FeOOH deposition on FTO. The inset images show the difference between as deposited FeOOH (Left side, pale orange colour, before annealing) and Fe_2O_3 (right side, red in colour, after annealing at 520°C).

It is demonstrated by Zandi[99] *et al.*, that the electrodeposited hematite films outperformed its planar counterparts prepared by ALD (Atomic Layer Deposition) method and the enhancement is due to the difference in morphology which inturn enhances the photoelectrochemical properties. Care must be taken with each electrodeposition parameters because such as electrolyte composition, pH, temperature, electrodeposition potential, electrode substrate, deposition time and annealing temperature could impact the morphology of the film which inturn influences the photoelectrochemical property[100].

The morphology and the surface analyses of the electrosynthesized hematite photoanode were carried out by employing SEM, AFM, XPS and contact angle measurement. The outcomes are depicted in **Figure 14**.





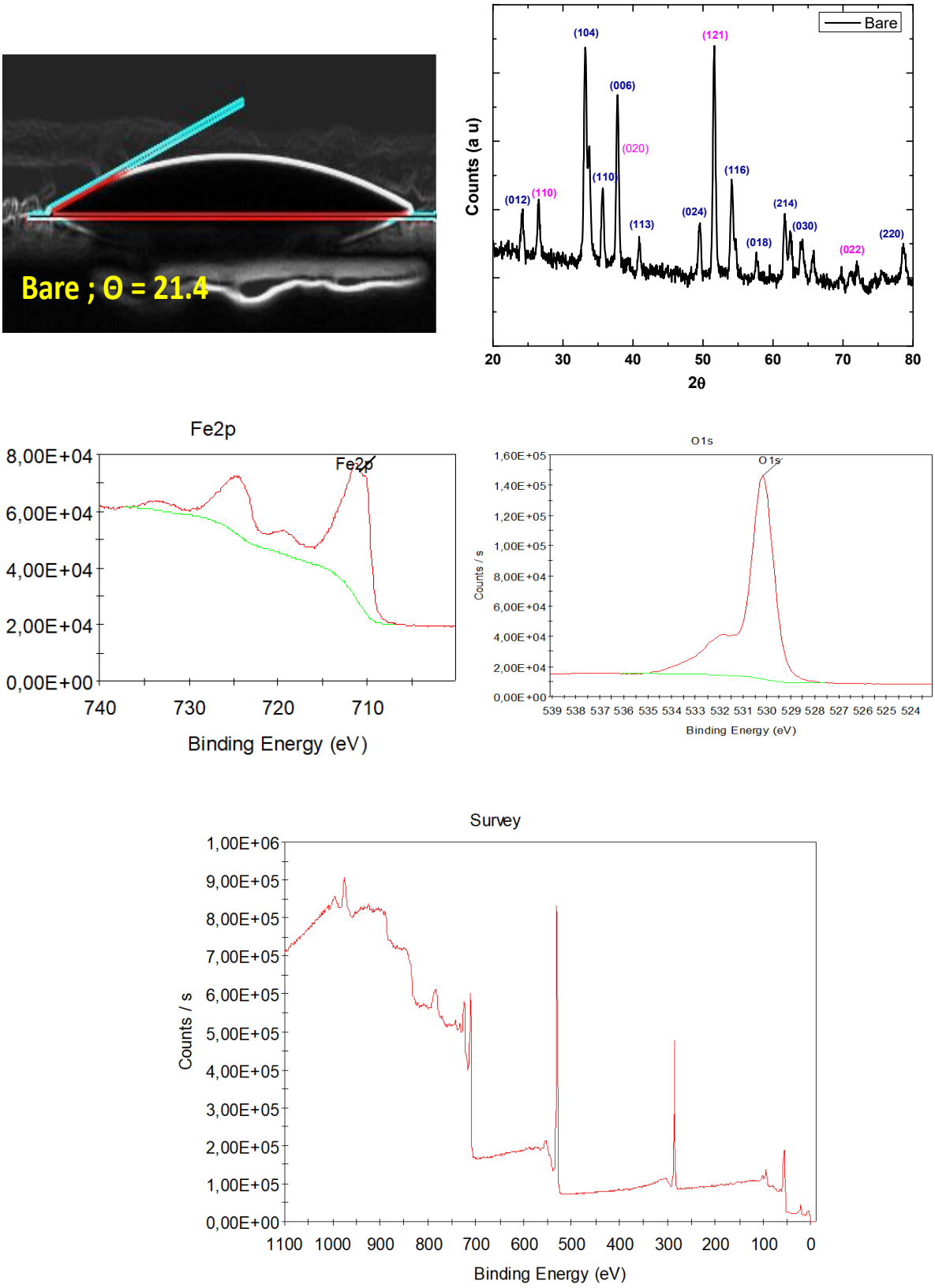


Figure 14. Various surface analysis methods like SEM, AFM, Contact angle, XRD and XPS were used to characterize the as prepared hematite photoanode.

The survey XPS spectrum displays the contribution of Fe_{2p}, O_{2s} in close agreement with the element composition of Fe_2O_3. Small traces corresponding to Sn_{3d} and F_{1s} are also visible. The intensity attenuation of Sn_{3d} (487 eV) and F_{1s} (685 eV) signals is an indication of deposition of Fe_2O_3 on FTO. The X-ray diffraction spectrum shows the features of iron oxide corresponding to hematite crystal structure. The contact angle measurement indicates that the as-prepared hematite photoanode is hydrophylic with a contact angle of 21.4°. From the SEM & AFM analysis, it is proved that the electrodeposition yields nanostructured hematite.

Nanostructuring is not only enhancing the surface area but also creates many localized processes as nicely summarized by Ali Eftekhari *et al*[101] and Yi Yang *et al*[102]. To name the few, as pointed out by Songcan Wang *et al.*,[103] nanostructuring the photoelectrodes (i) gives more active sites for redox reactions, (ii) enhances the absorption coefficient, (iii) reduces the diffusion distance of holes and electrons to the reaction sites, (iv) modifies the optical and electronic properties, (v) decreases the trapping or recombination of holes and electrons because of minimum surface defects, (vi) decreases the light reflection. Nanostructuring is particularly beneficial in the case of hematite to overcome the problem of short hole diffusion length[20].

3.8.2. Anthraquinone Modified Hematite By Reductive Electrografting Process:

Diazonium compounds are generally represented as $R\text{-}N_2^+X^-$, where R represents alkyl or aryl group, X^- is an organic or inorganic counter anion. The easiness, rapidness and strong covalent bonding between the R group and the surface atoms make the diazonium electrografting process more attractive. Diazonium salts are generally prepared by treating aromatic amines with nitrous acid that results in nitrosyl cation and the reaction is commonly known as *nitrosylation*. The nitrous acid is usually obtained *in-situ* by reacting the sodium nitrite with mineral acid. Thus obtained diazonium salts are usually unstable in aqueous solution at room temperature due to the loss of diazonium as N_2 gas and hence the diazonium salts are usually isolated as tetrafluoroborate or hexafluorophosphate salts that are stable at room temperature. Alternatively, diazonium compounds can be generated *in-situ* and this approach does not require the direct synthesis and isolation.

Surface modification gained particular interest for the materials employed in energy storage and conversion devices. Among several surface modification methods, diazonium based surface modification has received more attention[104]. The surface modification based on aryl diazonium salt was firstly reported by Delamar[105] *et al.*,by electrochemical reduction of

(4-nitrophenyl)diazonium tetrafluoroborate on a glassy carbon electrode and the reaction pathway of the grafting process is given in **Figure 5.**

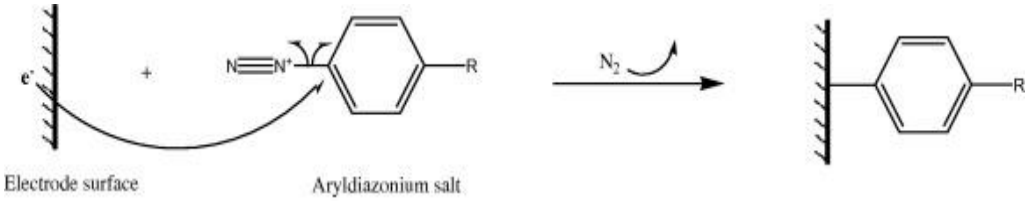


Figure 15. Schematic illustration of electrode surface modification by aryl groups based on diazonium electrografting

The quinone modified electrodes are widely used for the electrochemical synthesis of H_2O_2 by electrocatalytic two electron reduction of oxygen and the group of Kaido Tammeveski has published series of papers on this concept[106]. It is proved that the oxygen reduction reaction of quinone follows EC mechanism as shown below:[106a, 107]

$$Q + e^- \rightarrow Q^{\bullet -} \quad \text{(Electrochemical step)} \quad (23)$$

$$Q^{\bullet -} + O_2 \rightarrow O_2^{\bullet -} + Q \quad \text{(Chemical step)} \quad (24)$$

$$2\ O_2^{\bullet -} + H_2O \rightarrow O_2 + HO_2^- + OH^- \quad \text{(Disproportionation)} \quad (25)$$

$$O_2^{\bullet -} + H_2O + e^- \rightarrow HO_2^- + OH^- \quad \text{(Reduction)} \quad (26)$$

Where Q represents the quinone moieties on the electrode surface. Step I (equation - 23) is the electrochemical step where Step II (equation - 24), the chemical step, determines the rate of the reaction which depends on the concentration of $Q^{\bullet -}$ on the electrode surface and these semiquinone radical ions are extremely active as confirmed by using cyclic voltammetry[108]. Steps III and IV (equations –25 & 26) are fast and leading to the formation of H_2O_2. Hence it is good to have more amount of quinone groups on the surface inorder to obtain the H_2O_2 in higher quantity. High thickness of AQ can be obtained by exploiting the mediating effect in the electroreduction of AQ diazonium salt by sweeping the potential to more negative values as demonstrated by Daasbjerg *et al.*,[109]. Based on that, we have attempted to electrograft thick layer of AQ on hematite surface.

For AQ electrografting on hematite, 2mM of 9,10-dioxo-9,10-dihydroanthracene-2-diazonium (AQD) with 0.1M Bu_4NBF_4 (tetrabutylammonium tetrafluoroborate) in acetonitrile was used, the solution was purged with argon gas for 20 minutes prior to electrografting. Typical 3-electrode cell setup with hematite as working electrode, stainless steel mesh as counter electrode and saturated calomel electrode (SCE) as reference electrode were used. Cyclic voltammogram was recorded between the potential range of +0.55V and -1.5V vs SCE at the scan rate of 0.1V/Sec for 10 cycles and the voltammogram is shown in **Fig.,16.**

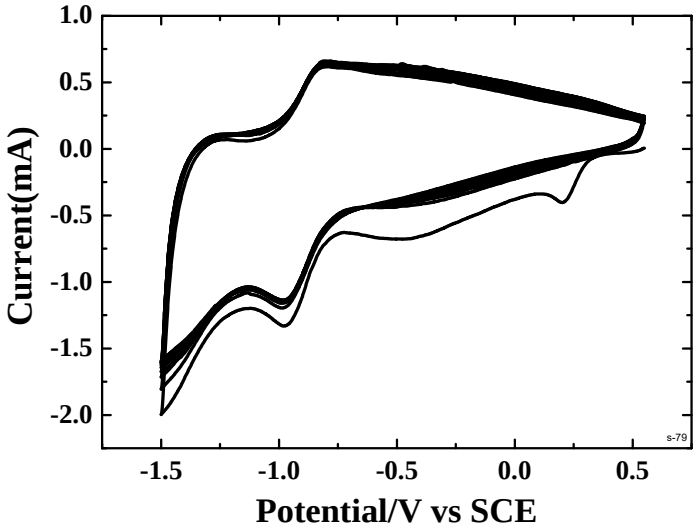
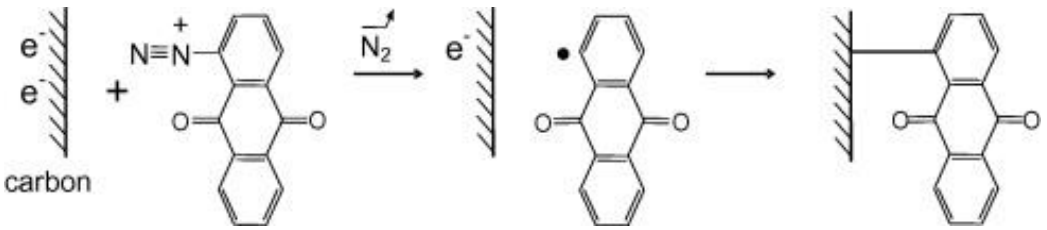


Figure 16. Electrografting of AQ on hematite. Cyclic voltammogram recorded during redox electrografting to immobilize anthraquinone moiety on hematite using 100mV/sec scan rate for 10 cycles in 2mM diazonium anthraquinone salt (AQD) in 0.1M Bu_4NBF_4 / CH_3CN.

The reduction peak around 0.3V vs SCE corresponds to the reduction of diazonium salt which disappears after the first cycle and the other reduction peak around -0.9V corresponds to the one electron reduction of AQ to anion radical AQ ($AQ^{\bullet -}$) and this process is schematically explained in **Scheme 4**.



Scheme 4. Process involved in covalent attachment of AQ on electrode surface by the reduction of diazonium anthraquinone salt. Carbon is given as a model electrode but the same scheme is applicable to hematite too.

Some unprecedented features are seen in the electrografting voltammogram compared to Daasbjerg *et al*.,[109]. At first, in our case, the reduction wave of the diazonium salt at 0.3V vs SCE vanished after the first cyle due to the blocking of the surface whereas in their case there is no change in diazonium salt reduction wave upon cycling and also they observed the increase of peak current with increase of cycle numbers for the second reduction peak which is in contrast to our case (around -1.0V vs SCE). It clearly indicates that the redox mediated electrografting is not occuring on the hematite surface and also the more cathodic potential range used for this electrografting is, in general, not preferable to hematite.

Hence, the normal diazonium electrografting method without any mediation by redox groups was adapted and so the cyclic voltammogram was recorded between the reduced potential range of +0.5 and -0.3V vs SCE as shown in the **figure 17.** The reduction peak corresponding to diazonium salt appeared at 0.25V and the peak still remained even after first cycle and decreasing with increase of cycle numbers.

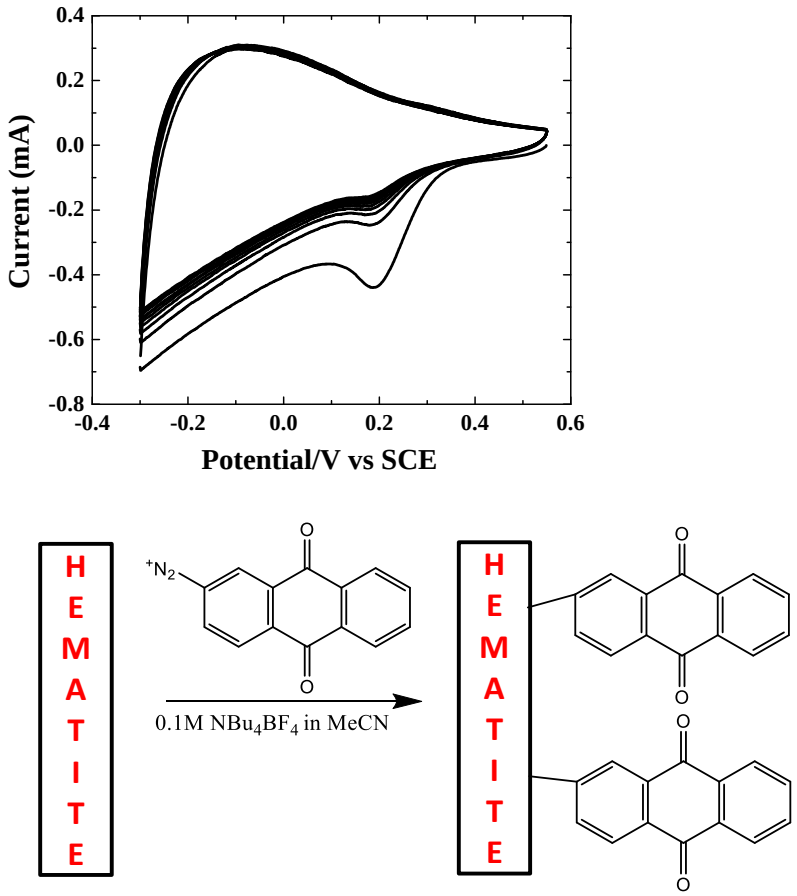


Figure 17. Electrografting of AQ on hematite. Cyclic voltammogram with limited potential range recorded during redox electrografting to immobilize anthraquinone moiety on hematite using 100mV/sec scan rate for 10 cycles in 2mM diazonium anthraquinone salt (AQD) in 0.1M Bu_4NBF_4 / CH_3CN.

In order to ascertain the covalent anchoring of AQ on hematite, as typically, the AQ immobilized hematite sample is used to record the cyclic voltammogram in supporting electrolyte in the absence of AQ salt. As **figure 18** indicates, the peaks corresponding to AQ are clearly visible and the peaks are present nearly at the constant potential of around -1.2 Vvs SCE. Moreover, the peak current at -1.2 Vvs SCE varies linearly with increase of scan rate. Based on literature[110], these redox peaks are attributed to the conversion of AQ to AQH_2 as showed in **figure 18.** These results confirm that the AQ moieties are covalently attached on the surface of hematite, not just physisorbed. If they are physisorbed instead of immobilization, then during characterization in supporting electrolyte the peak potentials will be usually at different potentials and don't show the linear variation of peak current with scan rate increment.

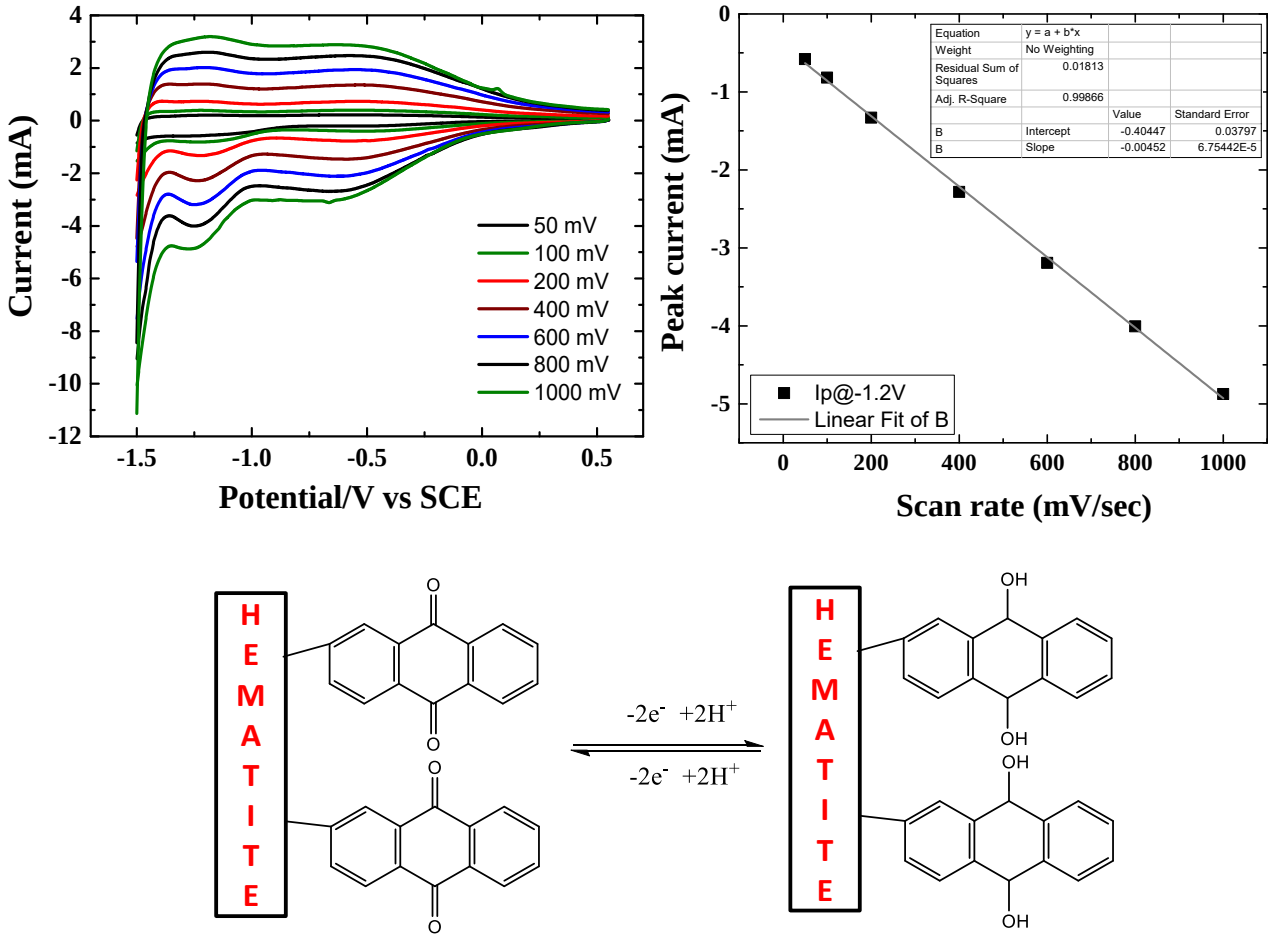


Figure 18. Characterization of immobilized AQ. The cyclic voltammograms recorded at different scan rates by using AQ immobilized hematite in 0.1M Bu_4NBF_4 / CH_3CN shows a constant peak potential at -1.2V vs SCE that clearly shows the successful anchoring of AQ moieties on hematite surface. Linear variation of peak current(at -1.2V vs SCE) with increment of scan rate gives further support to electrografting. The redox peak is due to the conversion of quinone to hydroquinone involving two proton – two electron process.

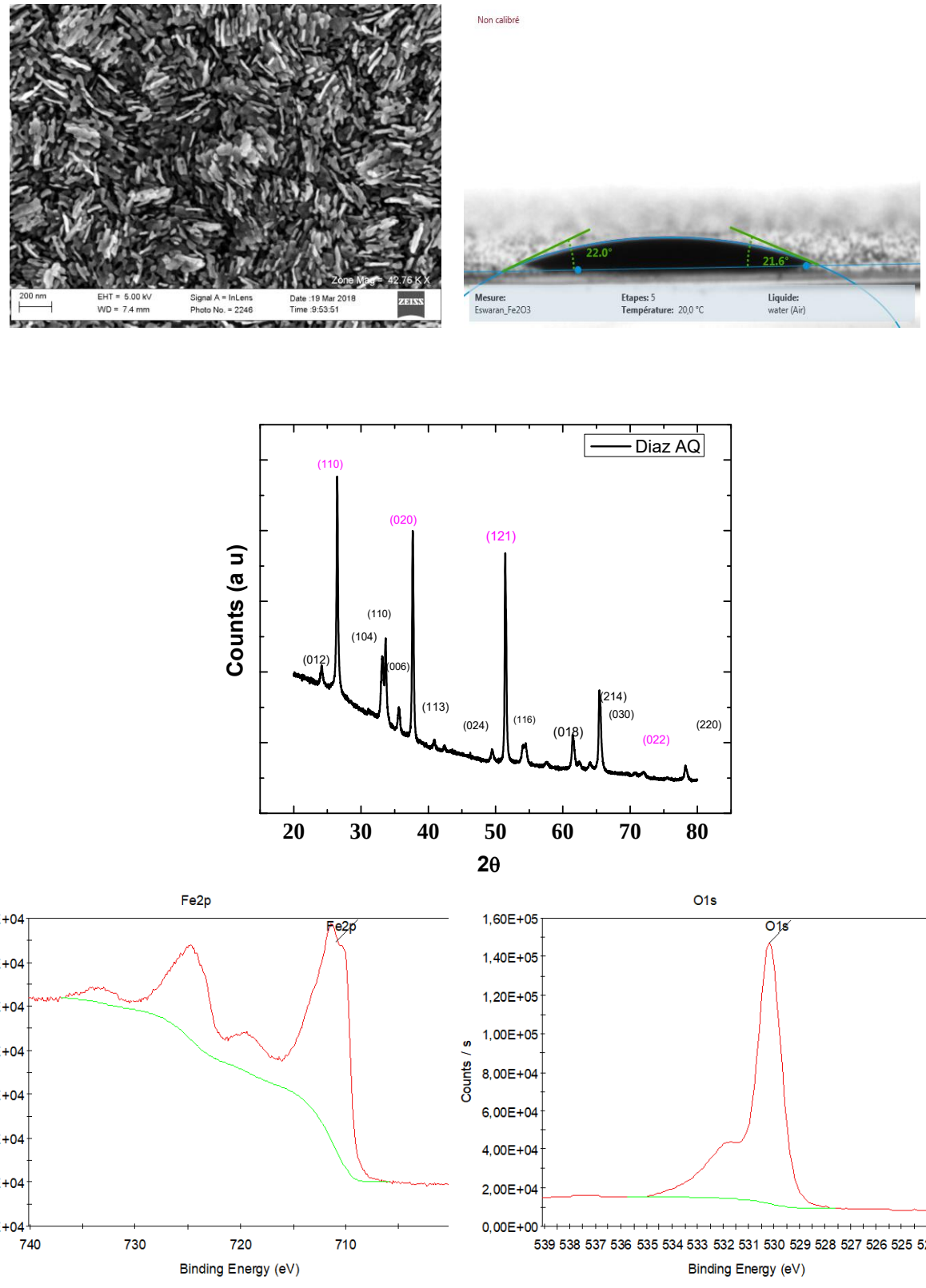


Figure 19. Surface characterization of diazonium AQ modified hematite surface by SEM, contact angle measurement, XRD and XPS.

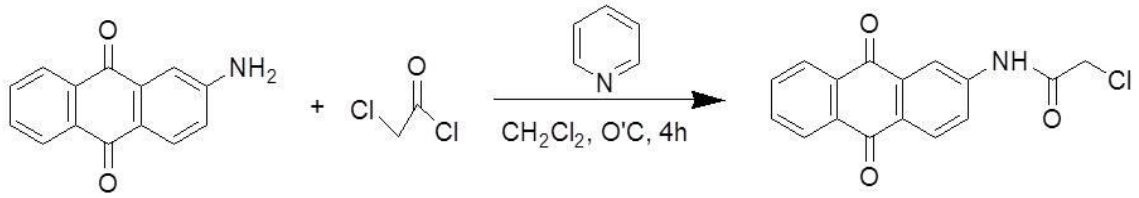
From the SEM image, it is clear that the immobilization of AQ by diazonium electrografting process did not change the nanostructured morphology of hematite. This image looks akin to bare hematite that proves the AQ layer is very thin. This is further confirmed by the contact angle that shows a little variation (22°) compared to bare hematite (21.4°). Also the XRD spectrum shows the features corresponding to only hematite phase. This is further supported by the XP spectra of Fe_{2p} and O_{1s}.

3.8.3. Hematite Surface Modified with poly-vinyl Anthraquinone Ionic Liquid:

The catalytic anthraquinone (AQ) moieties are immobilized on the surface of hematite by using electrografting method leads to the formation of thin monolayer and in order to increase the amount of surface anthraquinone further, the redox active poly ionic liquid with anthraquinone moiety has been used and that can be covalently attached on the hematite surface by using Surface Initiated Atom Transfer Radical Polymerization (SI-ATRP) method. This will form AQ polymer brushes on the hematite surface and hence better catalytic property can be expected. The synthesis of electroactive AQ monomer ionic liquid is discussed below:

3.8.3.1. Synthesis of Monomer N-ethyleneamidoanthraquinone -N-vinylimidazolium bis(trifluoromethylsulfonyl)imide:

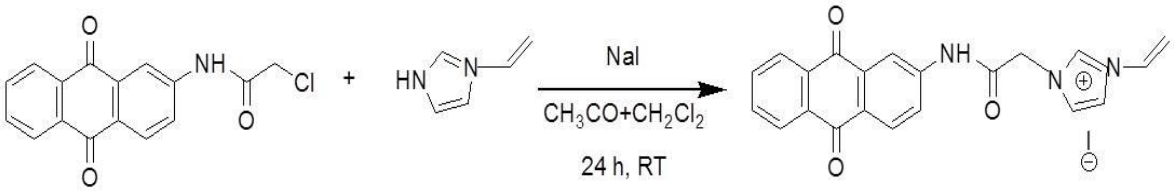
(i) Synthesis of Chloroethyleneamidoanthraquinone :



At 0°C, in argon atmosphere, 2-aminoanthraquinone (1g, 4.5 mmol), pyridine (0.5 ml, 6.2 mmol) and 100 ml of dichloromethane were mixed and stirred. To this, solution of chloro acetyl chloride (0.4 ml, 5.4 mmol) in 30 ml dichloromethane was added dropwise. After 4 hour stirring, the solution was filtered and extracted with 3M HCl followed by with saturated NaCl solution. The resulting organic solution was dried over $MgSO_4$. After evaporating the solvent, the crude product is formed as a brown residue which was recrystallized by dissolved in dichloromethane and then slow addition of hexane which yields a solution with two distinct phases. Filter this solution, purified product will be retained as a precipitate, dried it under vacuum.

Brown crystalline solid: Yield: 22.24%, 0.34 g

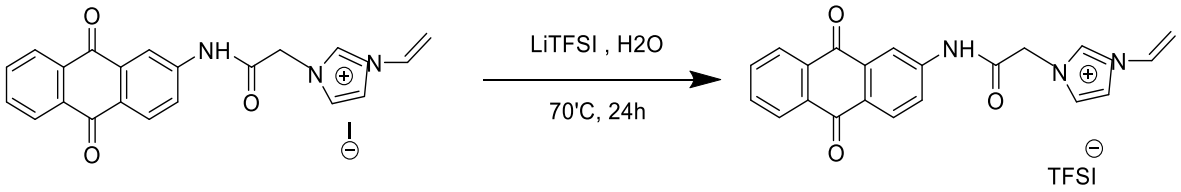
(ii) Synthesis of N-ethyleneamidoanthraquinone-N-vinyl imidazolium iodide



At first, 1-vinyl imidazole (0.09g, 0.8 mmol) and sodium iodide (0.14g, 1mmol) were dissolved in equal amounts of acetone and dichloromethane, next chloro ethyleneamidoanthraquinone (0.26g, 0.8 mmol) was added to this solution. The mixture was stirred for 24 hours at room temperature. Then the precipitate was filtered and washed with distilled water. This crude product was purified with dichloromethane and hexane to obtain brown powder.

Yield – 90% , 0.23 g

(iii) Synthesis of N-ethyleneamidoanthraquinone-N-vinyl imidazolium TFSI

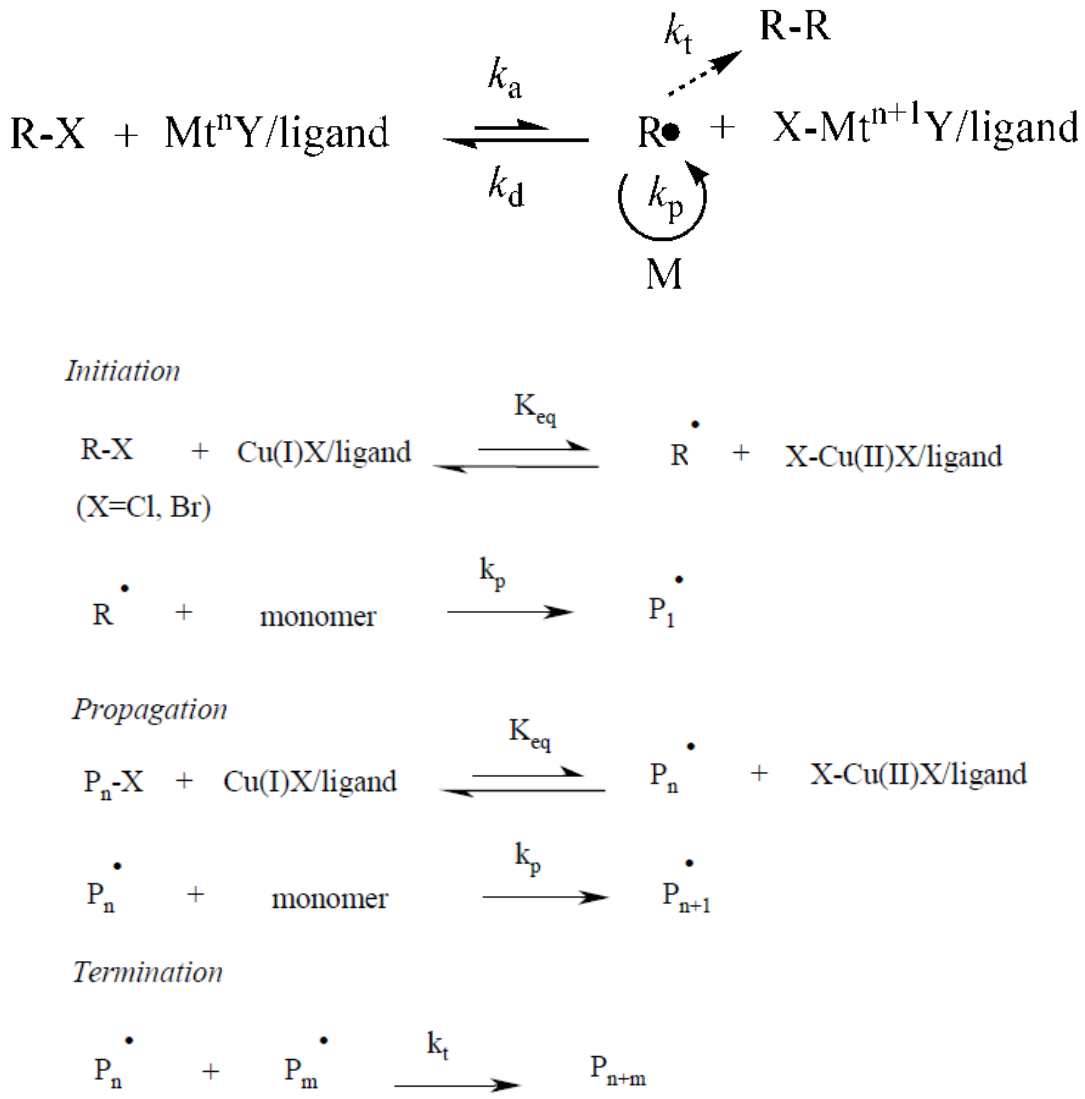


This is the ion-exchange step involves N-ethyleneamidoanthraquinone-N- imidazolium iodide (0.23 g, 0.5 mmol, 1 equiv) dissolved in solution of lithium bis(trifluoromethylsulfonyl) imide (1.98g, 6.9 mmol, 1.22 equiv) in 20 ml of dissolved water. Then the reaction mixture is refluxed for 24 hours at 70°C. Two different phases are formed and the organic phase is separated out from the aqueous phase by dichloromethane. After that, the dichloromethane was evaporated by rotavapor and the resulting ionic liquid is kept under vacuum for 24 hours.
Yield : 84%, 0.193 g.

3.8.3.1.1. Surface Initiated Atom Transfer Radical Polymerization (SI-ATRP) : A brief note:

In 1995, Matyjszewski[111] and Sawamoto[112] groups independently reported a new kind of controlled living radical polymerization method which is widely known as atom transfer radical polymerization (ATRP) that later revolutionized the synthesis of polymers with well-

controlled designs and functionalities. The following **scheme 5** depicts the general mechanism of ATRP process.



Scheme 5. General mechanism behind ATRP process by taking copper as a catalyst.

As shown in the above scheme, in ATRP, there will be a dynamic equilibrium between the alkyl halide (R─X) and the corresponding alkyl radical ($R^{\bullet}$) along with a transition metal complex. To maintain the radical concentration at a minimum level, the equilibrium shift towards the dormant species so that the radical termination reaction will be suppressed and provide control over the polymer architecture and molecular weight. However, it is impossible to avoid the termination completely in ATRP and the termination enhance the deactivator (i.e. X-Mt^{n+1}Y/ligand) concentration, and as a result, the equilibrium move towards the dormant speies and hence the radical concentration will be suppressed, thus the polymerization itself is a self regulating and this effect is called as persistent radical effect

(PRE)[113]. To support this point, by using electron paramagnetic resonance (EPR), it is proved[114] that during polymerization the deactivator concentration increases to 5─10% compared to the activator concentration at the beginning. Thus in general to gain control over the ATRP process, normally 10% deactivator (compared to activator concentration) is added to the reaction mixture to shift the equilibrium towards the dormant species.

Initiator:

Since the initiator is responsible for the polymer growth, the initiator concentration governs the molecular weight of the resulting polymer[115]. Alkyl halides (RX) are generally used as initiators and also it is proved that tertiary alkyl halides are performing as better initiators than the secondary alkyl halides which are better than the primary halides. The initiators should not undergo any side reactions. Care must be given to factors such as steric, polar and redox properties, prior to choosing an initiator. However, the simple rule is that R group should be similar in initiator and the monomer[116]. For instance, to polymerize styrene, (1-bromoethyl)benzene is generally used[117] ; ethyl 2-bromoisobutyrate and ethyl 2-bromopropionate are usually used for polymerizing meth(acrylates)[116] ; 2-bromopropionitrile can be employed for the polymerization of acrylonitiles[118]. Few examples of initiators are given in **Figure 20**. Apart from bromide, chloride and iodine based initiators are also used[119]. Because of the strong H─F bond that hinders the homolytic cleavage, fluorine can not be used as initiator for ATRP.

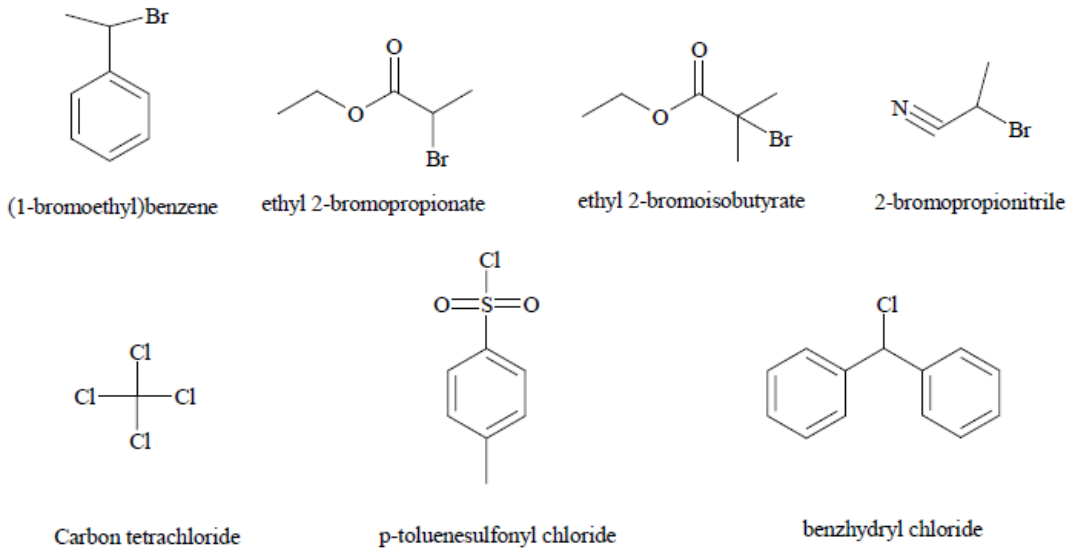


Figure 20. Some examples of initiators commonly used in ATRP process.

Transition Metal:

The main requirment for the metal is that it should exhibit an one electron redox behaviour and show higher attraction towards halogen and lower attraction towards hydrogen atom and alkyl radicals[116]. Several metals such as iron[120], ruthenium[121], nickel[122], molybdenum[123], rhenium[119c], rhodium[124] and palladium[125] have been reported. However, copper is commonly used because of its low cost and versatility[126].

Ligand:

The ligand plays important role in ATRP process. Firstly, in the organic reaction medium the metal is solubilized by the ligand. The ligand governs the selectivity by electronic and steric effects. It also affects redox property of the final metal complex. Generally, nitrogen based ligands are used to form a complex with copper. **Figure 21** shows some bidentate (4,4'-di-5-nonyl-2,2'-bipyridine, dNbpy and 2,2'-bipyridine, Bipy)[111], tridentate (pentamethyldiethylenetriamine, PMDETA)[127] and tetradentate (tris(2-(dimethylamino)ethyl)amine, Me_6-TREN)[128] ligands employed to form complex with copper in ATRP. Phosphine based ligands such as tributylphosphine or triphenylphosphine are commonly used to ligate with iron to form a complex[120a, 120b]. Other metals such as rhenium, ruthenium, palladium, nickel and rhodium are also ligating with phosphorous based ligands.

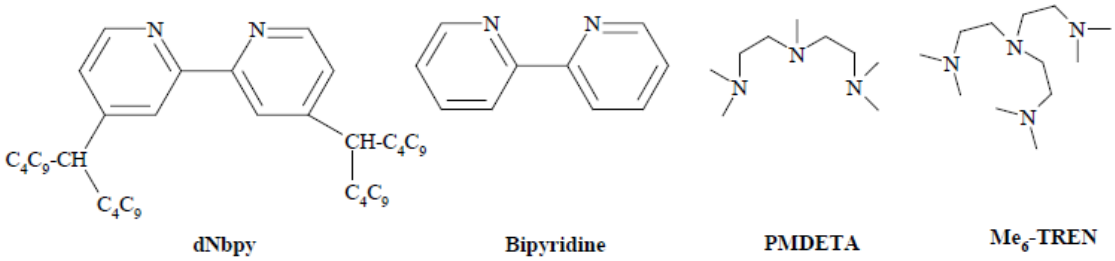


Figure 21. Commonly used nitrogen based ligands in ATRP.

3.8.4. Surface Modification of glassy carbon electrode (GCE) by SI-ATRP:

3.8.4.1. Initiation and polymerization:

Before doing SI-ATRP on hematite, it was performed on glassy carbon electrode (GCE) that was taken as a model system. Saturated calomel electrode was used as a reference electrode, metallic mesh as a counter electrode and GCE as a working electrode. Prior to polymerization, working electrode surface has to be terminated with initiator. As mentioned

earlier, this can be done by immobilizing the surface with alkyl halide. GCEs are terminated with bromide by means of oxidative electrografting by using 2-bromoethylamine. The aqueous solution of 5mM 2-bromoethylamine with 0.1M $LiClO_4$ was used as the electrolyte. Cyclic voltammetry was employed by cycling the potential between 0.5 to 1.6V vs SCE for 20 cycles and the voltammogram is given in **figure 22**.

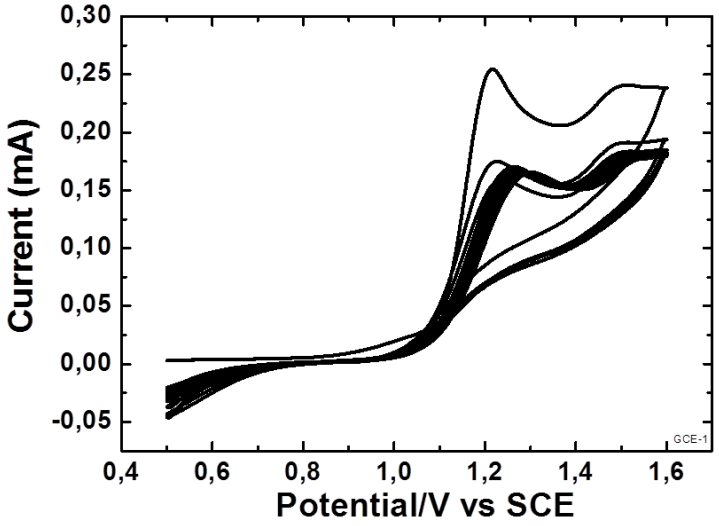
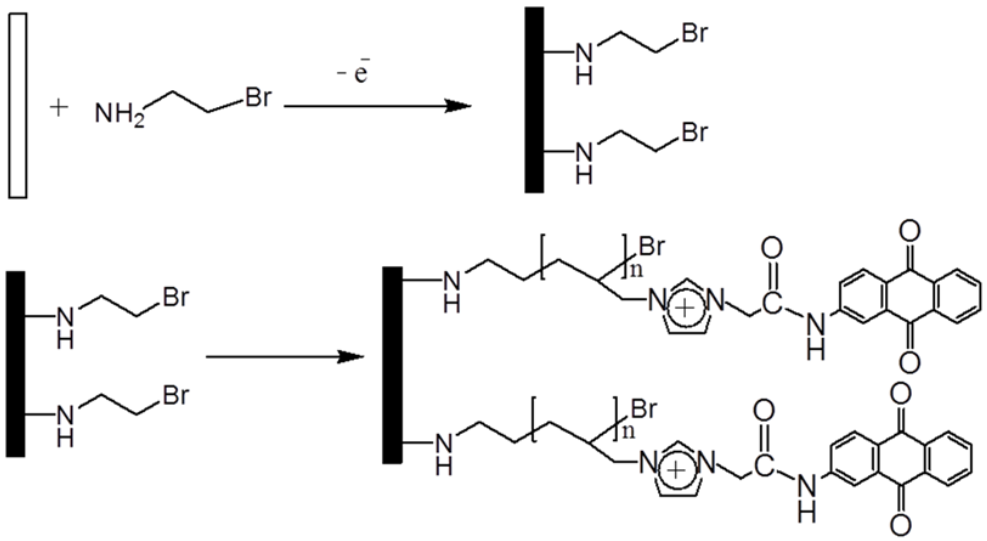


Figure 22. CV of oxidative electrografting of 2-bromoethylamine on GCE at a scan rate of 0.1V/sec.

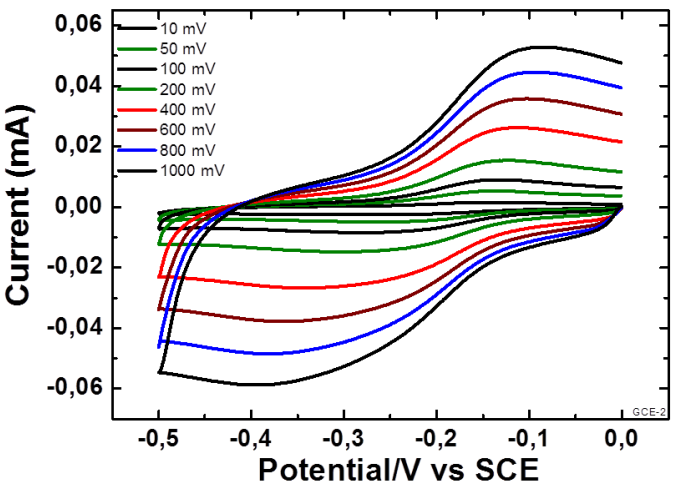
As seen in above figure, there is an irreversible oxidation peak at around 1.25V vs SCE. This peak corresponds to the oxidation of the amine group to form aminyl radical that immediately reacts with the surface and forming a thin layer, and thats why the peak current decreases with the increase of cycle numbers[129]. The bromine terminated GCE was washed well with acetonitrile. Then for polymerization, the initiator terminated GCE was taken into acetonitrile solution containing 2 mM of the AQ monomer, the complexing agent – PMDETA (1.2µL), the catalyst – Cu(I)Cl (4 µM), the deactivator Cu(II)Cl (1.4µM) under Argon atmosphere at 50°C for 2 h.

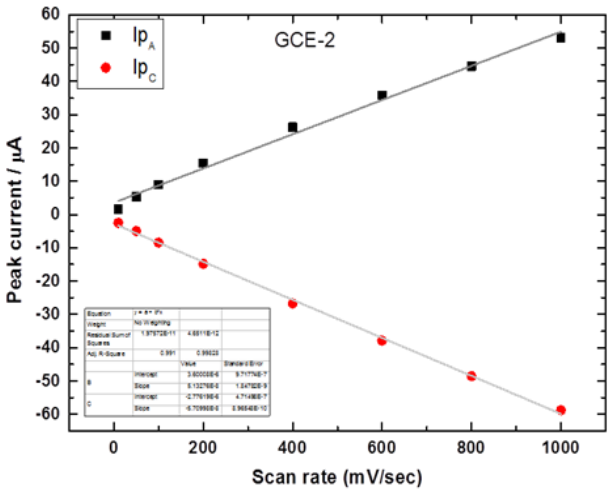
Scheme 6. Top scheme indicates the covalent attachment of initiator by means of oxidative electrografting, Bottom scheme shows imidazolium based ionic liquid with anthraquinone redox moiety polymerization using ATRP in acetonitrile medium.



3.8.4.2. Characterization of immobilized AQ moieties:

In order to confirm the anchoring of AQ on GCE, as typically, the immobilized sample is checked in supporting electrolyte in the absence of AQ salt in 0.1M H_2SO_4. As **figure 23** indicates, the peaks corresponding to AQ are clearly visible and the redox peaks are present nearly at the constant potential even at various scan rates corresponding to the two proton – two electron process. Moreover, the peak current at -0.35 Vvs SCE varies linearly with increase of scan rate. These results confirm that the AQ moieties are anchored on the surface of GCE, not just adsorbed. If they are adsorbed instead of immobilization, then during characterization in supporting electrolyte the peak potentials will be usually at different potentials and don't show the linear variation of peak current with scan rate increment.





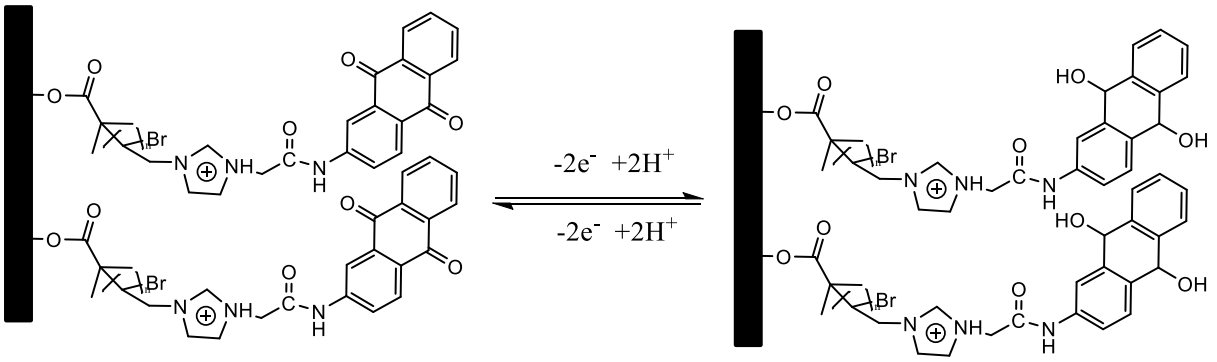


Figure 23. (a) Characterization of modified GCE in aq.solution of 0.1M H_2SO_4 at different scan rates clearly shows the redox peaks corresponding to attached AQ moieties. (b) The peak currents vary linearly with scan rates indicating that the AQ moieties are attached to the electrode surface. (c) two electron/two proton transfer of quinone-hydroquinone redox couple.

3.8.5. Surface Modification of Hematite by SI-ATRP:

3.8.5.1. Initiation process on hematite:

Similar to GCE, in a similar way, prior to ATRP - initiation process was also performed on hematite samples by means of oxidative electrografting by using 2-bromoethylamine. The aqueous solution of 5mM 2-bromoethylamine with 0.1M $LiClO_4$ was used as the electrolyte. Cyclic voltammetry was used by cycling the potential between 0.5 to 1.6V vs SCE for 20 cycles. As seen in **Figure 24**, there is no irreversible oxidation peak at around 1.25V vs SCE which corresponds to the oxidation of the amine group to form aminyl radical. There is no electrochemical evidence of oxidative electrografting occurred on hematite samples. In this potential window, the hematite sample is quite stable, there is no remarkable change has been observed on the hematite surface. It seems that the initiation has not occurred on the hematite surface and it is confirmed by the fact that the cyclic voltammograms recorded in blank solution (aqueous solution contains only 0.1M $LiClO_4$) and for bromine termination (aqueous solution contains 5mM 2-bromoethylamine with 0.1M $LiClO_4$) look almost similar, the increase of current around 1.2V may be attributed to the oxygen evolution of hematite.

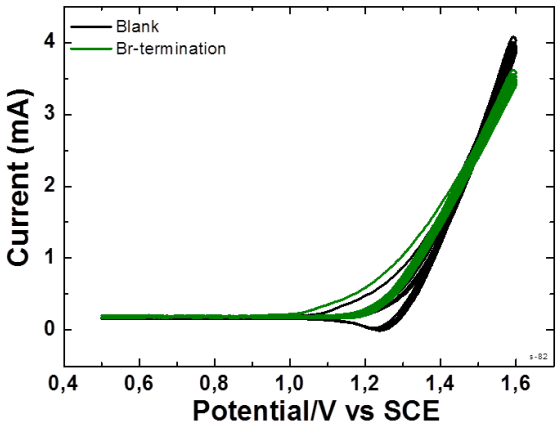
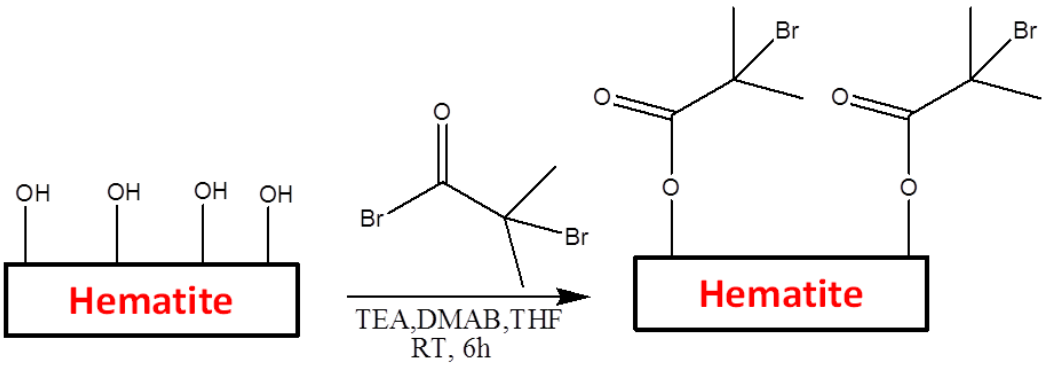


Figure 24. Cyclic voltammograms of oxidative electrografting of 2-bromoethylamine on hematite at a scan rate of 0.1V/sec(green colour) and blank. No electrochemical evidence corresponding to oxidative electrografting process indicates that the surface is not terminated with bromine.

3.8.5.2. Bromine termination by exploiting the surface hydroxyl groups :

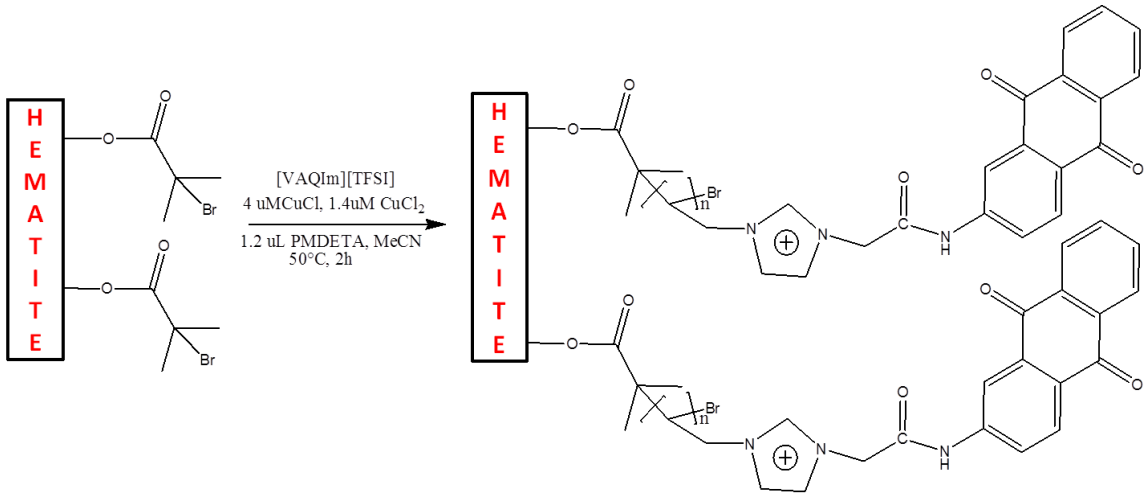
To immobilize the initiator, another approach[130] has been adopted. Prior to the immobilization of the initiator, the hematite samples were washed well with distilled water, acetonitrile followed by THF (tetrahydrofuran). The available hydroxyl groups on the surface were converted into bromide groups by immersing the hematite samples in a THF solution containing α-bromoisobuturyl bromide (BiB) (305 mg, 1.33 mmol), trimethylamine (TEA) (1.48 mg, 1.46 mmol) and small amount of DMAP (dimethylamino pyridine) (10 mg) for 4 hours at room temperature. Then the hematite samples were washed with distilled water, acetonitrile followed by THF.



Scheme 7. Schematic representation of alkyl bromide termination on hematite surface by exploiting the available hydroxyl groups on the surface

3.8.5.3. SI-ATRP of AQ & characterization:

For polymerization, the initiator terminated hematite samples were taken into acetonitrile solution containing 2 mM of the AQ monomer [VAQIm][TFSI], the complexing agent – PMDETA (1.2µL), the catalyst – Cu(I)Cl (4 µM), the deactivator Cu(II)Cl (1.4µM) under Argon atmosphere at 50°C for 2 h. After SI-ATRP, the sample is washed well with acetonitrile and water.



Scheme 8. Illustration of immobilization process of imidazolium based ionic liquid containing redox active anthraquinone moiety on the hematite photoanode by ATRP method.

After the immobilization of [VAQIm][TFSI] on hematite surface, to confirm the attachment of redox active ionic liquid, the cyclic voltammograms were recorded at different scan rates in bare supporting electrolyte – 0.1M NBu_4BF_4 in CH_3CN, by using surface modified hematite as working electrode, stainless steel mesh as a counter electrode and saturated calomel electrode as a reference. The corresponding cyclic voltammograms are given in **figure 25** that shows the typical redox peaks of AQ to AQH2 conversion. The linear variation of peak current with respect to scan rate is the direct evidence of the covalent attachment of antraquinone ionic liquid on the hematite surface.

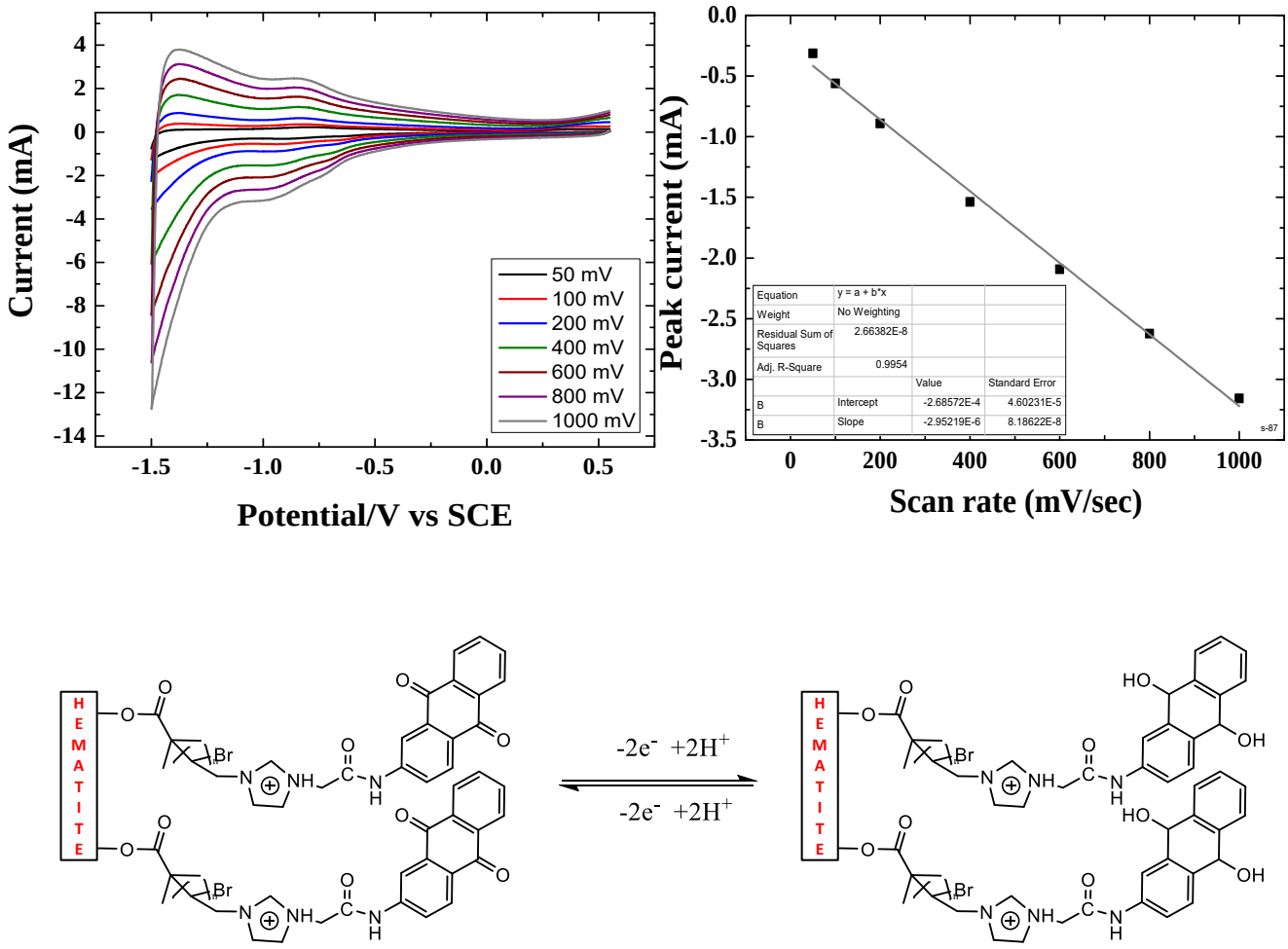


Figure 25. (a) Characterization of modified hematite in non-aq.solution of 0.1M NBu_4BF_4 at different scan rates clearly shows the redox peaks corresponding to attached AQ moieties. (b) The peak currents vary monotonically with scan rates indicating that the AQ moieties are attached to the electrode surface.

From the surface characterization by SEM and AFM, it displays the rough surface with nanostructured morphology. The immobilization AQ PIL impacts the contact angle very much (11.5°) compared to bare (21.4°) and diazonium AQ (22°) modified surface. The contact value is almost halved supports the surface functionalization by polymer brushes of AQ PIL. From XRD and XPS, the hematite phase is confirmed.

Surface characterization of AQ ionic liquid immobilized hematite:

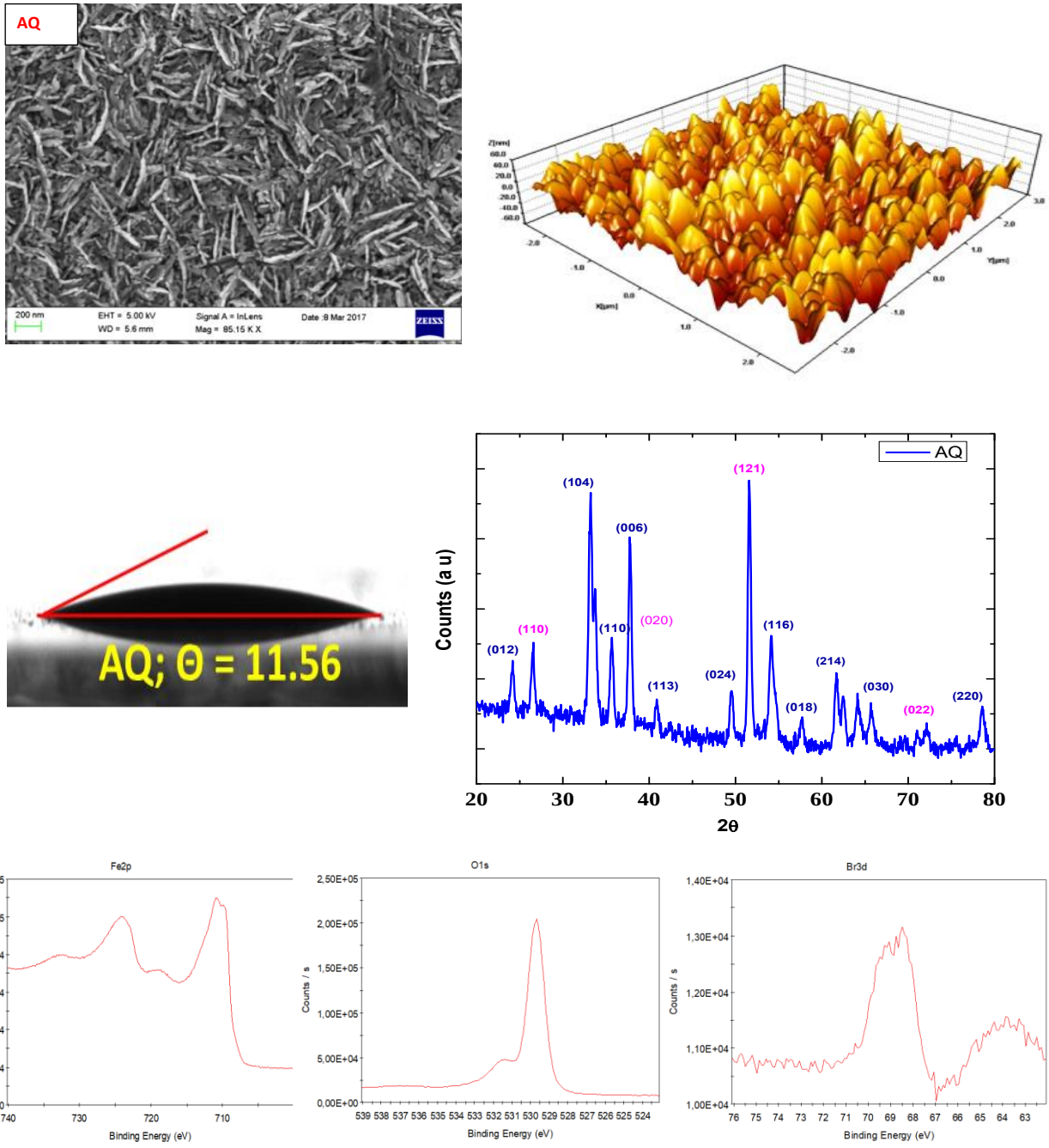


Figure 26. Surface analyses show the retention of nanostructured morphology of hematite photoanode even after the immobilization of AQ PIL brushes. The contact angle value is almost halved with respect to that of bare hematite displays the surface modification. XRD and XPS suggest the existence of hematite phase.

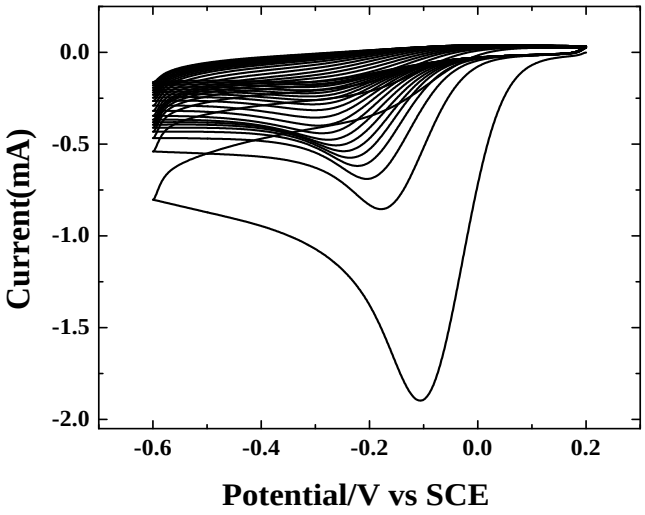
3.8.6. Surface Modification of Hematite by SI-ATRP with aryl bromide initiator:

Bromine termination by using diazonium phenyl bromide through electrografting :

As mentioned earlier, alkyl bromide termination is highly preferable for SI-ATRP. From our previous experiments on electrografting of AQ on hematite, it is clear that hematite can be electrografted by using diazonium salts. So the plan is to check the role of aryl bromide as intiator for ATRP of AQ ionic liquid.

3.8.6.1. Initiation on hematite:

By means of reductive diazonium electrografting by using p-diazonium phenyl bromide, the hematite surface is modified with bromide. The aqueous solution of 5mM p-diazonium phenyl bromide with 0.1M NBu_4BF_4 is used as the electrolyte. Cyclic voltammogram was recorded by cycling the potential between 0.2 to -0.6V vs SCE for 20 cycles and the voltammogram is given in figure 27. The reductive peak around -0.1V vs SCE corresponds to the reduction of diazonium that leads to the removal of nitrogen and the covalent attachment of phenyl bromide on hematite and hence the peak current decreases further with the increase of cycle numbers.



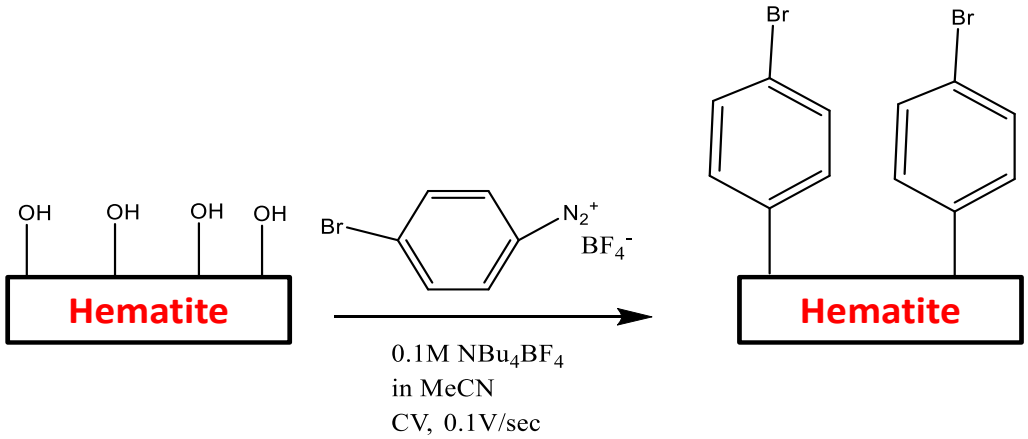
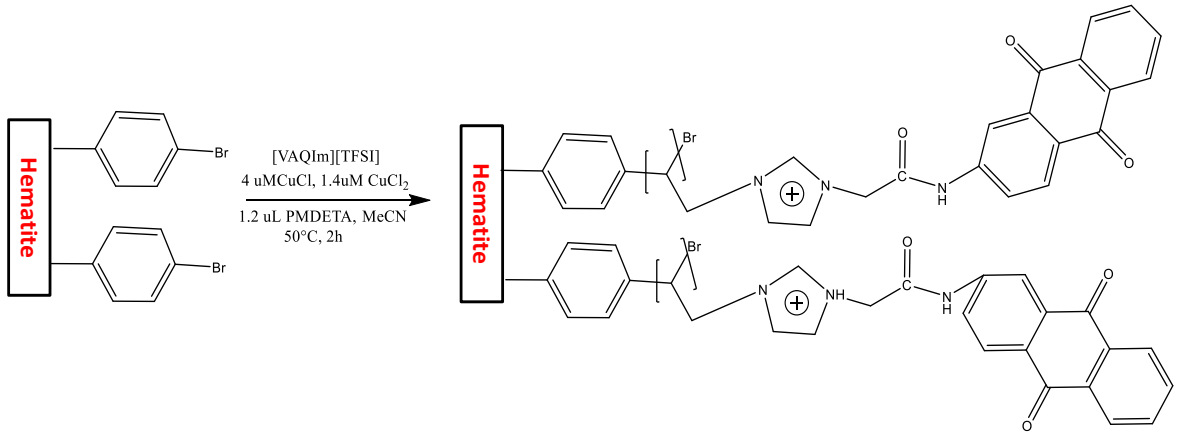


Figure 27. CV corresponding to reductive diazonium electrografting of phenyl bromide on hematite electrode. The peak around -0.1V corresponds to the reduction of diazonium during the first scan, this peak disappears and the current decreases during further scans indicate that there is a covalent attachment of bromide on the surface. Saturated calomel electrode was used as a reference electrode, metallic mesh as a counter electrode and hematite as working electrode, scan rate = 100 mV/sec.

3.8.6.2. SI-ATRP of AQ & characterization:

Then the same procedure was followed for polymerization, the alkyl bromide initiator terminated hematite sample was taken into acetonitrile solution containing 2 mM of the AQ monomer [VAQIm][TFSI], the complexing agent – PMDETA (1.2µL), the catalyst – Cu(I)Cl (4 µM), the deactivator Cu(II)Cl (1.4µM) under Argon atmosphere at 50°C for 2 h. After SI-ATRP, the sample is washed well with acetonitrile and water.



Scheme 9. Illustration of immobilization process of imidazolium based ionic liquid containing redox active anthraquinone moiety on the hematite photoanode by ATRP method.

After the immobilization of [VAQIm][TFSI] on hematite surface, to confirm the attachment of redox active ionic liquid, the cyclic voltammograms were recorded at different scan rates in bare supporting electrolyte – 0.1M NBu_4BF_4 in CH_3CN, by using surface modified hematite as working electrode, stainless steel mesh as a counter electrode and saturated calomel electrode as a reference. The corresponding cyclic voltammograms are given in **figure 28** that shows the typical redox peaks of AQ to AQH2 conversion. The linear variation of peak current with respect to scan rate is the direct evidence of the covalent attachment of antraquinone ionic liquid on the hematite surface.

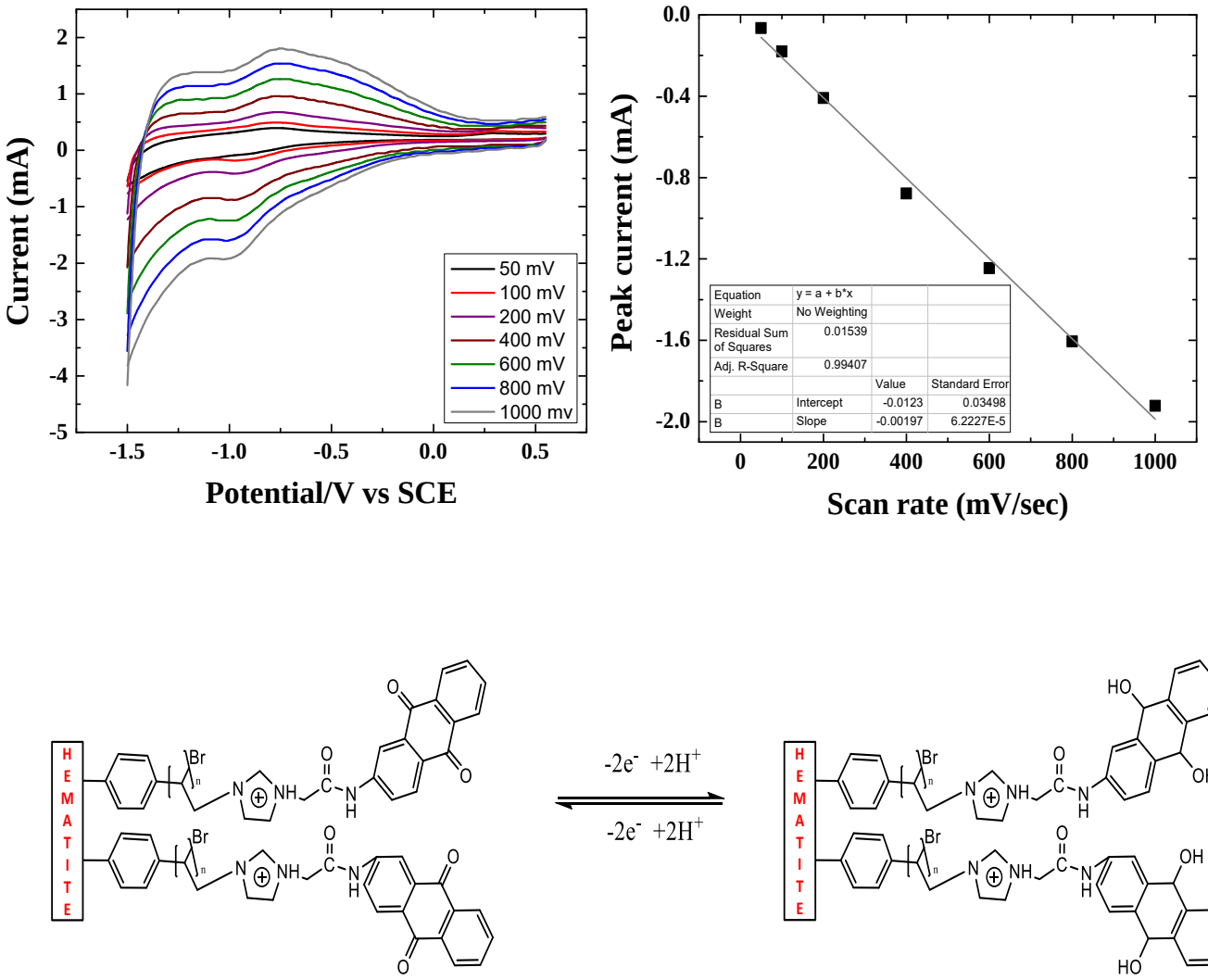
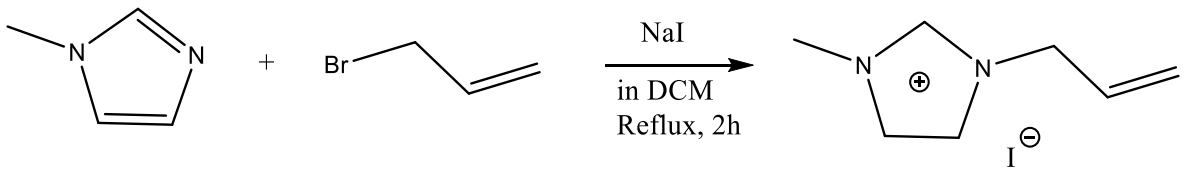
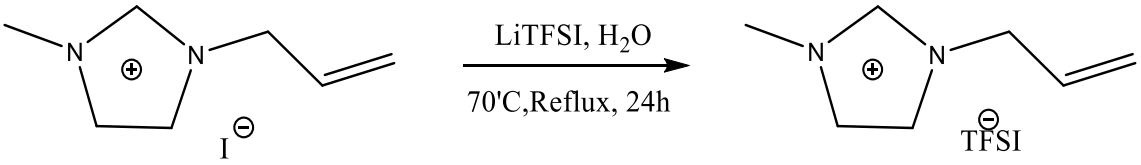


Figure 28. (a) Characterization of modified hematite in non-aq.solution of 0.1M NBu_4BF_4 at different scan rates clearly shows the redox peaks corresponding to attached AQ moieties. (b) The peak currents vary monotonically with scan rates indicating that the AQ moieties are attached to the electrode surface.

3.8.7. Surface Modification of Hematite by SI-ATRP with N-methyl-N`-vinylimidazolium bis(trifluoromethylsulfonyl)imide:

3.8.7.1.1. Synthesis of N-methyl-N`-vinylimidazolium bis(trifluoromethylsulfonyl)imide

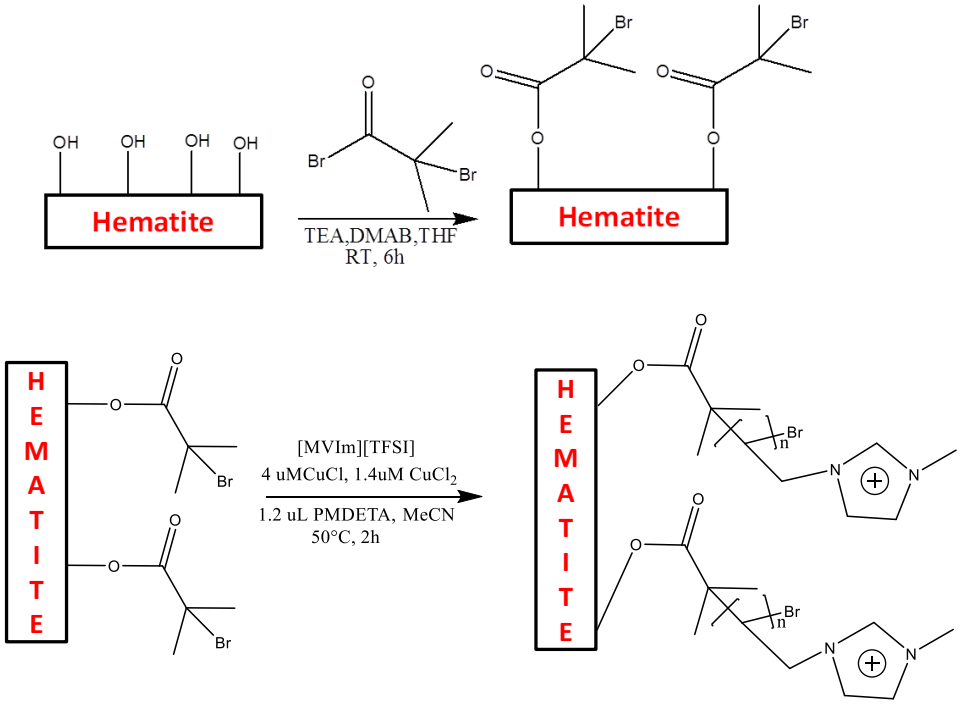




N-methyl-N`-vinylimidazolium bis(trifluoromethylsulfonyl)imide was synthetized as followed. Vinylimidazole (10 mmol) was dissolved in 20 ml of dichloromethane. Then allyl bromide (30 mmol) was added into the solution under vigorous stirring. The mixture was then refluxed for 2 hrs. Finally, the solvent and un-reacted allyl bromide was eliminated under reduced pressure and the product was dried under vacuum for 24 hrs giving 90% yield. For getting the final monomer, anion exchange step was performed by addition of 1.2 equiv. of LiTFSI in 20 ml distilled water into the intermediate product. The mixture was heated at 70°C during 24 hrs under vigorous stirring. The organic layer was then recovered and washed 3 times with 20 ml of distilled water, the water traces were eliminated with $MgSO_4$ followed by drying under vacuum overnight.

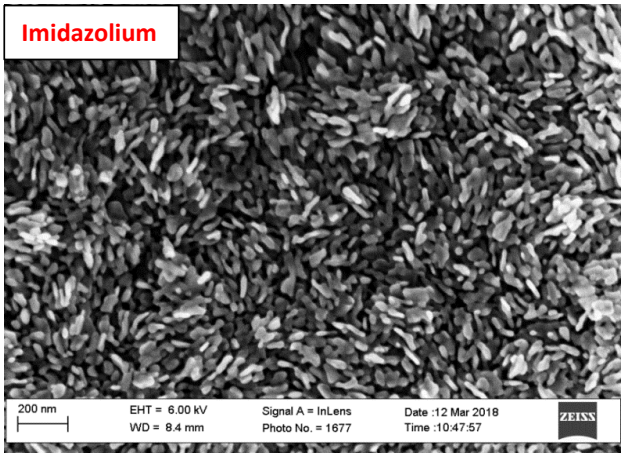
3.8.7.1.2. Immobilization of N-methyl-N`-vinylimidazolium bis(trifluoromethylsulfonyl)imide on hematite:

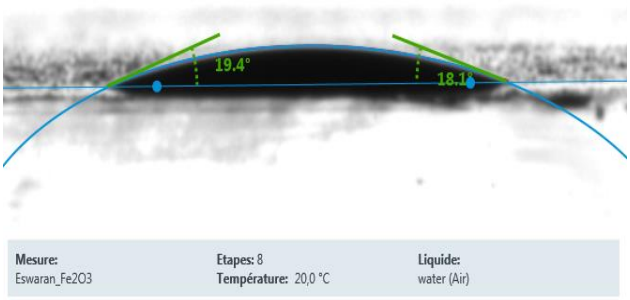
The same procedure described in section 3.8.5.2. and 3.8.5.3. was followed to anchor N-methyl-N`-vinylimidazolium bis(trifluoromethylsulfonyl)imide on hematite. By exploiting the surface hydroxyl groups on hematite, the bromide initiator was immobilized followed by the immobilization of ionic liquid by SI-ATRP process as schematically shown below:

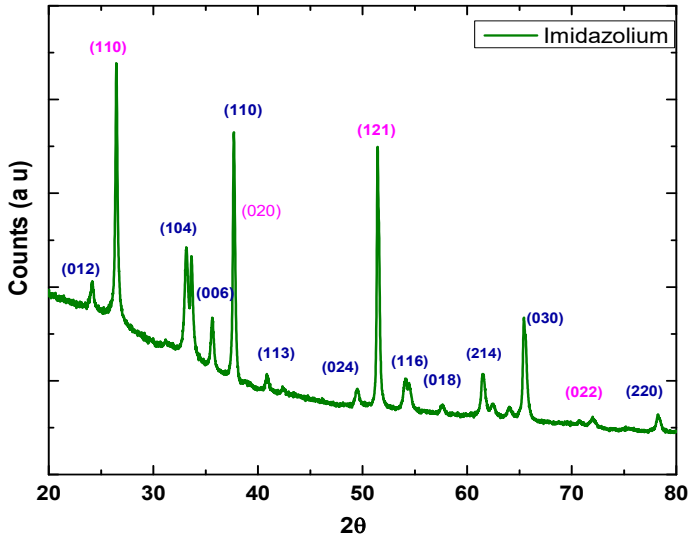


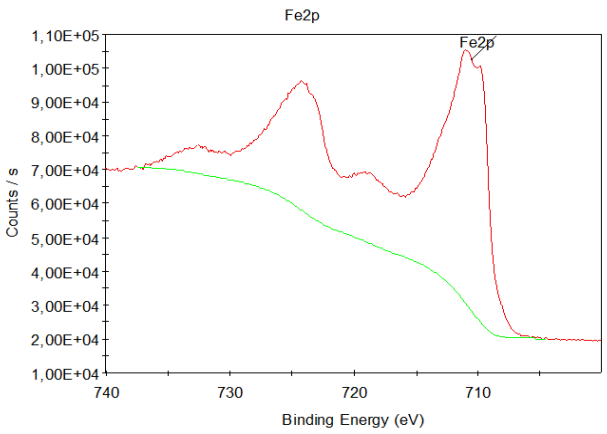
Scheme 10. Schematically showing the immobilization process of N-methyl-N`-vinylimidazolium bis(trifluoromethylsulfonyl)imide on hematite photoanode by ATRP method.

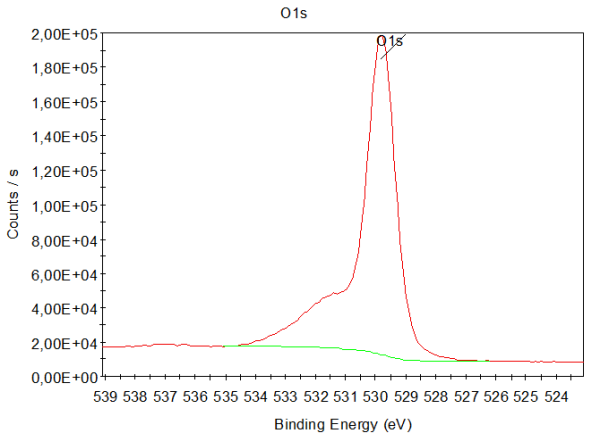
Surface characterization of vinyl imidazolium ionic liquid immobilized hematite:











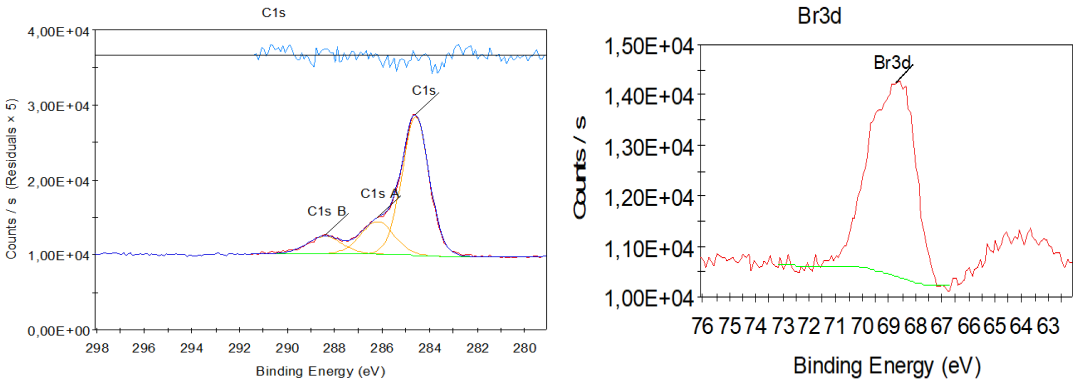


Figure 29. SEM image clearly shows the nanostructured morphology similar to bare hematite. The contact angle measurement gives the value of 19.4° that stays close to the unmodified hematite. XRD and XPS confirm the presence of α-Fe_2O_3. From XPS, the elements present in the imidazolium ionic liquid has been identified.

Different surface characterization methods like SEM, contact angle, XRD and XPS were employed to analyze the immobilization of N-methyl-N`-vinylimidazolium bis(trifluoromethylsulfonyl)imide on hematite photoanode. From SEM, the nanostructuration morphology of hematite obtained by anodic electrodeposition process can be clearly seen. The contact angle value (19.4°) is closer to bare hematite value (21.4°), but larger than AQ PIL modified hematite (11.6°). XRD and XPS confirm the presence of hematite phase and other elements available in the ionic liquid indicate the successful surface functionalization.

Conclusion:

Nanostructured hematite photoanodes were prepared by anodic electrodeposition process and surface functionalization with anthraquinone and imidazolium based poly ionic liquid with and without anthraquinone moieties was performed by diazonium electrografting process and surface initiated atom transfer radical polymerization process respectively. The surface modification of hematite was confirmed and analyzed by electrochemistry and various surface analyses such as SEM, AFM, Contact angle, XRD and XPS.

3.9. Photoelectrochemical Investigation:

3.9.1. Introduction:

In the previous section, fabrication of hematite photoanode and its surface modification with diazonium anthraquinone, bromide initiator and poly ionic liquids were shown. It is very important to understand the role of surface modification in photoelectrochemical water oxidation process and hence the main theme of this section is to examine the role of surface modification of hematite on photoelectrochemical water splitting. In literature[73] there is ambiguity over the role of surface modification whether the surface modifier enhances the water oxidation process by promoting the surface kinetics across the semiconductor – electrolyte interface as a catalyst or reducing the surface recombination by passivating the surface states as a non catalytic passivating layer.

The surface modifiers such as TiO_2[131], Al_2O_3[43], SiO_x[132] and Ga_2O_3[65] are not catalytically active but still promoting the photoeffect and this enhancement is unambiguously attributed to the surface state passivation. Whereas thin films of oxygen evolution reaction (OER) catalysts on semiconductors show enhanced photoeffect but whether the enhancement originated from accelerated surface reaction or suppression of surface recombination is mostly unclear. Durrant group by using Transient Absorption Spectroscropy (TAS) investigated CoO_x and Ga_2O_3 modified hematite photoanode, CoO_x used as an electrocatalyst and Ga_2O_3 as a surface passivation layer[71]. From TAS study, they proved that the CoO_x and Ga_2O_3 are not enhancing the water oxidation kinetics but retarding the electron – hole recombination and thereby promoting the water oxidation . By using Intensity Modulated Photocurrent Spectroscopy (IMPS), Peter group showed that treatment of hematite electrodes with cobalt solution suppressed the surface recombination but not accelerated the hole transfer[133]. Dunwei Wang group also used IMPS to examine the influence of $NiFeO_x$ overlayer on hematite and they found out that $NiFeO_x$ catalytic overlayer shows cathodic shift in onset potential bacause of the suppression of surface recombination rather than surface charge transfer promotion[73].

Also the oxygen evolution reaction (OER) is a slow process on hematite surface since it takes few seconds to take place[44] and the OER mechanism is still under investigation. Several pathways are suggested based on spectroelectrochemical studies such as electrochemical impedance spectroscopy (EIS)b[46, 45, 134], IMPS[133], infrared (IR) spectroscopy[48] and by TAS[44, 50] and the main conclusion from those studies are that some iron based intermediates are

involved which are trapping the holes and these intermediates are subsequently transferring them to the electrolyte. These surface states are initially regarded only as the recombination centers but now it is proved that these states are involved in charge transfer processes.

3.9.1.1. Aim of this part :

- To examine the influence and comparision of diazonium AQ and AQ poly ionic liquid
- To study the role of surface modification i.e., whether it enhances the charge transfer or suppresses the surface recombination
- To understand the mechanistic pathway of charge transfer process i.e., direct charge transfer or surface state mediated charge transfer.

3.10. IMPS & IS theory and our methodology:

The methods that are applicable to investigate the kinetics in metals cannot be applied to semiconductors, because the potential variation will reflect in Helmholtz layer for the metals whereas the variation of potential will change the space charge region in semiconductors and hence not possible to analyze the rate constants. But the intensity of light will affect the concentration of photogenerated holes, and hence the methods involving the perturbation of light intensity would be helpful to analyze the kinetics in semiconductors. IMPS is one of the light intensity perturbation methods.

If the light intensity is modulated with small amplitude, the photocurrent will be modulated at the same frequency, but the phase and magnitude will be generally different. The response of the modulated photocurrent comprises both the hole current and electron current and these can be plotted as a real and imaginary part of the photocurrent in a Nyquist plot as shown in **Fig.,30**. Surface recombination is dominated at low frequencies which gives a semicircle situated in the upper quadrand of the complex plane and is generally known as "recombination semicircle". When the frequency, ω_{max}, matches the relaxation constant of the system, the imaginary photocurrent attains a maximum.

$$\omega_{max} = k_{trans} + k_{rec} \qquad (27)$$

where, k_{trans} and k_{rec} are charge transfer and recombination rate constants respectively.

Owing to the fast modulation, the recombination is frozen at the high frequency intercept. According to Ponomarev and Peter[135], the intercept value corresponds to the product of the hole current (j_h) and capacitance factor [$C_H/(C_{SC} + C_H)$], where C_H is Helmholtz capacitance

and C_{SC} is space charge capacitance. The lower quadrand of the semicircle is interpreted as "RC attenuation semicircle" or RC time constant of the cell because it gives the attenuation by the total series resistance of the cell and the capacitance (both Helmholtz and space charge capacitance). The frequency at the minimum of the semicircle corresponds to the inverse of the product of the series resistance and capacitance of the cell, but usually the Helmholtz capacitance is neglected for the materials with considerable charge carrier density. Thus normalizing the photocurrent at high frequency intercept against hole current provides a value of capacitance factor $[C_H/(C_{SC} + C_H)] \approx 1$. provided $C_{SC} \ll C_H$.

$$\omega_{min} = (R_{series}C_{sc})^{-1} \tag{28}$$

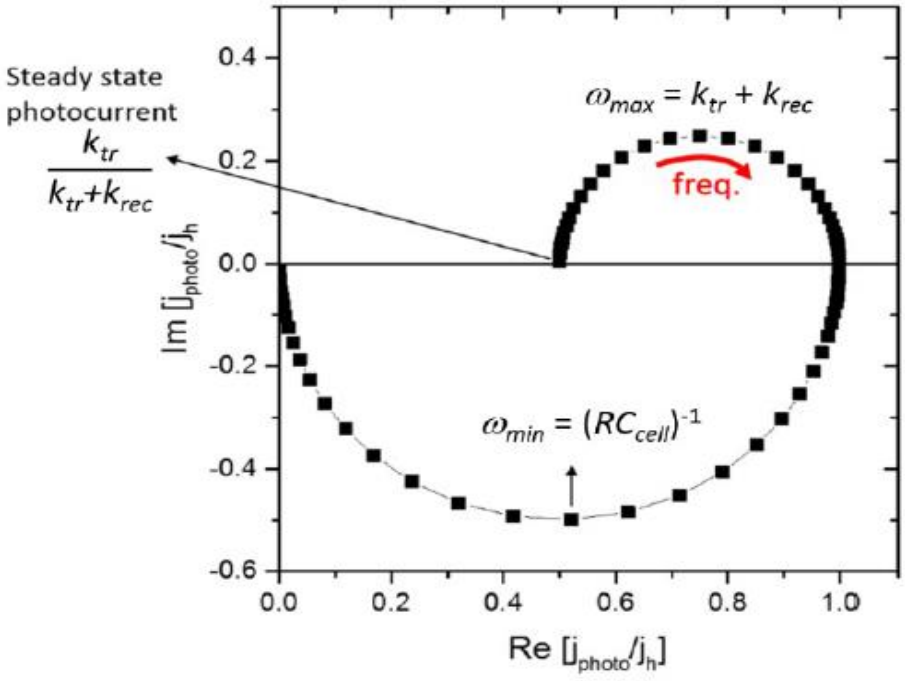


Figure 30. An example IMPS spectrum representing the recombination and attenuation semicircles in the upper and lower quadrands respectively. Charge transfer efficiency, rate constants of charge transfer and recombination, and cell capacitance can be obtained at different points of this spectrum[72].

The intersection of the semicircle at low frequency gives the charge transfer efficiency which is the ratio between the holes that come to the surface and that inject to the electrolyte.

$$\eta_{trans} = \frac{k_{trans}}{k_{trans} + k_{rec}} \tag{29}$$

This model is based on three important assumptions; first assumption is that the recombination and trapping in the bulk are neglected, because the bulk processes (typically <100 ns) are faster than the surface processes (typically 100 ms to 1 s). Secondly, the surface charge transfer and recombination process should happen on the same time scale as IMPS measurement. Finally, the band bending is not affected during the modulated illumination that means the space charge capacitance and the density of majority carriers should remain constant during the modulated illumination. Detailed theory about IMPS can be found in the literature[135-136]

Methodology:

Consider an example of IMP spectrum in Nyquist form and it has the shape as given below in **fig.31.,** The spectrum has real photocurrent in the X-axis and the corresponding imaginary part in the Y-axis.

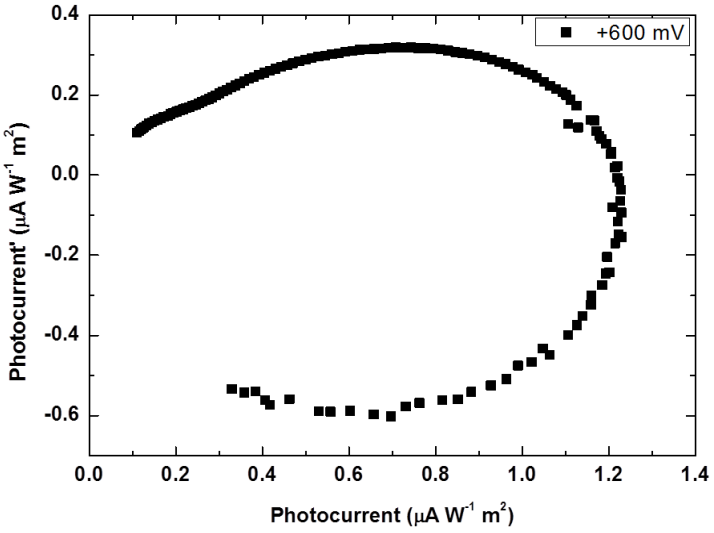


Figure 31. An example of IMP spectrum recorded at 600mV vs Ag/AgCl for bare hematite sample. This Nyquist plot contains real photocurrent in the X-axis and the corresponding imaginary photocurrent on the Y-axis.

Secondly, calculate the exact real photocurrent value at the high frequency intercept by using the formula, y = ax + b. Find the value of 'x' where 'y' becomes zero as shown below. The measured real current at high frequency intercept is = $1.2193e^{-6}$. In the next step, divide the real and imaginary photocurrents by the value of real current at high frequency and the resulting plot is known as normalized IMPS plot. From this plot, the initial value at the low

frequency give the transfer efficiency (η_{trans}) that is given as k_{trans} / (k_{trans} + k_{rec}). Where k_{trans} is hole transfer rate constant and k_{rec} is the recombination rate constant.

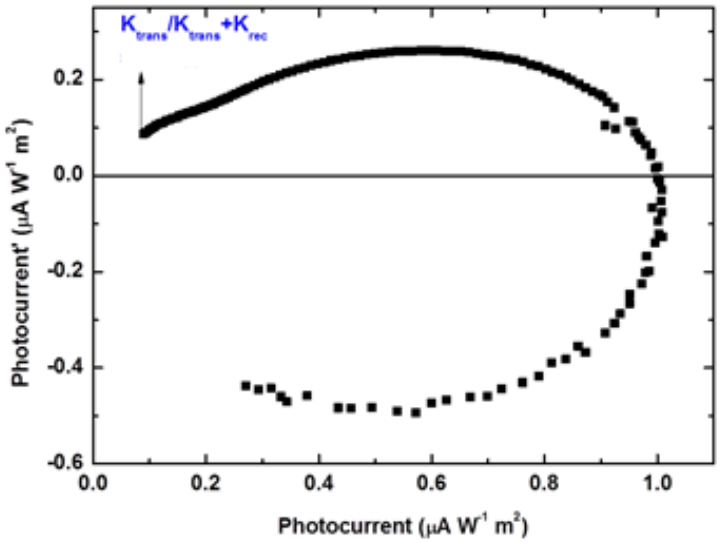


Figure 32. Normalized IMPS plot obtained by dividing the real photocurrent measured at high frequency intercept. The initial value at low frequency of this normalized plot yield the value of η_{trans}.

In order to calculate the value of maximum frequency (F_{max} or ω_{max}), the imaginary photocurrent is plotted against the log of frequency that gives the value of frequency values at maximum(F_{max}) and minimum (F_{min} or ω_{min}) values. F_{max} is where the imaginary photocurrent is maximum and F_{min} is where the imaginary photocurrent becomes minimum.

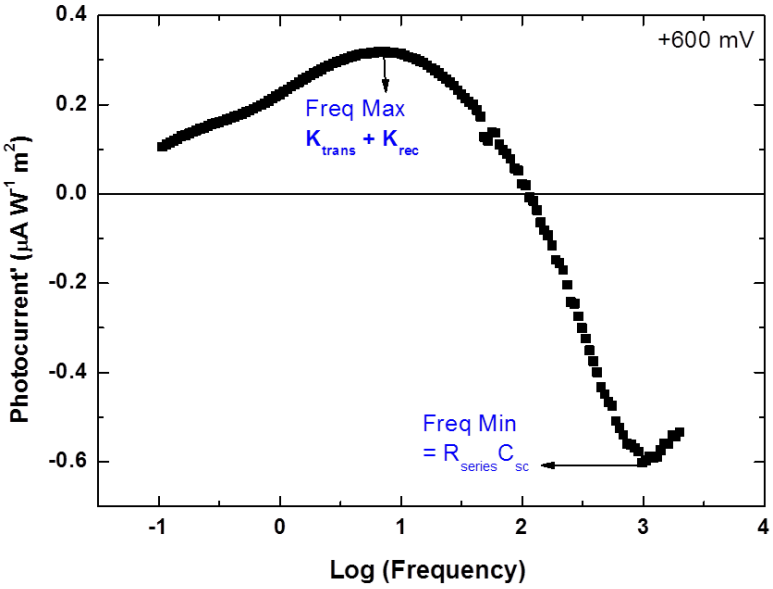


Figure 33. Plot of imaginary photocurrent vs Log(frequency) to calculate the value of F_{max} and F_{min}.

F_{max} gives the value of k_{trans} + k_{rec}. and from F_{min} , RC attenuation can be calculated but it is not of interest in this part of work. From η_{trans} and F_{max}, the charge transfer and recombination rate constants can be obtained as given below:

$$\eta_{trans} = \frac{k_{trans}}{k_{trans} + k_{rec}}$$

$$F_{max} = k_{trans} + k_{rec} \quad (30)$$

From equations (29) & (30), calculate the value of k_{trans}. If k_{trans} value is known, then from equation (30), the value of k_{rec} can be calculated.

Impedance Spectroscopy:

In general, impedance spectroscopy (IS) gives the electrical response of the sample interms of resistances and capacitances. IS comprises the measurement of ac electrical current I(ω) or ac voltage V(ω) at a certain angular frequency ω. Thus the impedance, Z(ω), is given as:

$$Z(\omega) = \frac{V(\omega)}{I(\omega)} \quad (31)$$

To maintain Z(ω) is independent of the amplitude of the perturbation, small sinusoidal ac perturbation is applied in such a way that I(ω) is linear with respect to V(ω), or vice-versa. The relationship between the input and output is generally known as transfer function. At each point of frequency variation, we obtain corresponding impedance and the spectrum usually consists of some features like arcs. The careful interpretation of these features provides the information regarding the kinetic and charge storage properties of the investigating system. To analyze the complex plane impedance plots, relevant equivalent circuits must be used to extract the resistances and capacitances that give information about charge accumulation, recombination and charge transfer. The resistances are related with carrier flux whereas the capacitances are associated with charge storage mechanism and the capacitances are classified into dielectric and chemical capacitances. Dielectric capacitance is due to the internal electric field developed by space charge separation whereas the chemical capacitance is associated with the variation of chemical potential, or carrier concentration. By fitting the impedance spectra measured at different voltages with a single equivalent circuit, the corresponding capacitances and resistances are obtained at different voltages.

3.11. Photoelectrochemical characterization details :

3.11.1. ***Photoelectrochemical (PEC) characterization setup:*** Photoelectrochemical measurements were performed at room temperature utilizing a commercially available Zahner Zennium CIMPS-2 system (Zahner Elektrik GmbH), which combines a potentiostat, a monochromatic light source and a PECC-2 cell. Area of the illuminated electrode was 0.785 cm^2 and area for dark curve calculation was 3.14 cm^2. The PEC cell setup consists of three electrode arrangement with a Ag/AgCl in 3M KCl reference electrode and a platinum coil counter electrode with 0.1 M NaOH aqueous solution. The samples were illuminated from the backside. All potentials were corrected to the reversible hydrogen electrode (RHE) according to the following equation: $E_{RHE} = E_{Ag/AgCl} + E^{\circ}_{Ag/AgCl} + 0.0059\ pH$

3.11.2. ***Linear sweep (LSV) and Chopped light voltammetry:*** The LSVs were recorded with different light intensities at a scan rate of 1 mV/sec. For the chopped light voltammetry, the light intensity used was 100 W/m^2 at a scan rate of 10 mV/sec, and the light on-off for every 2 seconds. The wavelength used was 455 nm for both the experiments.

3.11.3. ***IMPS measurements:*** IMPS measurements were performed in 0.1M NaOH solution by using bare and surface modified hematite photoanodes for the potential range of 0.876V to 1.626V vs RHE at a frequency range of 0.1 Hz to 2000 Hz. IMPS was performed by modulating the intensity of the light with amplitude of 10 mV, the intensity of the light source was 225W/m^2 with the wavelength of 455 nm.

3.11.4. ***Impedance measurements:*** Impedance experiments in presence of light(PEIS) and in dark(EIS) were performed in 0.1M NaOH solution by using bare and surface modified hematite photoanodes for the potential range of 0.876V to 1.626V vs RHE at a frequency range of 0.01Hz to 50000 Hz. IS was performed by modulating the amplitude of 10 mV, the intensity of the light source was 100W/m^2 with the wavelength of 455 nm.

3.12. Influence of Diazonium AQ on hematite photoelectrochemistry :

3.12.1. In non-aqueous medium:

The photoactivity of hematite photoanode prepared by anodic electrodeposition process was assessed by recording chopped light voltammogram in 0.1M $LiClO_4$ dissolved in CH_3CN solution containing 1mM ferrocene based redox couples as shown in **Fig.,34.** The main advantage of chopped light voltammogram is that it gives information about light and dark curves in a same voltammogram and also provides information regarding recombination process.

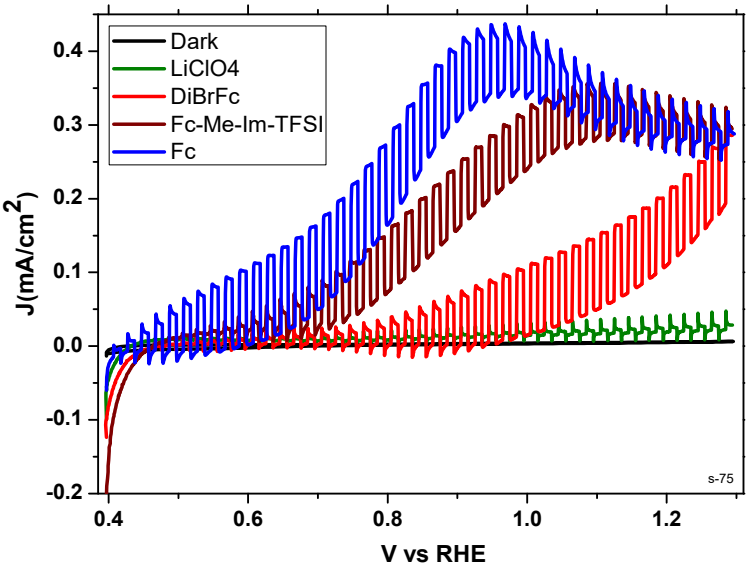


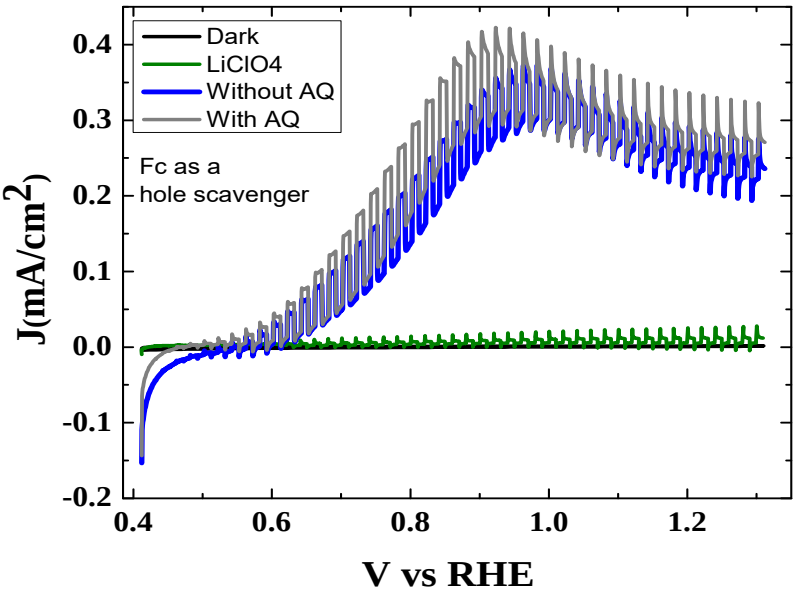
Figure 34. Chopped light voltammograms of hematite photoanode recorded in ferrocene based redox molecules dissolved in 0.1M $LiClO_4$ in CH_3CN. The dark linear sweep voltammetry curve measured in 0.1M $LiClO_4$ in CH_3CN (black). The light intensity was 100 W/m^2, and the wavelength used was 455 nm, light on-off for every 2 seconds. Scan rate = 10 mV/sec for all the experiments. The illuminated area used for the calculation is 0.785 cm^2 and for that of dark curve is 3.14 cm^2.

As clearly seen in this figure 34, since there is no charge carrier generation in dark, there is no current in the dark curve measured in 0.1M $LiClO_4$ in CH_3CN (black colour), however at illumination which creates charge carriers and as a result there will be photo induced chemical reactions and thus there is a small magnitude of photocurrent (green colour). The photocurrent is greatly enhanced with the addition of ferrocene based redox molecule in solution. Three ferrocene based molecules namely, ferrocene, dibromoferrocene and ferrocene methyl imidazolium TFSI ionic liquid are used as redox molecules. Among them, minimum photocurrent is observed in the case of dibromoferrocene and maximum photocurrent is given

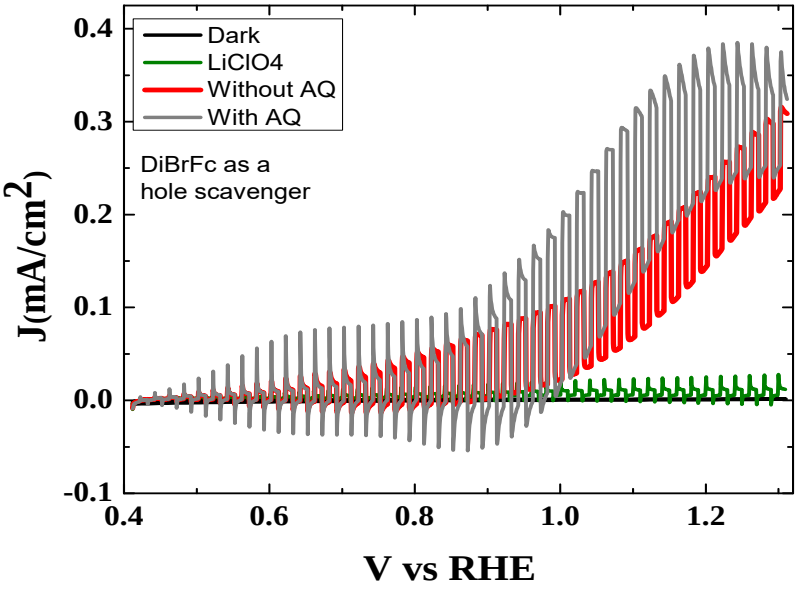
by ferrocene, the photocurrent for ferrocene methyl imidazolium TFSI ionic liquid lies in the medium range. This is attributed to the formal potential of the molecules. The formal potential of these molecules can be given as: Formal potential[Ferrocene < ferrocene methyl imidazolium TFSI < Dibromoferrocene], since ferrocene has lower formal potential than the other two molecules, it shows higher photocurrent because its redox potential value lies closer to the valence band so that holes can easily oxidize ferrocene to ferrocenium ion. In the case of dibromoferrocene, the formal potential is higher and hence the redox potential is far from the valence band thus the holes cannot relatively oxidize easily resulting out the lower photocurrent. For ferrocene methyl imidazolium TFSI ionic liquid, the formal potential is in the middle range, so the photocurrent also is in the medium range.

The impact of AQ immobilized by diazonium electrografting process is shown in Figure 35., The chopped light voltammograms recorded for AQ modified hematite shows the enhancement in photocurrent. Here also the trend follows the same manner as discussed above based on the formal potential of the hole scavengers, i.e., formal potential[Ferrocene < ferrocene methyl imidazolium TFSI < Dibromoferrocene]. The hole scavenger with lowest formal potential gives higher current and the same above discussion can be applied here.

A)



B)



C)

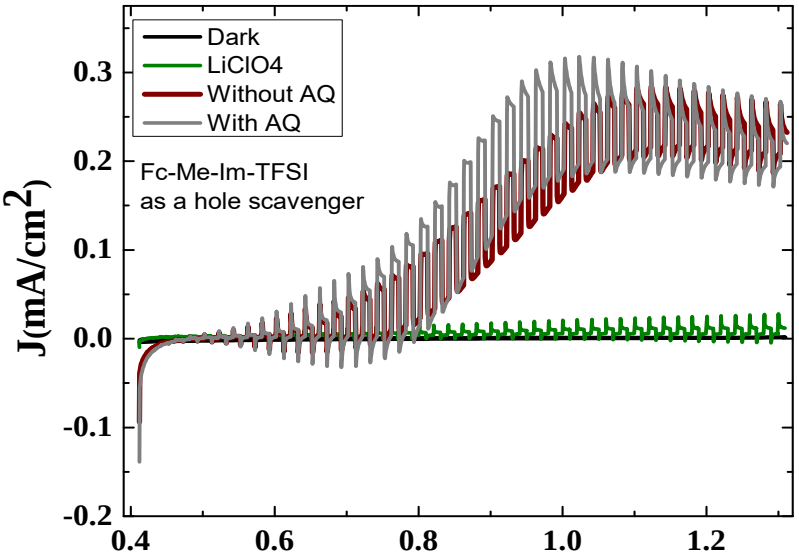


Figure 35. Influence of AQ layer on PEC properties of hematite in non-aqueous medium. (A) Ferrocene as a hole scavenger. Chopped light voltammograms of n-Fe_2O_3 in 0.1M $LiClO_4$ in CH_3CN(green) & 1 mM Fc + 0.1M $LiClO_4$ in CH_3CN (blue colour) and the dark LSV curve measured in 0.1M $LiClO_4$ in CH_3CN (black); Chopped light voltammograms of n-Fe_2O_3 immobilized with AQ in 1 mM Fc + 0.1M $LiClO_4$ in CH_3CN (grey colour) **(B) Dibromoferrocene as a hole scavenger.** Chopped light voltammograms of n-Fe_2O_3 in 0.1M $LiClO_4$ in CH_3CN(green) & 1 mM DiBrFc + 0.1M $LiClO_4$ in CH_3CN (red colour) and the dark LSV curve measured in 0.1M $LiClO_4$ in CH_3CN (black); Chopped light voltammograms of n-Fe_2O_3 immobilized with AQ in 1 mM DiBrFc + 0.1M $LiClO_4$ in CH_3CN (grey colour) **(C) Ferrocene methyl imidazolium TFSI ionic liquid as a hole scavenger in solution.** Chopped light voltammograms of n-Fe_2O_3 in 0.1M $LiClO_4$ in CH_3CN(green) & 1 mM Fc-Me-Im-TFSI + 0.1M $LiClO_4$ in CH_3CN (brown colour) and the dark LSV curve measured in 0.1M $LiClO_4$ in CH_3CN (black); Chopped light voltammograms of n-Fe_2O_3 immobilized with AQ in 1 mM Fc-Me-Im-TFSI + 0.1M $LiClO_4$ in CH_3CN (grey colour). The

enhancement of photocurrent with AQ-modified surface than that of unmodified surface is clearly observed. The light intensity was 100 W/m^2, and the wavelength used was 455 nm, light on-off for every 2 seconds. Scan rate = 10 mV/sec for all the experiments. Area of the illuminated electrode is 0.785 cm^2 and area for dark curve calculation is 3.14 cm^2

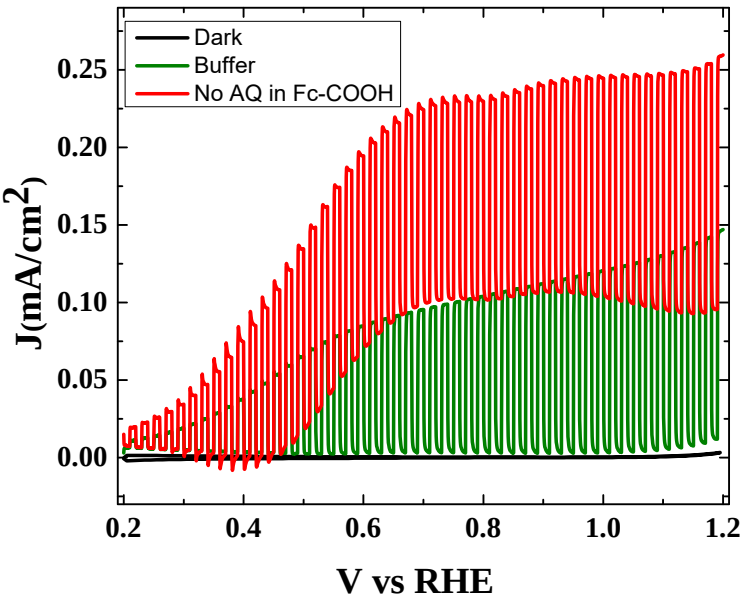
3.12.2. In aqueous medium:

The hematite samples are characterized photoelectrochemically before and after anthraquinone electrografting by using 1mM ferrocene carboxylic acid as hole scavenger in aqueous citrate buffer solution. These samples are characterized in bare aqueous pH-5.5 citrate buffer solution. The light intensity used was 100 W/m^2, and the wavelength used was 455 nm, light on-off for every 2 seconds. Scan rate = 10 mV/sec for all the experiments. Area of the illuminated electrode is 0.785 cm^2 and area for dark curve calculation is 3.14 cm^2.

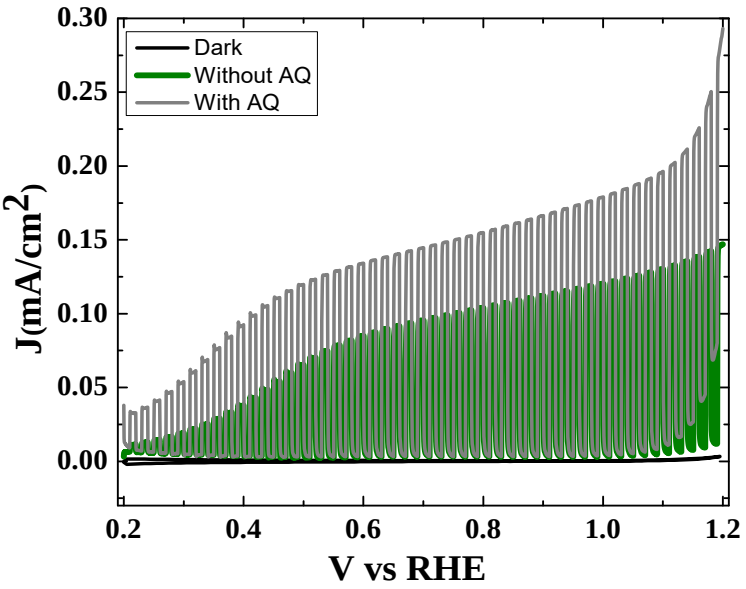
As shown in **fig.,36.** since in dark condition, there will be no charge carriers and hence there is no photocurrent as given by black curves. But while illumination, the AQ immobilized hematite sample is showing higher photocurrent compared to the bare hematite sample in ferrocene carboxylic acid solution which acts as a hole scavenger and also in bare citrate buffer solution. As given in Fig.36.b, the photocurrent of bare hematite sample in bare citrate solution at 1.2V vs RHE is around 0.15 mA/cm^2 whereas the AQ modified hematite sample shows 0.30 mA/cm^2 at that same potential. This photocurrent is due to the hole oxidation of water as per the following equation:

$$2H_2O + 4h^+ \rightarrow 4H^+ + O_2\uparrow \quad \text{(Working electrode)}$$

(A)



(B)



(C)

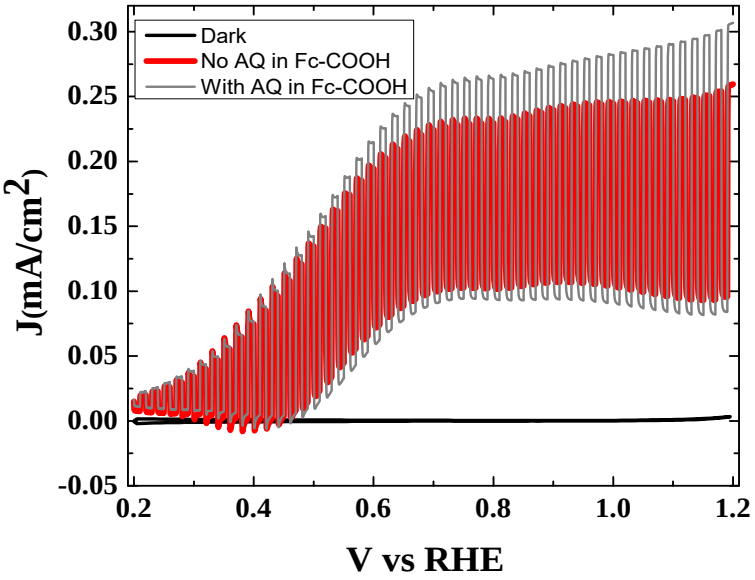
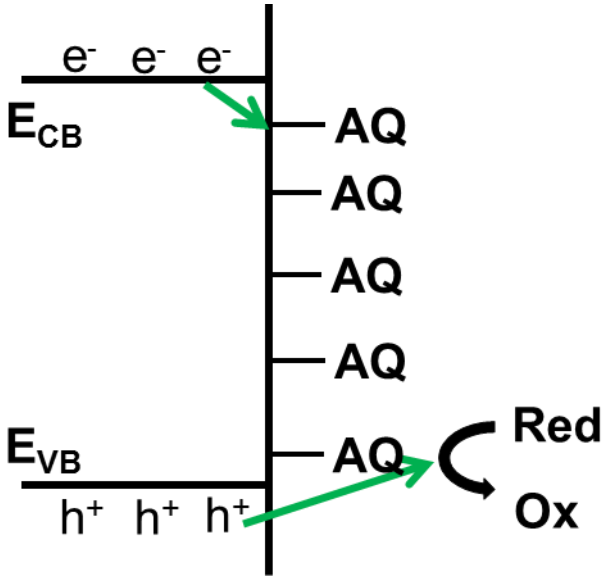


Figure 36. **Influence of AQ layer on PEC properties in aqueous solution. (A)Without AQ moieties on surface.** Chopped light voltammograms of n-Fe_2O_3 in aq.pH-5.5 citrate buffer(green) & in 1 mM Fc-COOH in pH-5.5 citrate buffer (Red) and the dark curve measured in pH-5.5 citrate buffer (black) **(B)Without hole scavenger in solution.** Chopped light voltammograms of n-Fe_2O_3 in aq.pH-5.5 citrate buffer – without AQ electrografting (green) & with AQ electrografting (Grey) and the dark curve measured in pH-5.5 citrate buffer (black) **(C) With hole scavenger in solution** Chopped light voltammograms of n-Fe_2O_3 in aq.pH-5.5 citrate buffer with 1 mM Fc-COOH in pH-5.5 citrate buffer – before AQ electrografting (Red), & – after AQ electrografting (Grey) and the dark curve measured in pH-5.5 citrate buffer (black) . The enhancement of photocurrent with AQ-modified surface

than that of unmodified surface is clearly observed. The light intensity was 100 W/m^2, and the wavelength used was 455 nm, light on-off for every 2 seconds. Scan rate = 10 mV/sec for all the experiments. Area of the illuminated electrode is 0.785 cm^2 and area for dark curve calculation is 3.14 cm^2

The reason for the enhancement of photocurrent is due to the fact that the immobilized AQ layers act as electron scavenger that attracts the electrons from the conduction band and prevents the holes from recombination. This process helps to increase the population and life-time of holes which move to the interface and do oxidation at faster kinetics and hence the photocurrent is higher. This process is schematically explained in the following scheme 11. Moreover, the AQ-modified hematite surface exhibit more stability and reproducibility in aqueous citrate buffer solution compared to non-aqueous acetonitrile solution. This point is highly desirable in the context of photoelectrochemical actuator that has to function in aqueous medium..

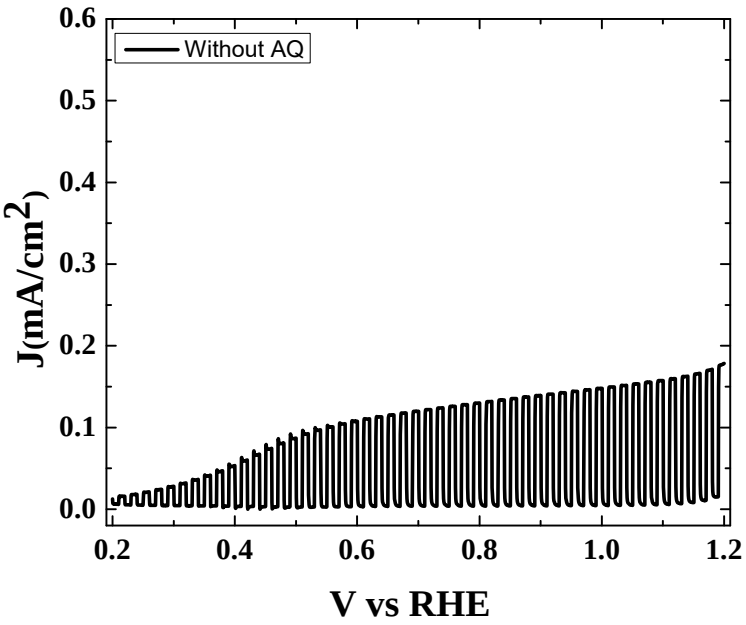


Scheme 11. The electrografted AQ layers prevent charge recombination at the surface by acting as electron scavenger and thus increasing the photocurrent.

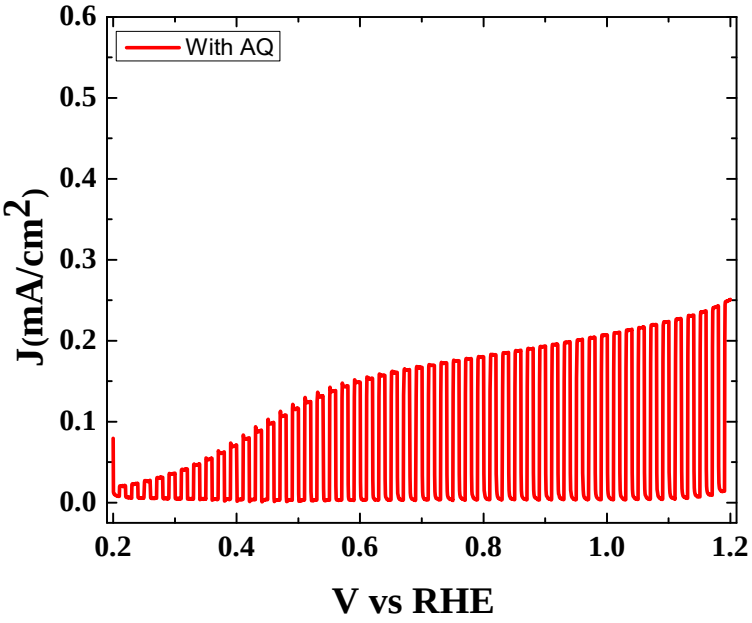
3.13. Diazonium AQ vs ATRP AQ – A comparision :

As shown earlier, the surface of hematite was funtionalized with two kinds of AQ moieties, firstly with the AQ immobilization by reductive diazonium electrografting (Diaz-AQ) and the other one is immobilized with the imidazolium based poly ionic liquid with AQ group by SI-ATRP process (ATRP-AQ). In the previous section, we have clearly witnessed the enhancement of photocurrent by Diaz AQ groups. To compare the influence of ATRP AQ, chopped light voltammograms of unmodified and surface functionalized hematite photoanodes were recorded in pH-5.5 citrate buffer and the results are given below:

(A)


Without AQ
J(mA/cm2)
V vs RHE

(B)


With AQ
J(mA/cm2)
V vs RHE

(C)

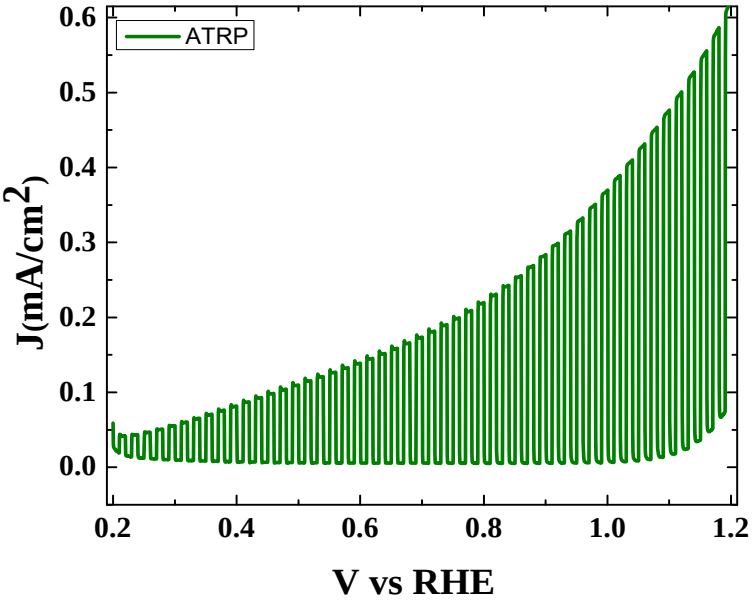

ATRP
J(mA/cm2)
V vs RHE

Figure 37. **Influence of Diaz and ATRP AQ layer on PEC properties of hematite in aqueous solution. (A) Without AQ moieties on surface.** Chopped light voltammograms of bare n-Fe_2O_3 in aq.pH-5.5 citrate buffer (black). **(B) With Diaz AQ moieties on surface.** Chopped light voltammograms of Diaz AQ modified n-Fe_2O_3 in aq.pH-5.5 citrate buffer (Red). **(C) With ATRP AQ moieties on surface.** Chopped light voltammograms of ATRP AQ modified n-Fe_2O_3 in aq.pH-5.5 citrate buffer (Green).

As depicted in the Fig.,8, the unmodified hematite shows 0.18 mA/cm^2 at 1.2V vs RHE whereas the Diaz AQ modified hematite shows 0.25 mA/cm^2, but the ATRP AQ modified hematite exhibits 0.62 mA/cm^2. However the diaz AQ enhances the photocurrent compared to unmodified hematite, the magnitude of enhancement is relatively smaller with respect to ATRP AQ. More than three times of photocurrent enhancement has been observed for ATRP AQ. This photocurrent enhancement can be attributed to the higher amount of AQ moieties present in ATRP AQ. Because the AQ deposited by reductive diazonium electrografting usually forms a monolayer whereas the ATRP process yields nanostructured polymer brush morphology that contains huge amount of AQ groups[137]. It is also important to note that surface modification by Diaz AQ resulting out only AQ groups on the hematite surface whereas the polymer brushes obtained by ATRP process not only having AQ groups but also other groups namely imidazolium, bromide and carbonyl groups, so it is vital to investigate and understand the role of various chemical functional groups present in the polymer brush on the photoelectrochemical properties.

3.14. Linear Sweep Voltammograms (LSV):

To gain deeper understanding of the role of surface modification on PEC properties of hematite, linear sweep voltammograms was recorded at 1 mV/sec scan rate with different surface modified hematite photoanodes in 0.1M NaOH aqueous solution. The photocurrent – voltage neasurements were done with the same three electrode cell in Zahner setup. The area of the illuminated sample is 0.785 cm^2. 455 nm monochromatic light source was used with a power density of 100W/m^2.

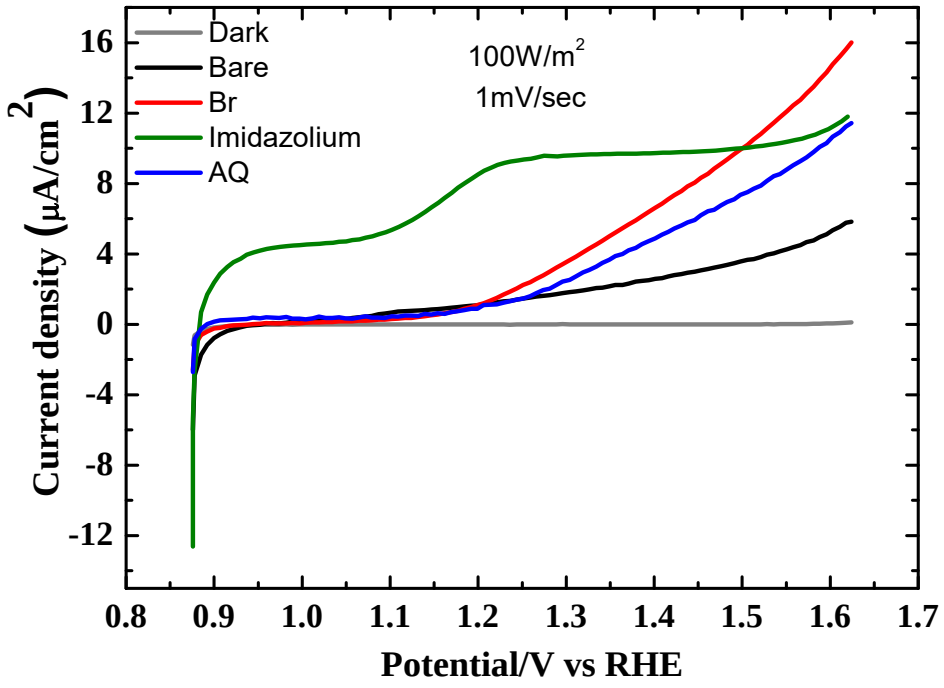


Figure 38. Linear sweep voltammograms recorded in 0.1M NaOH aqueous solution with different surface modified hematite photoanodes at a scan rate of 1 mV/sec in presence of 100W/m^2 power density of 455 nm monochromatic light. Area of the illuminated electrode is 0.785 cm^2 and area for dark curve calculation is 3.14 cm^2.

As mentioned in the previous chapter, the four different types of hematite photoanodes were studied. One is terminated with the bromide initiator and denoted as ‘‘Br‘‘, the other one is immobilized with poly ionic liquid which has no redox active AQ moieties and given as “Imidazolium“, and the one functionalized with AQ containing poly ionic liquid is expressed as “AQ“. The unmodified hematite photoanode was taken as a reference and marked as “Bare“. Fig.38 shows the LSVs of surface modified hematite photoanodes and reveals that no current is visible for the bare sample in the dark condition throughout the measured potential range because of the absence of charge carriers. While illumination, the bare sample provides photocurrent due to the formation of minority carriers that oxidize water into oxygen. The initiator immobilized hematite shows outstanding photocurrent compared to unmodified hematite, for instance, at 1.6V vs RHE the bare hematite shows a photocurrent density of 4 μA/cm^2 whereas the bromide terminated sample exhibits more than 12 μA/cm^2. This three fold enhancement of photocurrent can be attributed to the electronegativity of bromide which establishes a negative electric field and effectively extracts the photoinduced holes that results in accelerated hole transfer to enhance PEC water oxidation and the similar trend is also observed in the literature[138]. Imidazolium hematite reveals interesting features compared to

other samples, its LSV curve has two plateaus and even at the low voltage it shows higher photocurrent compared to remaining samples. It has relatively higher photocurrent until 1.5V, afterthat bromide modified sample overtakes. AQ modified sample shows higher photocurrent compared to unmodified sample but relatively lower than imidazolium and bromide modified hematite sample. The enhanced photoactivity of surface modified hematite photoanodes with poly ionic liquids can be attributed to the chemical composition and nanostructuration of the polymer. The enhanced water photooxidation with poly ionic liquid modified hematite samples can be assigned to the existence of nitrogen in the imidazolium ring that act as electron rich dopant and creating a high electron density and as a result generating a positive charge density on carbon which situated in between the nitrogen atoms in the imidazolium ring. This carbon atom adsorbs OH^- and so enhancing the photocatalytic cycle of oxygen evolution reaction. The similar observation of enhanced electrocatalytic OER and ORR with imidazolium based poly ionic liquid has been reported recently by our group[139]. From these studies, it is clearly shown that bromide and imidazolium are the key players in the improvement of PEC water oxidation.

However, in semiconductor photoelectrochemistry, the water oxidation photocurrent is generally given as[72]

$$J_{ph} = \varphi\, \eta_{LH}\, \eta_{CS}\, \eta_{CT} \qquad (32)$$

Where, J_{ph} is the water oxidation photocurrent, φ is the light intensity, η_{LH} is the light harvesting efficiency, η_{CS} is charge separation efficiency in the bulk and η_{CT} is the charge transfer efficiency from the semiconductor to the electrolyte.

In our case, φ is the light intensity and the same light intensity ($100 W/m^2$) is used for recording all the LSV curves. The light harvesting efficiency, η_{LH}, is generally governed by the absorption coefficient and band gap of the material. Since we did not alter anything in the bulk and we illuminate from the back side, the band gap and the absorption coefficient of the material has to be unchanged. The charge separation efficiency, η_{CS}, is usually determined by the width of the space charge layer and the diffusion length of minority carrier. Since the material is undoped, the charge separation efficiency is also unchanged. But we are observing different photocurrent density with surface modified hematite, so the only remaining parameter η_{CT} might be the reason for the observation of different photocurrent. The charge transfer efficiency, η_{CT}, is also known as injection efficiency and given as the amount of photogenerated holes injected from the semiconductor into the electrolyte and its value gives

an idea about the kinetic competition between charge transfer and surface recombination process[72]. It is already shown that surface modification, usually with cocatalysts, alter the charge transfer efficiency either by improving the charge transfer efficiency or by suppressing the surface recombination process[73, 140]. To understand clearly, which surface process is responsible for the enhancement of charge transfer efficiency, IMPS is widely used.

3.15. IMPS analysis:

Fig.39, reveals the complex IMPS plots for surface modified hematite photoanodes at various applied bias potentials. It clearly shows that the low frequency intercept increases with increase of applied bias potential because of the suppression of recombination at more positive potentials and hence the charge transfer efficiency [k_{tr} / k_{tr} + k_{rec}] represented by low frequency intercept increases. At more positive potentials, the decrease in recombination is in close agreement with the increment of photocurrent in LSV curves as shown in Fig.38.

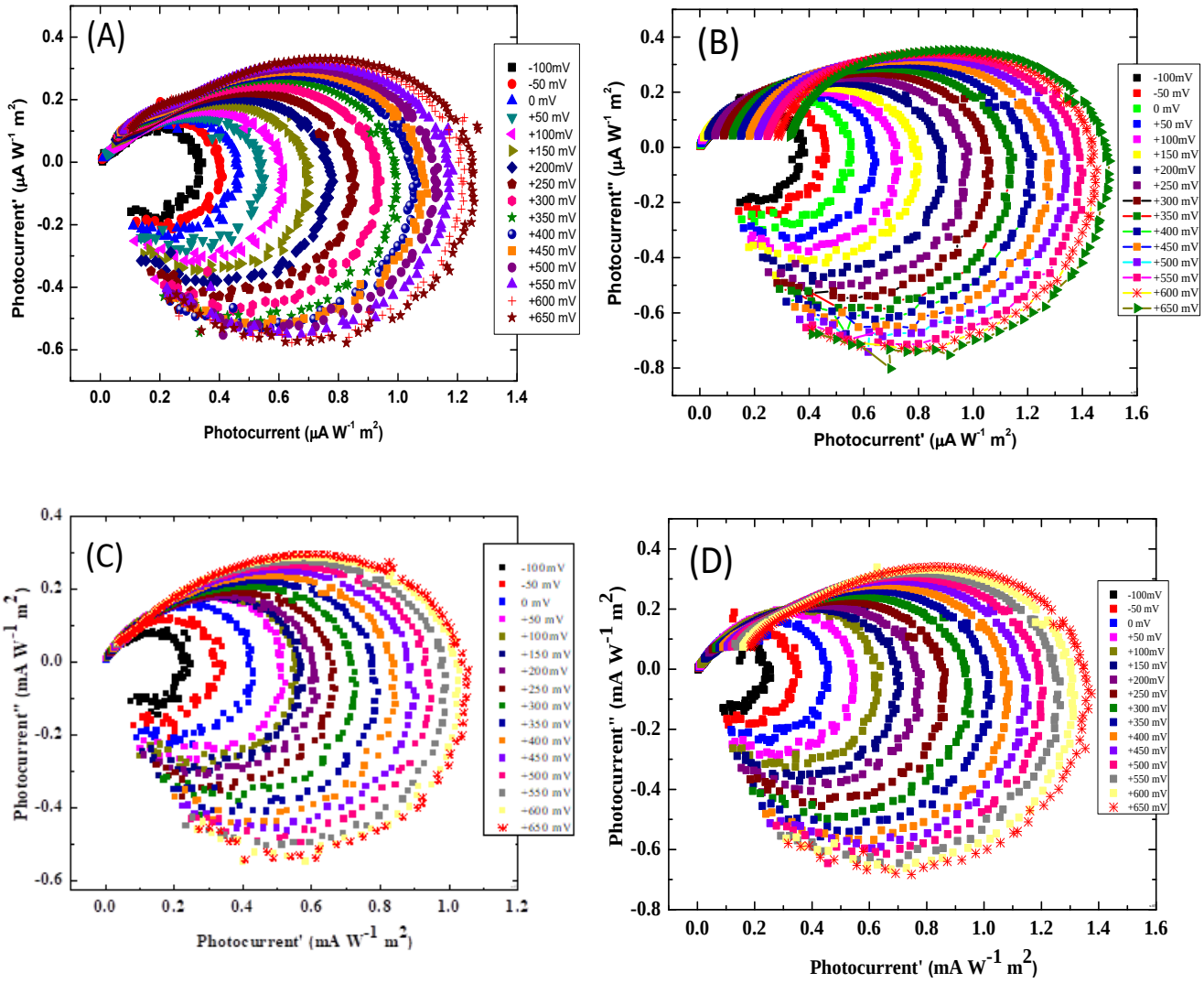


Figure39. IMPS spectra of surface modified hematite photoanodes at different applied potentials. (A) Bare hematite, (B) Bromide terminated hematite, (C) hematite immobilized with ionic liquid contains no AQ redox active moiety, (D) hematite functionalized with AQ poly ionic liquid.

Using equations (29) and (30), the charge transfer efficiency(η_{trans}), rate constant of charge transfer(k_{trans}) and recombination(k_{rec}) can be evaluated for the unmodified and various surface modified hematite photoanodes and the results are shown in Fig.40.

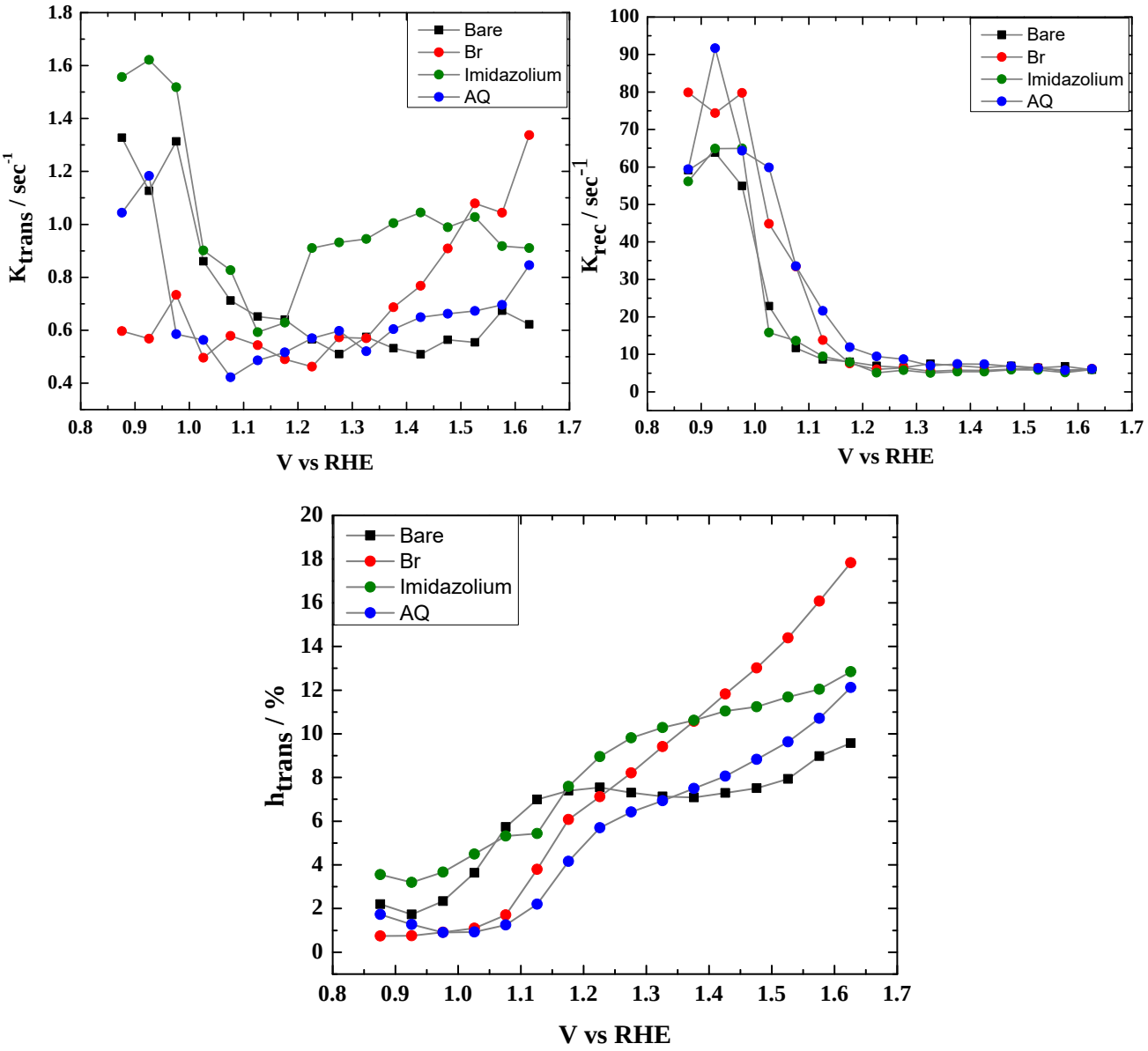


Figure 40. Charge transfer rate constant and recombination rate constant for unmodified and various surface modified hematite photoanodes are given in the left and right side respectively

in the top figure. The bottom figure displays the charge transfer efficiency of surface modified hematite electrodes.

The k_{rec} is very similar for all the samples whereas the k_{trans} changes with increase of applied potential. Particularly from 1.2V, the k_{rec} values are almost flat and as pointed out by Zachäus et al[72]. the constant k_{rec} means that there is no change in band bending in this potential regime. As the band bending increases with increase of potential, actually the k_{rec} should decrease monotonically, because it depends on the surface concentration of electrons. The flat region in the k_{rec} plot is mainly attributed to the Fermi level pinning caused by the build-up of holes in the surface or in the surface states. In general, the transfer efficiency increases with increase of rate of charge transfer and decrease of rate of recombination, but in our case, we have observed the increase in charge transfer efficiency but not a remarkable change in rate of recombination, hence the rate of charge transfer is mainly contributing for the enhancement of charge transfer efficiency. From this observation, it is clear that the surface modification did not alter the surface recombination processes *i.e.*,the surface modification is not completely passivating the surface states where the recombination occurs, but improving the charge transfer process and hence the charge transfer efficiency.

3.16. PEIS analysis:

The dangling bonds in the surface of a semiconductor give rise to electronic states within the bandgap and generally coined as surface states that can either be intrinsic to the semiconductor surface or extrinsic if their existence depends on the environmental factors of the semiconductor such as the adsorbates or electrolytes. These surface states play a major role in interfacial reaction kinetics of illuminated semiconductor photoelectrodes[141] by acting as minority carriers recombination centers.

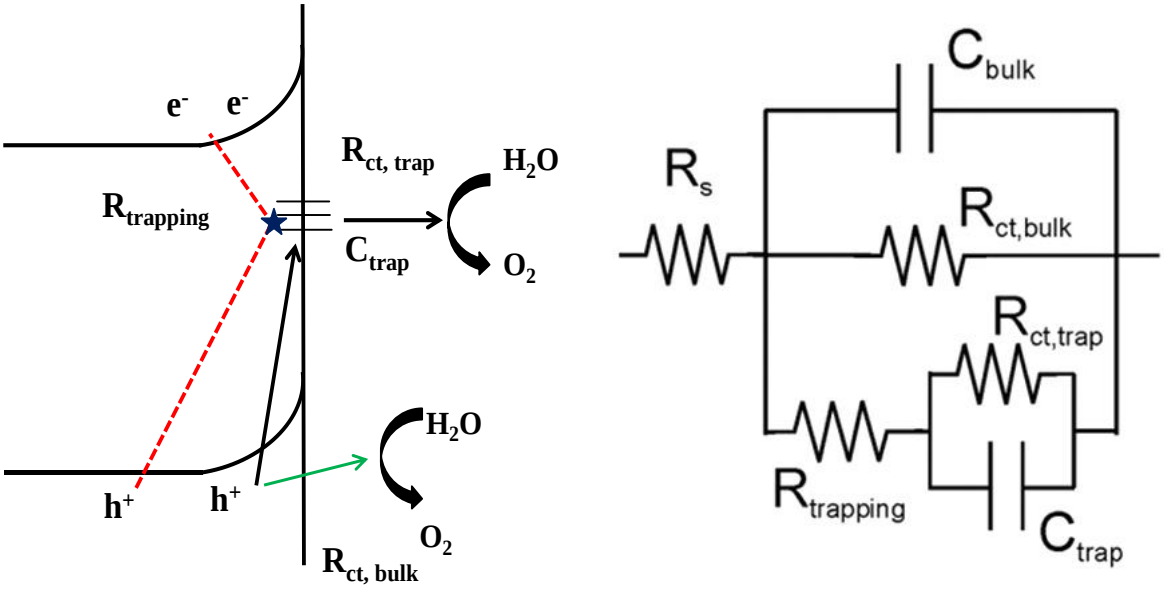


Figure 41. Scheme of the charge transfer processes occuring at the semiconductor – solution interface indicating direct and indirect charge transfer processes (Left) and its corresponding equivalent circuit (Right).

These recombination process competes with the charge transfer process from the semiconductor bands. The surface states not only act as the recombination center but also involving in the charge transfer process; if the minority carriers are directly transferred from the semiconductor bands to the solution then it is known as *direct charge transfer* process, on the other hand if the minority carriers are transferred via the surface states it is called *indirect charge transfer* process and so it is very important to distinguish between them. In the case of indirect charge transfer, the photogenerated minority carriers are trapped in the surface states followed by the oxidation of water or recombination with trapped electrons. These charge transfer processes and the corresponding equivalent circuit are given in **Fig.41**. This equivalent circuit is based on the work of Klahr *et al.,* with an assumption that the water oxidation reaction is driven by surface states[66]. In this equivalent circuit, four resistances and two capacitances are used; a series resistance corresponds to the solution resistance, R_s; trapping resistance at surface states where charge carriers recombine is attributed to R_{trap}; $R_{ct,trap}$ gives the indirect charge transfer(via surface states) resistance and $R_{ct,bulk}$ gives the direct charge transfer(via valence band) resistance; the bulk capacitor C_{bulk} attributed to the space charge capacitance and C_{trap} corresponds to surface state capacitance. After fitting the impedance spectra by using this equivalent circuit, the obtained resistance and capacitance values are plotted against applied potential as given in **Fig.42**.

The surface state capacitance, C_{trap}, for the bare and surface modified hematite photoanodes shows a Gaussian type distribution with applied voltage is confirming the presence of surface states as reported in the literature for hematite[47, 66]. As pointed out by Z Wang et al., the activation of oxygen evolution reaction(OER) intermediates gives rise to this Gaussian distribution and the maximum of this capacitance mostly comes out closer to the onset potential due to the accumulation of holes in the surface state prior to the steady state photocurrent for the oxidation of water can be maintained[142]. Also the shift in the C_{trap} peaks suggesting the change in the distribution of intermediate surface states[142]. The semiconductor – electrolyte interface and the deposition procedure strongly governs the surface state capacitance. For instance, as reported in the literature, the distribution of hematite surface states varies in a drastic manner with respect to the solution used such as water, ethanol and acetonitrile[143], the surface state capacitive peak anodically shifts with pH[144] and also the deposition method influences the capacitive features as reported by Zandi and Hamann[145].

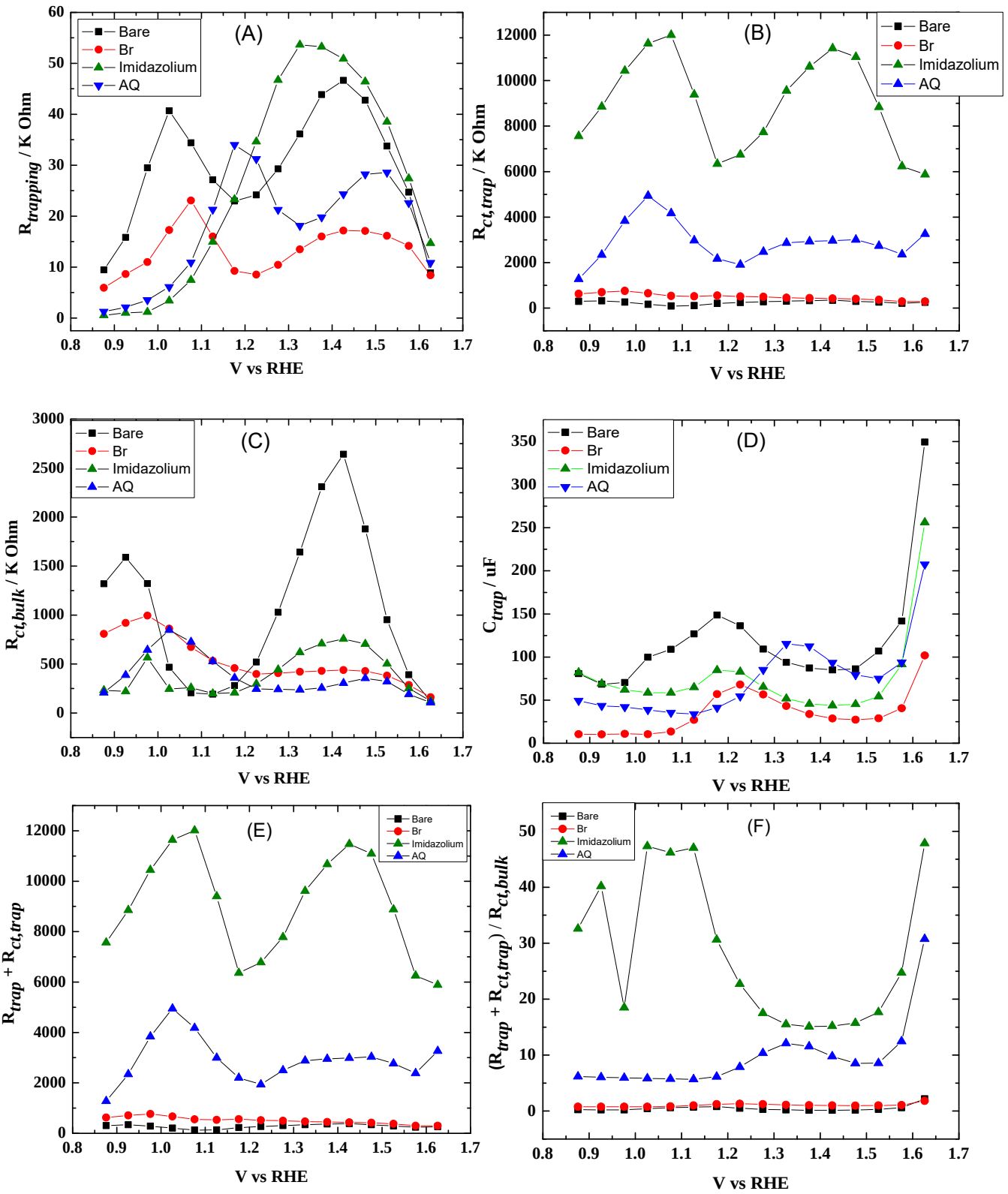


Figure 42. Resistance and capacitance values plotted against applied potentials, obtained from the fitting of photoelectrochemical impedance spectra

The decrease of C_{trap} capacitance with surface modification indicates the mitigation of concentration of surface states. The decrement of C_{trap} capacitance with surface modification is having a correlation to a concomitant increase of the charge transfer resistance, $R_{ct,trap}$. This result confirms our assumption of presence of surface states even after the surface modification, thus the surface modification did not passivate completely the surface states but altering the interfacial properties. So now the question is that whether the charge transfer taking place via this surface state or through the valence band.

In order to understand that, the resistances associated with surface states mediated charge transfer namely $R_{ct,trap}$ and $R_{trapping}$ are compared with respect to the direct charge transfer resistance $R_{ct,bulk}$ and the corresponding ratio is given in Fig.42.e, The ionic liquid modified hematite photoanodes show higher resistances to the surface state mediated charge transfer whereas the bromide modified and bare hematite photoanodes exhibit lower resistances to the surface state mediated charge transfer which means that the ionic liquid immobilized hematite photoanodes favor the direct charge transfer but bare and bromide modified hematite photoanodes prefer the surface state mediated charge transfer. From the literature also, it is confirmed that the unmodified hematite photoanode shows surface state mediated charge transfer[66].

Interesting observation here is that bromide modified hematite photoanode shows lower C_{trap} capacitance as well as lower $R_{ct,trap}$ resistance. But at the same time, bromide modified hematite shows better photoelectrocatalytic performance and it may be attributed to the fact that bromide can establish a negative electric field on the electrode surface that would help to extract efficiently the photogenerated holes and the similar observation was reported in the literature[138a, 146]

3.17. Mott – Schottky analysis:

Mott-Schottky plots were obtained by plotting the C_{bulk}^{-2} values of bare and surface modified hematite samples against the applied potential as given in the **fig.43** to find out the flat band potential. From the straight line equation (y = mx+c), the value of `x`(flat band potential) is calculated where `y` becomes zero and thus estimated flat band values are tabulated in **Table 1**. Mott-Schottky equation is given as follows:

$$C^{-2} = \frac{2}{\varepsilon\varepsilon_0 A^2 e N_D}\left(V - V_{fb} - \frac{kT}{e}\right) \qquad (33)$$

Where, C is capacitance; $\mathcal{E}$ is dielectric constant(32 for hematite); $\mathcal{E}_o$ is permittivity; A is the whole area of the electrode; e is elementary charge; N_D is doping density; V is applied potential; V_{fb} is flat-band potential; k is Boltzmann constant and T is absolute temperature.

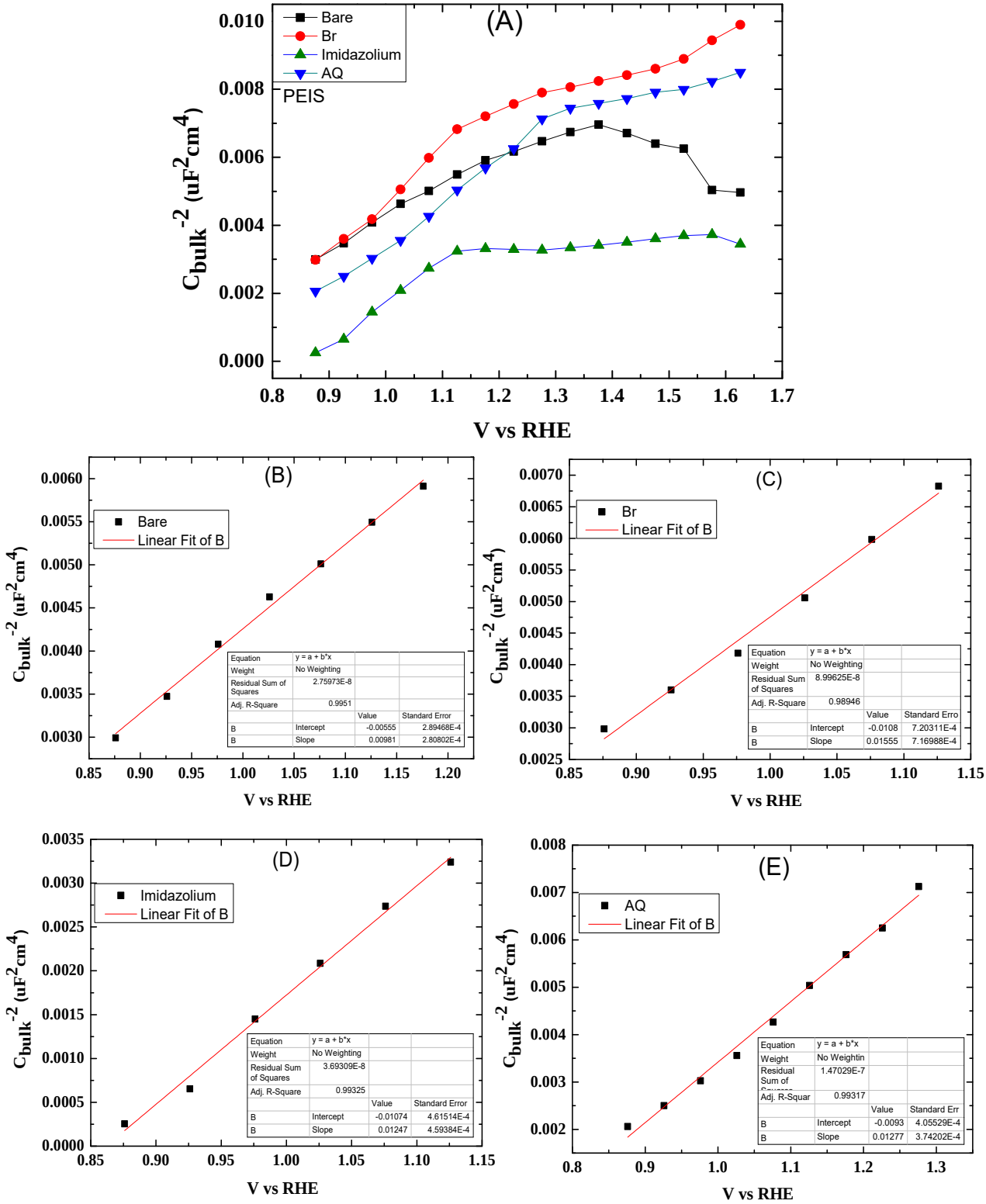


Figure 43. Mott – Schottky plots obtained from C-bulk values for various surface modified hematite photoanodes.

Table 1. Flat band potentials obtained for various surface modified hematite samples.

Sample	Flat band potential [V vs RHE]
Bare	0.54
Br	0.67
Imidazolium	0.83
AQ	0.71

As seen clearly from the table, the surface modification is altering the flat band of the hematite, the flat band potential for bare hematite is at 0.54V vs RHE, whereas it is 0.64V vs RHE for bromide terminated sample, 0.83V for imidazolium and 0.71V for AQ modified samples.

3.18. Conclusion:

Photoelectrochemistry of AQ electrografted electrosynthesized hematite photoanodes was evaluated in aqueous and non-aqueous medium with ferrocene based different hole scavengers such as ferrocene, dibromoferrocene, ferrocene carboxylic acid and ferrocene methyl imidazolium TFSI ionic liquid and found out that the formal potential of the hole scavenger governs the photocurrent, i.e., if the formal potential is higher then the photocurrent will be lower and vice-versa. It is obvious and recently proved in literature that AQ can act as a photoelectrocatalyst and reduce oxygen to hydrogen peroxide. Also H_2O_2 is required as a fuel for MnO_2 based micromotor. Hence AQ is colvalently immobilized over the surface of hematite by electrografting as well as SI-ATRP process and hematite with AQ immobilized by SI-ATRP process shows better performance because of the fact that SI-ATRP process usually forms nanostructured polymer brush like morphology and hence the amount of AQ will be higher compared to the electrografting process that yields only a monolayer of AQ. To gain deeper insights of the influence of physico-chemical nature of the redox active AQ based ionic liquid on photoelectrochemical water oxidation, various surface modified hematite samples such as hematite photoanode with only bromide initiator (Br) and with imidazolium based poly ionic liquid that contains no redox active group (Imidazolium), then finally with redox active AQ ionic liquid (AQ) were analyzed and compared with unmodified hematite sample (Bare) in a step by step manner. The detailed photoelectrochemical investigations like

linear sweep voltammetry, intensity modulated photocurrent spectroscopy and photoelectrochemical impedance spectroscopy were carried out which reveal that the surface modification obviously altering the flat band potential, interfacial properties particularly reducing the surface state concentration and governs the charge transfer process. In particular, the bromide terminated hematite photoanode exhibits higher photocurrent due to the formation of a negative electric field in the semiconductor – electrolyte interface that effectively pulls out the holes from the valence band for water oxidation. The ionic liquid modified hematite samples favor the direct charge transfer of holes from the valence band whereas the bromide modified and bare hematite photoanodes prefer the indirect surface state mediated charge transfer. The enhanced photoactivity of surface modified hematite photoanodes with poly ionic liquids can be attributed to the chemical composition and nanostructuration of the polymer. The enhanced water photooxidation with poly ionic liquid modified hematite samples can be assigned to the existence of nitrogen in the imidazolium ring that act as electron rich dopant and creating a high electron density and as a result generating a positive charge density on carbon which situated in between the nitrogen atoms in the imidazolium ring. This carbon atom adsorbs OH^- and so enhancing the photocatalytic cycle of oxygen evolution reaction. Although this work imply that poly ionic liquid is capable of boosting photoelectrochemical performance, fundamental understanding of the enhancement by ionic liquid at a molecular level is still required.

References:

1. Lewis, N. S.; Nocera, D. G., Powering the planet: Chemical challenges in solar energy utilization. *Proceedings of the National Academy of Sciences* **2006,** *103* (43), 15729-15735.
2. Turner, J. A., A Realizable Renewable Energy Future. *Science* **1999,** *285* (5428), 687-689.
3. Bossel, U., Does a Hydrogen Economy Make Sense? *Proceedings of the IEEE* **2006,** *94* (10), 1826-1837.
4. (a) Bolton, J. R.; Strickler, S. J.; Connolly, J. S., Limiting and realizable efficiencies of solar photolysis of water. *Nature* **1985,** *316* (6028), 495-500; (b) Weber, M. F.; Dignam, M. J., Splitting water with semiconducting photoelectrodes—Efficiency considerations. *International Journal of Hydrogen Energy* **1986,** *11* (4), 225-232.
5. Reiss, H.; Heller, A., The absolute potential of the standard hydrogen electrode: a new estimate. *The Journal of Physical Chemistry* **1985,** *89* (20), 4207-4213.
6. (a) Bard, A. J.; Bocarsly, A. B.; Fan, F. R. F.; Walton, E. G.; Wrighton, M. S., The concept of Fermi level pinning at semiconductor/liquid junctions. Consequences for energy conversion efficiency and selection of useful solution redox couples in solar devices. *Journal of the American Chemical Society* **1980,** *102* (11), 3671-3677; (b) Fan, F. R. F.; Bard, A. J., Semiconductor electrodes. 24. Behavior of photoelectrochemical cells based on p-type gallium arsenide in aqueous solutions. *Journal of the American Chemical Society* **1980,** *102* (11), 3677-3683.
7. Gerischer, H., Electrochemical Behavior of Semiconductors under Illumination. *Journal of The Electrochemical Society* **1966,** *113* (11), 1174-1182.
8. Calvet, W.; Murugasen, E.; Klett, J.; Kaiser, B.; Jaegermann, W.; Finger, F.; Hoch, S.; Blug, M.; Busse, J., Silicon based tandem cells: novel photocathodes for hydrogen production. *Physical Chemistry Chemical Physics* **2014,** *16* (24), 12043-12050.
9. Morrison, S. R., Electrochemistry at semiconductor and oxidized metal electrodes. **1980**.
10. Weber, M. F.; Dignam, M. J., Efficiency of Splitting Water with Semiconducting Photoelectrodes. *Journal of The Electrochemical Society* **1984,** *131* (6), 1258-1265.
11. Gerischer, H., On the stability of semiconductor electrodes against photodecomposition. *Journal of Electroanalytical Chemistry and Interfacial Electrochemistry* **1977,** *82* (1), 133-143.
12. Fujishima, A.; Honda, K., Electrochemical Photolysis of Water at a Semiconductor Electrode. *Nature* **1972,** *238* (5358), 37-38.
13. Archer, M. D. A. N., Arthur J, *Nanostructured and Photoelectrochemical Systems for Solar Photon Conversion*.

14. Pan, L.; Kim, J. H.; Mayer, M. T.; Son, M.-K.; Ummadisingu, A.; Lee, J. S.; Hagfeldt, A.; Luo, J.; Grätzel, M., Boosting the performance of Cu2O photocathodes for unassisted solar water splitting devices. *Nature Catalysis* **2018,** *1* (6), 412-420.
15. Chen, X.; Liu, L.; Yu, P. Y.; Mao, S. S., Increasing Solar Absorption for Photocatalysis with Black Hydrogenated Titanium Dioxide Nanocrystals. *Science* **2011,** *331* (6018), 746-750.
16. Liu, Z.; Hou, W.; Pavaskar, P.; Aykol, M.; Cronin, S. B., Plasmon Resonant Enhancement of Photocatalytic Water Splitting Under Visible Illumination. *Nano Letters* **2011,** *11* (3), 1111-1116.
17. Solarska, R.; Królikowska, A.; Augustyński, J., Silver Nanoparticle Induced Photocurrent Enhancement at WO3 Photoanodes. *Angewandte Chemie International Edition* **2010,** *49* (43), 7980-7983.
18. Janáky, C.; Rajeshwar, K.; de Tacconi, N. R.; Chanmanee, W.; Huda, M. N., Tungsten-based oxide semiconductors for solar hydrogen generation. *Catalysis Today* **2013,** *199*, 53-64.
19. Hardee, K. L.; Bard, A. J., Semiconductor Electrodes: V . The Application of Chemically Vapor Deposited Iron Oxide Films to Photosensitized Electrolysis. *Journal of The Electrochemical Society* **1976,** *123* (7), 1024-1026.
20. Tilley, S. D.; Cornuz, M.; Sivula, K.; Grätzel, M., Light-Induced Water Splitting with Hematite: Improved Nanostructure and Iridium Oxide Catalysis. *Angewandte Chemie International Edition* **2010,** *49* (36), 6405-6408.
21. Kim, J. Y.; Magesh, G.; Youn, D. H.; Jang, J.-W.; Kubota, J.; Domen, K.; Lee, J. S., Single-crystalline, wormlike hematite photoanodes for efficient solar water splitting. *Scientific Reports* **2013,** *3*, 2681.
22. Kudo, A.; Ueda, K.; Kato, H.; Mikami, I., Photocatalytic O2 evolution under visible light irradiation on BiVO4 in aqueous AgNO3 solution. *Catalysis Letters* **1998,** *53* (3), 229-230.
23. (a) Li, M.; Zhao, L.; Guo, L., Preparation and photoelectrochemical study of BiVO4 thin films deposited by ultrasonic spray pyrolysis. *International Journal of Hydrogen Energy* **2010,** *35* (13), 7127-7133; (b) Liang, Y.; Tsubota, T.; Mooij, L. P. A.; van de Krol, R., Highly Improved Quantum Efficiencies for Thin Film BiVO4 Photoanodes. *The Journal of Physical Chemistry C* **2011,** *115* (35), 17594-17598.
24. Pihosh, Y.; Turkevych, I.; Mawatari, K.; Uemura, J.; Kazoe, Y.; Kosar, S.; Makita, K.; Sugaya, T.; Matsui, T.; Fujita, D.; Tosa, M.; Kondo, M.; Kitamori, T., Photocatalytic generation of hydrogen by core-shell WO3/BiVO4 nanorods with ultimate water splitting efficiency. *Scientific Reports* **2015,** *5*, 11141.
25. Yourey, J. E.; Bartlett, B. M., Electrochemical deposition and photoelectrochemistry of CuWO4, a promising photoanode for water oxidation. *Journal of Materials Chemistry* **2011,** *21* (21), 7651-7660.

26. Zhang, H.; Yilmaz, P.; Ansari, J. O.; Khan, F. F.; Binions, R.; Krause, S.; Dunn, S., Incorporation of Ag nanowires in CuWO4 for improved visible light-induced photoanode performance. *Journal of Materials Chemistry A* **2015,** *3* (18), 9638-9644.
27. Hill, J. C.; Choi, K.-S., Synthesis and characterization of high surface area CuWO4 and Bi2WO6 electrodes for use as photoanodes for solar water oxidation. *Journal of Materials Chemistry A* **2013,** *1* (16), 5006-5014.
28. Pyper, K. J.; Yourey, J. E.; Bartlett, B. M., Reactivity of CuWO4 in Photoelectrochemical Water Oxidation Is Dictated by a Midgap Electronic State. *The Journal of Physical Chemistry C* **2013,** *117* (47), 24726-24732.
29. Bohra, D.; Smith, W. A., Improved charge separation via Fe-doping of copper tungstate photoanodes. *Physical Chemistry Chemical Physics* **2015,** *17* (15), 9857-9866.
30. Ye, W.; Chen, F.; Zhao, F.; Han, N.; Li, Y., CuWO4 Nanoflake Array-Based Single-Junction and Heterojunction Photoanodes for Photoelectrochemical Water Oxidation. *ACS Applied Materials & Interfaces* **2016,** *8* (14), 9211-9217.
31. Hu, D.; Diao, P.; Xu, D.; Xia, M.; Gu, Y.; Wu, Q.; Li, C.; Yang, S., Copper(ii) tungstate nanoflake array films: sacrificial template synthesis, hydrogen treatment, and their application as photoanodes in solar water splitting. *Nanoscale* **2016,** *8* (11), 5892-5901.
32. Lhermitte, C. R.; Bartlett, B. M., Advancing the Chemistry of CuWO4 for Photoelectrochemical Water Oxidation. *Accounts of Chemical Research* **2016,** *49* (6), 1121-1129.
33. Woodhouse, M.; Parkinson, B. A., Combinatorial Discovery and Optimization of a Complex Oxide with Water Photoelectrolysis Activity. *Chemistry of Materials* **2008,** *20* (7), 2495-2502.
34. Woodhouse, M.; Parkinson, B. A., Combinatorial approaches for the identification and optimization of oxide semiconductors for efficient solar photoelectrolysis. *Chemical Society Reviews* **2009,** *38* (1), 197-210.
35. Osterloh, F. E., Inorganic Materials as Catalysts for Photochemical Splitting of Water. *Chemistry of Materials* **2008,** *20* (1), 35-54.
36. Abdi, F. F.; Berglund, S. P., Recent developments in complex metal oxide photoelectrodes. *Journal of Physics D: Applied Physics* **2017,** *50* (19), 193002.
37. Marusak, L. A.; Messier, R.; White, W. B., Optical absorption spectrum of hematite, αFe2O3 near IR to UV. *Journal of Physics and Chemistry of Solids* **1980,** *41* (9), 981-984.
38. Sivula, K.; Le Formal, F.; Grätzel, M., Solar Water Splitting: Progress Using Hematite (α-Fe2O3) Photoelectrodes. *ChemSusChem* **2011,** *4* (4), 432-449.
39. Katz, M. J.; Riha, S. C.; Jeong, N. C.; Martinson, A. B. F.; Farha, O. K.; Hupp, J. T., Toward solar fuels: Water splitting with sunlight and "rust"? *Coordination Chemistry Reviews* **2012,** *256* (21), 2521-2529.

40. Young, K. M. H.; Klahr, B. M.; Zandi, O.; Hamann, T. W., Photocatalytic water oxidation with hematite electrodes. *Catalysis Science & Technology* **2013,** *3* (7), 1660-1671.

41. Balberg, I.; Pinch, H. L., The optical absorption of iron oxides. *Journal of Magnetism and Magnetic Materials* **1978,** *7* (1), 12-15.

42. Sastri, M. V. C.; Nagasubramanian, G., Studies on ferric oxide electrodes for the photo-assisted electrolysis of water. *International Journal of Hydrogen Energy* **1982,** *7* (11), 873-876.

43. Le Formal, F.; Tétreault, N.; Cornuz, M.; Moehl, T.; Grätzel, M.; Sivula, K., Passivating surface states on water splitting hematite photoanodes with alumina overlayers. *Chemical Science* **2011,** *2* (4), 737-743.

44. Le Formal, F.; Pendlebury, S. R.; Cornuz, M.; Tilley, S. D.; Grätzel, M.; Durrant, J. R., Back Electron–Hole Recombination in Hematite Photoanodes for Water Splitting. *Journal of the American Chemical Society* **2014,** *136* (6), 2564-2574.

45. Peter, L. M.; Wijayantha, K. G. U.; Tahir, A. A., Kinetics of light-driven oxygen evolution at α-Fe2O3 electrodes. *Faraday Discussions* **2012,** *155* (0), 309-322.

46. Klahr, B.; Gimenez, S.; Fabregat-Santiago, F.; Bisquert, J.; Hamann, T. W., Electrochemical and photoelectrochemical investigation of water oxidation with hematite electrodes. *Energy & Environmental Science* **2012,** *5* (6), 7626-7636.

47. Upul Wijayantha, K. G.; Saremi-Yarahmadi, S.; Peter, L. M., Kinetics of oxygen evolution at α-Fe2O3 photoanodes: a study by photoelectrochemical impedance spectroscopy. *Physical Chemistry Chemical Physics* **2011,** *13* (12), 5264-5270.

48. Zhang, Y.; Zhang, H.; Liu, A.; Chen, C.; Song, W.; Zhao, J., Rate-Limiting O–O Bond Formation Pathways for Water Oxidation on Hematite Photoanode. *Journal of the American Chemical Society* **2018,** *140* (9), 3264-3269.

49. Zandi, O.; Hamann, T. W., Determination of photoelectrochemical water oxidation intermediates on haematite electrode surfaces using operando infrared spectroscopy. *Nature Chemistry* **2016,** *8*, 778.

50. Cowan, A. J.; Barnett, C. J.; Pendlebury, S. R.; Barroso, M.; Sivula, K.; Grätzel, M.; Durrant, J. R.; Klug, D. R., Activation Energies for the Rate-Limiting Step in Water Photooxidation by Nanostructured α-Fe2O3 and TiO2. *Journal of the American Chemical Society* **2011,** *133* (26), 10134-10140.

51. (a) Tamirat, A. G.; Rick, J.; Dubale, A. A.; Su, W.-N.; Hwang, B.-J., Using hematite for photoelectrochemical water splitting: a review of current progress and challenges. *Nanoscale Horizons* **2016,** *1* (4), 243-267; (b) Iandolo, B.; Wickman, B.; Zorić, I.; Hellman, A., The rise of hematite: origin and strategies to reduce the high onset potential for the oxygen evolution reaction. *Journal of Materials Chemistry A* **2015,** *3* (33), 16896-16912.

52. Jaegermann, W.; Tributsch, H., Interfacial properties of semiconducting transition metal chalcogenides. *Progress in Surface Science* **1988,** *29* (1), 1-167.
53. Sinn, C.; Meissner, D.; Memming, R., Charge Transfer Processes at WSe2 Electrodes with pH-Controlled Stability. *Journal of The Electrochemical Society* **1990,** *137* (1), 168-172.
54. Schefold, J.; Kühne, H. M., Charge transfer and recombination kinetics at photoelectrodes: A quantitative evaluation of impedance measurements. *Journal of Electroanalytical Chemistry and Interfacial Electrochemistry* **1991,** *300* (1), 211-233.
55. Zhang, Z.; Yates, J. T., Band Bending in Semiconductors: Chemical and Physical Consequences at Surfaces and Interfaces. *Chemical Reviews* **2012,** *112* (10), 5520-5551.
56. Ashkenasy, G.; Cahen, D.; Cohen, R.; Shanzer, A.; Vilan, A., Molecular Engineering of Semiconductor Surfaces and Devices. *Accounts of Chemical Research* **2002,** *35* (2), 121-128.
57. Du, C.; Zhang, M.; Jang, J.-W.; Liu, Y.; Liu, G.-Y.; Wang, D., Observation and Alteration of Surface States of Hematite Photoelectrodes. *The Journal of Physical Chemistry C* **2014,** *118* (30), 17054-17059.
58. Berger, T.; Monllor-Satoca, D.; Jankulovska, M.; Lana-Villarreal, T.; Gómez, R., The Electrochemistry of Nanostructured Titanium Dioxide Electrodes. *ChemPhysChem* **2012,** *13* (12), 2824-2875.
59. Yang, S.; Prendergast, D.; Neaton, J. B., Tuning Semiconductor Band Edge Energies for Solar Photocatalysis via Surface Ligand Passivation. *Nano Letters* **2012,** *12* (1), 383-388.
60. Kuang, Y.; Yamada, T.; Domen, K., Surface and Interface Engineering for Photoelectrochemical Water Oxidation. *Joule* **2017,** *1* (2), 290-305.
61. Hu, S.; Shaner, M. R.; Beardslee, J. A.; Lichterman, M.; Brunschwig, B. S.; Lewis, N. S., Amorphous TiO₂ coatings stabilize Si, GaAs, and GaP photoanodes for efficient water oxidation. *Science* **2014,** *344* (6187), 1005-1009.
62. Lichterman, M. F.; Carim, A. I.; McDowell, M. T.; Hu, S.; Gray, H. B.; Brunschwig, B. S.; Lewis, N. S., Stabilization of n-cadmium telluride photoanodes for water oxidation to O2(g) in aqueous alkaline electrolytes using amorphous TiO2 films formed by atomic-layer deposition. *Energy & Environmental Science* **2014,** *7* (10), 3334-3337.
63. Paracchino, A.; Laporte, V.; Sivula, K.; Grätzel, M.; Thimsen, E., Highly active oxide photocathode for photoelectrochemical water reduction. *Nature Materials* **2011,** *10*, 456.
64. Paracchino, A.; Mathews, N.; Hisatomi, T.; Stefik, M.; Tilley, S. D.; Grätzel, M., Ultrathin films on copper(i) oxide water splitting photocathodes: a study on performance and stability. *Energy & Environmental Science* **2012,** *5* (9), 8673-8681.
65. Hisatomi, T.; Le Formal, F.; Cornuz, M.; Brillet, J.; Tétreault, N.; Sivula, K.; Grätzel, M., Cathodic shift in onset potential of solar oxygen evolution on hematite by 13-group oxide overlayers. *Energy & Environmental Science* **2011,** *4* (7), 2512-2515.

66. Klahr, B.; Gimenez, S.; Fabregat-Santiago, F.; Hamann, T.; Bisquert, J., Water Oxidation at Hematite Photoelectrodes: The Role of Surface States. *Journal of the American Chemical Society* **2012,** *134* (9), 4294-4302.

67. Li, Z.; Luo, W.; Zhang, M.; Feng, J.; Zou, Z., Photoelectrochemical cells for solar hydrogen production: current state of promising photoelectrodes, methods to improve their properties, and outlook. *Energy & Environmental Science* **2013,** *6* (2), 347-370.

68. Tolod, K. R.; Hernández, S.; Russo, N., Recent Advances in the BiVO4 Photocatalyst for Sun-Driven Water Oxidation: Top-Performing Photoanodes and Scale-Up Challenges. *Catalysts* **2017,** *7* (1), 13.

69. Ma, Y.; Kafizas, A.; Pendlebury, S. R.; Le Formal, F.; Durrant, J. R., Photoinduced Absorption Spectroscopy of CoPi on BiVO4: The Function of CoPi during Water Oxidation. *Advanced Functional Materials* **2016,** *26* (27), 4951-4960.

70. Ma, Y.; Le Formal, F.; Kafizas, A.; Pendlebury, S. R.; Durrant, J. R., Efficient suppression of back electron/hole recombination in cobalt phosphate surface-modified undoped bismuth vanadate photoanodes. *Journal of Materials Chemistry A* **2015,** *3* (41), 20649-20657.

71. Barroso, M.; Mesa, C. A.; Pendlebury, S. R.; Cowan, A. J.; Hisatomi, T.; Sivula, K.; Grätzel, M.; Klug, D. R.; Durrant, J. R., Dynamics of photogenerated holes in surface modified α-Fe₂O₃ photoanodes for solar water splitting. *Proceedings of the National Academy of Sciences* **2012,** *109* (39), 15640-15645.

72. Zachäus, C.; Abdi, F. F.; Peter, L. M.; van de Krol, R., Photocurrent of BiVO4 is limited by surface recombination, not surface catalysis. *Chemical Science* **2017,** *8* (5), 3712-3719.

73. Thorne, J. E.; Jang, J.-W.; Liu, E. Y.; Wang, D., Understanding the origin of photoelectrode performance enhancement by probing surface kinetics. *Chemical Science* **2016,** *7* (5), 3347-3354.

74. Du, C.; Yang, X.; Mayer, M. T.; Hoyt, H.; Xie, J.; McMahon, G.; Bischoping, G.; Wang, D., Hematite-Based Water Splitting with Low Turn-On Voltages. *Angewandte Chemie International Edition* **2013,** *52* (48), 12692-12695.

75. Yang, X.; Du, C.; Liu, R.; Xie, J.; Wang, D., Balancing photovoltage generation and charge-transfer enhancement for catalyst-decorated photoelectrochemical water splitting: A case study of the hematite/MnOx combination. *Journal of Catalysis* **2013,** *304*, 86-91.

76. Nakato, Y.; Ueda, K.; Yano, H.; Tsubomura, H., Effect of microscopic discontinuity of metal overlayers on the photovoltages in metal-coated semiconductor-liquid junction photoelectrochemical cells for efficient solar energy conversion. *The Journal of Physical Chemistry* **1988,** *92* (8), 2316-2324.

77. Nakato, Y.; Tsubomura, H., Structures and functions of thin metal layers on semiconductor electrodes. *Journal of Photochemistry* **1985,** *29* (1), 257-266.

78. Badia-Bou, L.; Mas-Marza, E.; Rodenas, P.; Barea, E. M.; Fabregat-Santiago, F.; Gimenez, S.; Peris, E.; Bisquert, J., Water Oxidation at Hematite Photoelectrodes with an Iridium-Based Catalyst. *The Journal of Physical Chemistry C* **2013,** *117* (8), 3826-3833.
79. Zhong, D. K.; Cornuz, M.; Sivula, K.; Grätzel, M.; Gamelin, D. R., Photo-assisted electrodeposition of cobalt–phosphate (Co–Pi) catalyst on hematite photoanodes for solar water oxidation. *Energy & Environmental Science* **2011,** *4* (5), 1759-1764.
80. Yu, Q.; Meng, X.; Wang, T.; Li, P.; Ye, J., Hematite Films Decorated with Nanostructured Ferric Oxyhydroxide as Photoanodes for Efficient and Stable Photoelectrochemical Water Splitting. *Advanced Functional Materials* **2015,** *25* (18), 2686-2692.
81. Xu, D.; Rui, Y.; Li, Y.; Zhang, Q.; Wang, H., Zn-Co layered double hydroxide modified hematite photoanode for enhanced photoelectrochemical water splitting. *Applied Surface Science* **2015,** *358*, 436-442.
82. Young, K. M. H.; Hamann, T. W., Enhanced photocatalytic water oxidation efficiency with Ni(OH)2 catalysts deposited on α-Fe2O3via ALD. *Chemical Communications* **2014,** *50* (63), 8727-8730.
83. Ronald, H.; Achim, L., Applications of Transition-Metal Catalysts to Textile and Wood-Pulp Bleaching. *Angewandte Chemie International Edition* **2006,** *45* (2), 206-222.
84. Brillas, E.; Sirés, I.; Oturan, M. A., Electro-Fenton Process and Related Electrochemical Technologies Based on Fenton's Reaction Chemistry. *Chemical Reviews* **2009,** *109* (12), 6570-6631.
85. Puértolas, B.; Hill, A. K.; García, T.; Solsona, B.; Torrente-Murciano, L., In-situ synthesis of hydrogen peroxide in tandem with selective oxidation reactions: A mini-review. *Catalysis Today* **2015,** *248*, 115-127.
86. Rosaria, C.; Lorenzo, A.; Francesco, M.; Mario, P., Hydrogen Peroxide: A Key Chemical for Today's Sustainable Development. *ChemSusChem* **2016,** *9* (24), 3374-3381.
87. https://www.gminsights.com/industry-analysis/hydrogen-peroxide-market
88. Yi, Y.; Wang, L.; Li, G.; Guo, H., A review on research progress in the direct synthesis of hydrogen peroxide from hydrogen and oxygen: noble-metal catalytic method, fuel-cell method and plasma method. *Catalysis Science & Technology* **2016,** *6* (6), 1593-1610.
89. Pfleiderer, H.-J. R. a. G., I. G. Farbenindustrie AG. *Chem. Abstr.* **1939,** *33* (49), 337.
90. M., C. M. J.; Gema, B. B.; G., F. J. L., Hydrogen Peroxide Synthesis: An Outlook beyond the Anthraquinone Process. *Angewandte Chemie International Edition* **2006,** *45* (42), 6962-6984.
91. Lunsford, J. H., The direct formation of H2O2 from H2 and O2 over palladium catalysts. *Journal of Catalysis* **2003,** *216* (1), 455-460.
92. Sayama, K., Production of High-Value-Added Chemicals on Oxide Semiconductor Photoanodes under Visible Light for Solar Chemical-Conversion Processes. *ACS Energy Letters* **2018,** *3* (5), 1093-1101.

93. Shiragami, T.; Nakamura, H.; Matsumoto, J.; Yasuda, M.; Suzuri, Y.; Tachibana, H.; Inoue, H., Two-electron oxidation of water to form hydrogen peroxide sensitized by di(hydroxo)porphyrin GeIV complex under visible-light irradiation. *Journal of Photochemistry and Photobiology A: Chemistry* **2015,** *313*, 131-136.

94. Fuku, K.; Sayama, K., Efficient oxidative hydrogen peroxide production and accumulation in photoelectrochemical water splitting using a tungsten trioxide/bismuth vanadate photoanode. *Chemical Communications* **2016,** *52* (31), 5406-5409.

95. Kojiro, F.; Yuta, M.; Yugo, M.; Takashi, F.; Takahiro, G.; Kazuhiro, S., Photoelectrochemical Hydrogen Peroxide Production from Water on a WO3/BiVO4 Photoanode and from O2 on an Au Cathode Without External Bias. *Chemistry – An Asian Journal* **2017,** *12* (10), 1111-1119.

96. Fuku, K.; Miyase, Y.; Miseki, Y.; Gunji, T.; Sayama, K., WO3/BiVO4 photoanode coated with mesoporous Al2O3 layer for oxidative production of hydrogen peroxide from water with high selectivity. *RSC Advances* **2017,** *7* (75), 47619-47623.

97. Spray, R. L.; Choi, K.-S., Photoactivity of Transparent Nanocrystalline Fe2O3 Electrodes Prepared via Anodic Electrodeposition. *Chemistry of Materials* **2009,** *21* (15), 3701-3709.

98. Martinez, L.; Leinen, D.; Martín, F.; Gabas, M.; Ramos-Barrado, J. R.; Quagliata, E.; Dalchiele, E. A., Electrochemical Growth of Diverse Iron Oxide (Fe3O4, α-FeOOH , and γ-FeOOH) Thin Films by Electrodeposition Potential Tuning. *Journal of The Electrochemical Society* **2007,** *154* (3), D126-D133.

99. Zandi, O.; Schon, A. R.; Hajibabaei, H.; Hamann, T. W., Enhanced Charge Separation and Collection in High-Performance Electrodeposited Hematite Films. *Chemistry of Materials* **2016,** *28* (3), 765-771.

100. Tamboli, S. H.; Rahman, G.; Joo, O.-S., Influence of potential, deposition time and annealing temperature on photoelectrochemical properties of electrodeposited iron oxide thin films. *Journal of Alloys and Compounds* **2012,** *520* (Supplement C), 232-237.

101. Eftekhari, A.; Babu, V. J.; Ramakrishna, S., Photoelectrode nanomaterials for photoelectrochemical water splitting. *International Journal of Hydrogen Energy* **2017,** *42* (16), 11078-11109.

102. Yang, Y.; Niu, S.; Han, D.; Liu, T.; Wang, G.; Li, Y., Progress in Developing Metal Oxide Nanomaterials for Photoelectrochemical Water Splitting. *Advanced Energy Materials* **2017,** *7* (19), 1700555-n/a.

103. Wang, S.; Yun, J.-H.; Wang, L., Chapter Nine - Nanostructured Semiconductors for Bifunctional Photocatalytic and Photoelectrochemical Energy Conversion. In *Semiconductors and Semimetals*, Mi, Z.; Wang, L.; Jagadish, C., Eds. Elsevier: 2017; Vol. 97, pp 315-347.

104. Assresahegn, B. D.; Brousse, T.; Bélanger, D., Advances on the use of diazonium chemistry for functionalization of materials used in energy storage systems. *Carbon* **2015,** *92* (Supplement C), 362-381.

105. Delamar, M.; Hitmi, R.; Pinson, J.; Saveant, J. M., Covalent modification of carbon surfaces by grafting of functionalized aryl radicals produced from electrochemical reduction of diazonium salts. *Journal of the American Chemical Society* **1992,** *114* (14), 5883-5884.

106. (a) Tammeveski, K.; Kontturi, K.; Nichols, R. J.; Potter, R. J.; Schiffrin, D. J., Surface redox catalysis for O2 reduction on quinone-modified glassy carbon electrodes. *Journal of Electroanalytical Chemistry* **2001,** *515* (1), 101-112; (b) Jürmann, G.; Schiffrin, D. J.; Tammeveski, K., The pH-dependence of oxygen reduction on quinone-modified glassy carbon electrodes. *Electrochimica Acta* **2007,** *53* (2), 390-399; (c) Seinberg, J.-M.; Kullapere, M.; Mäeorg, U.; Maschion, F. C.; Maia, G.; Schiffrin, D. J.; Tammeveski, K., Spontaneous modification of glassy carbon surface with anthraquinone from the solutions of its diazonium derivative: An oxygen reduction study. *Journal of Electroanalytical Chemistry* **2008,** *624* (1), 151-160; (d) Mooste, M.; Kibena, E.; Sarapuu, A.; Matisen, L.; Tammeveski, K., Oxygen reduction on thick anthraquinone films electrografted to glassy carbon. *Journal of Electroanalytical Chemistry* **2013,** *702* (Supplement C), 8-14.

107. Hossain, M. S.; Tryk, D.; Yeager, E., The electrochemistry of graphite and modified graphite surfaces: the reduction of O2. *Electrochimica Acta* **1989,** *34* (12), 1733-1737.

108. Li, Q.; Batchelor-McAuley, C.; Lawrence, N. S.; Hartshorne, R. S.; Compton, R. G., Semiquinone Intermediates in the Two-Electron Reduction of Quinones in Aqueous Media and their Exceptionally High Reactivity towards Oxygen Reduction. *ChemPhysChem* **2011,** *12* (7), 1255-1257.

109. Ceccato, M.; Bousquet, A.; Hinge, M.; Pedersen, S. U.; Daasbjerg, K., Using a Mediating Effect in the Electroreduction of Aryldiazonium Salts To Prepare Conducting Organic Films of High Thickness. *Chemistry of Materials* **2011,** *23* (6), 1551-1557.

110. (a) R., H. C. G.; G., W. G.; Li, J.; J., J. T. G.; G., C. R., Chemical Derivatisation of Multiwalled Carbon Nanotubes Using Diazonium Salts. *ChemPhysChem* **2004,** *5* (11), 1794-1799; (b) Pandurangappa, M.; Lawrence, N. S.; Compton, R. G., Homogeneous chemical derivatisation of carbon particles: a novel method for funtionalising carbon surfaces. *Analyst* **2002,** *127* (12), 1568-1571.

111. Wang, J.-S.; Matyjaszewski, K., Controlled/"living" radical polymerization. atom transfer radical polymerization in the presence of transition-metal complexes. *Journal of the American Chemical Society* **1995,** *117* (20), 5614-5615.

112. Kato, M.; Kamigaito, M.; Sawamoto, M.; Higashimura, T., Polymerization of Methyl Methacrylate with the Carbon Tetrachloride/Dichlorotris-(triphenylphosphine)ruthenium(II)/Methylaluminum Bis(2,6-di-tert-butylphenoxide) Initiating System: Possibility of Living Radical Polymerization. *Macromolecules* **1995,** *28* (5), 1721-1723.

113. Fischer, H., The Persistent Radical Effect: A Principle for Selective Radical Reactions and Living Radical Polymerizations. *Chemical Reviews* **2001,** *101* (12), 3581-3610.

114. (a) Matyjaszewski, K.; Kajiwara, A., EPR Study of Atom Transfer Radical Polymerization (ATRP) of Styrene. *Macromolecules* **1998,** *31* (2), 548-550; (b) Kajiwara, A.; Matyjaszewski, K.; Kamachi, M., Simultaneous EPR and Kinetic Study of Styrene Atom Transfer Radical Polymerization (ATRP). *Macromolecules* **1998,** *31* (17), 5695-5701; (c) Kajiwara, A.; Matyjaszewski, K., EPR and Kinetic Studies of Atom Transfer Radical Polymerization of (Meth)acrylates. *Polymer Journal* **1999,** *31*, 70.

115. Matyjaszewski, K.; Xia, J., Atom Transfer Radical Polymerization. *Chemical Reviews* **2001,** *101* (9), 2921-2990.

116. Matyjaszewski, K.; Wang, J.-L.; Grimaud, T.; Shipp, D. A., Controlled/"Living" Atom Transfer Radical Polymerization of Methyl Methacrylate Using Various Initiation Systems. *Macromolecules* **1998,** *31* (5), 1527-1534.

117. Wang, J.-S.; Matyjaszewski, K., Controlled/"Living" Radical Polymerization. Halogen Atom Transfer Radical Polymerization Promoted by a Cu(I)/Cu(II) Redox Process. *Macromolecules* **1995,** *28* (23), 7901-7910.

118. (a) Matyjaszewski, K.; Mu Jo, S.; Paik, H.-j.; Gaynor, S. G., Synthesis of Well-Defined Polyacrylonitrile by Atom Transfer Radical Polymerization. *Macromolecules* **1997,** *30* (20), 6398-6400; (b) Matyjaszewski, K.; Jo, S. M.; Paik, H.-j.; Shipp, D. A., An Investigation into the CuX/2,2'-Bipyridine (X = Br or Cl) Mediated Atom Transfer Radical Polymerization of Acrylonitrile. *Macromolecules* **1999,** *32* (20), 6431-6438.

119. (a) Kotani, Y.; Kamigaito, M.; Sawamoto, M., Living Radical Polymerization of Para-Substituted Styrenes and Synthesis of Styrene-Based Copolymers with Rhenium and Iron Complex Catalysts. *Macromolecules* **2000,** *33* (18), 6746-6751; (b) Percec, V.; Barboiu, B., "Living" Radical Polymerization of Styrene Initiated by Arenesulfonyl Chlorides and CuI(bpy)nCl. *Macromolecules* **1995,** *28* (23), 7970-7972; (c) Kotani, Y.; Kamigaito, M.; Sawamoto, M., Re(V)-Mediated Living Radical Polymerization of Styrene: ReO2I(PPh3)2/R−I Initiating Systems. *Macromolecules* **1999,** *32* (8), 2420-2424.

120. (a) Matyjaszewski, K.; Wei, M.; Xia, J.; McDermott, N. E., Controlled/"Living" Radical Polymerization of Styrene and Methyl Methacrylate Catalyzed by Iron Complexes. *Macromolecules* **1997,** *30* (26), 8161-8164; (b) Ando, T.; Kamigaito, M.; Sawamoto, M., Iron(II) Chloride Complex for Living Radical Polymerization of Methyl Methacrylate. *Macromolecules* **1997,** *30* (16), 4507-4510; (c) Kotani, Y.; Kamigaito, M.; Sawamoto, M., Living Radical Polymerization of Styrene by Half-Metallocene Iron Carbonyl Complexes. *Macromolecules* **2000,** *33* (10), 3543-3549.

121. (a) Ando, T.; Kato, M.; Kamigaito, M.; Sawamoto, M., Living Radical Polymerization of Methyl Methacrylate with Ruthenium Complex: Formation of Polymers with Controlled

Molecular Weights and Very Narrow Distributions. *Macromolecules* **1996,** *29* (3), 1070-1072; (b) François, S.; Albert, D.; F., N. A., Highly Efficient Ruthenium-Based Catalytic Systems for the Controlled Free-Radical Polymerization of Vinyl Monomers. *Angewandte Chemie International Edition* **1999,** *38* (4), 538-540; (c) del Río, I.; van Koten, G.; Lutz, M.; Spek, A. L., Haloalkane C−X Bond Activation by a Ruthenium(II) Complex: X-ray Characterization of a Ruthenium(III) Intermediate Species in the Atom Transfer Radical Polymerization of Methyl Methacrylate. *Organometallics* **2000,** *19* (3), 361-364; (d) Simal, F.; Demonceau, A.; Noels, A. F., Kharasch addition and controlled atom transfer radical polymerisation (ATRP) of vinyl monomers catalysed by Grubbs' ruthenium carbene complexes. *Tetrahedron Letters* **1999,** *40* (31), 5689-5693.

122. (a) Uegaki, H.; Kotani, Y.; Kamigaito, M.; Sawamoto, M., Nickel-Mediated Living Radical Polymerization of Methyl Methacrylate. *Macromolecules* **1997,** *30* (8), 2249-2253; (b) Uegaki, H.; Kotani, Y.; Kamigaito, M.; Sawamoto, M., NiBr2(Pn-Bu3)2-Mediated Living Radical Polymerization of Methacrylates and Acrylates and Their Block or Random Copolymerizations. *Macromolecules* **1998,** *31* (20), 6756-6761.

123. (a) Brandts, J. A. M.; van de Geijn, P.; van Faassen, E. E.; Boersma, J.; van Koten, G., Controlled radical polymerization of styrene in the presence of lithium molybdate(V) complexes and benzylic halides. *Journal of Organometallic Chemistry* **1999,** *584* (2), 246-253; (b) Le Grognec, E.; Claverie, J.; Poli, R., Radical Polymerization of Styrene Controlled by Half-Sandwich Mo(III)/Mo(IV) Couples: All Basic Mechanisms Are Possible. *Journal of the American Chemical Society* **2001,** *123* (39), 9513-9524.

124. Moineau, G.; Minet, M.; Dubois, P.; Teyssié, P.; Senninger, T.; Jérôme, R., Controlled Radical Polymerization of (Meth)acrylates by ATRP with NiBr2(PPh3)2 as Catalyst. *Macromolecules* **1999,** *32* (1), 27-35.

125. Lecomte, P.; Drapier, I.; Dubois, P.; Teyssié, P.; Jérôme, R., Controlled Radical Polymerization of Methyl Methacrylate in the Presence of Palladium Acetate, Triphenylphosphine, and Carbon Tetrachloride. *Macromolecules* **1997,** *30* (24), 7631-7633.

126. Pintauer, T.; Matyjaszewski, K., Atom transfer radical addition and polymerization reactions catalyzed by ppm amounts of copper complexes. *Chemical Society Reviews* **2008,** *37* (6), 1087-1097.

127. Xia, J.; Matyjaszewski, K., Controlled/“Living” Radical Polymerization. Atom Transfer Radical Polymerization Using Multidentate Amine Ligands. *Macromolecules* **1997,** *30* (25), 7697-7700.

128. Queffelec, J.; Gaynor, S. G.; Matyjaszewski, K., Optimization of Atom Transfer Radical Polymerization Using Cu(I)/Tris(2-(dimethylamino)ethyl)amine as a Catalyst. *Macromolecules* **2000,** *33* (23), 8629-8639.

129. Bui, T. T. V. Redox active ionic liquids from synthesis to surface modification : grafting and surface polymerization towards functional electrode materials. 2015.

130. Hansson, S.; Östmark, E.; Carlmark, A.; Malmström, E., ARGET ATRP for Versatile Grafting of Cellulose Using Various Monomers. *ACS Applied Materials & Interfaces* **2009,** *1* (11), 2651-2659.

131. Ahmed, M. G.; Kretschmer, I. E.; Kandiel, T. A.; Ahmed, A. Y.; Rashwan, F. A.; Bahnemann, D. W., A Facile Surface Passivation of Hematite Photoanodes with TiO2 Overlayers for Efficient Solar Water Splitting. *ACS Applied Materials & Interfaces* **2015,** *7* (43), 24053-24062.

132. Ahn, H.-J.; Yoon, K.-Y.; Kwak, M.-J.; Jang, J.-H., A Titanium-Doped SiOx Passivation Layer for Greatly Enhanced Performance of a Hematite-Based Photoelectrochemical System. *Angewandte Chemie International Edition* **2016,** *55* (34), 9922-9926.

133. Cummings, C. Y.; Marken, F.; Peter, L. M.; Tahir, A. A.; Wijayantha, K. G. U., Kinetics and mechanism of light-driven oxygen evolution at thin film α-Fe2O3 electrodes. *Chemical Communications* **2012,** *48* (14), 2027-2029.

134. Upul Wijayantha, K. G.; Saremi-Yarahmadi, S.; Peter, L. M., Kinetics of oxygen evolution at alpha-Fe2O3 photoanodes: a study by photoelectrochemical impedance spectroscopy. *Physical chemistry chemical physics : PCCP* **2011,** *13* (12), 5264-70.

135. Ponomarev, E. A.; Peter, L. M., A generalized theory of intensity modulated photocurrent spectroscopy (IMPS). *Journal of Electroanalytical Chemistry* **1995,** *396* (1), 219-226.

136. (a) Peter, L. M., Dynamic aspects of semiconductor photoelectrochemistry. *Chemical Reviews* **1990,** *90* (5), 753-769; (b) Li, J.; Peter, L. M., Surface recombination at semiconductor electrodes: Part III. Steady-state and intensity modulated photocurrent response. *Journal of Electroanalytical Chemistry and Interfacial Electrochemistry* **1985,** *193* (1), 27-47; (c) Peat, R.; Peter, L. M., A study of the passive film on iron by intensity modulated photocurrent spectroscopy. *Journal of Electroanalytical Chemistry and Interfacial Electrochemistry* **1987,** *228* (1), 351-364.

137. Bui-Thi-Tuyet, V.; Trippé-Allard, G.; Ghilane, J.; Randriamahazaka, H., Surface and Electrochemical Properties of Polymer Brush-Based Redox Poly(Ionic Liquid). *ACS Applied Materials & Interfaces* **2016,** *8* (42), 28316-28324.

138. (a) Li, Q.; Antony, R. P.; Wong, L. H.; Ng, D. H. L., Promotional effects of cetyltrimethylammonium bromide surface modification on a hematite photoanode for photoelectrochemical water splitting. *RSC Advances* **2015,** *5* (121), 100142-100146; (b) Feng, C.; Wang, L.; Fu, S.; Fan, K.; Zhang, Y.; Bi, Y., Ultrathin FeFx nanolayers accelerating hole transfer for enhanced photoelectrochemical water oxidation. *Journal of Materials Chemistry A* **2018,** *6* (40), 19342-19346.

139. Pham Truong, T. N.; Randriamahazaka, H.; Ghilane, J., Polymer Brushes Ionic Liquid as a Catalyst for Oxygen Reduction and Oxygen Evolution Reactions. *ACS Catalysis* **2018,** *8* (2), 869-875.

140. Dunn, H. K.; Feckl, J. M.; Müller, A.; Fattakhova-Rohlfing, D.; Morehead, S. G.; Roos, J.; Peter, L. M.; Scheu, C.; Bein, T., Tin doping speeds up hole transfer during light-driven water oxidation at hematite photoanodes. *Physical Chemistry Chemical Physics* **2014,** *16* (44), 24610-24620.

141. (a) Kelly, J. J.; Memming, R., The Influence of Surface Recombination and Trapping on the Cathodic Photocurrent at p-Type III-V Electrodes. *Journal of The Electrochemical Society* **1982,** *129* (4), 730-738; (b) Dare-Edwards, M. P.; Goodenough, J. B.; Hamnett, A.; Trevellick, P. R., Electrochemistry and photoelectrochemistry of iron(III) oxide. *Journal of the Chemical Society, Faraday Transactions 1: Physical Chemistry in Condensed Phases* **1983,** *79* (9), 2027-2041; (c) Bertoluzzi, L.; Lopez-Varo, P.; Jiménez Tejada, J. A.; Bisquert, J., Charge transfer processes at the semiconductor/electrolyte interface for solar fuel production: insight from impedance spectroscopy. *Journal of Materials Chemistry A* **2016,** *4* (8), 2873-2879.

142. Wang, Z.; Fan, F.; Wang, S.; Ding, C.; Zhao, Y.; Li, C., Bridging surface states and current–potential response over hematite-based photoelectrochemical water oxidation. *RSC Advances* **2016,** *6* (88), 85582-85586.

143. Klahr, B.; Gimenez, S.; Zandi, O.; Fabregat-Santiago, F.; Hamann, T., Competitive Photoelectrochemical Methanol and Water Oxidation with Hematite Electrodes. *ACS Applied Materials & Interfaces* **2015,** *7* (14), 7653-7660.

144. Iandolo, B.; Hellman, A., The Role of Surface States in the Oxygen Evolution Reaction on Hematite. *Angewandte Chemie International Edition* **2014,** *53* (49), 13404-13408.

145. Zandi, O.; Hamann, T. W., Enhanced Water Splitting Efficiency Through Selective Surface State Removal. *The Journal of Physical Chemistry Letters* **2014,** *5* (9), 1522-1526.

146. Qu, Y.; Wang, W.; Jing, L.; Song, S.; Shi, X.; Xue, L.; Fu, H., *Surface modification of nanocrystalline anatase with CTAB in the acidic condition and its effects on photocatalytic activity and preferential growth of TiO2*. 2010; Vol. 257, p 151-156.

Chapter – 4

General Conclusion & Perspective

4.1. Conclusion:

Herein we summarize all the results obtained during the course of this Ph.D together with some perspectives of this work.

The main objective of this thesis was to develop proof-of-concept device for photoelectrochemical micromotor. In this framework, to convert solar energy into chemical energy, specifically to hydrogen peroxide, surface functionalized hematite photoanodes with anthraquinone based materials were used. For the conversion of chemical to mechanical energy, manganese oxide micromotor was used.

In Chapter – 2, first part deals with the fabrication of MnO_2 micromotor by employing polymer assisted metal deposition and electrodeposition process. Compared to commonly used template assisted electrodeposition method, this process is quite simple, cheap and efficient. This process requires a charged polymer and hence an anionic polymer, Nafion, was chosen and over that nickel was electrolessely deposited. The resulting nickel film was showing good conductivity and used as a working electrode to electrodeposit PANI and MnO_2. The role of PANI layer is not only enhancing the stability but also act as a matrix to hold MnO_2 particles. By using cyclic voltammogram, MnO_2 microparticles were electrodeposited over PANI coated Ni film. Thus prepared MnO_2 micromotor showed good bubble induced wireless propulsion and worked well across the pH range from 5.5 to 13. Various shapes such as square, rectangular and circular forms of micromotors were prepared and circular form exhibited higher speed among them, may be due to its curvature, and also the speed of the micromotor increases with increase of fuel concentration. The mechanisms behind the MnO_2 electrodepostion and oxygen bubble evolution reaction were discussed.

The next part describes the newly developed approaches to control the motion of micromotor. To achieve the potential applications from bubble propelled micromotors, to control its speed and direction is must. Usually the micromotors are controlled and directed by external means, such as an external magnetic field, electric field or ultrasound etc., These controlling methods are having certain disadvantages such as lack the possibility of having negative controls, or can only steer into one side and magnetic stimuli methods can be applied to only ferromagnetic materials. We have utilized the chemotactic behaviour of micromotor for control its movement. We have generated H_2O_2 electrochemically at the working electrode

by following the two electron pathway to reduce the available O_2 in the solution. The distantly placed micromotor gradually sense the concentration gradient of H_2O_2 and move towards the source of generation. Thus this positive chemotactic behaviour of micromotor helped to gain control over its movement. Further research is required to understand the reason behind this positive chemotaxis and also the systematic investigation is needed to know upto what distance the micromotor can sense the concentration gradient of fuel. In this chapter, we also showed the proof-of-concept of novel technology for controlling and steering micromotors, to fill the gap left by currently available devices. We have developed microvehicles by microfabrication process and thus developed microvehichles provide individual mechanical stimulation at different voltages and array-based stimulation patterns to single motors or clusters of motors, including controls, all integrated in a single device. Thus microfabricated motors were covered by PPy which undergoes volume(porosity) change based on the applied potential, thus enable and stop diffusion of H_2O_2 to MnO_2 surface, and inturn turning on or turning off the bubble generation. The devices can be developed for in situ drug delivery in future, however the unwanted bubble generation from the electrical contacts has to be solved. The novelty in our approach is that it is easy to microfabricate, there is no need of expensive external instruments like magnetic and acoustic sources, and it can be applied to a wide range of materials.

At Chapter – 3, first, we have investigated the surface fuctionalization of hematite photoanodes with AQ by electrografting and SI-ATRP methods. Monolayer of AQ was grafted over hematite photoanode by reductive electrografting. To our knowledge, this is the first attempt to graft AQ by diazonium electrografting on the semiconducting hematite photoanode. The grafted AQ was found to be very effective in photoelectrochemical reactions. The AQ electrografted hematite was characterized by SEM, XPS, XRD and contact angle measurements. From these measurements, it is found that the electrografted AQ layer is very thin and not altering the nanostructuring morphology of hematite as well as the contact angle property. AQ polymer brushes were grown on hematite by SI-ATRP process. To do so, monomer of N-ethyleneamidoanthraquinone-N-vinylimidazolium bis(trifluoromethylsulfonyl)imide was synthesized. For ATRP, the role of surface initiator is very crucial. It is found out that the initiator attached by using 2-bromoethylamine that works well for glassy carbon electrode is not suitable for hematite. Hence bromide termination by

exploiting hydroxyl groups available on the hematite surface was performed and it initiated well the growth of polymer brushes of AQ poly ionic liquid on the surface of hematite. The AQ polymer brushes immobilized hematite was characterized by SEM, AFM, XPS, XRD and contact angle measurements. The XRD and XPS confirms the hematite phase, and the contact angle value is almost halved, 11.5° compared to bare (21.4°) and diazonium AQ (22°). In both the cases, the covalent anchoring of AQ over hematite surface was confirmed by recording cyclic voltammogram in only supporting electrolyte solution at different scan rates and observed the typical redox peaks of AQ to AQH_2 conversion and also the linear variation of peak current with respect to its corresponding scan rate. It is also shown that bromide termination on hematite can be done by means of reductive diazonium electrografting by using p-diazonium phenyl bromide which also act as good initiator to grow the polymer brushes of AQ. To understand the role of imidazolium ring on photoelectrochemical properties, Imidazolium based ionic liquid without AQ redox group, namely N-methyl-N`-vinylimidazolium bis(trifluoromethylsulfonyl)imide was synthesized and grafted over hematite by SI-ATRP method showed the contact angle value (19.4°) closer to bare hematite(21.4°), but larger than AQ PIL modified hematite (11.6°).

Next the role of surface modification on photoelectrochemical behaviour of hematite was scrutinized. The main role of AQ is that it is capable of reducing O_2 into H_2O_2. Firstly, the photoelectrochemical behaviour of AQ electrografted hematite was investigated in presence of different hole scavengers and AQ grafted hematite photoanode outperformed the unmodified hematite. It is also found out that the formal potential of the hole scavengers play a crucial role in photoelectrochemistry. i.e., if the formal potential is higher then the photocurrent will be lower and vice-versa. It was observed that the photoelectrochemical performance of AQ electrografted hematite was lower compared to AQ poly ionic liquid immobilized hematite because the electrografting forms a monolayer of AQ whereas the SI-ATRP forms nanostructured polymer brushes of AQ. We believe that not only the higher amount of AQ but also the nanostructuration and the presence of imidazolium ring in AQ poly ionic liquid enhance the photoelectrochemical behaviour. Thus to gain a deeper understanding, various surface modified hematite samples such as hematite photoanode with only bromide initiator (Br) and with imidazolium based poly ionic liquid that contains no redox active group (Imidazolium), then finally with redox active AQ poly ionic liquid (AQ)

were photoelectrochemically analyzed by using LSV, IMPS as well as PEIS and compared with that of unmodified hematite sample (Bare) in a step by step manner and found out that the bromide initiator plays a vital role in enhancing the charge transfer by developing a negative electric field thus inturn effectively pulls out the holes from the valence band. The surface modifiers are not acting as catalysts but governs the fate of charge transfer by altering the interfacial properties. The ionic liquid modified hematite samples favor the direct charge transfer whereas the bromide and bare hematite photoanodes prefer the surface state mediated indirect charge transfer. The presence of carbon atom in between the nitrogen atoms in the imidazolium ring is believed to be the main reason for the improved water oxidation in the case of poly ionic liquid modified hematite photoanodes. This carbon atom adsorbs OH^- and so enhancing the photoelectrocatalytic cycle of oxygen evolution reaction.

Main highlights of this thesis are the following:

- To the best of our knowledge, this is the first report showing the successful reductive electrografting of AQ on hematite photoanode and also showed that the electrografted AQ enhances the photoelectrochemical behaviour of hematite photoanode.
- The most common method to immobilize ionic liquid on oxide surface is by employing silanol chemistry, but it is only applicable to silicon containing surfaces. In this thesis, we have shown a new approach to immobilize poly ionic liquid by employing SI-ATRP process on iron oxide surface. This new functionalization method, in our belief, can be applied to prepare well defined oxide – ionic liquid interfaces with improved stability and charge transport properties and be very useful in various electronic and electrochemical related applications.
- Generally, the ionic liquids are used as solvents, electrolytes and binders for electrochemical energy storage and conversion devices. Recently, there are some reports showing that the ionic liquids can be used as electrocatalyst for oxygen reduction and evolution reactions. But this is the first report showing the use of poly ionic liquids as photoelectrode surface modifiers and their role in PEC water splitting.

- There are few reports in the field of micromotors showing chemotaxis, pH taxis, thermotaxis and phototaxis etc. In this thesis, we have developed a new approach to show chemotaxis by electrochemically generating H_2O_2 by reducing available oxygen in the solution.

- Also proposed a new concept to control and steer the direction of micromotor by tuning the volume and porosity of polypyrrole. This method is having an advantage that it can be applied to any kind of materials whereas the available methods, for example, the magnetic control can be used only for the ferromagnetic materials.

4.2. Challenges & Perspective:

(i) pH of the solution:

The micromotor works well across the pH range from 5.5 to 13, but shows better performance at pH – 5.5 which is closer to physiological pH condition whereas the PEC system works well in pH – 5.5 citrate buffer solution as well as in pH – 13 alkaline solution. To develop the final device, PEC micromotor, the system should be optimized for the physiological pH – 7, so that it can be tried for making drug delivery and other bio related applications as well as for removing pollutants from the water resources.

(ii) Integration:

To realize the final photoelectrochemical micromotor device, the PEC system and the micromotor should be coupled together. Coulpling should be done without compromising the performance of each component. Also the biocompatability of the photoelectrode should be checked. On the other hand, the hematite is not having broad absorption spectrum range to cover enough all the visible and NIR range. Organic photoelectrodes can be tried because they have tunable opto-electronic properties and structural diversity. Deisigning and constructing highly efficient and biocompatible photoelectrode for photoelectrochemical micromotor are still a big challenge.

The light and fuel are the main energy parameters for developing the future PEC micromotors. So far, H_2O_2 is commonly used as a fuel for the bubble propulsion system, however H_2O_2 powered motors are not suitable for biomedical applications because of the toxicity of H_2O_2 that causes apoptosis and hence motors powered by other sources are to be developed for biomedical applications. In this context, glucose and enzymes powered micromotors have recently attracted much attention. Light can be used as an non-invasive external stimulus to control the movement of PEC micromotor. By varying the light intensity, the speed of the PEC micromotor can be adjusted. The direction of the PEC motor may be adjusted by changing the light source position. More research work is required in the direction of light controlled movement and direction of PEC micromotor.

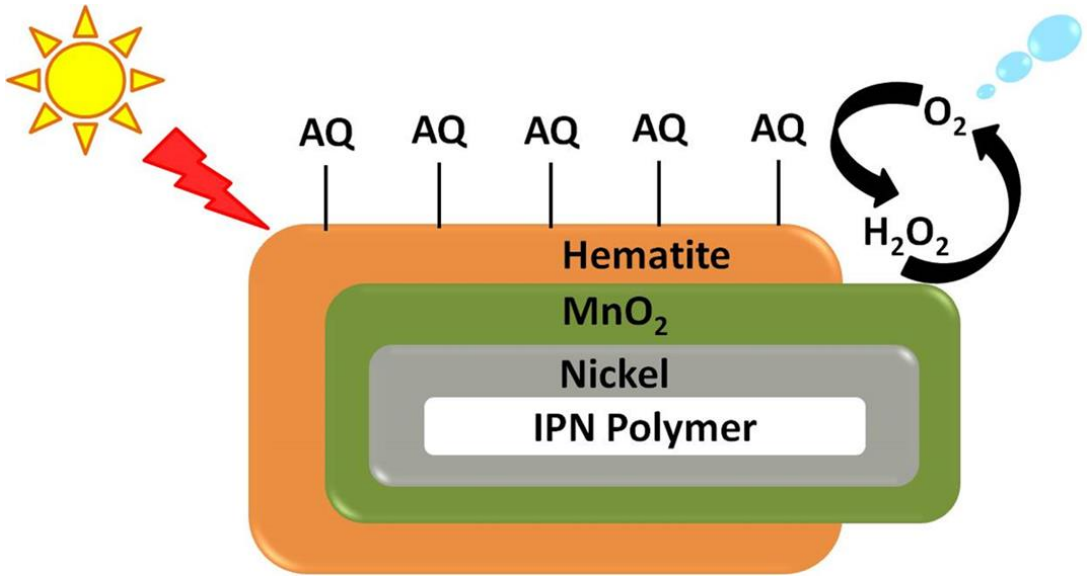


Figure 1. Schematic representation of wireless photoelectrochemical micromotor comprising of the anthraquinone immobilized PEC system as well as the MnO_2 micromotor system.

As shown in the Fig.1. the PEC micromotor device can be developed by integrating the AQ attached photoelectrode with MnO_2 micromotor. Electrodeposited hematite photoanode is not

a suitable photoelectrode since it needs high temperature annealing which will damage the MnO_2 micromotor. Also the spectral absorption range of hematite is not broad, hence the hematite to be replaced by suitable and compatible photoanode. There are some photoanodes that usually oxidize water into H_2O_2, for example g–C_3N_4, can also be tried to generate H_2O_2 directly and thus avoid the complexity. When the photoelectrode system generates H_2O_2, the MnO_2 micromotor uses this as a fuel and exhibit O_2 bubbles induced propulsion. Thus generated O_2 bubbles can be reduced back to H_2O_2 by the immobilized AQ. This cycle will be continued until the light shines. Thus the overall system will lead to the fabrication of wireless autonomous photoelectrochemical micromotor. The future work should be mainly focussed on three key points: first, develop efficient and functionalized biocompatible motor; second, optimize the motor in the environmentally benign light range; finally, optimize it for the biocompatible fuels.

Résumé

Les actionneurs sont des dispositifs aptes à convertir une énergie électrique en travail mécanique. Le mécanisme et le processus de conversion d'énergie dépendent des propriétés physico-chimiques du matériau utilisé. On peut citer les polymères électroactifs qui forment une vaste famille de matériaux stimulables aptes à changer de dimension et/ou de forme en réponse à des stimulations électriques appropriées. Il en résulte la transformation de l'énergie électrique en travail mécanique. Cette transformation d'énergie est appelée actionnement. Les dispositifs à base de polymère électroactif ont des propriétés uniques telles que des déformations électriquement contrôlables, une grande souplesse mécanique, une faible masse volumique et, dans la majorité des cas, un faible coût. Ces matériaux stimulables présentent une certaine similitude, du point de vue technique, avec les tissus musculaires naturels. C'est pourquoi ces matériaux stimulables sont également appelés muscles artificiels. Ces polymères électroactifs incluent les polymères piézoélectriques, les polymères électrostrictifs ainsi que les élastomères diélectiques. Ces matériaux stimulables trouvent leur application dans différents domaines tels la robotique et les organes artificiels.

Ce travail de thèse est une contribution à la mise au point de micromoteur pour un transporteur (mini- ou micro-bateau) bio-inspiré autonome et sans fil qui pourra être télécommandé à l'aide de la lumière. Ainsi, il sera possible de générer un travail mécanique par la conversion de l'énergie lumineuse des photons via une réaction photoélectrochimique en phase hétérogène. De plus, la dynamique de ce transporteur autonome sera contrôlée par un processus de chimiotactisme qui permet d'orienter son déplacement selon le gradient de concentration d'un messager chimique généré in-situ. Il sera envisagé d'utiliser ce type de mini-bateau pour transporter et libérer un composé chimique, tel un principe actif, vers un endroit cible où le messager chimique serait généré. Ce travail s'inscrit dans le projet Européen MICACT (Microactuators) de type ITN (Innovative Training Networks).

Dans ce contexte, l'objectif principal de cette thèse était d'étudier certains éléments en vue du développement d'un micromoteur photoélectrochimique doté de propriété de chimiotactisme dont la propulsion résulte de la dismutation du peroxyde d'hydrogène H_2O_2 catalysée par le manganèse MnO_2 générant ainsi la production local d'oxygène O_2 à l'état gazeux. La

production locale d'oxygène engendre un gradient local de pression qui génère une propulsion. Le peroxyde d'hydrogène sera produit localement à la surface du dispositif grâce à un processus photoélectrochimique mettant en jeu la photoréduction de l'oxygène en présence d'anthraquinone immobilisée. Ainsi, pour convertir l'énergie solaire en énergie chimique, des photoanodes d'hématite fonctionnalisées par l'anthraquinone ont été utilisées. Par la suite, cette énergie chimique sera convertie localement en énergie mécanique grâce à la dismustation de H_2O_2 en O_2 et H_2O en présence de MnO_2; la production d'O_2 engendre la propulsion. Afin de contrôler le déplacement du mini-transporteur, nous nous sommes inspirés du processus de chimiotactisme. En effet, dans la nature, pour détecter les produits chimiques environnants et y réagir, les organismes dépendent généralement d'un phénomène appelé chimiotaxie. Le processus de chimiotactisme n'est rien d'autre qu'une migration d'organismes due à un gradient de concentration d'un produit chimique particulier vers ou à partir d'un endroit particulier conduisant à un processus de marche aléatoire biaisé. Ainsi, selon la direction du mouvement, que le mouvement se fasse vers le produit chimique ou en s'en éloignant, la chimiotaxie est appelée respectivement chimiotaxie positive ou négative. Dans le monde biologique, on peut observer de nombreux exemples d'organismes qui utilisent la chimiotaxie pour communiquer et accomplir des tâches collectives. Ainsi, les bactéries peuvent sentir le gradient de concentration de l'attractif (se déplacer vers) et de la toxine (s'éloigner). De même, certains systèmes non biologiques présentent également un comportement chimiotaxique. Au lieu d'appliquer des champs externes, si les micromoteurs se déplacent en fonction du comportement chimiotactique, il sera possible d'ouvrir de nouvelles voies dans des applications biomédicales in vivo pour réaliser un contrôle spatial directionnel.

La première partie de thèse est consacré à la fabrication du micromoteur à base de MnO_2 en utilisant un procédé de dépôt et d'électrodéposition assisté par polymère ionique. Comparé à la méthode d'électrodéposition assistée par gabarit couramment utilisée, ce procédé est assez simple, bon marché et efficace. Ce procédé nécessite un polymère chargé, tel le Nafion, qui servira à la fois de matériau support et de confiner par interaction électrostatique un catalyseur pour la déposition chimique du nickel. Le film de nickel ainsi obtenu servira d'électrode pour l'électrodépostion de polymère conducteur, la polyaniline (PANI), au sein duquel sera déposé du MnO_2 par voie électrochimique. Le rôle de la couche PANI n'est pas seulement d'améliorer

la stabilité mais également comme une matrice emprisonnant les particules de MnO2 déposées. Le micromoteur à base de MnO_2 ainsi préparé a été testé dans une solution tamponnée contenant de H_2O_2. Les résultats ont montré une propulsion induite par la libération de bulle d'O_2. Le processus de propulsion est observé dans une gamme de pH allant de 5,5 à 13. Diverses formes de micromoteurs telles que des formes carrées, rectangulaires et circulaires ont été préparées. Dans la même condition expérimentale, la forme circulaire a une vitesse de déplacement plus élevée. Nous avons également observé que la vitesse de déplacement du micromoteur augmente avec la concentration de H_2O_2. Les mécanismes derrière l'électrodéposition du MnO_2 et la formation de bulle d'oxygène ont été discutés.

La partie suivante, en utilisant l'approche bio-inspirée pour contrôler son mouvement, nous avons exploré le comportement chimiotactique du micromoteur. A cette fin, H_2O_2 a été généré au moyen de la réduction électrochimique de l'O_2 dans la solution en utilisant une électrode de carbone. Il en résulte la mise en place spontanée d'un gradient de concentration de H_2O_2 à partir de la surface de l'électrode. Le micromoteur placé à distance donné par rapport à l'électrode détecte progressivement le gradient de concentration de H_2O_2 généré à la surface de l'électrode et se déplace spontanément vers la source de génération. Ainsi, ce comportement chimiotactique positif du micromoteur a aidé à contrôler son mouvement. Nous avons également développé des microvéhicules par procédé de microfabrication et avons ainsi développé des microvéhicules qui fournissent une stimulation mécanique individuelle à différentes tensions et des modèles de stimulation basés sur des réseaux à des moteurs uniques ou à des groupes de moteurs, y compris des commandes, tous intégrés dans un seul dispositif.

La seconde partie de la thèse est consacrée à l'élaboration et l'étude de photoanode d'hématite modifiée par l'anthraquinone. L'anthraquinone servira de piège à électrons lors de la génération de paire électron-trou lors de la photo-excitation du semiconducteur de type n, ici l'hématite. Par la suite, la photo-réduction d'O_2 en H_2O_2 sera favorisée par l'anthraquinone ainsi réduite. Il est alors possible de produire du H_2O_2 par un processus photoélectrochimique. Différentes méthodes d'immobilisation de l'anthraquinone ont été effectuées et étudiées : électrodéposition et les brosses de polymères. Les surfaces de l'hématite ainsi modifiées ont été caractérisées par différentes techniques : microscopie électronique à balayage (SEM), diffraction X (XRD), spectrométrie de photoélectrons induits par rayons (XPS) et mesure

d’angle de contact. Les propriétés photoélectrochimiques de l’hématite modifiée ont été étudiées en détail afin de mieux appréhender l’influence de la modification de surface. En particulier, nous avons étudié l’influence sur les propriétés photoélectrochimiques des différentes étapes lors de la polymérisation amorcée à partir d’une surface conduisant aux brosses de polymères. Pour cela, nous avons combiné différentes techniques photoélectrochimiques telles que la voltammétrie à balayage linéaire sous illumination intermittente, la spectroscopie d’impédance électrochimique et la technique Intensity Modulated Photocurrent Spectroscopy (IMPS). Les processus de photo-oxydation de H_2O ont été analysés. Les résultats montrent que la modification de surface module les propriétés photocatalytiques. Nous avons montré que ces modifications de surface entrainent une passivation de la photoanode. Cette passivation diminue la densité de pièges pour les porteurs de charge à la surface de l’anode conduisant une amélioration de rendement de l’oxydation de l’eau. Par ailleurs, cette modification de surface engendre un déplacement du potentiel de bande plat. Il est important de noter que ces espèces chimiques immobilisées à la surface de la photoanode ne sont pas des catalyseurs, au sens chimique du terme. Néanmoins, leur immobilisation module les propriétés physico-chimiques de l’interface de la photoanode en favorisant la participation du trou généré dans la bande de valence du semiconducteur à l’oxydation de l’eau. De même, il n’est pas exclu que l’immobilisation de ces molécules organiques à la surface de la photoanode génère un dipôle modulant le champ électrique locale et par la même occasion la courbure des bandes dans l’hématite.